MAGNETOHYDRODYNAMICS OF ACCRETION TO ROTATING MAGNETIZED STARS

A Dissertation

Presented to the Faculty of the Graduate School

of Cornell University

in Partial Fulfillment of the Requirements for the Degree of

Doctor of Philosophy

by

Sergei Dyda

August 2015

MAGNETOHYDRODYNAMICS OF ACCRETION TO ROTATING MAGNETIZED STARS

Sergei Dyda, Ph.D.

Cornell University 2015

Many astrophysical systems consist of a central object, an accretion disc and a large scale magnetic field. Understanding their interaction, in the case where the central object is a young star, is important for undertanding stellar evolution and planet formation. The key process in this system is accretion - matter in the disc falls into the potential well of the central object, providing energy to drive the system. The key problem is understanding how angular momentum is transported in the disc, allowing matter to accrete onto the star. We investigate several astrophysical scenarios to better understand angular momentum transport in accretion discs.

One scenario consists of a large scale "looped" magnetic field threading the disc - this magnetic field advects matter towards the star by driving angular momentum outwards along the field lines in the form of matter and Poynting jets. This enhances accretion rates at the surface of the star by a factor of a few.

Another scenario consists of feeding matter that is counter rotating with respect to the main part of the disc, as might happen if it were sourced by a nearby counter-rotating binary or molecular cloud. A shear layer forms at the interface of this rotating/counter-rotating matter, which depends sensitively on the viscous properties of the fluid. Accretion rates can be enhanced by factors of $10 - 10^4$.

Observations suggest that jets and winds are asymmetric about the disc

plane. We investigate possible magnetic field configurations which exhibit these asymmetric outflows by considering combinations of stellar dipole fields and an aligned or misaligned disc field. We find that the inclusion of a dipole field or a strong enough disc field produces asymmetric outflows at late times despite initial conditions being symmetric.

We explore one possible mechanism for generating the large scale magnetic field required by these systems to produce outflows, the α-dynamo. We find that an α-dynamo operating in the disc produces primarily dipole magnetic fields around the star. Seed fields initially too weak to launch outflows can grow sufficiently to launch outflows with densities consistent with observations.

BIOGRAPHICAL SKETCH

Sergei Dyda was born September 20, 1985 in Montreal, Canada. He completed his Bachelor of Science degree at McGill University, majoring in Mathematics and Physics in 2007. He completed a Master of Science degree in physics at the University of Toronto, under the supervision of Professor Amanda Peet in 2008. His PhD work in theoretical physics, in the area of magnetohydrodynamics (MHD) simulations of protostars, was conducted at Cornell University from 2008-2015 under the supervision of Professor Richard Lovelace and Dr. Marina Romanova.

His scientific interests include accretion processes, astrophysical jets and winds, disc instabilities and magnetic dynamos. To the befuddlement of his non-Canadian thesis advisors, he spends much of his free time coaching ice hockey and thinking about sports analytics.

To my family - for understanding even though you don't understand.

ACKNOWLEDGEMENTS

Firstly I want to acknowledge my biological family for the financial and emotional support since day one. Wally was always supportive of me studying physics even though I assured him it would never lead to a job. I miss my old man a lot and his spirit continues to inspire my work. Claudette, thanks for your tireless efforts in raising your children right - I might have been a better physicist if I'd received the odd oscilliscope at Christmas time, but I can't imagine that making me a better person. Lydia, I'm sorry I recommended you study physics in school too. It's really worked out well for me, but I guess it's not for everyone. Elisabeth, we're more alike than either of us wants to admit - thanks for pushing me to do great things. To Ginette, hopefully this inspires you to finish your thesis that has been on the backburner since the 1980's. Carol - for showing me the importance of keeping my child-like imagination. To Ihor - no words come to mind, but then again, none were ever needed. To my grandparents, thanks for teaching me what real hard work looks like.

To Marina and Richard, thanks for having given a washed up fourth year grad student a chance in your research group. You've both made me into the scientist I am today - I'm so grateful for you having brought me into the world of magnetohydrodynamics, I wish I'd found out about this fascinating area years ago. Thanks to my close research collaborators Patrick, Megan, Galia, Sasha, Loren and Dan. I cannot begin to thank you for everything you've taught me over the years. I could not be blessed with better collaborators and friends. I hope we collaborate on new projects again, sooner, rather than later.

Thanks to the scientists with whom I've had the privelage of being mentored by as I've embarked on my scientific career - Michael Hilke, Ken Ragan, Robert Brandenberger, Dmitry Jakobson, Amanda Peet, David Chernoff, Enrico Pajer,

Eanna Flanagan & Ira Wasserman. Thanks to the enumerable grad students who contributed to the fertile academic environment here at Cornell during my 7 years. In particular, thanks to Zach and Alex who with me called "The Institute" their home. Thanks to Dusty, Jenn and Gala for all the nights eating burgers and deep philosophical discussions. Thanks to those who have inspired me to become a better physics teacher, notably Phil Krasicky, Mukund Vengalattore, Erich Mueller and Seamus Davis - I value the lessons learned TAing for you and will put them to good use. Thanks to my colleagues from undergrad, with whom the physics seed was planted so many years ago - William, Guillaum, Jean-Michel, Bertrand, Tayeb, Patrick, Patrick Fourrier, Christian, Liz, Olga, Bobak, Charles, Michael, Philippe, Greg, Jean, Leila and Dave.

To those who have helped me grow as a person and in life - Diego, Paul, Edipo, Tyler, Jon, Hristo, Lister, Aaron, Jody, Julien, Jeffy, Tim, Todd, Adam, Silpa, Max, Brad, Alex, Natalie & Gaspard.

To those who have made their way into my life through ice hockey, my only other great passion - To the Chapter House Team, though our championship picture no longer hangs on the Chappie's hallowed walls, it's memory, I know, continues to burn, immortal, in our hearts. Thanks to Coach Schafer, Syer and Scott for letting me clip game footage for 2 years. Seeing how you run your world class program from the inside has been inspiring. Thanks to everyone I've had the honor of interacting with through Cornell Club Hockey. In particular, thanks to Michael Robinson, Ryan Kindret, Chris Newman and John McKinley who taught me to be a better coach and leader. Thanks to all the players for all your commitment over the years and sharing in the passion of the game we love. I will never forget winning the NECHL championship in 2012 in double OT in Syracuse and bringing the Cup back to Pixies. Winning at the rink

ignites a child-like passion like nothing else in life.

Finally, I would like to acknowledge High Point Farm and Early Morning Farm for providing much healthful produce that has sustained me over the last 7 years.

Sergei Dyda

August 3, 2015

Ithaca, NY

TABLE OF CONTENTS

CHAPTER 1

INTRODUCTION

1.1 Disc Accretion

On astronomical scales, gravity is the dominant force. Though there exist many different types of astronomical bodies many of them can be thought of to first order as consisting of a central object, interacting gravitationally with an accretion disc of matter around it. This grossly simplified picture captures the basic physics for a host of astronomical systems, spanning many orders of magnitude in length scale, from pre-main-sequence stars with accretion discs, to galaxies powered by AGNs. Knowing that gravity is the main force responsible for the physics of accretion discs allows us to estimate the energy scales involved. Consider a unit mass m falling in from infinity towards a central object of mass M_* and radius r_*. It's change in gravitational potential energy

$$E_{\rm grav} = -\frac{GM_*m}{r_*}, \tag{1.1}$$

where G is the gravitational constant, provides an estimate for the amount of energy available to the central engine per unit mass accreting onto it. For typical stellar parameters $M_* \sim M_\odot \approx 2 \times 10^{33}$ g and $r_* \sim R_\odot \approx 6 \times 10^{10}$ cm this yields an energy per unit mass $E/m \sim 2 \times 10^{15}$ erg/g. For a typical neutron star $M_* \sim M_\odot \approx 2.8 \times 10^{33}$ g and $r_* \sim R_\odot \approx 1 \times 10^{6}$ cm this yields an energy per unit mass $E/m \sim 2 \times 10^{20}$ erg/g. As a means of comparison, let us compare this to the amount of energy that is released in the nuclear reaction when hydrogen atoms fuse to form helium

$$E_{\rm nuc} = 0.007mc^2, \tag{1.2}$$

where c is the speed of light. Substituting in numbers we find $E_{\rm nuc}/m \approx 6 \times 10^{18}$ erg/g. So the gravitational energy available is a few orders of magnitude larger or smaller than the nuclear energy available, depending on how compact the central object i.e. the ratio M_*/r.

To improve the estimate for the power involved in the accretion process consider the forces acting on the accreting gas. Consider a spherically symmetric mass of ionized gas with no angular momentum accreting onto a central object of mass M_* and luminosity L. The gas feels a negative radial gravitational force due to the central object and a positive radial force from the pressure of the outflowing radiation. Since the proton mass is much larger than the electron mass, $m_p \gg m_e$, we may approximate the gravitational force acting on the gas as

$$F_{\rm grav} = -\frac{GM_* m_p}{r^2}. \tag{1.3}$$

Free electrons will be dragged along via Coulombic interaction. The outgoing radiation will interact most strongly via Thompson scattering with the free electrons. If S is the energy flux, then the force experienced by the electron is the rate at which it absorbs momentum $\sigma_T S/c$ where $\sigma_T = 6.7 \times 10^{-25}{\rm cm}^2$ is the Thompson scattering cross-section. The energy flux is $S = L/4\pi r^2$, so the the force from the outgoing radiation is

$$F_{\rm rad} = \frac{L\sigma_T}{4\pi c r^2}. \tag{1.4}$$

Setting these forces in equilibrium $F_{\rm grav} = F_{\rm rad}$ we can solve for the luminosity at which accretion is halted,

$$L_{\rm Edd} = \frac{4\pi G m_p c}{\sigma_T} \approx 1.3 \times 10^{38} \left(\frac{M}{M_\odot}\right) {\rm erg\ s}^{-1}, \tag{1.5}$$

the Eddington luminosity. We note that this is likely an over-estimate of the maximally allowed luminosity as we assumed spherical symmetric accretion

and one would expect accretion only in the accretion disc which covers some fraction of the surface enclosing the central object.

These simple energy arguments allow us to estimate the power available via the accretion process. However, we would also like to understand the dynamics. The basic puzzle can be summarized as follows. A particle undergoing circular motion at radius r around a central object of mass M_* will have an angular momentum per unit mass of

$$\frac{L}{m} = \sqrt{GM_* r}. \tag{1.6}$$

Therefore if the particle is to fall towards the central object it must lose angular momentum. The question is what is applying this torque on the particle, allowing it to shed angular momentum. Gravity cannot be responsible, as it is acting radially inwards and is therefore not applying a torque. One possibility is the entire disc is interacting with itself - if angular momentum is exchanged within the disc, some particles can move inwards while others move out.

Consider the accretion disc as a fluid undergoing Keplerian rotation - a typical fluid element will have a velocity $v = v_K + \delta v$ where the Keplerian velocity $v_K = \sqrt{GM_*/r}$ and the fluctuations $\delta v \ll v_K$. Consider now two adjacent rings in the disc. The existence of fluctuations allow for fluid elements in the faster moving, inner ring, to move into the outer, slower moving ring and the slower moving fluid elements in the outer ring to move into the faster moving inner ring. This exerts a shear stress

$$\sigma_{r\phi} \sim \eta \frac{\partial v_\phi}{\partial r} \tag{1.7}$$

where the dynamical viscosity

$$\eta \sim \rho \lambda \delta v \tag{1.8}$$

is a function of the length scale of velocity fluctuations λ and the magntitude of the velocity fluctuations δv and the density ρ. It is related to the dynamical viscosity $\nu = \eta/\rho$. This allows for angular momentum to be transported from the inner part of the disc to the outer part of the disc. This mechanism relies on there being a differential rotation in the disc.

Another source of viscosity in the disc is the magnetorotational instability (MRI) (Balbus & Hawley 1998 for review). Suppose the accretion disc is threaded by a weak magnetic field. The field lines serve to connect differentially rotating regions of the disc and serve as a means of transporting angular momentum between them. Consider the toy model whereby two chunks of matter in the disc are connected by a magnetic field line. One can think of this as two masses connected by a spring. Suppose one mass m_i has been displaced slightly inwards from its initial orbit and the other mass m_o has been slightly displaced radially outward. The differential rotation will cause the spring (magnetic loop) to stretch. As it stretches it will slow down the faster moving m_i and speed up the slower moving m_o. This has the effect of decreasing the angular momentum of m_i and increasing the angular momentum of m_o. Therefore m_i will move further inwards, m_o will move further outwards and the effect can grow.

The study of the microphysics behind viscosity in accretion discs is still an important area of research - from a pragmatic point of view, because we know that angular momentum exchange must occur in order to drive accretion we take an effective theory point of view and subscribe to an α-disc prescription propoed by Shakura & Sunyaev (1973) whereby we represent the kinematic viscosity

$$\nu = \alpha c_s h \tag{1.9}$$

where c_s is the sound speed of the disc, h the half-disc thickness and $\alpha \leq 1$ is a dimensionless coupling that is meant to capture all the microphysics of viscosity.

Magnetic fields can also play an important role in the transport of angular momentum by acting on large scales. A variety of models have been proposed whereby outflows of matter and radiation are launched via action of a large scale magnetic field. These rely on there being various magnetic field configurations in these systems - possible sources include dynamo action in the star or disc or advection of the field from the collapsing molecular cloud or binary companion that fed the disc. The existence of such outflows is well supported observationally. Furthermore, both observations and theoretical and numerical work support the paradigm that outflows are magnetically launched. This thesis explores different aspects of MHD driven outflows and accretion processes in a viscous disc. As a source of motivation, we first introduce the basic MHD equations in flat space and also in curved space for the Kerr metric. We then show how these can lead to outflows via Blandford-Payne centrifugal launching.

1.2 Magnetohydrodynamics

1.2.1 Classical MHD

Our starting point for describing the dynamics of the electric **E** and magnetic **B** fields is ideal, non-relativistic, steady state, magnetohydrodynamics (MHD). In

particular, they are characterized by the continuity equation

$$\nabla \cdot (\rho \mathbf{v}) = 0, \tag{1.10a}$$

where ρ is the matter density and $\mathbf{v}$ is the matter velocity, the four Maxwell equations, Ampère's law

$$\nabla \times \mathbf{B} = \frac{4\pi}{c}\mathbf{J}, \tag{1.10b}$$

where $\mathbf{J}$ is the current density, Coulomb's law

$$\nabla \cdot \mathbf{E} = 4\pi\rho_e, \tag{1.10c}$$

where ρ_e is the electric charge density, Faraday's law

$$\nabla \times \mathbf{E} = 0, \tag{1.10d}$$

the no-monopoles condition

$$\nabla \cdot \mathbf{B} = 0, \tag{1.10e}$$

Ohm's law, assuming perfect conductivity,

$$\mathbf{E} + \frac{1}{c}(v \times \mathbf{B}) = 0, \tag{1.10f}$$

and the "force-free" part of Euler's equation

$$\rho_e \mathbf{E} + \frac{1}{c}(\mathbf{J} \times \mathbf{B}) = 0. \tag{1.10g}$$

They are non-relativistic in two senses of the word. Firstly, we are assuming that the matter velocity $v \ll c$. Secondly, we are assuming that we can neglect any GR effects. This approximation is justified for distance scales $r \gg r_s \sim GM/c^2$, the Schwarzschild radius of the central object.

1.2.2 MHD in General Relativity

The situation changes in general relativity because we must now take into account a non-flat metric. Fortunately, the Kerr and Schwarzschild metrics used to model the space around compact objects have a natural 3 + 1 dimensional splitting: one can imagine slicing the 4-d space into several 3-d slices and moving them forward in time. This technique, known as the membrane paradigm, allows one to write out the MHD equations in a form that is largely unchanged from their classical counterparts. The caveat is that these largely unchanged equations of motion apply to a set of fiducial observers (FIDOs) that are anchored to fixed coordinates in the space. Below we show how this technique yields a set of equations closely analogous to the classical MHD equations. This will be useful to rederive classical MHD results, which apply to non-relativistic objects, and extending them to relativistic objects such as neutron stars or black holes.

The Kerr metric for a black hole of mass M and angular momentum J in Boyer-Lindquist (t, r, θ, ϕ) coordinates is given by (Thorne, Price & Macdonald 1986)

$$ds^2 = g_{tt}dt^2 + 2g_{t\phi}dtd\phi + g_{\phi\phi}d\phi^2 + g_{rr}dr^2 + g_{\theta\theta}d\theta^2, \tag{1.11}$$

where

$$g_{tt} = -\left(1 - \frac{2Mr}{\Sigma}\right), \qquad g_{t\phi} = -\frac{2aMr\sin^2\theta}{\Sigma}, \qquad g_{\phi\phi} = \frac{A\sin^2\theta}{\Sigma},$$
$$g_{rr} = \frac{\Sigma}{\Delta}, \qquad g_{\theta\theta} = \Sigma,$$

and we have defined the functions

$$\Sigma \equiv r^2 + a^2\cos^2\theta, \qquad \Delta \equiv r^2 + a^2 - 2Mr, \qquad A \equiv (r^2 + a^2)^2 - a^2\Delta\sin^2\theta,$$

and the angular momentum per unit mass is $a \equiv J/M$.

We will find it useful to sometimes work in two alternative coordinate systems. We define the magnetic field (MF) coordinates (t, r, θ, ϕ') as the frame co-rotating with the magnetic field lines. The metric is

$$ds^2 = \tilde{g}_{tt}dt^2 + 2\tilde{g}_{t\phi}dtd\phi' + g_{\phi\phi}(d\phi')^2 + g_{rr}dr^2 + g_{\theta\theta}d\theta^2, \tag{1.12}$$

where $\phi' = \phi - \Omega_0 t$, Ω_0 is the angular velocity of the magnetic field lines and the tilde metric coefficients are related to the usual Boyer-Lindquist coordinates by

$$\tilde{g}_{tt} = g_{tt} + 2g_{t\phi}\Omega_0 + g_{\phi\phi}\Omega_0^2, \qquad \tilde{g}_{t\phi} = g_{t\phi} + g_{\phi\phi}\Omega_0. \tag{1.13}$$

Alternatively, we can decompose the metric into 3+1 dimensions; an "absolute" 3-dimensional space and a "Universal" time. These are chosen so the absolute space defines a family of orthogonal hypersurfaces. Universal time is analogous to its Galilean counterpart; ticking away in absolute space. At each point in absolute space we imagine a fiducial observer (FIDO), at rest with respect to the black hole. The FIDOs act as the "local observers". Fortuitously, Universal time in Kerr corresponds to surfaces of constant Boyer-Lindquist time $t = \text{const}$. The FIDOs correspond to observers rotating with the black hole and sometimes referred to as zero angular momentum observers (ZAMOs). The metric is split as

$$ds^2 = -\alpha^2 dt^2 + \gamma_{ik}(dx^i + \beta^i dt)(dx^k + \beta^k dt), \tag{1.14}$$

where the square of the lapse function is given by

$$\alpha^2 = \frac{g_{t\phi}^2 - g_{tt}g_{\phi\phi}}{g_{\phi\phi}} = \frac{\Sigma\Delta}{A}, \tag{1.15a}$$

the shift vector has non-zero component

$$\beta^\phi = \frac{g_{t\phi}}{g_{\phi\phi}} = -\frac{2aMr}{A}, \tag{1.15b}$$

and we have defined the absolute space metric

$$\gamma_{ij} = \begin{cases} g_{ij} & \text{if } i = j \\ 0 & \text{if } i \neq j \end{cases} \tag{1.15c}$$

Physically the lapse function α can be thought of as a redshift factor, the conversion rate between a local FIDO time measurement τ and Universal time t. For example, if a FIDO at radius r_0 emits a photon of frequency f_0, a distant observer (who necessarily measures Universal time) will measure a frequency $f = \alpha(r_0)f_0$. The shift vector β^i describes the velocity of the FIDOs with respect to the coordinates. In this picture, the coordinates are fixed with respect to distant observers. Since FIDOs are stationary with respect to the hole, they will be moving relative to the coordinates with a velocity

$$\left(\frac{dx^i}{dt}\right)\bigg|_{\text{FIDO}} = -\beta^i \equiv \omega. \tag{1.16}$$

Each of the FIDOs defines a local, orthonormal basis e_μ. In Kerr these are given by

$$e_t = \frac{1}{\alpha}\left(\frac{\partial}{\partial_t} - \boldsymbol{\beta}\right), \qquad e_r = \frac{1}{\sqrt{g_{rr}}}\partial_r, \qquad e_\theta = \frac{1}{\sqrt{g_{\theta\theta}}}\partial_\theta, \qquad e_\phi = \frac{1}{\sqrt{g_{\phi\phi}}}\partial_\phi, \tag{1.17}$$

where $\partial_\mu \equiv \frac{\partial}{\partial x^\mu}$ are the coordinate basis vectors.

We will denote all fluid velocities in the fixed star coordinate by

$$u^\mu = \frac{dx^\mu}{dt}. \tag{1.18}$$

These can be related to FIDO measured fluid velocities $\mathbf{v} = (v^i)$ through

$$v^i = \frac{dt}{d\tau}\left[\left(\frac{dx^i}{dt}\right)\bigg|_{\text{fluid}} - \left(\frac{dx^i}{dt}\right)\bigg|_{\text{FIDO}}\right] = \frac{1}{\alpha}\left(\frac{u^i}{u^t} + \beta^i\right). \tag{1.19}$$

We model the jet using the relativistc MHD equations in the axisymmetric ($\partial_\phi = 0$) and stationary ($\partial_t = 0$) approximation, which we list in differential form

$$\nabla \cdot [\Gamma mn(\alpha\mathbf{v} - \boldsymbol{\beta})] = 0, \tag{1.20a}$$

$$\nabla \cdot \mathbf{E} = 4\pi\rho_e, \tag{1.20b}$$

$$\nabla \times (\alpha\mathbf{B}) = 4\pi\alpha\mathbf{J} - \mathcal{L}_\beta(\mathbf{E}), \tag{1.20c}$$

$$\mathbf{E} + \mathbf{v} \times \mathbf{B} = 0, \tag{1.20d}$$

$$\nabla \times (\alpha\mathbf{E}) = \mathcal{L}_\beta\mathbf{B}, \tag{1.20e}$$

$$\nabla \cdot \mathbf{B} = 0, \tag{1.20f}$$

$$\rho_e\mathbf{E} + \mathbf{J} \times \mathbf{B} = 0, \tag{1.20g}$$

$$\frac{d\varepsilon}{d\tau} = -\frac{1}{\alpha^2}\nabla \cdot (\alpha\mathbf{S}) - \overleftrightarrow{\boldsymbol{\sigma}} : \overleftrightarrow{\boldsymbol{T}}, \tag{1.20h}$$

$$\frac{d\mathbf{S}}{d\tau} = \varepsilon\mathbf{g} + \overleftrightarrow{\boldsymbol{H}} \cdot \mathbf{S} - \frac{1}{\alpha}\nabla \cdot (\alpha \overleftrightarrow{\boldsymbol{T}}), \tag{1.20i}$$

where m is the average particle mass, n the particle number density, $\boldsymbol{v}$ the 3-velocity, $\mathbf{E}$ the electric field, $\mathbf{B}$ the magnetic field, $\mathbf{J}$ the current density, ρ_e the charge density, ε the energy density, $\mathbf{S}$ the Poynting vector, $\overleftrightarrow{\boldsymbol{T}}$ the stress-energy tensor and we have further defined the special relativistic (SR) time dilation factor

$$\Gamma = (1 - \mathbf{v}^2)^{-1/2},$$

the FIDO time derivative

$$\frac{d}{d\tau} = \frac{1}{\alpha}[\partial_t - \boldsymbol{\beta} \cdot \nabla],$$

the FIDO gravitational acceleration

$$\mathbf{g} = -\frac{1}{\alpha}\nabla(\alpha), \tag{1.20j}$$

the gravitomagnetic tensor

$$\overleftrightarrow{\boldsymbol{H}} = \frac{1}{\alpha}\nabla\boldsymbol{\beta},$$

the FIDO shearing rate

$$\sigma_{ik} = -\frac{1}{2}(H_{ki} + H_{ik}),$$

and the Lie derivative of a vector $\mathbf{A}$ along a vector field $\mathbf{B}$ is given by

$$\mathcal{L}_{\mathbf{B}}\mathbf{A} = \mathbf{B}\,(\nabla\cdot\mathbf{A}) - \mathbf{A}\,(\nabla\cdot\mathbf{B})\,.$$

We stress again that above, all vector quantities are FIDO measured observables.

We will denote all fluid velocities in the fixed star coordinate by

$$u^{\mu} = \frac{dx^{\mu}}{dt}. \tag{1.21}$$

These can be related to FIDO measured fluid velocities $\mathbf{v} = (v^i)$ through

$$v^i = \frac{dt}{d\tau}\left[\left(\frac{dx^i}{dt}\right)\Big|_{\text{fluid}} - \left(\frac{dx^i}{dt}\right)\Big|_{\text{FIDO}}\right] = \frac{1}{\alpha}\left(\frac{u^i}{u^t} + \beta^i\right). \tag{1.22}$$

The total energy density ε, Poynting vector $\mathbf{S}$ and stress-energy tensor T^{ij} are the sums of the contributions from the jet, which we model as a perfect fluid (PF), and the electromagnetic field (EM). They are given by

$$\varepsilon = T^{tt}_{PF} + T^{tt}_{EM} = \left(\rho + P|\mathbf{v}|^2\right)\Gamma^2 + \frac{1}{8\pi}\left(|\mathbf{E}|^2 + |\mathbf{B}|^2\right), \tag{1.23}$$

$$\mathbf{S} = T^{ti}_{PF} + T^{ti}_{EM} = (\rho + P)\Gamma^2\mathbf{v} + \frac{1}{4\pi}(\mathbf{E}\times\mathbf{B}), \tag{1.24}$$

$$T^{ik} = T^{ik}_{PF} + T^{ik}_{EM} = (mn + P)v^iv^k + P\gamma^{ik} + \frac{1}{4\pi}\left[-\left(E^iE^k + B^iB^k\right) + \frac{1}{2}\left(|\mathbf{E}|^2 + |\mathbf{B}|^2\right)\gamma^{ik}\right], \tag{1.25}$$

where ρ is the energy density and P the pressure in the fluid rest frame. We need to postulate an equation of state for the fluid and follow the discussion in Weinberg (1972).

Consider a fluid of structureless point particles, interacting only through collisions. Such a fluid has equation of state

$$\rho - nm \simeq (\bar{\gamma} - 1)^{-1}P, \tag{1.26}$$

where the adiabatic index

$$\bar{\gamma} = \begin{cases} 5/3 & \text{nonrelativistic} \\ 4/3 & \text{ultra-relativistic} \end{cases} \tag{1.27}$$

depends on the regime of the gas. Since we are interested in the case of relativistic jets, we will work in the ultra-relativistic limit. The second law of thermodynamics states

$$kTd\sigma = Pd\left(\frac{1}{n}\right) + d\left(\frac{\rho}{n}\right), \tag{1.28}$$

where k is Boltzmann's constant, T the temperature and $k\sigma$ is the entropy per particle. Substituting (1.26) into (1.28) yields

$$kTd\sigma = Pd\left(\frac{1}{n}\right) + (\bar{\gamma}-1)^{-1}d\left(\frac{P}{n}\right) = \frac{n^{\bar{\gamma}-1}}{\bar{\gamma}-1}d\left(\frac{P}{n^{\bar{\gamma}}}\right). \tag{1.29}$$

Assuming entropy is constant, we can integrate both sides, and simplify by recalling that the adiabatic index and entropy are related via the number of degrees of freedom f through

$$\sigma = \frac{f}{2} = (\bar{\gamma}-1)^{-1}. \tag{1.30}$$

This yields the simple relation

$$P = nkT. \tag{1.31}$$

In the ultra-relativistic regime $|\mathbf{v}|^2 \simeq 1$, (1.26) and (1.31) imply the energy density, poynting vector and stress-energy take the form

$$\varepsilon \simeq nm\left(1 + \frac{4kT}{m}\right)\Gamma^2 + \frac{1}{8\pi}\left(|\mathbf{E}|^2 + |\mathbf{B}|^2\right), \tag{1.32}$$

$$\mathbf{S} \simeq nm\left(1 + \frac{4kT}{m}\right)\Gamma^2\mathbf{v} + \frac{1}{4\pi}(\mathbf{E}\times\mathbf{B}), \tag{1.33}$$

$$T^{ik} = nm\left[\left(1 + \frac{4kT}{m}\right)v^i v^k + \frac{kT}{m}\gamma^{ik}\right] + \frac{1}{4\pi}\left[-\left(E^i E^k + B^i B^k\right) + \frac{1}{2}\left(|\mathbf{E}|^2 + |\mathbf{B}|^2\right)\gamma^{ik}\right]. \tag{1.34}$$

1.3 Magnetohydrodynamic Outflow Models

1.3.1 Blandford-Payne

Blandford-Payne (BP) is a magnetohydrodynamic model where matter is centrifugally launched and collimated by a large scale magnetic field. It was one of the earliest models that used a magnetic field to drive matter and angular momentum loss from an accretion disc . We use it as motivation for how large scale magnetic fields can launch outflows and drive angular momentum loss and accretion in the disc.

To gain some insight into the BP process we first explore a purely mechanical model where the role of the magnetic field is played by a rigid, rotating wire and the matter is a small bead free to slide along its length. We then derive an analogous mechanism by solving the time independent, axisymmetric MHD equations assuming a self-similar flow, perfectly conducting disc and cold magnetosphere. Finally, we extend this result to the case of a Kerr black hole by determining the conditions necessary for massive particles to be launched. We plot some of the resulting orbits for different magnetic field. In summary, we show that MHD provides a robust mechanism for centrifugally launching matter.

Mechanical Model

To develop an intuition for the physics responsible for matter jet launching, we first examine the problem classically. If the process is primarily magnetically driven, then particle trajectories will, to first approximation, follow magnetic

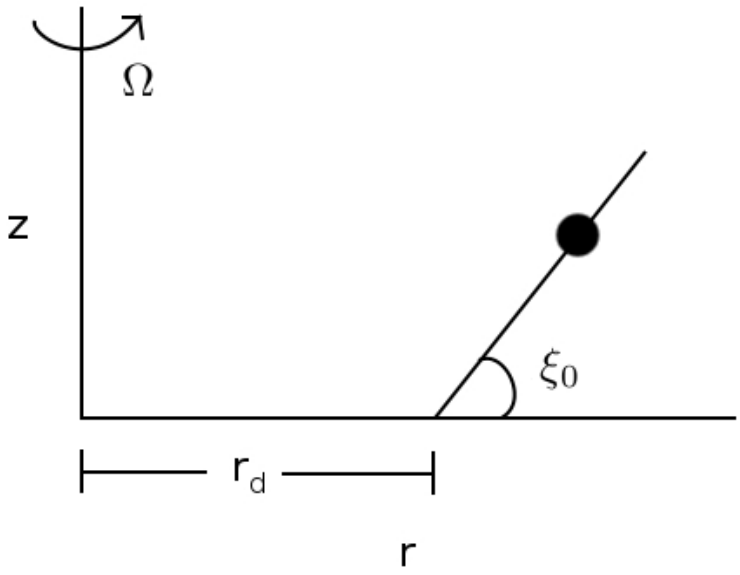

Figure 1.1: Geometric setup for mechanical toy model for centrifugal matter jet launching. Matter (bead) constrained to move along a magnetic field line (wire)

field lines (Blandford & Payne 1982). A simple toy model of the process is therefore a bead constrained to move along a wire making an angle ξ_0 with the equatorial plane, rotating at constant Keplerian angular velocity Ω at a distance r_d from the rotation axis as shown in Figure 1.1.

The effective potential describing this setup is given by

$$V_{eff} = -\frac{GM}{r_d}\left[\frac{1}{2}\left(\frac{r}{r_d}\right)^2 + \frac{r_d}{(r^2+z^2)^{1/2}}\right]. \tag{1.35}$$

It is a sum of a centrifugal term arising from the rotation and a gravitational term arising from a mass, assumed to be concentrated at the center of the disc . It is easiest to verify that this is the correct expression by calculating the forces produced by this potential and seeing that each term does in fact yield the cen-

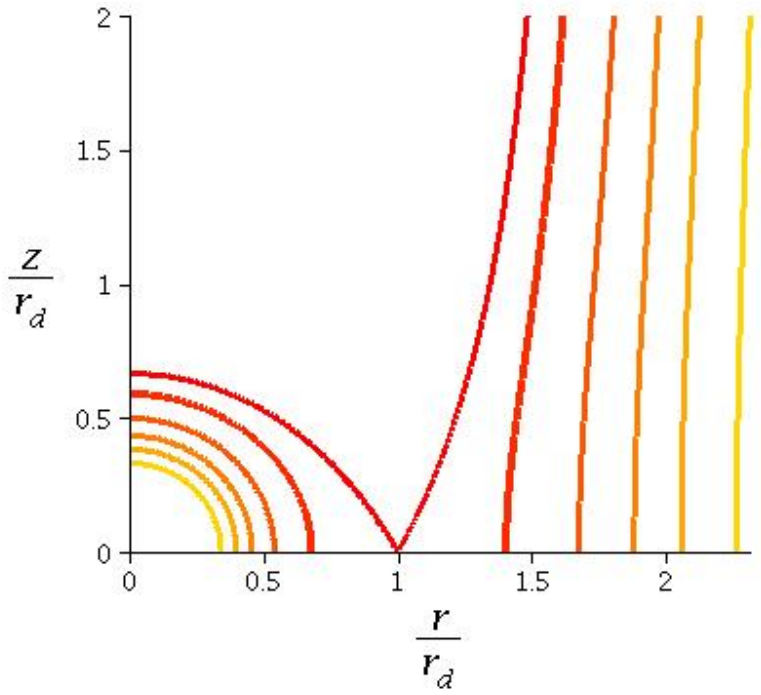

Figure 1.2: Equipotential surfaces $dV_{eff} = 0$ in r-z plane. The angle relative to the horizontal at the footpoint $r = r_d$ determines the critical angle below which centrifugal jet launching can occur

trifugal and gravitational forces experienced by the bead.

We plot the equipotential surfaces near the equitorial plane of the disc in Figure 1.2. In particular, we are interested in the equipotential surface at the magnetic field line footpoint in the equitorial plane of the disc

$$V_{eff}(r_d, 0) = -\frac{3}{2}\frac{GM}{r_d}. \tag{1.36}$$

The angle this equipotential makes with the horizontal can be calculated by expanding the potential to second order in the displacements Δr, Δz along the equipotential

$$\left|V_{eff}(r_d + \Delta r, \Delta z) - V_{eff}(r_d, 0)\right| = O(\Delta r^3, \Delta z^3). \tag{1.37}$$

This yields the constraint

$$\Delta z = \sqrt{3}\Delta r, \tag{1.38}$$

corresponding to an angle $\xi_0 = 60^\circ$ in the r-z plane. Particles (beads) moving on magnetic field lines (wires) aligned at this critical angle will feel no net force i.e $F = dV/dx = 0$. Particles moving on magnetic fields at a smaller angle than ξ_0 will be flung outward centrifugally, whereas centrifugal launching at larger angles is impossible. The classical case shows us that in this model the relevant criteria for determining if matter is centrifugally launched is the angle of the equipotential surface at the magnetic foot point.

Classical MHD

MHD in Kerr Metric

Rigid Rotation Particle Trajectories We want to investigate the kinematics of massive particles in the Kerr metric (1.11). For convenience, we will set the particle mass $m = 1$. Then the four-velocity norm $u_\mu u^\mu = -1$ can be expanded in MF coordinates as

$$\tilde{g}_{tt}(u^t)^2 + 2\tilde{g}_{t\phi}u^t u^\phi + g_{\phi\phi}(u^{\phi'})^2 + g_{rr}(u^r)^2 + g_{\theta\theta}(u^\theta)^2 = -1 \tag{1.39}$$

Parametrising the path in the coordinate θ i.e

$$r = r(\theta), \qquad \phi' = \phi'(\theta) \tag{1.40}$$

we may express the components of the particle velocities as

$$u^r = \frac{\partial x^r}{\partial \lambda} = \frac{\partial x^r}{\partial x^\theta}\frac{\partial x^\theta}{\partial \lambda} = r_{,\theta}u^\theta, \qquad u^{\phi'} = \frac{\partial x^{\phi'}}{\partial \lambda} = \frac{\partial x^{\phi'}}{\partial x^\theta}\frac{\partial x^\theta}{\partial \lambda} = \phi'_{,\theta}u^\theta, \tag{1.41}$$

where we have assumed that the particle trajectory was parametrised by an affine parameter λ. Under such a parametrisation, we can express the norm of the four-velocity as

$$\tilde{g}_{tt}(u^t)^2 + 2\tilde{g}_{t\theta}u^t u^\theta + \tilde{g}_{\theta\theta}(u^\theta)^2 = -1 \tag{1.42}$$

where we have defined

$$\tilde{g}_{t\theta} = \left(g_{t\phi} + g_{\phi\phi}\Omega_0\right)\phi'_{,\theta}, \qquad \tilde{g}_{\theta\theta} = g_{\theta\theta} + g_{rr}\left(r_{,\theta}\right)^2 + g_{\phi\phi}\left(\phi'_{,\theta}\right)^2 \tag{1.43}$$

Noting that the energy of the particle in this frame $\tilde{\epsilon}$ is

$$\tilde{u}_t = \tilde{g}_{tt}u^t + \tilde{g}_{t\theta}u^\theta \equiv -\tilde{\epsilon}, \tag{1.44}$$

we can solve for the components of the velocity four-vector

$$u^\theta = \sqrt{\frac{(\tilde{\epsilon})^2 + \tilde{g}_{tt}}{(\tilde{g}_{t\theta})^2 - \tilde{g}_{tt}\tilde{g}_{\theta\theta}}}, \qquad u^t = -\frac{\tilde{\epsilon}}{\tilde{g}_{tt}} - \frac{\tilde{g}_{t\theta}}{\tilde{g}_{tt}}\sqrt{\frac{(\tilde{\epsilon})^2 + \tilde{g}_{tt}}{(\tilde{g}_{t\theta})^2 - \tilde{g}_{tt}\tilde{g}_{\theta\theta}}}. \tag{1.45}$$

We see that the kinematics of particles undergoing rigid rotation is completely described by the particle energy. As a simple application, we can calculate the velocity of the particles and the Lorentz factor in the FIDO (or equivalently ZAMO) frames

$$\Gamma = v^t = u^t\alpha, \qquad v^\phi = \frac{1}{\alpha}\left(\frac{\phi'_{,\theta}u^\theta}{u^t} + (\Omega_0 - \omega)\right), \qquad v^\theta = \frac{1}{\alpha}\frac{u^\theta}{u^t}, \qquad v^r = \frac{1}{\alpha}\frac{r_{,\theta}u^\theta}{u^t}. \tag{1.46}$$

Effective Potential Consider a particle with fixed angular velocity Ω_0, as measured by a distant observer in Boyer-Lindquist coordinates. In the MF frame, a particle at rest has $u^\theta = 0$. All of its energy will therefore be potential energy. Plugging in this condition into (1.45), we conclude the particles dynamics are determined by the effective potential

$$V_{\text{eff}} \equiv \tilde{\epsilon} = \sqrt{-\tilde{g}_{tt}}. \tag{1.47}$$

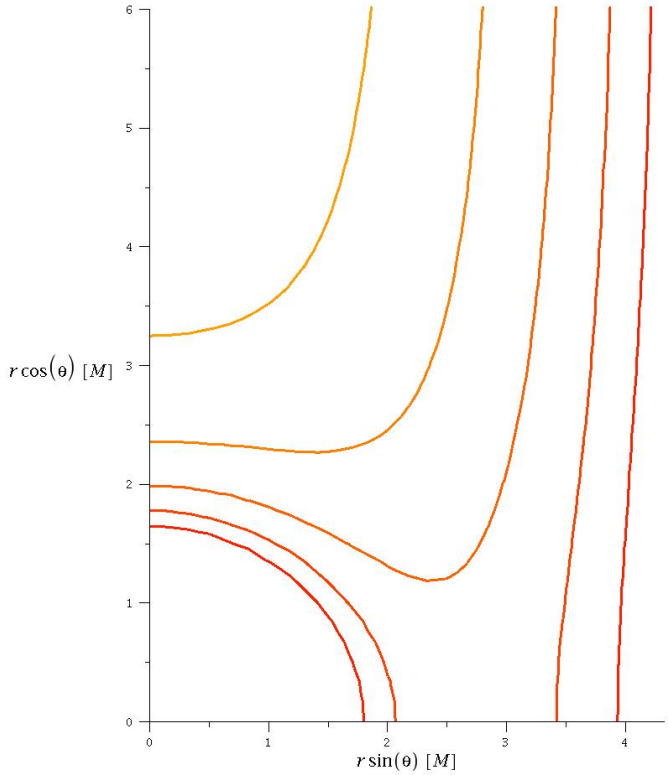

Figure 1.3: Equipotential surfaces of V_{eff} in the $r\sin\theta - r\cos\theta$ plane for black hole spin $a = 0$.

As we have seen with the classical case, it is useful to plot the equipotential surfaces of V_{eff}. We do this for the non-spinning $a = 0$ case (Figure 1.3) and the fast spinning $a = 0.9$ case (Figure 1.4).

We now turn our attention to understanding the shape of V_{eff} in the equatorial plane. The angle of the equipotential surface and the equitorial plane ξ is, from geometry

$$\tan\xi = -r\left(\frac{d\theta}{dr}\right)\Big|_{\theta=\pi/2} = r\left(\frac{V_{\text{eff,r}}}{V_{\text{eff},\theta}}\right)\Big|_{\theta=\pi/2}. \tag{1.48}$$

We note that

$$V_{\text{eff},\theta}\big|_{\theta=\pi/2} = 0 \tag{1.49}$$

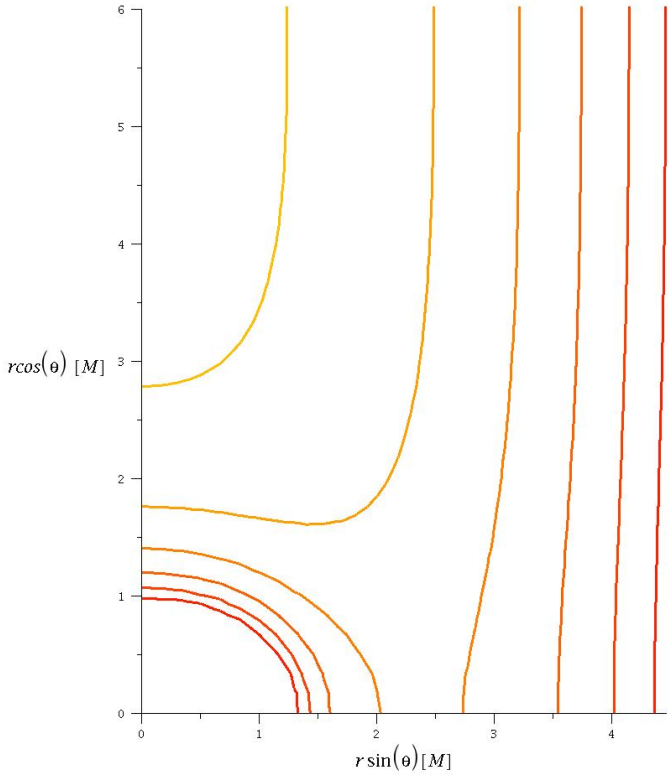

Figure 1.4: Equipotential surfaces of V_{eff} in the $r\sin\theta - r\cos\theta$ plane for black hole spin $a = 0.9$.

for all radii. We also note that

$$V_{\text{eff,r}}\Big|_{\theta=\pi/2} = 0. \tag{1.50}$$

at all radii r_d where the disc is rotating at Keplerian velocity (Bardeen, Press & Teukolsky 1972)

$$\Omega_0 = \frac{M^{1/2}}{r_d^{3/2} + aM^{1/2}}. \tag{1.51}$$

Assuming a Keplerian disc , we evaluate (1.48) using L'Hospital's rule

$$\begin{aligned} \tan\xi_0 &= r_d \sqrt{-\left(\frac{V_{eff,rr}}{V_{eff,\theta\theta}}\right)\Big|_{\theta=\pi/2, r=r_d}} \\ &= \sqrt{\frac{3}{1 - 4aM^{1/2}r_d^{-3/2} + 3a^2 r_d^{-2}}}. \end{aligned} \tag{1.52}$$

This calculation is the GR analogue to the classical result of the previous section. The results are plotted in Figure 1.5.

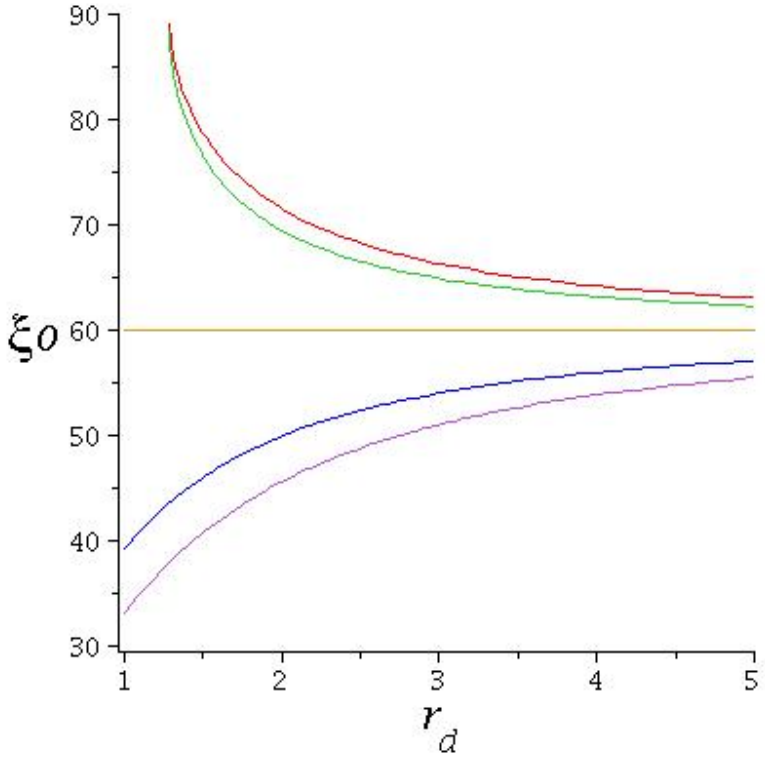

Figure 1.5: Critical angle ξ_0 as a function of magnetic footpoint r_d for black-hole spins a=0.9[red], a=0.6[green], a=0 [gold],a=-.6 [blue], a=-.9 [purple]. Note the recovery of the classical result for non-spinning black holes

Kinematics of Massive Particles in Force Free Magnetosphere We are now interested in applying this formalism to particles whose motion is governed by magnetic fields generated by the disc . We will model each field line as being anchored at some footpoint in the plane of the disc . Assuming that this motion is primarily magnetically driven, it is a good approximation to say that the particle trajectories will follow magnetic field lines. We therefore identify each particle trajectory with the footpoint of the corresponding field line.

Purely Poloidal Magnetic Field The simplest case to consider is a purely poloidal magnetic field. In the MF frame, the trajectories will be planar (ϕ' = const.).

This simplifies (1.45) considerably,

$$u^\theta = \sqrt{\frac{(\tilde{\epsilon}_0)^2 + \tilde{g}_{tt}}{\tilde{g}_{tt}\tilde{g}_{\theta\theta}}}, \qquad u^t = -\frac{\tilde{\epsilon}_0}{\tilde{g}_{tt}}, \tag{1.53}$$

where the energy $\tilde{\epsilon}_0$ is evaluated at the footpoint in the disc at $\theta = \pi/2, r = r_0$. Particles can be pulled from the disc by centrifugal forces provided the angle of the magnetic field line with the equitorial plane is less than ξ_0. They can continue their motion provided they have sufficient energy i.e. $\tilde{\epsilon}_0 > V_{\text{eff}}$

Consider for instance field lines anchored at $r = r_0$ and inclined at an angle ξ in the $r\cos\theta - r\sin\theta$ plane, described by

$$r = \frac{r_0 \tan\xi_0}{\sin\theta\tan\xi - \cos\theta}. \tag{1.54}$$

For these trajectories we plot the resulting velocities in the MF frame (Figure 1.6). We have taken the footpoint to lie at the marginally stable orbit. We note that the velocity eventually reaches c, indicating the breakdown of such a model. The inuitive reason for this is as follows. The angular velocity of the particle is constant, fixed at the angular velocity of the disc at the footpoint. As the particle radius increases monotonically, so too does the particle velocity in the toroidal direction, eventually causing it to surpass the speed of light. We conclude that the case with purely poloidal magnetic fields is unphysical.

Poloidal and Toroidal Magnetic fields Let us assume that the magnetic field lines now also have a toroidal component. As before we work in the force-free approximation where particle trajectories follow magnetic field lines. In addition to the ansatz (1.54) we take the field lines to vary in the toroidal direction as

$$\phi' = -\frac{\eta\Omega_0}{\cos\xi}\left(r\sin\theta - r_0\right). \tag{1.55}$$

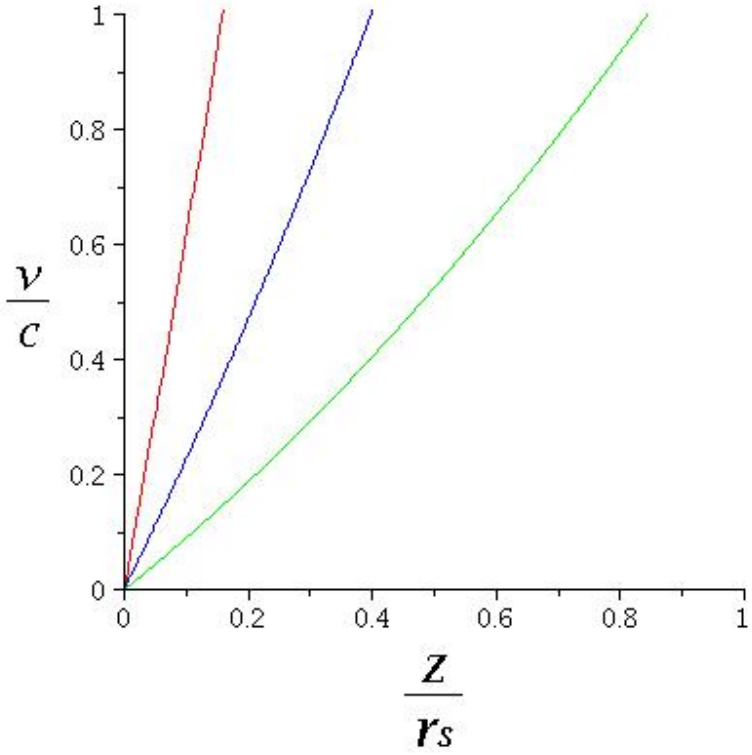

Figure 1.6: Particle velocities as a function of height above disc for purely poloidal magnetic fields for black hole spin a=0.7. Launching angles are $\xi = 30°$ [red],$\xi = 45°$[blue],$\xi = 60°$[green]. Motion will occur in a $\phi' =$ const. plane.

We plot the particle trajectories for $\eta = 1$ and various launching angles $\xi < \xi_0$ in Figure 1.7.

1.4 Conclusion

This chapter has served as a motivation that magnetic fields can act to launch matter from accretion discs. This launched matter allows the disc to shed angular momentum, which can allow accretion to proceed in the disc.

The structure of this thesis is as follows. In Chapter 2, we derive the Grad-

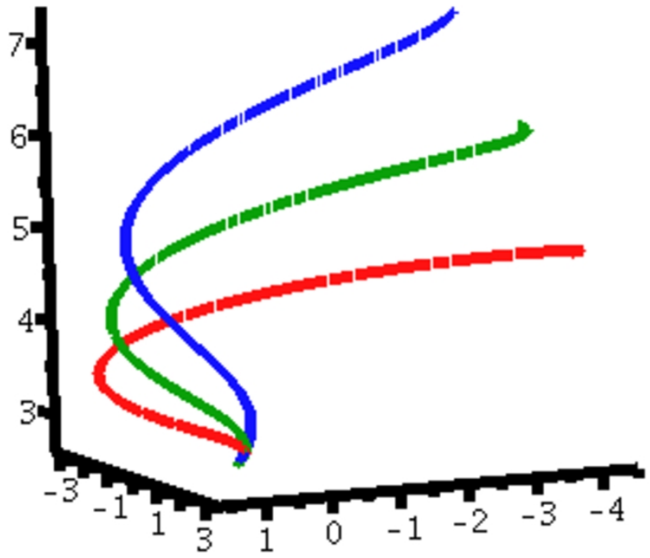

Figure 1.7: Particle trajectories for poloidal and toroidal magnetic fields with $\eta = 1$ and launching angles $\xi = 30°$ [red],$\xi = 45°$[green],$\xi = 60°$[blue].

Shafranov equation using classical ideal MHD and ideal GRMHD. This equation models the time-independent, axisymmetric magnetic field configuration in the corona for YSO (in the classical case) and Schwarzschild black holes or neutron stars (in the GRMHD case). We find solutions in the stationary regime, as well as an adiabatic regime where we assume the system is still governed by the Grad-Shafranov equation but account for the differential rotation of the disc. We show that this leads to strong field gradients near the rotation axis of the central object. We compute some basic properties of a jet in ideal GRMHD such as its opening angle, mass flux and Poynting flux. This preliminary investigation, based on past work in this area, serves to underscore the basic physics of magnetically launched outflows and motivate more physically realistic time dependent simulations.

Chapter 3 describes the MHD code used to perform the 2.5D, axisymmetric simulations that encompass the body of this thesis. We describe the basic equations, the Godunov type solver used to solve them as well as sketch the basic setup for inital and boundary conditions.

Chapter 4 is based on the paper Dyda et al. (2013). We consider an initial magnetic field configuration of "loops" threading the disc, which is a solution to the Grad-Shafranov equation. The differential rotation of the disc causes the innermost loops to open and magnetically launch outflows. We show that these outflows are composed of a Poynting flux dominated jet and a matter dominated disc wind. The radial infall of matter can be described by a simple two term model - a viscous term from the α-disc prescription and an advection term regulated by the strength of the large scale field.

Chapter 5 is based on two papers, an analytical study Quach, Dyda & Lovelace (2015) and a numerical study Dyda et al. (2015a) of counter-rotating accretion discs. The analytical work considered a thin Keplerian accretion disc where at some radius the rotation direction of the matter was in the opposite direction to the inner part of the disc. We performed a linear analysis of perturbations around this radius and found a Kelvin-Helmholtz instability that is essentially three dimensional. It grows at least on order the Keplerian time scale and is predicted to lead to strong heating and mixing of the rotating/counter-rotating components. The numerical study involves performing various HD simulations of geometries involving rotating/counter-rotating components in the disc. Shear layers form at the rotating/counter-rotating boundary, leading to large $10^2 - 10^4$ enhancements to the accretion rate as angular momentum is exchanged and matter loses its centrifugal barrier.

Chapter 6 is based on the paper Dyda et al. (2015b). Many observations indicate that there are asymmetries in jet/counter jets of YSOs. We show that starting from symmetric initial conditions, asymmetries can still form in the jet/counter jet. Increasing the density in the midplane of the disc causes the magnetic field lines in the upper and lower corona to decouple, allowing for outflow asymmetries. Likewise configurations with a stellar dipole and an extended disc wind can have asymmetric outflows as the two magnetic fields interact and accretion onto the star is inhibited by the dipole and forced to proceed asymmetrically via funnel flow.

Chapter 7 is based on a paper Dyda et al. (2015c). Large scale magnetic fields are required for MHD launching. We consider one possible source for this magnetic field, an α-dynamo operating in the disc. We find that the α-dynamo generates a dipole and higher order poles around the star. Sufficient magnetic flux is generated in the disc to grow a seed field initially too weak to launch observable outflows to one that can launch outflows with mass flux consistent with observations.

Chapter 8 summarizes our findings.

CHAPTER 2

GRAD-SHAFRANOV EQUATION

The Grad-Shafranov (GS) equation models the equilibrium configurations of a conducting fluid and a magnetic field (Grad & Rubin 1958, Shafranov 1966). This has been applied to a number of astrophysical situations such as neutron stars, YSO and AGN. In this chapter, we explore the GS equation as it applies to the magnetosphere of a central object coupled to a thin, conducting, Keplerian accretion disc .

We first derive the classical Grad-Shafranov equation, relevant to equilibrium configurations of a conducting fluid outside of compact objects with radius $R_* \gg r_s = 2GM/c^2$ i.e general relativistic effects are negligible. This applies to YSOs for instance. We then derive the general relativistic version of the equation in the Schwarzschild geometry using the membrane paradigm. This version of the equation is necessary for describing the magnetosphere outside neutron stars and black holes. In both cases we solve the equation numerically and discuss possible implications of such a configurations. The goal in understanding such equilibrium is in using them as good initial conditions in time dependent MHD simulations.

2.1 Classical Grad-Shafranov Equation

We first derive the GS equation from classical magnetohydrodynamics (MHD), under the assumptions that the fields are stationary and axisymmetric. In addition, we work in the coronal or force-free approximation, in the sense that the

magnetic energy density dominates over the plasma kinetic energy density. We consider a configuration where the magnetic field lines thread the accretion disc . The differential rotation of the disc leads to a twisting of the field lines, which acts as a source of pressure and causes the field line configuration to open up. We explore the solutions to the GS equation numerically. We provide a brief description of our code, and describe various tests and special cases used to check that it runs as expected.

Electromagnetic Field

Our task is to determine the electric and magnetic fields outside the central object. We will work in cylindrical (R, ϕ, Z) coordinates. By axisymmetry, the magnetic field can be written as

$$\mathbf{B} = \mathbf{B}_p + B_\phi \hat{\phi}, \tag{2.1}$$

where the poloidal field is

$$\mathbf{B}_p = B_R \hat{R} + B_Z \hat{Z}. \tag{2.2}$$

The magnetic field is produced by the dynamics of the disc , rotating in the $\hat{\phi}$ direction. A suitable ansatz for the vector potential is therefore

$$\mathbf{A} = A_\phi \hat{\phi} = \frac{1}{R}\Psi(R, Z), \tag{2.3}$$

where we have used axisymmetry to restrict the form of the flux function Ψ. The poloidal components of the magnetic field can thus be computed as

$$B_R = -\frac{1}{R}\frac{\partial \Psi}{\partial Z}, \tag{2.4a}$$

$$B_Z = \frac{1}{R}\frac{\partial \Psi}{\partial R}. \tag{2.4b}$$

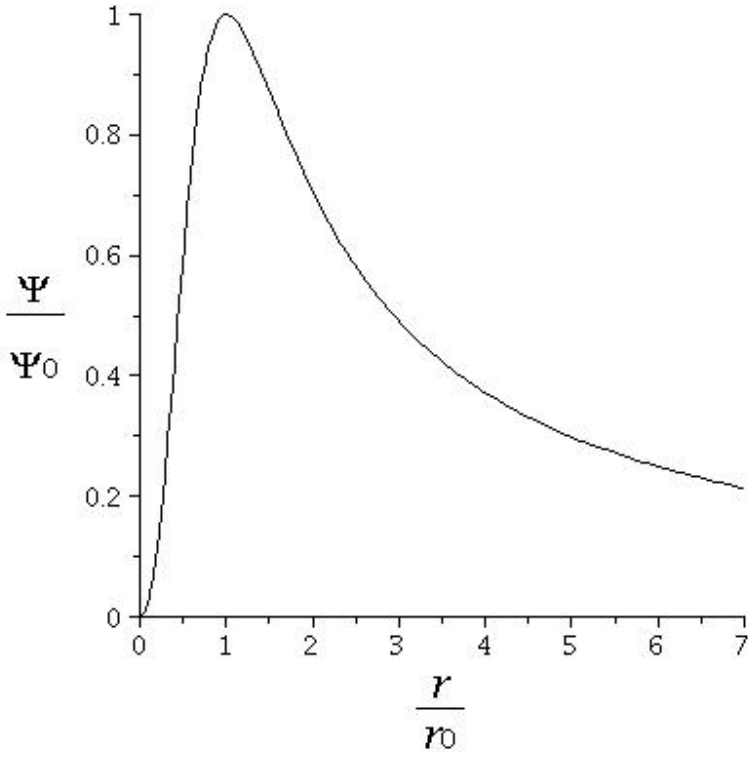

Figure 2.1: Representative form of the flux function Ψ at the surface of the disc where the radius is plotted in units of the length scale r_0 and the flux has been normalized by its value at this radius

A typical form of this function is

$$\Psi(R,0) = \frac{B_0}{2}\frac{R^2}{1+2(\frac{R}{R_0})^3}, \tag{2.5}$$

where B_0 is the axial magnetic field strength in the center of the disc and R_0 is the radius of the O-point. This is the point in the poloidal plane around which all poloidal magnetic field lines that do not extend to infinity twist around. Our classical approximation hence reduces to assuming $r_s \ll R_0$. We plot (2.5) in Fig 2.1.

We can safely work in the classical regime when

$$R_0 \gg r_s \sim \frac{GM}{c^2}, \tag{2.6}$$

the Schwarschild radius of the black hole. We will assume that the disc in undergoing Keplerian rotation with angular velocity

$$\Omega = \left(\frac{GM}{r^3}\right). \tag{2.7}$$

By axisymmetry and (1.10d) (electric fields are irrotational)

$$E_\phi = 0. \tag{2.8}$$

The $\hat{\phi}$ component of (1.10f) then gives us

$$\mathbf{v}_p = \kappa \mathbf{B}_p, \tag{2.9}$$

where κ is a proportionality factor that is allowed to vary along the field line. Intuitively, this is because $\mathbf{u}_p$ and $\mathbf{B}_p$ lie in the same plane yet produce a zero cross product. Physically (2.9) is telling us that the poloidal trajectory of particles follow the poloidal field lines. However, the parametrisation κ is allowed to vary with position, equivalent to allowing the particle velocity to change in time. Substituting this result into (1.10a) we find

$$\begin{aligned} 0 = \nabla \cdot (\rho \mathbf{v}) &= \nabla \cdot (\rho \mathbf{v}_p + \rho v_\phi \hat{\phi}) \\ &= \nabla \cdot (\rho \kappa \mathbf{B}_p + \rho v_\phi \hat{\phi}) \\ &= \nabla \cdot (\rho \kappa \mathbf{B}) - r^{-1} \partial_\phi \left(\rho \kappa B_\phi + \rho v_\phi\right) \\ &= \nabla \cdot (\rho \kappa \mathbf{B}) \end{aligned} \tag{2.10}$$

where we have used axisymmetry in the final step. Expanding this result and using (1.10e) we find

$$\mathbf{B} \cdot \nabla(\rho \kappa) = 0. \tag{2.11}$$

By axisymmetry and the poloidal magnetic field components (2.4a), (2.4b) it follows by inspection that

$$\rho = \frac{F(\Psi)}{4\pi\kappa}, \tag{2.12}$$

where $F(\Psi)$ is an arbitrary function of the magnetic flux surface. Similarly, inspection of (1.10f) reveals that we may define a function $G(\Psi)$ through

$$\mathbf{E} = -G(\Psi)\nabla\Psi, \tag{2.13}$$

which satisfies the constraint

$$u_\phi - \kappa B_\phi = rG(\Psi). \tag{2.14}$$

We complete our description of the magnetic field by introducing a function $H(\Psi)$ satisfying

$$H(\Psi) = RB_\phi. \tag{2.15}$$

Ampères law gives us some intuition into the function $H(\Psi)$: it is $2/c$ times the current flowing across a surface with radius R defined by $\Psi(R, Z) = \text{const.}$. The goal is now to determine the unknown functions F, G, H and Ψ.

Let us now consider the behavior of the magnetic field on the disc at $Z = 0$. Using (1.10f) and evaluating the $\hat{R}$ component we find

$$E_R = -\frac{1}{c}(v_\phi B_Z - v_Z B_\phi) = -\Omega\frac{\partial\Psi}{\partial R}, \tag{2.16}$$

where we have used that $v_Z = 0$ and $v_\phi = R\Omega$ on the disc and substituted in (2.4b). Comparing with (2.13) we conclude

$$G(\Psi) = \frac{\Omega(R)}{c}. \tag{2.17}$$

It follows that $\Omega = \Omega(\Psi)$ can be viewed as a function of the flux surface Ψ.

Next we compute the current density using (1.10b)

$$\mathbf{J} = \frac{1}{4\pi}\left[-\left(\frac{1}{R}H'\frac{\partial\Psi}{\partial Z}\right)\hat{R} - \left(\frac{1}{R}\Delta^*\Psi\right)\hat{\phi} + \left(\frac{1}{R}H'\frac{\partial\Psi}{\partial R}\right)\hat{Z}\right], \tag{2.18}$$

where $'$ denotes a derivative with respect to the argument of a function of a single variable and we have defined the operator

$$\Delta^* = \frac{\partial^2}{\partial R^2} - \frac{1}{R}\frac{\partial}{\partial R} + \frac{\partial^2}{\partial Z^2}. \tag{2.19}$$

The electric charge density is given by

$$\rho_e = \frac{1}{4\pi}\nabla \cdot \mathbf{E} = -\frac{1}{4\pi c}\left[\left(\frac{\Omega}{c}\right)\nabla^2\Psi + \nabla\Psi \cdot \nabla\left(\frac{\Omega}{c}\right)\right]. \tag{2.20}$$

Substituting these results into (1.10g) and taking the component along the direction of $\nabla\Psi$ yields the Grad-Shafranov (GS) equation

$$\left[1 - \left(\frac{R\Omega}{c}\right)^2\right]\Delta^*\Psi - \frac{\nabla\Psi}{2R^2} \cdot \nabla\left(\frac{R^4\Omega^2}{c^2}\right) + H(\Psi)H' = 0. \tag{2.21}$$

Quasi-Stationary Evolution

Though the Grad-Shafranov equation was derived in the stationary limit, it is interesting to consider how the field line structure would be affected were we to account for the differential rotation of the disc. This is the quasi-stationary limit, where we assume that the relaxation time for the system is much faster than the Keplerian time, so we may assume the system is in the stationary equilibrium described by the Grad-Shafranov equation (2.21). Assuming that closed field lines are differentially sheared however will change the allowed field line structures.

The differential rotation of the disc can lead to a twisting of magnetic field lines. Consider a field line that pierces the disc at radius R_1 and again at radius R_2. Assuming these footpoints remained fixed, the rotation of the disc will lead to the field line becoming twisted. For a given field line we have

$$\frac{Rd\phi}{B_\phi} = \frac{ds_p}{B_p}, \tag{2.22}$$

where $ds_p = \sqrt{dR^2 + dZ^2}$ is the poloidal line element and $B_p = \sqrt{B_R^2 + B_Z^2}$. The total twist of the field line is therefore

$$\Delta\phi = -\int_1^2 ds_p \frac{B_\phi}{RB_p} = -H(\Psi)\int_1^2 \frac{ds_p}{R^2 B_p} = \Omega(R_0)t\left[\frac{\Omega(R_1)}{\Omega(R_0)} - \frac{\Omega(R_2)}{\Omega(R_0)}\right]. \tag{2.23}$$

Most of the twisting of the field lines occur in the region $0 \leq Z \leq Z(t)$ where $Z(t)$ is the location of the edge of the jet. Here, the radius of the jet is nearly constant, so we can approximate $\Psi = \Psi(R)$. From (2.23) it follows that

$$R^2 \frac{d\phi}{dZ} = \frac{RB_\phi}{B_Z}. \tag{2.24}$$

For simplicity, we consider the case $v_Z = dZ/dt = \text{const}$. It follows that in this case

$$H(\Psi) = R^2\Omega(\Psi)\frac{B_Z}{v_Z}. \tag{2.25}$$

Inside the head of the jet, the GS equation (2.21) reduces to

$$\frac{d^2\Psi}{dR^2} + \frac{(\lambda-1)}{(\lambda+1)}\frac{1}{R}\frac{d\Psi}{dR} + \frac{\lambda}{\lambda+1}\left(\frac{d\Psi}{dR}\right)^2 \frac{1}{\Omega}\frac{d\Omega}{d\Psi} = 0, \tag{2.26}$$

where $\lambda \equiv \left(\frac{R\Omega}{c}\right)^2 [\frac{c}{v_Z} - 1]$. (2.26) is the Grad-Shafranov type equation describing the field line structure assuming an adiabatic shearing by the accretion disc.

2.1.1 Numerical Solutions

We want to solve the classical Grad-Shafranov equations numerically i.e we must find functions Ψ and $H(\Psi)$ which satisfy (2.21) and also have appropriate boundary conditions. Likewise we want to solve (2.26) for Ψ to understand the effects of shearing from the differential rotation of the disc. We note that this problem is very similar to solving Laplace's equation in electromagnetism, since the Grad-Shafranov operator (2.19) is similar in form to the Laplacian. We can

therefore use a similar numerical approach, namely a successive over-relaxation (SOR) algorithm.

In addition to axisymmetry we assume symmetry about the disc plane - our computational region is therefore the region $0 < R < 10$, $0 < Z < 10$. Along the disc choose Ψ given by (2.5) and set $\Psi = 0$ along the outer boundaries and the axis.

The self-relaxation algorithm works by rewriting (2.21) in discrete form and expressing the value of Ψ at the i, j coordinate as a function of variables at neighbouring cells. One iteration of the algorithm then consists of using this equation to update Ψ in the entire computational region. This process is repeated until a solution is found to be stable i.e. it varies by less than some factor ϵ which we set to $\epsilon = 10^{-5}$. We show the results of such an approach by plotting the flux function below.

We use a SOR algorithm to solve (2.21). Step 1 consists of using an analytic trial function for the poloidal current

$$H(\Psi) = H_0|\Psi|^{\alpha}\,(\Psi - \Psi_0)^{\beta}\,, \tag{2.27}$$

where $\alpha = \beta = 1/4$ and the coupling H_0 is refered to as FK in our code. We then solve for Ψ using an SOR routine. The results of such an algorithm for various values of H_0 can be seen in Fig.2.3. In Step 2 we loosen this prescription and allow H to vary. We specify a value of the twist and solve for the poloidal current by integrating along 9 field lines originating within the O-point and using (2.23) and (2.25). $H'(\Psi)$ is found by assuming it has the same form as our analytic model (2.27)

$$H'(\Psi) = \frac{\alpha H(\Psi)}{\Psi} - \frac{\beta H(\Psi)}{(\Psi_0 - \Psi)} \tag{2.28}$$

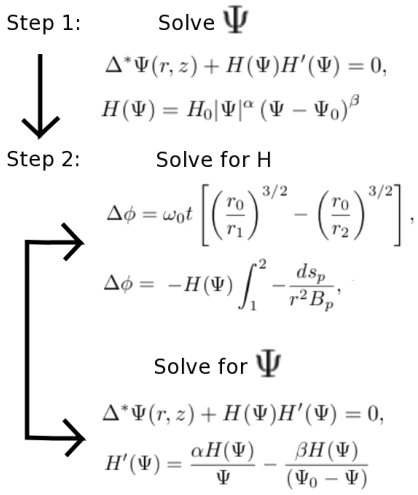

Figure 2.2: Summary of our algorithm for solving the 2D Grad-Shafranov equation where we treat the poloidal current $H(\Psi)$ semi-analytically.

but we substitute in the values of H found by integrating along the field lines. This semi-analytic treatment is used because there are not enough H data points to reliably calculate its derivative. Only 9 field lines are integrated over because they must all originate within the O-point for the integral to reliably converge. After calculating H and H' in this way, we recalculate Ψ. This process is repeated until the desired level of convergence is achieved. In our trials, we waited until Ψ was changing by less than 0.1% between succesive iterations. Step 1 is necessary in order for there to be actual field lines over which to integrate. We think of step 2 as a perturbation around the analytic solution that is arrived at in step 1. Our algorithm, and the accompanying equations, are summarized in Fig. 2.2.

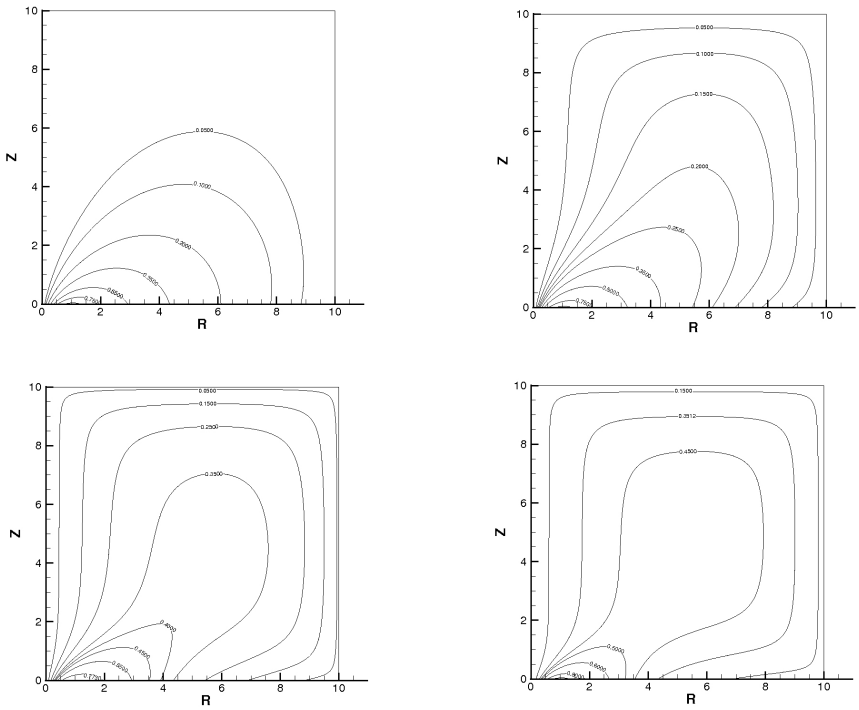

Figure 2.3: Ψ = const. contours for $H_0 = 0$ (upper left), $H_0 = 0.2$ (upper right), $H_0 = 0.5$ (lower left) and $H_0 = 1.0$ (lower right)

Step 1

We first show the results from Step 1 of the algorithm, solving for the potential function with an analytic model for the current. We choose $\alpha = \beta = 0.25$ and show contour plots for Ψ = const. for different values of the poloidal current strength $H_0 = 0$ (upper left), 0.2 (upper right), 0.5 (lower left) and 1.0 (lower right) in Fig. 2.3. We note that as the coupling H_0 is increased, more field lines "open" up. Step 2 of our algorithm requires well defined field lines to integrate over, so Step 1 is key as it produces a potential with continuous lines.

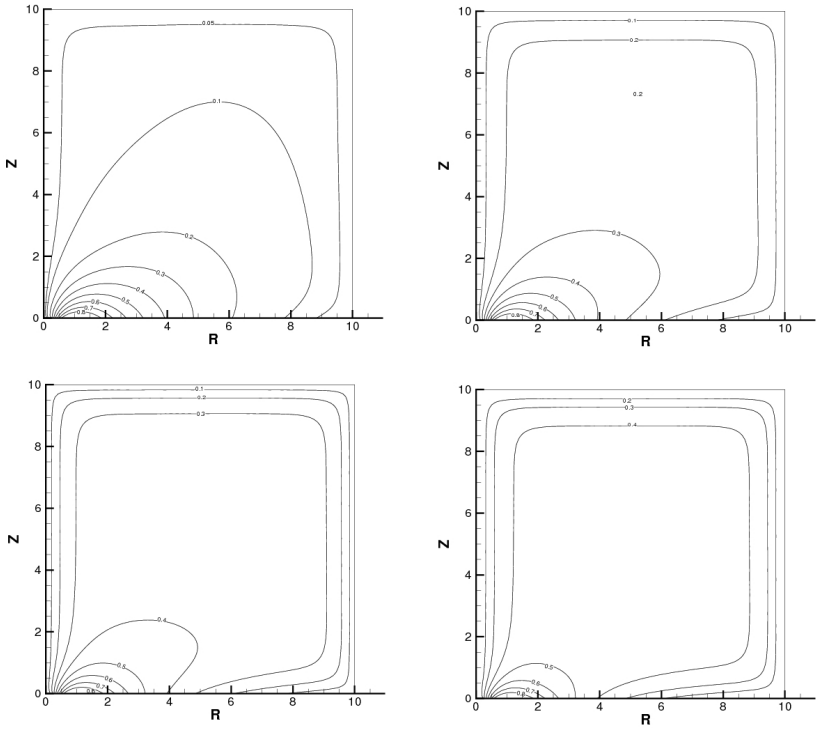

Figure 2.4: Ψ = const. contours for $H_0 = 0.1$ and $t = 1.0$ (upper left), $t = 3.0$ (upper right), $t = 5.0$ (lower left) and $t = 7.0$ (lower right)

Step 2

We first check to see how our final result depends on the twist parameter t. We have plotted the Ψ = const. contours found with $H_0 = 0.1$ and twist values $t = 1$ (upper left), $t = 3$ (upper right), $t = 5$ (lower left) and $t = 7$ (lower right) of Fig. 2.4. As expected, for increasing values of twist, more field lines open up. We want to ensure that our final result depends only weakly on the choice of coupling H_0. For fixed twist t = 3, we show the Ψ contours obtained with $H_0 = 0.1$ (upper left), $H_0 = 0.2$ (upper right), $H_0 = 0.5$ (lower left) and $H_0 = 1.0$ (lower right) of Fig. 2.5. In addition, we plot the relationship between the current

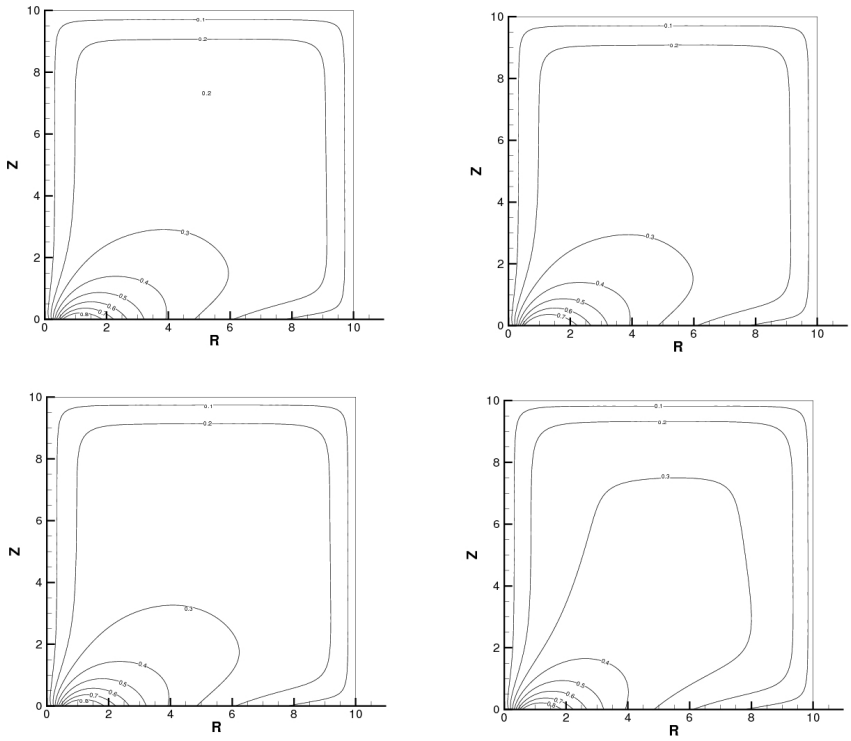

Figure 2.5: Ψ = const. contours for $t = 3.0$ and $H_0 = 0.1$ (upper left), $H_0 = 0.2$ (upper right), $H_0 = 0.5$ (lower left) and $H_0 = 1.0$ (lower right).

function obtained analytically and numerically by integrating along field lines. This is shown for $H_0 = 1.0$ and $t = 3$ in Fig. 2.6 and shows reasonable agreement. This is precisely what is wanted since we do not want our final result to depend on the trial function used.

Using the same self-relaxation algorithm we find the following solution for the flux function Ψ. We note that unlike in the purely stationary case, the differential shear, parametrized by the twist t, causes the field lines to open up. This increases the field gradient near the rotation axis, which is an important effect for magnetically launching and collimating jets.

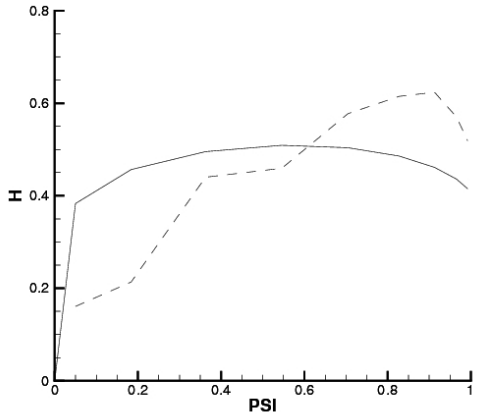

Figure 2.6: Plot of analytical (solid) and numerical (dashed) current function obtained in the case $H_0 = 1.0$ and $t = 3$, showing reasonable agreement between the two methods of obtaining the flux function.

2.2 General Relativistic Grad-Shafranov Equation

Electromagnetic Field

Our task is to determine the electric and magnetic fields outside the black hole horizon. We will work in Boyer-Lindquist (r, θ, ϕ) coordinates. Further we will assume that the energy density is Poynting dominated and neglect the matter contribution. By axisymmetry, the magnetic field can be written as

$$\boldsymbol{B} = \boldsymbol{B}^p + B^\phi, \tag{2.29}$$

where the poloidal field is

$$\boldsymbol{B}^p = B^r + B^\theta. \tag{2.30}$$

The magnetic field is produced by the dynamics of the disc , rotating in the $\vec{e}_\phi$ direction. A suitable ansatz for the vector potential is therefore

$$\boldsymbol{A} = A^\phi = \Psi(r, \theta), \tag{2.31}$$

where we have used axisymmetry to restrict the form of the flux function Ψ. The poloidal components of the magnetic field can thus be computed using

$$(\nabla \times A)^i = \frac{1}{2\sqrt{|\gamma|}} \tilde{\epsilon}^{ijk} \left(\frac{\partial A_k}{\partial x^j} - \frac{\partial A_j}{\partial x^k} \right), \tag{2.32}$$

where $\tilde{\epsilon}^{ijk}$ is the Levi-Cevita symbol (see Landau & Lifshitz 1959 for instance) . This yields

$$B^r = \frac{1}{\sqrt{|\gamma|}} \frac{\partial \Psi}{\partial \theta}, \tag{2.33a}$$

$$B^\theta = -\frac{1}{\sqrt{|\gamma|}} \frac{\partial \Psi}{\partial r}. \tag{2.33b}$$

Expanding out the continuity equation (1.20a) we find

$$\begin{aligned} 0 &= \nabla \cdot [\Gamma nm(\alpha \mathbf{v} - \beta)] \\ &= \nabla \cdot [\Gamma nm\alpha \mathbf{v}^p] + \nabla \cdot \left[\Gamma nm(\alpha v^\phi - \beta^\phi) \right] \\ &= \nabla \cdot [\Gamma nm\alpha\kappa \mathbf{B}^p] \\ &= \mathbf{B}^p \cdot \nabla [\Gamma nm\alpha\kappa] \end{aligned} \tag{2.34}$$

Axisymmetry and the form of the poloidal magnetic field components allow us to conclude that

$$\Gamma nm = \frac{F(\Psi)}{4\pi\alpha\kappa}, \tag{2.35}$$

where $F(\Psi)$ is an arbitrary function of the magnetic flux surface. Similarly, inspection of (1.20d) allows us to conclude

$$\mathbf{E} = -G(\Psi)\nabla\Psi, \tag{2.36}$$

where $G(\Psi)$ is a function satisfying the constraint

$$G(\Psi) = v^\phi - \kappa B^\phi. \tag{2.37}$$

In analogy with the classical case, we define the toroidal magnetic field in terms of an unknown function $H(\Psi)$ through

$$B^{\phi} = \sqrt{\frac{\Sigma}{A\Delta}} \frac{H(\Psi)}{\sin^2\theta}. \tag{2.38}$$

We can gain a physical intuition for the unknown function $H(\Psi)$ by integrating Ampère's law (1.20c) on a disc $S = \{r \leq r_0, \theta \leq \theta_0\}$. The total current crossing this disc is then given by

$$I = \frac{H(\Psi)}{2}. \tag{2.39}$$

The physical interpretation of $H(\Psi)$ is therefore consistent with the corresponding function defined for the classical case. Let us consider the behaviour of the fields at the surface of the disc $\theta = 0$. Using (1.20d) and applying $v^{\theta} = 0$ we find

$$E^{r} = -\frac{1}{g_{rr}} \frac{\partial \Psi}{\partial r} \frac{(\Omega + \beta^{\phi})}{\alpha}, \tag{2.40}$$

where we have introduced $\Omega = (\alpha v^{\phi} - \beta^{\phi})$, the angular velocity of the disc as measured by a distant observer. Comparing with (2.36) we find that

$$G(\Psi) = \frac{(\Omega + \beta^{\phi})}{\alpha} = \frac{(\Omega - \omega)}{\alpha} \tag{2.41}$$

where ω is the angular velocity of the FIDOs. Physically, this indicates that the difference in angular velocity of the disc and the FIDOs, as measured by a distant observer, is only a function of the magnetic flux surface. Therefore, the distant observer can think of a flux surface as the surface along which the difference in jet and FIDO angular velocity is constant. In the classical limit, where FIDO's are stationary with respect to the coordinates, this reproduces the function $G(\Psi)$ introduced in the classical case. Next we calculate the electric charge density by substituting (2.36) into (1.20b) which yields

$$4\pi\rho_e = -\nabla \cdot [G(\Psi)\nabla\Psi]\,. \tag{2.42}$$

Similarly we obtain the current density from (1.20c)

$$4\pi\alpha \mathbf{j}^p = -\nabla H(\Psi) \times \nabla \boldsymbol{e}_\phi, \tag{2.43a}$$

$$\frac{4\pi}{\sqrt{g_{\phi\phi}}} j^\phi = -\frac{1}{\alpha}\nabla \cdot \left(\frac{\alpha}{g_{\phi\phi}}\nabla\Psi\right) + G(\Psi)\left(\nabla\Psi \cdot \nabla G(\Psi)\right) - G(\Psi)G'(\Psi)\left(\nabla\Psi\right)^2 \tag{2.43b}$$

Substituting these results into the force-free Euler equation (1.20g) yields the Grad-Shafranov equation

$$\nabla \cdot \left\{\frac{\alpha}{g_{\phi\phi}}\left[1 - G^2(\Psi) g_{\phi\phi}\right]\nabla\Psi\right\} + G(\Psi)G'(\Psi)(\nabla\Psi)^2 + \frac{1}{\alpha g_{\phi\phi}} H(\Psi)H'(\Psi) = 0. \tag{2.44}$$

We note that in the limit $\alpha \to 1$, $g_{\phi\phi} \to r^2 \sin^2\theta$ (2.44) reduces to the classical Grad-Shafranov equation (2.21) with the flux functions $G(\Psi)$ and $H(\Psi)$ defined as in the classical case.

2.2.1 Numerical Solutions

We want to solve the Grad-Shafranov equation in Schwarzschild geometry. In cylindrical coordinates, (2.44) takes the form

$$\alpha^2\left[1 - R^2G^2(\Psi)\right]\Delta^*\Psi(R,Z) - \frac{\alpha^4}{2R^2}\nabla\Psi(R,Z)\cdot\nabla\left[\frac{R^4G^2(\Psi)}{\alpha^2}\right] + H(\Psi)H'(\Psi) = 0, \tag{2.45}$$

where the Grad-Shafranov operator in cylindrical coordinates is given by

$$\Delta^* = \frac{\partial^2}{\partial R^2} - \frac{1}{R}\frac{\partial}{\partial R} + \frac{\partial^2}{\partial Z^2}, \tag{2.46}$$

the lapse function is

$$\alpha = \sqrt{1 - r_S/r}, \tag{2.47}$$

and the function describing the rotation of the field lines is given by

$$G(\Psi) = \frac{\Omega}{\alpha}. \tag{2.48}$$

where $r_S = 2GM/c^2$ is the Schwarschild radius of the central object. Above $'$ denotes a derivative with respect to Ψ.

We are interested in determining the functions $\Psi(R, Z)$, $G(\Psi)$ and $H(\Psi)$ which are a solution of (2.45). This requires imposing a set of boundary conditions and regularity conditions. Picking boundary conditions involves choosing the form of the unknown function along a specified boundary of the solution region. Physically, this is like choosing the form of your model. A regularity condition is a condition that you impose on the solution of your model. It differs from a boundary condition in that you are not constraining your solution i.e reducing the degrees of freedom of your problem. Rather regularity conditions allow you to choose from the solutions obtained from the boundary conditions those that are physically reasonable based on the regulairty conditions imposed. We discuss both these, as they relate to our problem, in more detail below.

Boundary Conditions

The GS equation is a second order differential equation for Ψ, with two a priori unspecified functions $G(\Psi)$ and $H(\Psi)$. Therefore we must impose conditions for Ψ on the boundaries of the solution region. Based on previous work we choose to impose a dipole-like field along the plane of the disc and perfectly conducting boundaries along all the other sides

$$\Psi(R, 0) = \frac{a^3 R^2}{(a^2 + R^2)^{3/2}} \left[1 - (R/R_0 - 1)^2/81\right], \tag{2.49a}$$

$$\Psi(0, Z) = 0, \tag{2.49b}$$

$$\Psi(R_{max}, Z) = 0, \tag{2.49c}$$

$$\Psi(R, Z_{max}) = 0, \tag{2.49d}$$

where R_{max}, Z_{max} are the maximum radial and axial distances respectively, R_0 is the location of the O-point and $a \equiv R_0/\sqrt{2}$.

Next we must choose a model for the accretion disc . We will consider two possible models, the unphysical "vacuum" case where

$$\Omega = 0 \tag{2.50}$$

and the "Keplerian" case where magnetic field lines are assumed to be anchored to a differentially rotating Keplerian disc begining at $R_{ISCO} = 3R_S$, the innermost stable circular orbit of the black hole, and extending to the edge of the solution region. Hence

$$\Omega(R) = \begin{cases} \Omega(R_{ISCO}) & R_S \leq R \leq R_{ISCO} \\ \sqrt{\frac{GM}{R^3}} & R \geq R_{ISCO} \end{cases} \tag{2.51}$$

The value of Ω for $R < R_{ISCO}$ was chosen as such so it would be continuous. We note that the region inside the ISCO is so much smaller than the Keplerian region that it will have little effect on our results. Lines are assumed to be frozen into the disc , but are free to pass through the event horizon. Hence there will be no twisting of the field lines in such a configuration.

Regularity Conditions

The more challenging problem involves solving for the function $H(\Psi)$. To do this we first consider two singular surfaces of the GS equation, the event horizon where

$$\alpha(r_S) = 0 \tag{2.52}$$

and the light cylinder defined as the surface where

$$\alpha(r_{LC}) = R\Omega. \tag{2.53}$$

Physically, this is the surface where the toroidal velocity of the field lines, as measured by a FIDO $v = R\Omega/\alpha$, equals the speed of light. We note that unlike the event horizon, the light cylinder radius is a non-trivial function of θ. We will argue that though the GS equation is singular on these surfaces, we can still get physically sensible results by imposing regularity conditions on these surfaces, which restrict the forms of the allowed solution.

As originally discussed in Thorne, Price & Macdonald (1986), the only physical condition that can be applied at the event horizon is that a freely falling observer (FFO) should measure finite values for all fields. Hence, to ensure that our solution for Ψ is physical we will consider a general expansion asymptotically close to the horizon, as measured by the FIDOs, boost into the FFO frame and determine which terms can be retained in the solution given that $\mathbf{E}_{FFO}$ and $\mathbf{B}_{FFO}$ must be finite.

The GS equation is singular at the event horizon because the second order radial derivative vanishes. By inspection of (2.45) the lowest order terms in the expansion of the flux function near the horizon is

$$\begin{aligned}\Psi(r,\theta) = \; & \Psi_0(\theta) + \tilde{\Psi}_1(\theta)(r-r_S)\log(r-r_S) + \Psi_1(\theta)(r-r_S) \\ & + \hat{\Psi}_2(\theta)(r-r_S)^2\log^2(r-r_S) + \tilde{\Psi}_2(\theta)(r-r_S)^2\log(r-r_S) \\ & + \Psi_2(\theta)(r-r_S)^2 + ...\end{aligned} \tag{2.54}$$

One can boost from the FIDO frame to the FFO frame with a radial boost of velocity and corresponding time dilation factor

$$v = \sqrt{\frac{2M}{r}} \qquad\qquad \gamma = \frac{1}{\alpha}. \tag{2.55}$$

Requiring that all FFO fields are finite, we can conclude that in the FIDO frame we must have

$$\mathbf{E}_\perp, \mathbf{B}_\perp \quad \text{finite} \tag{2.56a}$$

$$\mathbf{E}_{\parallel}, \mathbf{B}_{\parallel} \propto \frac{1}{\alpha} \tag{2.56b}$$

The subscripts above refer to the direction relative to the horizon i.e. $\perp$ is r and $\parallel$ is in the θ, ϕ directions. Though the $\parallel$ components of the fields may diverge, a special combination of electric and magnetic fields remains finite, in particular

$$\mathbf{E}_{\parallel} - \mathbf{n} \times \mathbf{B}_{\parallel} \sim \alpha \tag{2.57}$$

remains finite, where $\mathbf{n}$ is the unit normal to the horizon. First, we conclude from (2.56a) that $\Psi(r_S, \theta)$ must be finite. From the ϕ component of (2.57), since $E_\phi = 0$ by axisymmetry, we conclude that $B_\theta \sim \alpha$. Therefore

$$\frac{\partial \Psi}{\partial r} \quad \text{finite} \tag{2.58}$$

at the horizon and we conclude that $\tilde{\Psi}_1 = 0$. We substitute (2.54) into (2.45) and consider the resulting equation order by order. First we note that the logarithmic terms cannot be balanced, and so conclude that $\hat{\Psi}_2 = \tilde{\Psi}_2 = 0$. The lowest order piece of the expansion yields the condition

$$H(\Psi)H'(\Psi) = \Omega(\Psi)\sin(\theta)\left[\Omega' \sin\theta \left(\frac{d\Psi}{d\theta}\right)^2 + \Omega \cos\theta \frac{d\Psi}{d\theta} + \Omega \sin\theta \frac{d^2\Psi}{d\theta^2}\right], \tag{2.59}$$

where all quantities are evaluated at the horizon. Integrating we find

$$H(\Psi) = \pm\Omega(\Psi)\sin\theta \frac{d\Psi}{d\theta}, \tag{2.60}$$

where the integration constant is set to zero by imposing that there be no current along the central axis $H(r_S, 0) = 0$. Using the θ component of (2.57) as well as the expressions for toroidal magnetic field (2.38) and poloidal electric field (2.36) we conclude we must take the positive expression i.e.

$$H(\Psi) = \Omega(\Psi)\sin\theta \frac{d\Psi}{d\theta}. \tag{2.61}$$

We stress that (2.61) is a regularity condition and not a boundary condition. In other words, it is a condition that we impose on the current function, so that

the resulting magnetic and electric fields will both satisfy the GS equation and be physical (non divergent) at the horizon. In contrast, a boundary condition would be a free function that could be imposed at the event horizon, which (2.61) is not.

Now consider the GS equation along the light cylinder. Along the light cylinder, the first term of (2.45) can remain finite despite $\partial_{rr}\Psi$, $\partial_{zz}\Psi$ diverging. This means the GS equation admits solutions that are discontinuous at the light cylinder. Physically, this corresponds to solutions where there is a current buildup along the light cylinder. If we demand that there not be any such discontinuous jumps in the current, then the second derivatives will be continuous and the first term of the GS equation will vanish at the light cylinder. It therefore reduces to the condition

$$H(\Psi)H'(\Psi) = \Omega\Omega'(\Psi)R^2|\nabla\Psi|^2 + 2\alpha^2\frac{\cot\theta}{r^2}\frac{\partial\Psi}{\partial\theta} - \frac{\alpha^2}{r}\left(1-3\alpha^2\right)\frac{\partial\Psi}{\partial r}, \tag{2.62}$$

for $r = r_{LC}$.

Let us now ensure that we have not overconstrained our problem. Our solution region is the 1^{st} quadrant of the R-Z plane, with a quarter circle cut out, the event horizon. Ψ has been specified everywhere along the boundary except along the quarter circle. Assuming all field lines begin somewhere along the disc , Ω can be determined everywhere by specifying it along the disc . The current can be determined by knowing the potential along the light cylinder. Finally, the potential can be deduced along the horizon from the current and the regularity condition at the horizon.

Successive Over-Relaxation Algorithm

We use an SOR algorithm to solve (2.45) numerically. Step 1 consists of solving the vacuum GS equation, where the poloidal current H(Ψ) = 0. Subsequent steps require walking along lines of Ψ = const. Solving the vacuum equation ensures that there are well defined field lines to walk along. We then solve the full problem as follows. Starting at each grid point along the disc and outside r_{ISCO}, we walk along a field line until the horizon is crossed. If a line crosses the event horizon, we calculate the current using (2.61). After walking along each field line, we go back and assign a current $H(\Psi)$ and angular velocity $\Omega(\Psi)$ to each gridpoint (i,j). We do this by interpolating the $\Psi(i, j)$ value with those at the horizon (for the currents) and those along the disc (for the angular velocity) We then update Ψ using the GS equation (2.45). These steps are repeated until subsequent iterations yield a change smaller than the required tolerance.

We note this varies slightly from the procedure described in section 2.2.1. This is because we are interested in MC configurations, where every field line begins on the disc and ends on the event horizon. Ψ does not have to be calculated on the horizon from the current; rather the current can be calculated from the Ψ value near the horizon, which was not imposed. We would be unable to do this in a Blandford-Znajek configuration where field lines crossing the horizon extend to infinity, because such configurations impose Neumann boundary conditions at infinity, and we would need the horizon regularity condition to determine Ψ for these field lines crossing the horizon.

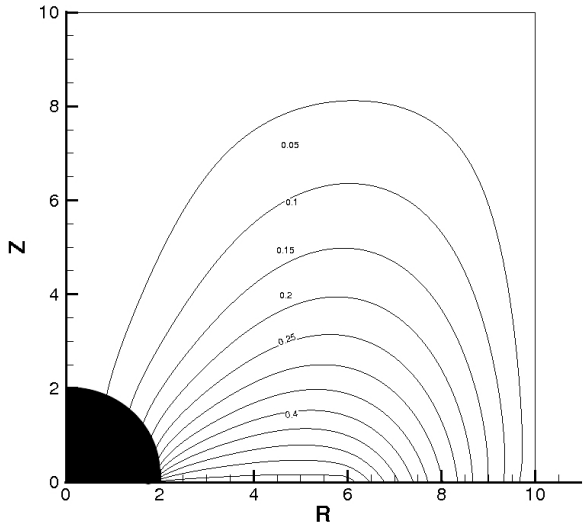

Figure 2.7: Magnetic flux function Ψ equipotential lines in poloidal plane for vacuum Schwarzschild case

Vacuum Case

The simplest, albeit unphysical case is for a non-rotating disc with boundary conditions for the angular velocity along the disc given by (2.50). This is a good test for our code, and also used as the initial configuration for subsequent solutions. We see from (2.61) that $H(\Psi) = 0$ and the GS equation reduces to

$$\Delta^*\Psi(R, Z) = 0. \tag{2.63}$$

The contours of Ψ = const. are plotted in Fig. 2.7

Keplerian Disk

The next simplest and non-trivial case is for a Keplerian disc . We assume the angular velocity along the disc is given by (2.51) Our results are plotted in Fig.2.8.

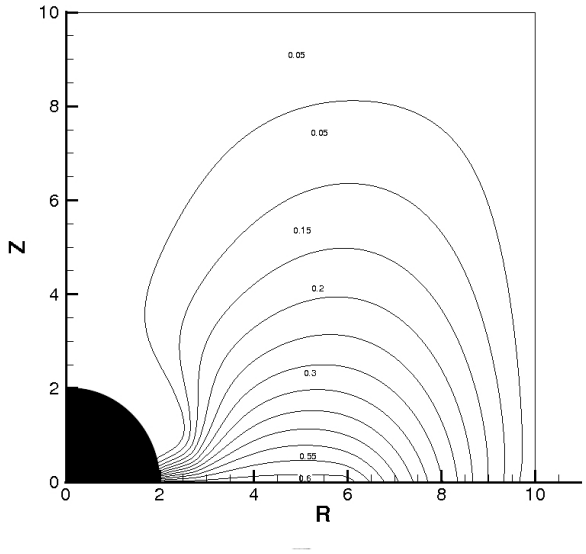

Figure 2.8: Magnetic flux function Ψ equipotential lines in poloidal plane for the Schwarzschild case with Keplerian disc

2.3 Jet Model

By assuming that the magnetosphere is dominated by the electromagnetic energy we show that the system is described by the Grad-Shafranov equation. However, if we relax this assumption, we can construct models of jets that have matter outflows. Below we sketch one such model, where we assume a certain form for the vector potential and derive the form of the matter jet.

Electromagnetic Field

In this section we derive expressions for the components of the electric and magnetic fields, consistent with the MHD equations and our assumptions of stationary, axisymmetric, thin jets. By the assumed axisymmetry and the no monopoles condition (1.20f) we can break up the magnetic field into its poloidal

B^p and toroidal B^ϕ components

$$\mathbf{B} = \mathbf{B}^p + \mathbf{B}^\phi. \tag{2.64}$$

The poloidal magnetic field will be generated by a vector potential $\boldsymbol{\psi}$ in the toroidal direction

$$\mathbf{B}^p = \nabla \times (\boldsymbol{\psi}^\phi), \tag{2.65}$$

where by axisymmetry $\boldsymbol{\psi} = \boldsymbol{\psi}(r, \theta)$. Let us denote the outer boundary of the jet by a function $\Theta(r)$. Define a dimensionless polar angular variable

$$\epsilon \equiv \left(\frac{\theta}{\Theta(r)} \right)^2. \tag{2.66}$$

As an ansatz for the vector potential, we will use

$$\psi(r, \theta) = \psi(\epsilon). \tag{2.67}$$

This corresponds to the ansatz (7a) used in Lovelace, Berk & Contopoulos (1991). Using this ansatz and the definition of the curl

$$(\nabla \times A)^i = \frac{1}{2\sqrt{|\gamma|}} \tilde{\epsilon}^{ijk} \left(\frac{\partial A_k}{\partial x^j} - \frac{\partial A_j}{\partial x^k} \right),$$

where $\tilde{\epsilon}^{ijk}$ is the Levi-Cevita symbol, we compute the poloidal components and find

$$B^r = \frac{1}{\sqrt{|\gamma|}} \partial_\theta \psi(\epsilon), \tag{2.68}$$

$$B^\theta = -\frac{1}{\sqrt{|\gamma|}} \partial_r \psi(\epsilon). \tag{2.69}$$

We note the Jacobians

$$\frac{\partial \epsilon}{\partial r} = -2 \frac{\theta^2}{\Theta^3} \frac{\partial \Theta}{\partial r}, \qquad \frac{\partial \epsilon}{\partial \theta} = 2 \frac{\theta}{\Theta^2}, \tag{2.70}$$

allow us to relate the magnetic field components through

$$B^\theta = \sqrt{\epsilon} \frac{\partial \Theta}{\partial r} B^r. \tag{2.71}$$

Substituting Ohm's law (1.20d) into Faraday's law (1.20e) we obtain the "frozen-in" field equation

$$\nabla \times [(\alpha \mathbf{v} - \boldsymbol{\beta}) \times \mathbf{B}] = 0. \tag{2.72}$$

The poloidal component of this equation implies that $\mathbf{v}^p \propto \mathbf{B}^p$. Physically this can be seen as follows. First note $E^\phi = 0$ because of the axisymmetry assumption and E-fields are irrotational. From Ohm's law, we see this implies $(\mathbf{v} \times \mathbf{B})^\phi = 0$. This can only hold if $\mathbf{v}^p$ and $\mathbf{B}^p$ are parallel, since they both lie in the plane orthogonal to the toroidal direction.

In general, we can break up a poloidal vector into a radial and a polar part, $\mathbf{v}^p = (v^r, 0, v^\theta) \propto \mathbf{B}^p = (B^r, 0, B^\theta)$. It follows that

$$v^r B^\theta = v^\theta B^r. \tag{2.73}$$

Substituting (2.71) we find

$$v^\theta = v^r \frac{B^\theta}{B^r} = \sqrt{\epsilon} \frac{\partial \Theta}{\partial r} v^r. \tag{2.74}$$

To proceed further, we expand out the no monopoles condition (1.20f) explicitly using our curvilinear coordinates (r,θ,ϕ) as [1]

$$\partial_r \left(\sqrt{|\gamma|} B^r \right) + \partial_\theta \left(\sqrt{|\gamma|} B^\theta \right) + \partial_\phi \left(\sqrt{|\gamma|} B^\phi \right) = 0. \tag{2.75}$$

The last term vanishes by axisymmetry of the field and the metric components. Using (2.71) to eliminate the polar magnetic field and substituting the determinant of the metric yields

$$\partial_r \left[\frac{(r^2 + a^2)^{3/2} \theta}{(r^2 + a^2 - 2Mr)^{1/2}} B^r \right] + \partial_\theta \left[\frac{(r^2 + a^2)^{3/2}}{(r^2 + a^2 - 2Mr)^{1/2}} \frac{\theta^2}{\Theta} \frac{\partial \Theta}{\partial r} B^r \right] = 0. \tag{2.76}$$

[1] A note on this expansion. The usual formula for a divergence in curvilinear coordinates reads (see Arfken et al. 2012 for instance) $\nabla \cdot B = \partial_r (\bar{B}^r \sqrt{g_{\theta\theta}} \sqrt{g_{\phi\phi}} + ...)$ where $\bar{B}^r \equiv \sqrt{g_{rr}} B^r$ is the value of the field in an orthonormal frame. In the language of the membrane paradigm, it is the physical value of the field measured by a FIDO in his local coordinate frame. This explains the factor of $\sqrt{|\gamma|}$ above.

It is easily verified that the solutions are

$$B^r = \left(\frac{\Delta}{\Sigma}\right)^{1/2} \frac{\Phi}{(r^2+a^2)\Theta^2(r)}, \qquad \theta \le \Theta(r) \tag{2.77a}$$

$$B^r = \left(\frac{\Delta}{\Sigma}\right)^{1/2} \frac{\Phi}{(r^2+a^2)\theta^2}, \qquad \theta > \Theta(r) \tag{2.77b}$$

Substituting this result back into (2.71) yields

$$B^\theta = \left(\frac{\Delta\epsilon}{\Sigma}\right)^{1/2} \frac{\partial\Theta(r)}{\partial r} \frac{\Phi}{(r^2+a^2)\Theta^2(r)}, \qquad \theta \le \Theta(r) \tag{2.78a}$$

$$B^\theta = \left(\frac{\Delta\epsilon}{\Sigma}\right)^{1/2} \frac{\partial\Theta(r)}{\partial r} \frac{\Phi}{(r^2+a^2)\theta^2}, \qquad \theta > \Theta(r) \tag{2.78b}$$

We now want to massage the toroidal part of (2.72). This is most easily done in tensor notation, where the equation reads

$$\nabla \times [(\alpha \mathbf{v} - \boldsymbol{\beta}) \times \mathbf{B}] = \epsilon^{nmi} \partial_m \epsilon_{ijk} (\alpha v^j - \beta^j) B^k = 0, \tag{2.79}$$

where $\epsilon_{ijk} = \sqrt{|\gamma|}\tilde{\epsilon}_{ijk}$ is the Levi-Cevita tensor on the absolute space. Using the identity $\epsilon^{nmi}\epsilon_{ijk} = 2(\delta^n_j\delta^m_k - \delta^m_j\delta^n_k)$, the toroidal $n = \phi$ component reads

$$\partial_k[\sqrt{|\gamma|}(\alpha v^\phi - \beta^\phi)B^k] = \partial_j[\sqrt{|\gamma|}(\alpha v^j - \beta^j)B^\phi]. \tag{2.80}$$

Expanding this out (a cancellation occurs for the $k = j = \phi$ terms), and using (1.20f) to eliminate any terms involving derivatives of B on the left hand side (LHS) we find

$$B^\theta \partial_\theta[\sqrt{|\gamma|}(\alpha v^\phi - \beta^\phi)] + B^r \partial_r[\sqrt{|\gamma|}(\alpha v^\phi - \beta^\phi)] = \partial_\theta(\sqrt{|\gamma|}\alpha v^\theta B^\phi) + \partial_r(\sqrt{|\gamma|}\alpha v^r B^\phi). \tag{2.81}$$

For the LHS we transform the θ and r partial derivatives acting on $\sqrt{|\gamma|}$ using (2.70) and show that these contributions vanish. What we are left with is

$$\sqrt{|\gamma|}B^\theta \partial_\theta \Omega + \sqrt{|\gamma|}B^r \partial_r \Omega = \partial_\theta(\sqrt{|\gamma|}\alpha v^\theta B^\phi) + \partial_r(\sqrt{|\gamma|}\alpha v^r B^\phi), \tag{2.82}$$

where we have defined $\Omega = (\alpha v^\phi - \beta^\phi)$, the angular velocity of the jet as seen by a distant observer. We will assume that $\Omega = \Omega(r)$, which corresponds to ansatz (10b) in Lovelace, Berk & Contopoulos (1991). It is easily verified that the solution to (2.82) with this assumption is

$$B^\phi(r) = \frac{\Phi(\Omega - \Omega_0)}{(r^2 + a^2)v^r \Theta^2(r)}, \qquad \theta \leq \Theta, \tag{2.83}$$

where Ω_0 is the angular velocity of the jet, as measured by a distant observer, at some fixed reference radius r_0 and Φ is the magnetic flux of the jet, assumed to be constant. To complete our study of the electromagnetic field near the jet we calculate the non-zero components of the electric field using (1.20d) and find

$$E^\theta = -(\mathbf{v} \times \mathbf{B})^\theta = -\frac{\Phi}{\alpha\Sigma}\frac{\theta}{\Theta^2(r)}(\beta^\phi + \Omega_0), \tag{2.84}$$

$$E^r = -(\mathbf{v} \times \mathbf{B})^r = \alpha\Phi\frac{\theta^2}{\Theta^3(r)}\frac{\partial\Theta}{\partial r}(\beta^\phi + \Omega_0). \tag{2.85}$$

Conservation Equations

We now want to use the conserved quantities (particle number, momentum, angular momentum, energy) to solve for the jet variables: velocity $\mathbf{v}$, boundary angle Θ, rotation rate Ω and density ρ. We proceed by integrating the relevant conservation equation over a cross section of the jet at fixed radial coordinate. For thin jets, this corresponds to the integration over $z = \text{const}$.

Baryon Conservation We integrate (1.20a) over a 3-volume containing a surface $r = \text{const}$ spanning the jet. By the divergence theorem we keep only the $\hat{r}$ component and find

$$\hat{M} = \iiint \nabla \cdot [\Gamma mn(\alpha\mathbf{v} - \boldsymbol{\beta})] = \int_0^{2\pi} d\phi \int_0^{\Theta} d\theta \;\; [\alpha\sqrt{|\gamma|}\,\Gamma mnv^r] = \text{const}. \tag{2.86}$$

$\hat{M}$ is the mass-flow rate in the jet across a surface of r = const.. The integral in ϕ can be carried out because of axial symmetry. However, to do the integral in θ we must assume a form for the number density which in general is $n(r, \theta)$. A simple choice is

$$n(r, \theta) = \bar{n}(r) f(\epsilon), \tag{2.87}$$

where $\bar{n}$ is the average jet number density and $f(\epsilon) \geq 0$ is a dimensionless number density profile normalized so as to satisfy

$$\int_0^1 d\epsilon \; f(\epsilon) = 1. \tag{2.88}$$

We note this is identical to ansatz (10d) in Lovelace, Berk & Contopoulos (1991).

In addition, we must also worry about polar dependence of the Γ factor. First note that the velocity dependence enters through the term

$$|v|^2 = g_{rr}(v^r)^2 + g_{\theta\theta}(v^\theta)^2 + g_{\phi\phi}(v^\phi)^2. \tag{2.89}$$

Since the θ dependence is coming from the last two terms, the requirement that $\Gamma \simeq \Gamma(r)$ amounts to demanding these two terms be subleading to the first term. Simplifying these conditions yields

$$\sqrt{r^2 + a^2 - 2Mr}\frac{\theta}{\Theta}\frac{\partial \Theta}{\partial r} \ll 1, \tag{2.90a}$$

$$\sqrt{r^2 + a^2}\theta(\Omega - \omega) \ll v^r. \tag{2.90b}$$

We will refer to this set of conditions as the radial jet regime. We will find that these assumptions simplify greatly the energy density, Poyting vector and stress-energy tensor. With these simple ansatz for the number density profile and relativistic boost factor, we can change integration variables $\theta d\theta \to 1/2\Theta^2 d\epsilon$ and carry out the integrations to find

$$\hat{M} = \pi(r^2 + a^2)\Theta^2 \Gamma m \bar{n} v^r = \text{const.} \tag{2.91}$$

Momentum Conservation We now want to apply momentum conservation to a surface of constant r in the jet. We first note that in the stationary regime (1.20i) reduces to

$$-\frac{1}{\alpha}(\boldsymbol{\beta}\cdot\nabla)\boldsymbol{S} = \boldsymbol{\varepsilon g} + \overleftrightarrow{\boldsymbol{H}}\cdot\mathbf{S} - \frac{1}{\alpha}\nabla\cdot(\alpha\boldsymbol{T}). \tag{2.92}$$

This is a vector equation, so we study each component separately. Using (1.20j) compute the components of the gravitational acceleration

$$g_r = -\frac{M(r^2-a^2)}{(r^2+a^2)\Delta}, \qquad g_\theta = \frac{2Mra^2\theta}{(r^2+a^2)^2}, \qquad g_\phi = 0. \tag{2.93}$$

Note that for this calculation, we differentiated the exact expression for the lapse function (1.15a) and then took the thin jet limit.

To further simplify things we derive results to eliminate the gravitomagnetic tensor from the momentum conservation equations. We note that

$$\begin{aligned}\iiint(\overleftrightarrow{\boldsymbol{H}}\cdot\mathbf{S})_\phi = \iiint H_{\phi k}S^k &\equiv \iiint\frac{1}{\alpha}\beta_{k;\phi}S^k \\ &= \iiint\frac{1}{\alpha}g_{\mu k}\beta^\mu{}_{;\phi}S^k \\ &= -\iiint\frac{1}{\alpha}\beta^\mu S_{\mu;\phi} \\ &= -\iiint\frac{1}{\alpha}(\boldsymbol{\beta}\cdot\nabla)\mathbf{S}_\phi\end{aligned} \tag{2.94}$$

where in the second and third step we have used that the metric is covariantly conserved, we have integrated by parts and in the final step used that the only non-vanishing component of the shift vector is β^ϕ. Since the integration is over an arbitrary surface, we conclude

$$(\overleftrightarrow{\boldsymbol{H}}\cdot\mathbf{S})_\phi = -\frac{1}{\alpha}(\boldsymbol{\beta}\cdot\nabla)\mathbf{S}_\phi. \tag{2.95}$$

Similarly

$$\begin{aligned}\iiint H_{\phi i} S^{\phi} &\equiv \iiint \frac{1}{\alpha}\beta_{i;\phi} S^{\phi} \\ &= \iiint \frac{1}{\alpha} g_{ij}\beta^{j}{}_{;\phi} S^{\phi} \\ &= -\iiint \frac{1}{\alpha}\beta^{\phi} S_{i;\phi} \\ &= -\iiint \frac{1}{\alpha}(\boldsymbol{\beta}\cdot\nabla)\mathbf{S}_i\end{aligned} \tag{2.96}$$

where in the second step we used that the metric is covariantly conserved and that the only non-vanishing component of the shift vector is β^{ϕ}. In the third step we integrated by parts. As this holds for an arbitrary integral we conclude

$$-\frac{1}{\alpha}(\boldsymbol{\beta}\cdot\nabla)\mathbf{S}_i = H_{\phi i} S^{\phi} \tag{2.97}$$

Integrating the ϕ component of (2.92), using (2.93) and (2.94), then applying the divergence theorem to integrate over a surface r = const. yields

$$2\pi L = \int_0^{2\pi} d\phi \int_0^{\Theta} d\theta \;\; \alpha\sqrt{|\gamma|}\, T^{r}{}_{\phi} = \text{const}, \tag{2.98}$$

where L is the angular momentum of an r = const. slice of the jet. Using the definition for the stress-energy tensor (1.34) we find

$$T^{r}{}_{\phi} = g_{\phi\phi}T^{r\phi} = (r^2+a^2)\theta^2\left[nm\left(1+\frac{4kT}{m}\right)\Gamma^2(\Omega+\beta^{\phi})\frac{v^r}{\alpha} - \frac{1}{4\pi}\left(\frac{\alpha\Phi^2(\Omega-\Omega_0)}{(r^2+a^2)^2 v^r \Theta^4}\right)\right]. \tag{2.99}$$

Substituting into (2.98) we find

$$\frac{\hat{M}\Gamma\xi}{2\pi\alpha}\left(1+\frac{4kT}{m}\right)(r^2+a^2)(\beta^{\phi}+\Omega)\Theta^2 - \frac{\alpha\Phi^2(\Omega-\Omega_0)}{16\pi v^r} = L, \tag{2.100}$$

where we have defined

$$\xi \equiv \int_0^1 \epsilon f(\epsilon) d\epsilon. \tag{2.101}$$

Similarly, we can study the poloidal components of momentum conservation of

(2.92). Integrating and simplifying using (2.97) we find

$$\int_{r_0}^{r} dr \int_0^{2\pi} d\phi \int_0^{\Theta} d\theta \;\; \alpha \sqrt{|\gamma|}\varepsilon g_i + \sqrt{|\gamma|} S_{\phi} \beta^{\phi}{}_{,i} = \int_0^{2\pi} d\phi \int_0^{\Theta} d\theta \;\; \alpha \sqrt{|\gamma|} T^{r}{}_{i} \qquad i = r, \theta \tag{2.102}$$

where we have eliminated the need of calculating the gravitomagnetic stress tensor by noting all non-zero elements are of the form $H_{i\phi}$ with $i = r, \theta$ and

$$\begin{aligned} \left(H_{i\phi} - H_{\phi i}\right) S^{\phi} &= \frac{1}{\alpha} \left(\beta_{\phi;i} - \beta_{i;\phi}\right) S^{\phi} \\ &= \frac{1}{\alpha} \left(\beta_{\phi,i} - \Gamma^{k}_{\phi i} \beta_k + \Gamma^{k}_{i\phi} \beta_k\right) S^{\phi} \\ &= \frac{1}{\alpha} \beta_{\phi,i} S^{\phi} \end{aligned} \tag{2.103}$$

Substituting in the appropriate components of the stress energy tensor and Poynting vectors and expanding to lowest order in the small parameter Θ, the r component of (2.102) reduces to

$$M \int_{r_0}^{r} \frac{(r^2 - a^2) dr}{\Theta^2 (r^2 + a^2)^2 \Delta} \approx \frac{1}{(r^2 + a^2)\Theta^2}. \tag{2.104}$$

Differentiating with respect to r, this can be written as a differential equation of the jet outer boundary

$$\frac{\partial \Theta}{\partial r} = -\Theta \left(\frac{2\Delta r + M(r^2 - a^2)}{2\Delta (r^2 + a^2)} \right) \tag{2.105}$$

The solution to (2.105) is found to be

$$\begin{aligned} \Theta(r) &= \Theta_0 \exp\left\{ - \int_{r_0}^{r} \left(\frac{2\Delta r + M(r^2 - a^2)}{2\Delta (r^2 + a^2)} \right) \right\} \\ &= \Theta_0 \left(\frac{\Sigma_0}{\Sigma} \right)^{1/4} \left(\frac{\Delta_0}{\Delta} \right)^{1/4}, \end{aligned} \tag{2.106}$$

where $\Theta_0, \Delta_0, \Sigma_0$ are the respective quantities evaluated at the reference value r_0. The θ component of (2.102) yields, up to leading order by treating Θ as a small parameter

$$\int_{r_0}^{r} dr \frac{M r a^2}{\Theta (r^2 + a^2)^3} = -\frac{\alpha^2}{\Theta^2} \frac{\partial \Theta}{\partial r}. \tag{2.107}$$

This can be written as the second order differential equation

$$\frac{\partial^2\Theta}{\partial r^2} - \frac{2}{\Theta}\left(\frac{\partial\Theta}{\partial r}\right)^2 + \frac{2M(r^2-a^2)}{\Delta(r^2+a^2)}\frac{\partial\Theta}{\partial r} + \frac{Mra^2}{\Delta(r^2+a^2)^2} = 0. \tag{2.108}$$

Fortuitously we find that up corrections of $O(M/r)$ (2.106) is a solution of (2.108). Our solution can therefore be considered valid far from the horizon.

Energy Conservation In the stationary case (1.20h) simplifies to

$$\nabla\cdot(\alpha^2\mathbf{S}) = -\alpha^2\sigma_{ik}T^{ik}. \tag{2.109}$$

In our thin jet approximation $\beta^\phi \approx \beta^\phi(r)$ so the RHS can be simplified using

$$\sigma_{ik}T^{ik} = -\frac{1}{\alpha}T^i{}_\phi\beta^\phi{}_{,i} \approx -\frac{1}{\alpha}T^r{}_\phi\beta^\phi{}_{,r}. \tag{2.110}$$

Substituting above we find

$$\nabla\cdot(\alpha^2\mathbf{S}) = \alpha T^r{}_\phi\beta^\phi{}_{,r}. \tag{2.111}$$

Integrating over a 3-volume bounded by surfaces r = constant along the jet we find, after using the divergence theorem on the LHS and performing the r integral on the RHS by parts

$$\begin{aligned}&\int_0^{2\pi}d\phi\int_0^{\Theta}d\theta\ \ \alpha^2\sqrt{|\gamma|}S^r = \\ &\int_{r_0}^{r}dr\int_0^{2\pi}d\phi\int_0^{\Theta}d\theta\ \ (\alpha\sqrt{|\gamma|}\,T^r{}_\phi)_{,r}\,\beta^\phi - \int_0^{2\pi}d\phi\int_0^{\Theta}d\theta\ \ (\alpha\sqrt{|\gamma|}\,T^r{}_\phi)\,\beta^\phi\big|_{r_0}^{r}\end{aligned} \tag{2.112}$$

The first term on the RHS yields an integration constant by the conservation of momentum equation (2.98). To proceed we need the Poynting vector component S^r. Using (1.33) we find

$$\begin{aligned}S^r &= (mn+P)\Gamma^2v^r + \frac{1}{4\pi}(\mathbf{E}\times\mathbf{B})^r \\ &= m\bar{n}f(\epsilon)\left(1+\frac{4kT}{m}\right)\Gamma^2v^r + \frac{1}{4\pi}\frac{\Phi^2(\beta^\phi+\Omega_0)(\Omega-\Omega_0)\theta^2}{(r^2+a^2)\Theta^4v^r}.\end{aligned} \tag{2.113}$$

Substituting (2.113) into (2.112), recalling the defintion of angular momentum (2.98) and carrying out the integrations yields

$$\frac{\alpha\hat{M}\Gamma}{2\pi}\left(1+\frac{4kT}{m}\right)-\frac{1}{16\pi}\frac{\alpha\Phi^2}{v^r}(\Omega_0-\omega)(\Omega-\Omega_0)=\frac{\alpha_0\hat{M}\Gamma_0}{2\pi}\left(1+\frac{4kT_0}{m}\right)+L(\omega_0-\omega), \quad (2.114)$$

where $\omega_0 = -\beta^\phi(r_0)$ is the FIDO angular velocity at the reference value of r_0 and we have picked the integration constant by evaluating the equation at r_0. After some tedious algebra, (2.100) and (2.114) can be combined to yield

$$\Omega = \omega + \frac{\alpha\left[\Gamma\alpha + \frac{2\pi L(\Omega_0-\omega_0)}{\hat{M}\left(1+\frac{4kT}{m}\right)} - \alpha_0\Gamma_0\frac{\left(1+\frac{4kT_0}{m}\right)}{\left(1+\frac{4kT}{m}\right)}\right]}{(\Omega_0-\omega)\xi\Gamma(r^2+a^2)\Theta^2}. \quad (2.115)$$

Evaluating at $r = r_0$ yields

$$\Omega_0 = \omega_0 + \frac{2\pi L\alpha_0}{\hat{M}\xi\Gamma_0\Sigma_0\Theta_0^2(1+\frac{4kT_0}{m})}. \quad (2.116)$$

Jet Properties

We would now like to explore the functions characterising the jet: radial velocity v_r, angular velocity Ω, opening angle Θ and magnetic field components. For purposes of plotting these solutions as a function of radial distance, it will be useful to express them as dimensionless quantities. We will therefore scale the above quantities by their value at the reference radius r_0 and introduce the dimensionless variables

$$\mathsf{V}^r = \frac{\bar{v}^r(r)}{\bar{v}^r(r_0)} = \left(\frac{\Sigma_0}{\Delta_0}\right)^{1/2}\left(\frac{\Delta}{\Sigma}\right)^{1/2} \quad (2.117a)$$

$$\mathsf{\Theta} = \frac{\Theta(r)}{\Theta_0} = \left(\frac{\Sigma_0}{\Sigma}\right)^{1/4}\left(\frac{\Delta_0}{\Delta}\right)^{1/4} \quad (2.117b)$$

$$\mathsf{B}^r = \frac{\bar{B}^r(r)}{\bar{B}^r(r_0)} = \left(\frac{\Sigma_0}{\Delta_0}\right)^{1/2}\left(\frac{\Delta}{\Sigma}\right)^{1/2} \quad (2.117c)$$

$$\Omega = \frac{\Omega}{\Omega_0} = \frac{(\Omega_0 - \omega_0)}{(\Omega_0 - \omega)} \left(\frac{\Sigma_0}{\Sigma}\right)^{1/2} \left(\frac{\Delta}{\Delta_0}\right)^{1/2} \left[\frac{\omega\,(\Omega_0 - \omega)\,\xi\Sigma\Theta^2 + \Gamma\alpha^2 + \frac{2\pi L\alpha}{M\left(1+\frac{4kT}{m}\right)(\Omega_0 - \omega_0)}}{\omega_0\,(\Omega_0 - \omega_0)\,\xi\Sigma_0\Theta_0^2 + \Gamma_0\alpha_0^2 + \frac{2\pi L\alpha_0}{M\left(1+\frac{4kT}{m}\right)(\Omega_0 - \omega_0)}} \right] \tag{2.117d}$$

where we emphasize that these are the dimensionless *physical* jet variables.

Physical Quantities

We calculate various physically relevant quantities of the jet in the stationary, axisymmetric, thin ($\theta^2 \ll 1$) approximation.

Energy Density First calculate the electric and magnetic field energy densities.

$$|\mathbf{B}|^2 = \gamma_{ij} B^i B^j = \Phi^2 \left[\frac{1}{(r^2 + a^2)^2 \Theta^4} + \frac{\theta^2}{\Theta^6} \left(\frac{\partial \Theta}{\partial r}\right)^2 \frac{(r^2 + a^2 - 2Mr)}{(r^2 + a^2)^2} + \frac{(\Omega - \Omega_0)^2}{(r^2 + a^2)(v^r)^2} \frac{\theta^2}{\Theta^4} \right], \tag{2.118}$$

$$|\mathbf{E}|^2 = \gamma_{ij} E^i E^j = \Phi^2 (\Omega_0 - \omega)^2 \frac{\theta^2}{\Theta^4} \left[\left(\frac{\theta}{\Theta}\right)^2 \left(\frac{\partial \Theta}{\partial r}\right)^2 + \frac{1}{(r^2 + a^2 - 2Mr)} \right]. \tag{2.119}$$

In the radial jet approximation (2.90) these simplify to

$$|\mathbf{E}|^2 \simeq \frac{\Phi^2\,(\Omega_0 - \omega)^2}{(r^2 + a^2 - 2Mr)} \frac{\theta^2}{\Theta^4}, \tag{2.120}$$

$$|\mathbf{B}|^2 \simeq \frac{\Phi^2}{\Theta^4\left(r^2 + a^2\right)^2}, \tag{2.121}$$

where we have further made the approximation that

$$\frac{\Omega - \Omega_0}{\Omega - \omega} \lesssim 1 \tag{2.122}$$

to simplify $|\mathbf{B}|^2$. Using (1.32) we calculate the jet energy density.

$$\begin{aligned} \varepsilon &\simeq nm\left(1 + \frac{4kT}{m}\right)\Gamma^2 + \frac{1}{8\pi}\left(|\mathbf{E}|^2 + \mathbf{B}|^2\right) \\ &\simeq m\bar{n} f(\epsilon)\left(1 + \frac{4kT}{m}\right)\Gamma^2 + \frac{1}{8\pi}\left(\frac{\Phi^2\,(\Omega_0 - \omega)^2}{(r^2 + a^2 - 2Mr)} \frac{\theta^2}{\Theta^4} + \frac{\Phi^2}{\Theta^4\left(r^2 + a^2\right)^2} \right), \\ &\simeq m\bar{n} f(\epsilon)\left(1 + \frac{4kT}{m}\right)\Gamma^2 + \frac{1}{8\pi} \frac{\Phi^2}{\Theta^4\left(r^2 + a^2\right)^2} \end{aligned} \tag{2.123}$$

where in the last step we have used the thin jet approximation.

Poynting Vector Using (1.33) we find the components of the Poyting vector to be

$$\begin{aligned} S^r &\simeq nm\left(1+\frac{4kT}{m}\right)\Gamma^2 v^r + \frac{1}{4\pi}(\mathbf{E}\times\mathbf{B})^r \\ &= m\bar{n}f(\epsilon)\left(1+\frac{4kT}{m}\right)\Gamma^2 v^r + \frac{1}{4\pi}\frac{\Phi^2(\beta^\phi+\Omega_0)(\Omega-\Omega_0)\theta^2}{(r^2+a^2)\Theta^4 v^r}. \end{aligned} \tag{2.124a}$$

$$\begin{aligned} S^\theta &\simeq nm\left(1+\frac{4kT}{m}\right)\Gamma^2 v^\theta + \frac{1}{4\pi}(\mathbf{E}\times\mathbf{B})^\theta \\ &= m\bar{n}f(\epsilon)\left(1+\frac{4kT}{m}\right)\Gamma^2\frac{\theta}{\Theta}\frac{\partial\Theta}{\partial r}v^r - \frac{\Phi^2}{4\pi}\frac{\theta^3}{\Theta^5}\frac{\partial\Theta}{\partial r}\frac{(\beta^\phi+\Omega_0)\,(\Omega-\Omega_0)}{(r^2+a^2)v^r}. \end{aligned} \tag{2.124b}$$

$$\begin{aligned} S^\phi &\simeq nm\left(1+\frac{4kT}{m}\right)\Gamma^2 v^\phi + \frac{1}{4\pi}(\mathbf{E}\times\mathbf{B})^\phi \\ &= m\bar{n}f(\epsilon)\left(1+\frac{4kT}{m}\right)\Gamma^2\frac{(\Omega+\beta^\phi)}{\alpha} + \frac{1}{4\pi}\frac{\Phi^2}{\alpha}\frac{1}{\Theta^4}\frac{(\beta^\phi+\Omega_0)}{(r^2+a^2)}\left(\alpha^2\frac{\theta^2}{\Theta^2}\left(\frac{\partial\Theta}{\partial r}\right)^2+1\right) \\ &\simeq m\bar{n}f(\epsilon)\left(1+\frac{4kT}{m}\right)\Gamma^2\frac{(\Omega+\beta^\phi)}{\alpha} + \frac{1}{4\pi}\frac{\Phi^2}{\alpha}\frac{1}{\Theta^4}\frac{(\beta^\phi+\Omega_0)}{(r^2+a^2)} \end{aligned} \tag{2.124c}$$

Stress-Energy Tensor Using (1.34) we calculate the components of the stress-energy tensor. We work in the radial jet approximation and take the leading order term in θ.

$$\begin{aligned} T^{rr} &\simeq nm\left[\left(1+\frac{4kT}{m}\right)(v^r)^2+\frac{kT}{m}\gamma^{rr}\right] + \frac{1}{4\pi}\left[-\left((E^r)^2+(B^r)^2\right)+\frac{1}{2}\left(|\mathbf{E}|^2+|\mathbf{B}|^2\right)\gamma^{rr}\right] \\ &\simeq \bar{n}f(\epsilon)m\left[\left(1+\frac{4kT}{m}\right)(v^r)^2+\frac{kT}{m}\frac{\Delta}{\Sigma}\right] \\ &+ \frac{\alpha^2\Phi^2}{4\pi\Theta^4}\left[\theta^2\left(\frac{\theta}{\Theta}\right)^2\left(\frac{\partial\Theta}{\partial r}\right)^2(\Omega_0-\omega)^2 - \frac{1}{2(r^2+a^2)^2}+\frac{\theta^2(\Omega_0-\omega)^2}{2\Delta}\right] \\ &\simeq \bar{n}f(\epsilon)m\left[\left(1+\frac{4kT}{m}\right)(v^r)^2+\frac{kT}{m}\frac{\Delta}{\Sigma}\right] - \frac{\alpha^2\Phi^2}{8\pi(r^2+a^2)^2\Theta^4}. \end{aligned} \tag{2.125a}$$

$$
\begin{aligned}
T^{\theta\theta} &\simeq nm\left[\left(1+\frac{4kT}{m}\right)(v^\theta)^2+\frac{kT}{m}\gamma^{\theta\theta}\right]+\frac{1}{4\pi}\left[-((E^\theta)^2+(B^\theta)^2)+\frac{1}{2}(|\mathbf{E}|^2+|\mathbf{B}|^2)\gamma^{\theta\theta}\right] \\
&\simeq \bar{n}f(\epsilon)m\left[\left(1+\frac{4kT}{m}\right)\frac{\theta^2}{\Theta^2}\left(\frac{\partial\Theta}{\partial r}\right)^2(v^r)^2+\frac{kT}{m}\frac{1}{\Sigma}\right] \\
&\qquad +\frac{1}{4\pi}\left[-(\frac{\Phi^2}{\Delta\Sigma}\frac{\theta^2}{\Theta^4}(\Omega_0-\omega)^2+\alpha^2\frac{\theta^2}{\Theta^2}\left(\frac{\partial\Theta}{\partial r}\right)^2\frac{\Phi^2}{\Sigma^2\Theta^4})+\frac{1}{2}(\frac{\Phi^2}{\Delta\Sigma}\frac{\theta^2}{\Theta^4}(\Omega_0-\omega)^2+\frac{\Phi^2}{\Sigma^3\Theta^4})\right] \\
&\simeq \bar{n}f(\epsilon)m\left[\left(1+\frac{4kT}{m}\right)\frac{\theta^2}{\Theta^2}\left(\frac{\partial\Theta}{\partial r}\right)^2(v^r)^2+\frac{kT}{m}\frac{1}{\Sigma}\right]-\frac{1}{8\pi}\frac{\Phi^2}{\Sigma^3\Theta^4}
\end{aligned}
\tag{2.125b}
$$

$$
\begin{aligned}
T^{\phi\phi} &\simeq nm\left[\left(1+\frac{4kT}{m}\right)(v^\phi)^2+\frac{kT}{m}\gamma^{\phi\phi}\right]+\frac{1}{4\pi}\left[-((B^\phi)^2)+\frac{1}{2}(|\mathbf{E}|^2+|\mathbf{B}|^2)\gamma^{\phi\phi}\right] \\
&\simeq \bar{n}f(\epsilon)m\left[\left(1+\frac{4kT}{m}\right)\frac{(\Omega-\omega)^2}{\alpha^2}+\frac{kT}{m}\frac{1}{\theta^2\Sigma}\right]+\frac{1}{4\pi}\left[-\frac{\Phi^2(\Omega-\Omega_0)^2}{\Sigma^2(v^r)^2\Theta^4}+\frac{\Phi^2(\Omega_0-\omega)^2}{2\Sigma\Delta\Theta^4}+\frac{\Phi^2}{2\Sigma^3\Theta^4\theta^2}\right] \\
&\simeq \frac{\bar{n}f(\epsilon)kT}{\theta^2\Sigma}+\frac{\Phi^2}{2\Sigma^3\Theta^4\theta^2}
\end{aligned}
\tag{2.125c}
$$

$$
\begin{aligned}
T^{r\theta} &\simeq nm\left(1+\frac{4kT}{m}\right)v^r v^\theta-\frac{1}{4\pi}\left[E^rE^\theta+B^rB^\theta\right] \\
&\simeq \bar{n}f(\epsilon)m\left(1+\frac{4kT}{m}\right)\frac{\theta}{\Theta}\frac{\partial\Theta}{\partial r}(v^r)^2-\frac{1}{4\pi}\frac{\Phi^2}{\Sigma}\frac{\theta}{\Theta^5}\frac{\partial\Theta}{\partial r}\left((\Omega_0-\omega)^2\theta^2+\frac{\Delta}{\Sigma^2}\right) \\
&\simeq \bar{n}f(\epsilon)m\left(1+\frac{4kT}{m}\right)\frac{\theta}{\Theta}\frac{\partial\Theta}{\partial r}(v^r)^2-\frac{1}{4\pi}\frac{\Phi^2\Delta}{\Sigma^3}\frac{\theta}{\Theta^5}\frac{\partial\Theta}{\partial r}
\end{aligned}
\tag{2.125d}
$$

$$
\begin{aligned}
T^{r\phi} &\simeq nm\left(1+\frac{4kT}{m}\right)v^r v^\phi-\frac{1}{4\pi}[B^rB^\phi] \\
&\simeq \bar{n}f(\epsilon)m\left(1+\frac{4kT}{m}\right)\frac{(\Omega-\omega)}{\alpha}v^r-\frac{1}{4\pi}\frac{\alpha\Phi^2(\Omega-\Omega_0)}{\Sigma^2\Theta^4v^r}
\end{aligned}
\tag{2.125e}
$$

$$T^{\theta\phi} \simeq nm\left(1+\frac{4kT}{m}\right)v^{\theta}v^{\phi} - \frac{1}{4\pi}[B^{\theta}B^{\phi}]$$
$$\simeq \bar{n}f(\epsilon)m\left(1+\frac{4kT}{m}\right)\frac{\theta}{\Theta}\frac{\partial\Theta}{\partial r}\frac{(\Omega-\omega)}{\alpha}v^{r} - \frac{1}{4\pi}\frac{\Phi^2\alpha\theta(\Omega_0-\Omega)}{(r^2+a^2)^2\Theta^4 v^r}\frac{\partial\Theta}{\partial r}. \tag{2.125f}$$

2.4 Conclusion

We began this chapter by deriving the Grad-Shafranov equation, which can be used to describe the magnetic field configuration outside a compact object. This was done in a flat space geometry relevant to protostars and in a Schwarzschild geometry, relevant to neutron stars. We then showed how closed field line solutions could be found using a simple SOR algorithm, similarly to how we would solve Laplace's equation in electromagnetism. We argued that in a quasi-stationary limit, where the differential rotation of the disc is taken into account but is assumed to be acting adiabatically so the Grad-Shafranov equation still describes the system, that field lines would naturally open up. We then went on to show how the same time-independent, axisymmetric MHD equations admit jet solutions of outflowing matter and radiation. We provide an example of such a model that is relevant to the study of compact objects where general relativistic effects are important such as neutron stars or black holes. The study of these solutions in terms of physically interesting variables such as the mass flux or the jet opening angle is critical - however, even in the simplest of cases it can prove to be mathematically challenging, as this example illustrates. Furthermore, observations suggest many outflow phenomena are non-stationary. Therefore, analytical calculations only serve to illustrate that magnetically launched and col-

limated outflows are possible. The goal is to develop time dependent, computer simulations which can more faithfully explore outflow scenarios. The ultimate goal being to find which simulations can reproduce the ever growing body of observations and discriminate between competing outflow scenarios. In the following chapter we describe such a possible numerical scheme.

CHAPTER 3

MAGNETOHYDRODYNAMICS CODE

The basic physical setup for the astrophysical processes of interest is as follows - there is a central object such as a T Tauri star or neutron star, a cold accretion disc and a hot corona. The accretion disc and corona is composed of a plasma and can therefore support a magnetic field. We model this system using a one-fluid model for the plasma, coupled to a large scale magnetic field. The central object interacts with the plasma gravitationally, and plasma can accrete onto the star. We allow some non-ideal effects such as viscosity to the plasma and a magnetic diffusivity. These dynamics are captured by the non-ideal MHD equations.

Astrophysical processes of interest are typically non-stationary and the MHD equations describing them non-linear because of non-ideal effects such as disc viscosity and magnetic diffusivity. Problems are analytically intractable and are best left to be solved numerically. Any intuition gleaned from analytical results are best used to guide ones interpretation of any numerical simulations.

Below we describe the basic MHD equations used in our code 3.1, describe how they are implemented numerically using Godunov methods 3.2, describe the initial conditions 3.3 and describe the boundary conditions 3.4. A complete description of our code, along with results of standard tests and various astrophysical applications can be found in the methods paper Koldoba et al. (2015).

3.1 Basic Equations

The plasma flows are assumed to be described by the equations of non-relativistic magnetohydrodynamics (MHD). In a non-rotating reference frame the equations are

$$\frac{\partial \rho}{\partial t} + \nabla \cdot (\rho \mathbf{v}) = 0 \,, \tag{3.1a}$$

$$\frac{\partial \rho \mathbf{v}}{\partial t} + \nabla \cdot \mathcal{T} = \rho \mathbf{g} \,, \tag{3.1b}$$

$$\frac{\partial \mathbf{B}}{\partial t} + c\, \nabla \times \mathbf{E} = 0 \,, \tag{3.1c}$$

$$\frac{\partial (\rho S)}{\partial t} + \nabla \cdot (\rho \mathbf{v} S) = Q \,. \tag{3.1d}$$

Here, ρ is the mass density, S is the specific entropy, $\mathbf{v}$ is the flow velocity, $\mathbf{B}$ is the magnetic field, $\mathcal{T}$ is the momentum flux density tensor, $\mathbf{E} = -\mathbf{v} \times \mathbf{B}/c + \eta_t \nabla \times \mathbf{B}/c$ is the electric field, Q is the rate of change of entropy per unit volume due to viscous and Ohmic heating in the disc, and c is the speed of light. We assume that the heating is offset by radiative cooling so that $Q = 0$. The gravitational potential is chosen to model the problem at hand. In the case of a T Tauri star we use $\mathbf{g} = -\left[GM/r^2\right]\hat{r}$, the Newtonian potential for a central object of mass M. In the case of a neutron star we use $\mathbf{g} = -\left[GM/(r - r_S)^2\right]\hat{r}$ (with $r_S \equiv 2GM/c^2$), the gravitational acceleration due to the central mass M with the relevant Paczyński-Wiita (1980) correction. We model the plasma as a non-relativistic ideal gas with equation of state

$$S = \ln\left(\frac{p}{\rho^\gamma}\right) \,, \tag{3.2}$$

where p is the pressure and $\gamma = 5/3$.

Both the viscosity and the magnetic diffusivity of the disc plasma are thought to be due to turbulent fluctuations of the velocity and magnetic field. Outside of

the disc, the plasma is considered ideal with negligible viscosity and diffusivity. The turbulent coefficients are parameterized using the α-model of Shakura and Sunyaev (1973). The turbulent kinematic viscosity is

$$\nu_t = \alpha_\nu \frac{c_s^2}{\Omega_K} , \tag{3.3}$$

where c_s is the midplane sound speed, Ω_K is the Keplerian angular velocity at the given radii and $\alpha_\nu \leq 1$ is a dimensionless constant. Similarly, the turbulent magnetic diffusivity is

$$\eta_t = \alpha_\eta \frac{c_s^2}{\Omega_K} , \tag{3.4}$$

where α_η is another dimensionless constant. The ratio,

$$\mathcal{P} = \frac{\alpha_\nu}{\alpha_\eta} , \tag{3.5}$$

is the magnetic Prandtl number of the turbulence in the disc which is expected to be of order unity (Bisnovatyi-Kogan & Ruzmaikin 1976). Shearing box simulations of MRI driven MHD turbulence in discs indicate that $\mathcal{P} \sim 1$ (Guan & Gammie 2009).

The momentum flux density tensor is given by

$$\mathcal{T}_{ik} = p\delta_{ik} + \rho v_i v_k + \left(\frac{\mathbf{B}^2}{8\pi} \delta_{ik} - \frac{B_i B_k}{4\pi} \right) + \tau_{ik} , \tag{3.6}$$

where τ_{ik} is the viscous stress contribution from the turbulent fluctuations of the velocity and magnetic field. As mentioned we assume that these can be represented in the same way as the collisional viscosity by substitution of the turbulent viscosity.

In the case of a Keplerian disc , the viscous stress is determined mainly by the gradient of the angular velocity because the azimuthal velocity is the dominant velocity of the disc. Therefore, in the spherical code we only included the

leading order contributions to the momentum flux density from turbulence

$$\tau_{r\phi} = -\nu_t \rho r \sin\theta \frac{\partial \omega}{\partial r} \,, \tag{3.7a}$$

$$\tau_{\theta\phi} = -\nu_t \rho \sin\theta \frac{\partial \omega}{\partial \theta} \,, \tag{3.7b}$$

where $\omega = v_\phi / r \sin\theta$ is the plasma angular velocity.

In the case of counter-rotating Keplerian disc s a shear layer forms between the counter-rotating components, where the angular velocity is nearly zero. The dominant velocity component is actually in the radial direction and is of order the free fall velocity. Therefore, in the cylindrical code we implemented the leading order contribution to the momentum flux density from turbulence

$$\begin{aligned} \tau_{R\phi} &= -\nu_t \rho R \frac{\partial \Omega}{\partial R} \,, & \tau_{Z\phi} &= -\nu_t \rho R \frac{\partial \Omega}{\partial z} \,, \\ \tau_{ZR} &= -\nu_t \rho \frac{\partial v_R}{\partial Z} \,, & \tau_{RR} &= -2\nu_t \rho \frac{\partial v_R}{\partial R} \,, \\ \tau_{\phi\phi} &= -2\nu_t \rho \frac{v_R}{R} \,, \end{aligned} \tag{3.8}$$

where $\Omega = v_\phi / R$ is the angular velocity of the gas.

The transition from the viscous-diffusive disc to the ideal plasma corona is handled by multiplying the viscosity and diffusivity by a dimensionless factor $\xi(\rho)$ which varies from $\xi = 0$ for $\rho \leq 0.25\rho_d$ to $\xi = (4/3)(\rho/\rho_d - 0.25)$ for $0.25\rho_d < \rho < \rho_d$ to $\xi = 1$ for $\rho > \rho_d$ (see Appendix B of Lii, Romanova, & Lovelace 2012). The disc half-thickness h is taken to be the vertical distance from $Z = 0$ to the $0.5\rho_d$ surface.

3.2 Godunov Methods

We would like to solve numerically the equations (3.1). One can imagine dividing the computational region into a finite sized grid, where each dynamical variable takes on a constant value in each grid cell. The problem now consists of evolving this initial data, which is piecewise constant but has discontinuities at each grid edge using the above equations. This is called the Riemann problem, and exact solutions are possible though they can be numerically complex and computationally expensive (Ryu, Jones & Frank 1995). One possible numerical scheme to the problem was proposed by Godunov (1959). We outline this method below in general terms and then describe how it is implemented in our specific code.

Consider a system of one-dimensional, conservative, hyperbolic equations of the form

$$\frac{\partial \mathcal{U}}{\partial t} + \frac{\partial \mathcal{F}(\mathcal{U})}{\partial x} = 0, \tag{3.9}$$

where $\mathcal{U} = \{U_1, U_2, ..., U_n\}$ is a vector of conservative variables and $\mathcal{F}(\mathcal{U}) = \{F_1, F_2, ..., F_n\}$ is the flux function which maps each conservative variable to its corresponding flux. (3.9) can be integrated to yield

$$\int_{\Delta\xi} \mathcal{U}_{ex}(\xi) d\xi = \int_{\Delta\xi} \mathcal{U}\,|_{t=0}\, d\xi + \mathcal{F}_L - \mathcal{F}_R, \tag{3.10}$$

where $\mathcal{U}_{ex}(\xi, \mathcal{U}_L, \mathcal{U}_R)$ represents the exact solution to the Riemann problem between the left and right states $\mathcal{U}_L$ and $\mathcal{U}_R$, $\xi = x/t$ is a self-similar distance variable, $\Delta\xi$ is the interval along which we integrate and $\mathcal{F}_L = \mathcal{F}(\mathcal{U}_L)$ and $\mathcal{F}_R = \mathcal{F}(\mathcal{U}_R)$ are the fluxes of the left and right states respectively. The solution to the Riemann problem is therefore a matter of computing the fluxes. These are approximated by assuming that at discontinuities, the fluxes obey the Rankine-

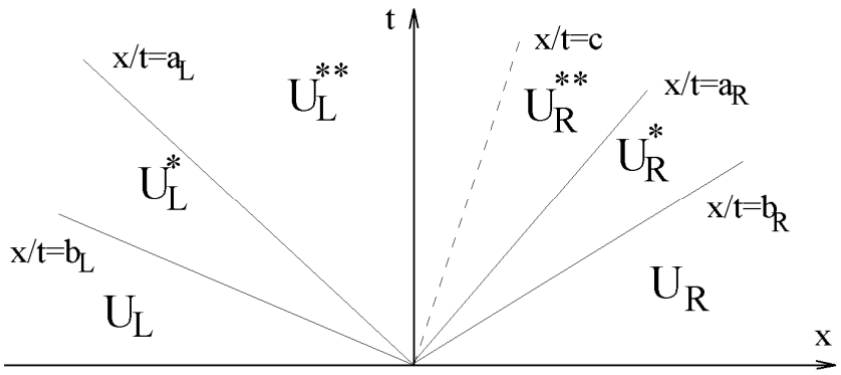

Figure 3.1: Left and right propagating magnetosonic waves with velocity b_L and b_R, left and right propagating Alfven waves with velocity a_L and a_R and a contact wave with velocity c create intermediate states U_L^*, U_L^{**}, U_R^* and U_R^{**}.

Hugoniot jump conditions

$$\dot{x}(\mathcal{U}_2 - \mathcal{U}_1) = \mathcal{F}_2 - \mathcal{F}_1, \tag{3.11}$$

where $\dot{x}$ is the velocity of the discontinuity, $\mathcal{U}_1$ and $\mathcal{U}_2$ are the conservative variables on eiter side of the discontinuity and $\mathcal{F}_1$ and $\mathcal{F}_2$ are the fluxes of the conservative variables across the discontinuity. Different numerical schemes approximate the velocity of the discontinuity in different ways. Our solver assumes that discontinuities propogate via 5 different waves - left and right propagating magnetosonic waves (b_L and b_R), left and right propagating Alfven waves (a_L and a_R) and a contact discontinuity (c). Initially there are two states, U_L and U_R separated at $x = 0$. As these waves propagate from $x = 0$, multiple intermediate states U_L^*, U_L^{**}, U_R^* and U_R^{**} develop, as can be depicted in a Riemann fan (Fig. 3.1).

The Rankine-Hugoniot conditions are applied at each of the above boundaries created by the propagating waves, to solve for the conservative variables in each of these intermediate states. The jump conditions can then be used to

calculate the fluxes, which by knowing the wavespeed and the time interval elapsed in this computational step allows for the conserved variable to be updated. This process is repeated at every cell boundary in the simulation region, in 2 dimensions, at every step forward in time. The timestep Δt is set by the Courant-Friedrichs-Levy (CFL) condition, which requires that no wave in the simulation region can cross multiple grid cells.

The conservative variables of (3.1) are taken to be

$$\mathcal{U} = \left\{\rho,\ \rho s,\ \rho v_x,\ \rho v_y,\ \rho v_z,\ B_y,\ B_z\right\}, \tag{3.12}$$

and the corresponding fluxes

$$\begin{aligned}\mathcal{F} = \Bigg\{&\rho v_x,\ \rho s v_x,\ \rho v_x^2 + p + \frac{B_y^2 + B_z^2}{4\pi},\ \rho v_x v_y - \frac{B_{x0} B_y}{4\pi},\\ &\rho v_z v_x - \frac{B_{x0} B_z}{4\pi},\ v_x B_y - v_y B_{x0},\ v_x B_z - v_z B_{x0}\Bigg\},\end{aligned} \tag{3.13}$$

This code is different from many other MHD codes used in astrophysics in that it uses entropy conservation rather than energy conservation. Using entropy, rather than energy conservation is computationally advantageous because the terms in the entropy conservation equation are all roughly the same order of magnitude. This leads to less numerical error. The disadvantage of this is that the code cannot model strong shocks, where energy is conserved but entropy is not. This is not inherently problematic as many astrophysical problems of interest are shock free.

Also note that we only compute two components of the magnetic field. We calculate the B_x component of the field by requiring that the no-monopoles condition holds. The details of this method were first described in Balsara & Spicer

(1999).

3.3 Initial Conditions

We must specify initial conditions for the conserved variables in the simulation region. These are chosen to be physically consistent with the model we are simulating. Below we outline the basic setup of the initial conditions, though the specific description of the initial conditions for each problem is included in each of the relevant chapters. All initial conditions are given in units of the code and can be converted to physical units by multiplying by the relevant dimensionful quantity, included with each problem.

Matter Distribution

Initially, matter of the disc and corona are assumed to be in mechanical equilibrium (Romanova et al. 2002). The initial density distribution is taken to be barotropic with

$$\rho(p) = \begin{cases} p/T_{\rm disc}, & p > p_b \ \text{ and } \ R \geq R_d \ , \\ p/T_{\rm cor}, & p < p_b \ \text{ or } \ R \leq R_d \ , \end{cases} \tag{3.14}$$

where p_b is the level surface of pressure that separates the cold matter of the disc from the hot matter of the corona and R_d is the initial inner disc radius. At this surface the density has an initial step discontinuity from value $p/T_{\rm disc}$ to $p/T_{\rm cor}$. The initial dimensionless temperature in the disc is $T_{\rm disc} = (p/\rho)_{\rm disc} = 5 \times 10^{-4}$, and the initial temperature in the corona is $T_{\rm cor} = (p/\rho)_{\rm cor} = 0.5$.

Because the density distribution is barotropic, the initial angular velocity is

a constant on coaxial cylindrical surfaces about the $z-$axis. Consequently, the pressure can be determined from the Bernoulli equation

$$F(p) + \Phi + \Phi_c = \mathcal{B}_0 \ , \tag{3.15}$$

where $\mathcal{B}_0$ is Bernoulli's constant,$\Phi = -GM/\sqrt{R^2 + Z^2}$ is the gravitational potential with $GM = 1$ in the code, $\Phi_c = \int_R^\infty rdr\, \Omega^2(r)$ is the centrifugal potential, and

$$F(p) = \begin{cases} T_{\rm disc} \ln(p/p_b) & p > p_b \ \text{ and } \ R \geq R_d \ , \\ T_{\rm cor} \ln(p/p_b) & p < p_b \ \text{ or } \ R \leq R_d \ . \end{cases} \tag{3.16}$$

Varying $\mathcal{B}_0$ allows one to vary the initial midplane disc density.

Angular Velocity

The initial angular velocity of the disc is slightly sub-Keplerian,

$$\Omega = (1 - 0.003)\Omega_K(R) \qquad R > R_d \ , \tag{3.17}$$

Inside of R_d, the matter rotates rigidly with angular velocity

$$\Omega = (1 - 0.003)\Omega_K(R_d) \qquad R \leq R_d. \tag{3.18}$$

We choose a sub-Keplerian disc to incite the disc to begin accreting at early times.

Magnetic Field

We consider a variety of magnetic field configurations in our studies, divided into two broad classes. One class consists of stellar dipole fields with flux function

$$\Psi_D = \frac{\mu R^2}{(R^2 + Z^2)^{3/2}} \ , \tag{3.19}$$

where μ = const is the star's dipole moment. Such a configuration is physically motivated by observations of T Tauri stars which exhibit dipole and higher order multipole magnetic fields (Donnati 2008).

Another class of magnetic fields is an extended disc field, of the type first studied by Blandford & Payne (1982) which was shown to exhibit time-independent wind solutions. One possibility of such a disc field is given by the flux function

$$\Psi_d = \frac{4}{3} B_0 R_0^2 \left(\frac{R}{R_0}\right)^{3/4} \frac{m^{5/4}}{(m^2 + Z^2/R^2)^{5/8}} , \tag{3.20}$$

which was used in many numerical studies (see for example Zanni et al. 2007). Another possibility for an extended disc field is given by the magnetic loop field

$$\Psi(R, Z) = A_1 R\, J_1(a_1 R) e^{-b_1|Z|} + A_2 R\, J_1(a_2 R) e^{-b_2|Z|} , \tag{3.21}$$

where J_1 is a Bessel function of the first kind, A_1, A_2 are integration constants and $a_i = (k^2 + b_i^2)^{1/2}$ for $i = 1, 2$. Qualitatively, the field appears as a number of loops threading the accretion disc. This configuration is found as a solution to the Grad-Shafranov equation which models the magnetic field configuration in an ideal force free magnetosphere.

Hence the magnetic field choice is based on a combination of what sort of field configuration these systems have been shown to have observationaly and the types of fields that have been shown theoreticaly to be able to support stationary wind solutions. Because these are just initial configurations, the system can in principle relax to more natural conditions after some evolution.

3.4 Boundary Conditions

Our simulations are 2.5D, meaning the simulation region consists of a poloidal plane region of grid cells, where fluxes are allowed in the azimuthal direction but are assumed to have no ϕ dependence. In cylindrical geometry this poloidal region consists of $N_R \times N_Z$ grid cells. In spherical geometry this consists of $N_r \times N_\theta$ grid cells.

Along each boundary of the simulation region there are two "ghost cells". The conservative variables in these cells are not calculated from fluxes but rather from the conservative variables of nearby cells in the simulation region or fixed at the start of the simulation. We require two ghost cells because of the way we compute derivatives in the simulation region.

There are two basic choices of boundary conditions for a conservative variable X - Neumann or free boundary conditions where

$$\frac{\partial X}{\partial n} = 0, \tag{3.22}$$

where n is the direction normal to the boundary. This is implemented numerically by setting the value of the variable in the ghost cells to the value of the variable in the last calculated cell $X_{\text{ghost}} = X_i$. Physically this is the type of boundary condition to impose when we want to allow fluxes out of the simulation region, for instance allowing mater and magnetic field to exit the simulation region. The other basic choice is a Dirichlet or fixed condition where

$$X_{\text{ghost}} = \text{const.}, \tag{3.23}$$

i.e the value in the ghost cell is fixed to some value, somewhat like an initial condition. Physically this choice of condition is made if there is a flux source

for example we assume there is a constant source of matter feeding gas at the outer edge of the disc for example. Alternatively, forcing a quantity to zero for instance the angular rotation along the axis can be useful so as to prevent the azimuthal velocity from reaching unphysically large values in this region. One must be careful with fixed conditions however, as they may cause unphysical waves to reflect back into the simulation region - analogous to the waves reflected along a string with fixed end.

Axisymmetry implies we must pick a boundary condition along the rotation axis. Likewise, we do not model what is happening *inside* the central object so we must pick boundary conditions at the star. Simulations are finite in extent so we must set conditions at the external boundary. Finally, in some simulations we assume a symmetry about the disc plane which allows us to set boundary conditions in the disc. The specific details on boundary conditions used in each simulation are described in the appropriate chapter.

CHAPTER 4

MATTER ADVECTION BY MAGNETIC FIELDS

Early studies of the advection and diffusion of a large-scale magnetic field threading a turbulent disc indicated that a *weak* large-scale field would diffuse outward rapidly (van Ballegooijen 1989; Lubow, Papaloizou, & Pringle 1994; Lovelace, Romanova, & Newman 1994; Lovelace, Newman, & Romanova 1997). This rapid outward diffusion may however be offset by the highly conducting surface layers of the disc where the magnetorotational instability (MRI) and associated turbulence is suppressed (Bisnovatyi-Kogan & Lovelace 2007; Rothstein & Lovelace 2008). The magnetic field is "frozen-in" in the conducting surface layers which tend to flow inward at approximately the disc accretion speed. This conclusion is supported by an analytic model for the vertical profiles of the velocity and field components of a stationary accretion disc developed by Lovelace, Rothstein, and Bisnovatyi-Kogan (2009). This model predicts that the inward or outward transport of the poloidal magnetic flux is determined by both the plasma β_0 (the ratio of the midplane plasma pressure to the midplane magnetic pressure) and the efficiency of the magnetic disc wind in removing angular momentum from the disc (Bisnovatyi-Kogan & Lovelace 2012). Guilet and Ogilvie (2012, 2013) independently developed an analytic model for the vertical structure of a turbulent/diffusive disc threaded by a large scale magnetic field, and they find a reduction in the rapid outward field diffusion.

Accretion discs around black holes are considered in many cases to be threaded by a large-scale magnetic field (Lovelace 1976). This field may be transported inward from the interstellar medium by the accreting disc plasma (as investigated here), or it may arise from dynamo activity in the disc (e.g.,

Pariev, Colgate, & Finn 2007). Of course the discs around magnetized stars may be threaded at large distances by the disconnected stellar magnetic field (Lovelace, Romanova, & Bisnovatyi-Kogan 1995). The large-scale field may be in the form of magnetic loops threading the disc and extending into a low density plasma corona as sketched in Figure 4.1. Differential rotation of the disc acts to open the magnetic loops which have footpoints at different radii (Newman, Newman, & Lovelace 1992). Also, the differential rotation acts to give an axisymmetric field. Such large scale magnetic fields can have an essential role in forming jets and winds.

In previous axisymmetric magnetohydrodynamic (MHD) simulations of a disc threaded by magnetic loops, the disc was treated as a conducting boundary condition with plasma outflow and Keplerian azimuthal velocity (Romanova et al. 1998). These simulations showed that the innermost loop inflates and opens significantly faster than the outer loops due to the larger differential rotation of the disc close to the star. The opened magnetic fields carry away energy, angular momentum, and mass from the disc. One or more neutral layers form between the regions of oppositely directed magnetic field lines leading to field reconnection and annihilation.

The aim of the present work is to understand the dynamics of the magnetic field loops *and* the dynamics of the disc in response to the twisting of the loops. The magnetic field mediates an outflow of energy, angular momentum and matter from the disc to a jet and wind. At the same time the disc accretion rate can be strongly enhanced by the angular momentum outflow to the jet or wind. We treat the disc as a viscous/diffusive plasma taking into account fully the back reactions of the coronal field on the disc. The turbulent viscosity ν_t of the disc

is modelled with an α_ν coefficient using the Shakura and Sunyaev (1973) prescription. The turbulent magnetic diffusivity η_t is modeled with a second α_η coefficient as proposed by Bisnovatyi-Kogan and Ruzmaikin (1976). The viscosity and diffusivity are assumed to arise from turbulence triggered by the magneto-rotational instability inside the disc (Balbus & Hawley 1998), but this turbulence is not modeled in the present simulations. The low density coronal plasma outside the disc is treated using ideal MHD.

We carry out axisymmetric simulations using a Godunov-type scheme to solve the MHD equations, including viscosity and magnetic diffusivity inside the disc as described by Ustyugova et al. (2006). Our initial magnetic field configuration consists of three loops in the simulation region. New unmagnetized matter is supplied to the disc at the outer boundary.

For this configuration the innermost loop opens up rapidly and forms a collimated magnetically dominated jet near the $z-$axis and an uncollimated matter dominated wind at larger distances from the axis. The second loop opens at a later time due to the smaller shear in the disc and it produces a matter dominated wind. The outermost loop reconnects before there is time for it to open.

The loop configuration allows us to evaluate *both* the accretion speed of the magnetic field and accretion speed of the disc matter. This allows a comparison with the analytic model of field accretion of Lovelace et al. (2009).

The paper is organized as follows: We discuss the setup for our simulations including the initial and boundary conditions in Section 4.1. Section 4.2 describes our results on the dynamics of the disc, the generation of jets and disc winds, and the accretion speeds of the matter and magnetic field. Section 4.3

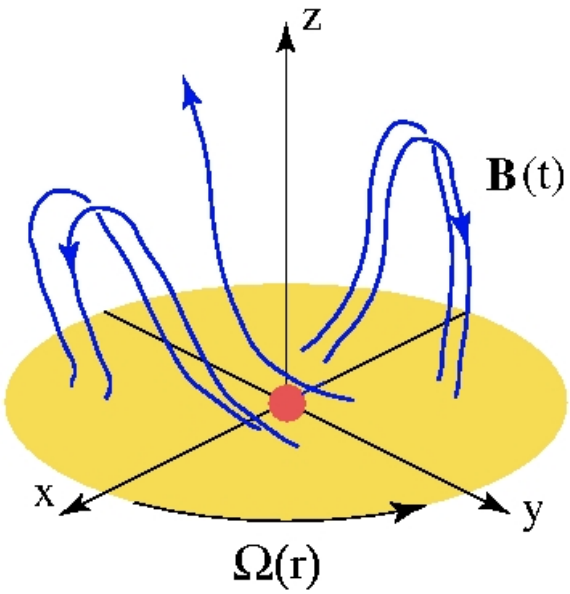

Figure 4.1: Sketch of an accretion disc threaded by open and closed magnetic field lines. Differential rotation of the disc will act to rapidly give an axisymmetric field configuration considered in this work.

gives the conclusions of this work.

4.1 Numerical Methods

4.1.1 Initial Conditions

Initial Magnetic Field

The initial magnetic field is described in cylindrical coordinates. This field is taken to be force-free in the sense that $\mathbf{J} \times \mathbf{B} = 0$ in the region $|Z| > 0$ with $\mathbf{B} = (B_R, B_\phi, B_Z)$, where $B_R = -R^{-1}\partial\Psi/\partial Z$ and $B_Z = R^{-1}\partial\Psi/\partial R$. Here, $\Psi(R, Z)$ is the

flux function which labels the field lines, $\mathbf{B} \cdot \nabla\Psi = 0$. This function satisfies the Grad-Shafranov equation,

$$\Delta^*\Psi(R,Z) = -H(\Psi)\frac{dH(\Psi)}{d\Psi} , \tag{4.1}$$

where

$$\Delta^* = \frac{\partial^2}{\partial R^2} - \frac{1}{R}\frac{\partial}{\partial R} + \frac{\partial^2}{\partial Z^2} ,$$

and $H = H(\Psi) = RB_\phi(R,Z)$ is the poloidal current function (Lovelace et al. 1986). For simplicity we take the poloidal current to be proportional to the flux, $H(\Psi) = k\Psi$, where k is a constant (Newman et al. 1992). The relevant solution to equation (4.1) is

$$\Psi(R,Z) = A_1 R\, J_1(a_1 R)e^{-b_1|Z|} + A_2 R\, J_1(a_2 R)e^{-b_2|Z|} , \tag{4.2}$$

where J_1 is a Bessel function of the first kind, A_1, A_2 are integration constants and $a_i = (k^2 + b_i^2)^{1/2}$ for $i = 1, 2$. Qualitatively, the field appears as a number of loops threading the accretion disc. We have chosen the parameters a_i such that three loops fit in our simulation region.

The solution (4.2) is valid in the region $|Z| > 0$ and assumes that initially there is a thin current carrying disc in the $Z = 0$ plane. The cusp in the initial field at $Z = 0$ disappears rapidly in a time $t_{\rm init} \sim h^2/\eta_t = (\alpha_\eta \Omega_K)^{-1} = P_0(2\pi\alpha_\eta)^{-1}(r/r_0)^{3/2}$ due to the diffusivity of the disc. Here, r_0 is the reference radius and P_0 the period of the Keplerian orbit. We have assumed $h/R \approx c_s/v_K$ which neglects the magnetic compression of the disc discussed by Wang, Sulkanen, and Lovelace (1990). For most of the range of r/r_0 this time is much smaller than the field evolution time scale.

Matter Distribution

Initially the matter of the disc and corona are assumed to be in mechanical equilibrium (Romanova et al. 2002). The initial density distribution is taken to be barotropic with

$$\rho(p) = \begin{cases} p/T_{\rm disc} & p > p_b \ \text{ and } \ r\sin\theta \geq r_b \ , \\ p/T_{\rm cor} & p < p_b \ \text{ or } \ r\sin\theta \leq r_b \ , \end{cases} \tag{4.3}$$

where p_b is the level surface of pressure that separates the cold matter of the disc from the hot matter of the corona and r_b is the initial value of the inner radius of the disc. At this surface the density has an initial step discontinuity from value $p/T_{\rm disc}$ to $p/T_{\rm cor}$.

Because the density distribution is barotropic, the initial angular velocity is a constant on coaxial cylindrical surfaces about the $z-$axis. Consequently, the pressure can be determined from Bernoulli's equation,

$$F(p) + \Phi + \Phi_c = \text{const} \ , \tag{4.4}$$

where $\Phi = -GM/|r - r_c|$ is the gravitational potential with the Paczyński-Wiita correction, $\Phi_c = \int_{r\sin\theta}^{\infty} \xi d\xi \ \omega^2(\xi)$ is the centrifugal potential, which depends only on cylindrical radius $R = r\sin\theta$, and

$$F(p) = \begin{cases} T_{\rm disc}\ln(p/p_b) & p > p_b \ \text{ and } \ r\sin\theta \geq r_b \ , \\ T_{\rm cor}\ln(p/p_b) & p < p_b \ \text{ or } \ r\sin\theta \leq r_b \ . \end{cases} \tag{4.5}$$

Angular Velocity

Initially the inner edge of the disc is located at $r_b = 5r_0$ in the equatorial plane, where r_0 is a reference length discussed below. The initial angular velocity of

the disc is slightly sub-Keplerian,

$$\Omega\Big|_{\theta=\pi/2} = (1 - 0.003)\Omega_K(r) \qquad r > r_b \ , \tag{4.6}$$

Inside of r_b, the matter rotates rigidly with angular velocity

$$\Omega\Big|_{\theta=\pi/2} = (1 - 0.003)\Omega_K(r_b) \qquad r \leq r_b. \tag{4.7}$$

The corotation radius $r_{\rm cr}$ is the radius where the angular velocity of the disc equals that of the star; that is, $r_{\rm cr} = (GM_*/\Omega_*^2)^{1/3}$. In this study we have chosen this radius to be the initial inner radius of the disc with $r_{\rm cr} = 5r_0$.

4.1.2 Boundary Conditions

Our simulation region has four boundaries: The surface of the star, the mid-plane of the disc, the rotation axis, and the external boundary. For each dynamical variable we impose boundary conditions consistent with our physical assumptions.

We assume axisymmetry as well as symmetry about the equatorial plane. On the star and the external boundary we want to allow fluxes and so impose free boundary conditions $\partial\mathcal{F}/\partial r = 0$, where $\mathcal{F}$ are the dynamical variables. In addition, along the external boundary in the disc region $\theta = 72^\circ - 90^\circ$, we allow matter to inflow but the inflowing matter has zero magnetic flux. In the coronal region $\theta = 0^\circ - 72^\circ$ we allow matter, entropy and magnetic flux to exit the simulation region.

In addition to the boundary conditions, which are required for the well-posedness of our problem, we impose additional conditions on variables to

eliminate numerical artifacts in the simulations. For instance, we require that the radial velocity at the surface of the star be negative. Thus there there is no outflow of matter, angular momentum, or energy from the star. We also require that along the external boundary the radial velocity be inwards inside the disc and outwards outside the disc so the disc matter will tend to accrete and matter in the corona will tend to be ejected.

Figure 4.2 shows the grid used in the described simulations. There are N_θ = 30 constant width cells in the $\theta-$direction. In the $r-$direction, the N_r = 67 grid cells increase in width as $dr_{j+1} = (1+0.0523)dr_j$ so as to give curvlinear rectangles with approximately equal sides (Ustyugova et al. 2006). The dependence of our results on the grid resolution is discussed in Appendix 4.A.

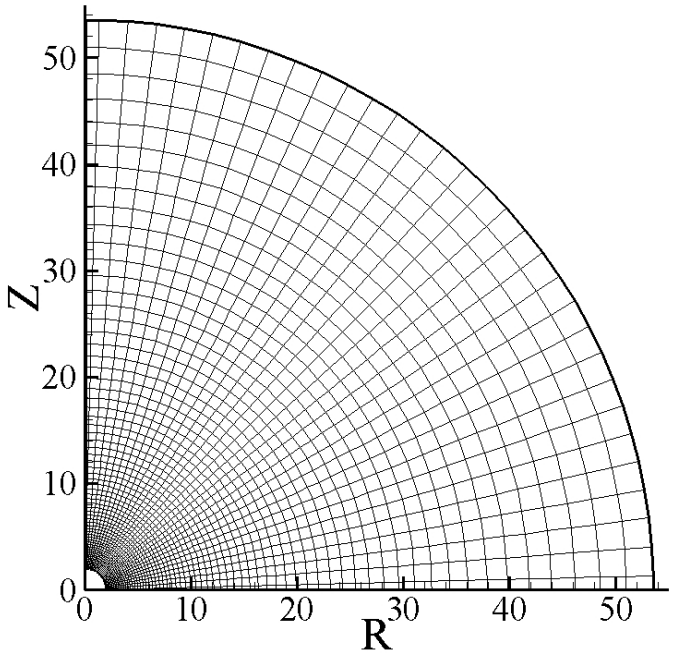

Figure 4.2: Grid used in the simulations.

4.1.3 Dimensional Variables

The MHD equations are written in dimensionless form so that the simulation results can be applied to different types of stars. The mass of the central star is taken as the reference unit of mass, $M_0 = M_*$. The reference length, r_0, is taken to be half the radius of the star. The initial inner radius of the disc is $r_b = 5r_0$. The reference value for the velocity is the Keplerian velocity at the radius r_0, $v_0 = (GM_0/r_0)^{1/2}$. The dimensionless temperature is T/v_0^2. The reference time-scale is the period of rotation at r_0, $P_0 = 2\pi r_0/v_0$. From the MHD equations, we get the relation $\rho_0 v_0^2 = B_0^2$, where B_0 is a reference magnetic field and ρ_0 is a reference density both at r_0. We take the reference magnetic field B_0 to be such that the reference density is appropriate for the considered star. The reference mass accretion rate is $\dot{M}_0 = \rho_0 v_0 r_0^2$. The reference disc accretion power is $\dot{E}_0 = GM_0\dot{M}_0/r_0$. The initial dimensionless temperature in the disc is $T_{\rm disc} = (p/\rho)_{\rm disc} = 5 \times 10^{-4}$, and the initial temperature in the corona is $T_{\rm cor} = (p/\rho)_{\rm cor} = 0.5$.

Results obtained in dimensionless form can be applied to objects with widely different sizes and masses. However, the present work focuses on neutron stars with the typical values shown in Table 4.1.

4.2 Results

We have carried out a large number of simulation runs for different values of the viscosity $0.05 \leq \alpha_\nu \leq 0.3$ and diffusivity $0.01 \leq \alpha_\eta \leq 0.3$ parameters and find that the simulations exhibit similar qualitative behaviour. Figure 4.3 shows the evolution of the poloidal field projections for a representative case where

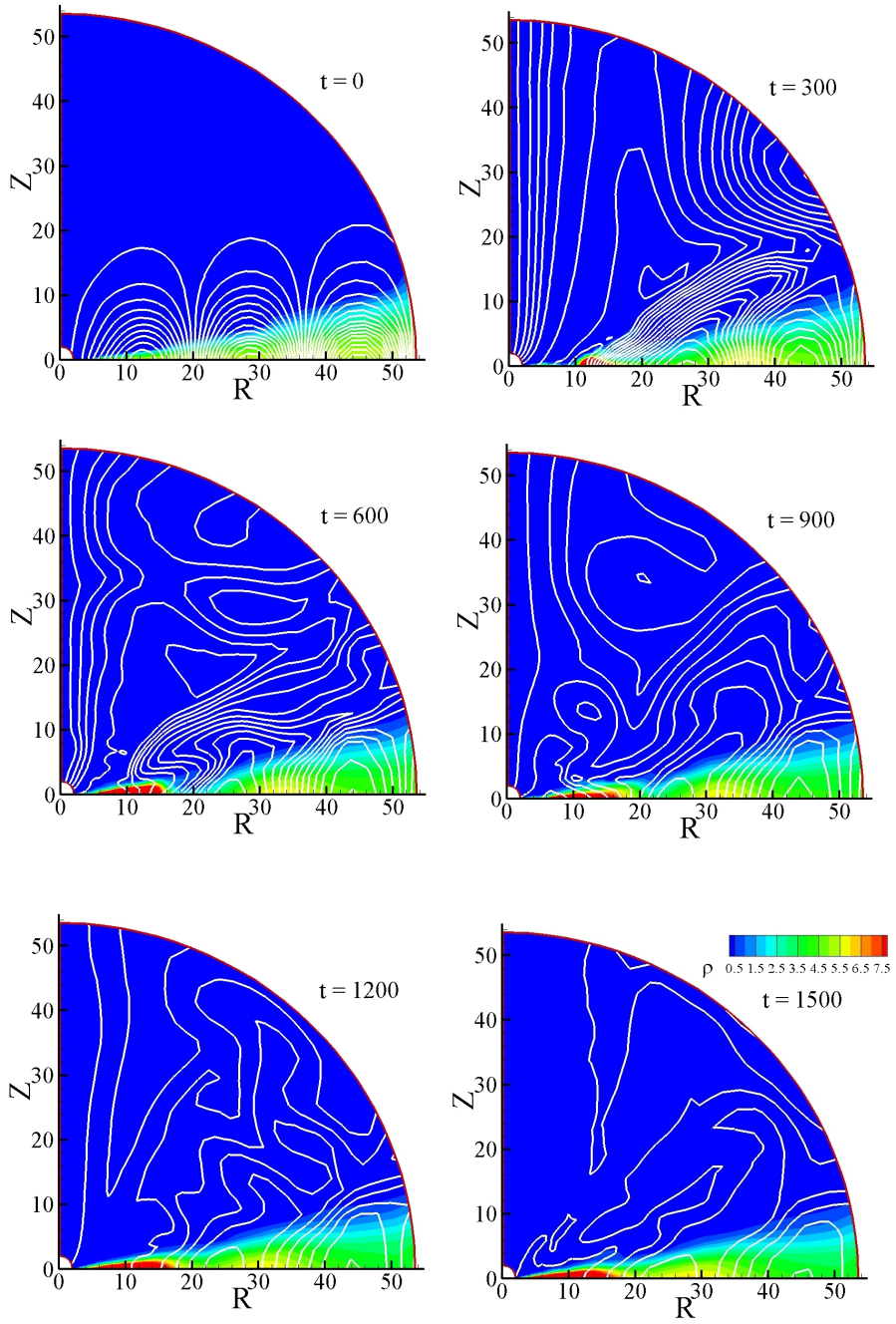

Figure 4.3: Plot of poloidal magnetic field lines (white) and matter density (colour) for $\alpha_\nu = 0.1$ and $\alpha_\eta = 0.1$ at $t = 0, \ = 300, \ .., 1500$, where t is the time measured in units of P_0 which is the period of the Keplerian orbit at the reference radius r_0. By $t = 300$ sufficient matter has fallen into the star to drag in the magnetic field. The latter forms a well collimated jet along the axis and a wind along the disc. This persists for some time, but eventually decays due to magnetic field reconnection and annihilation.

Parameters	Symbol	Value
mass	M_*	2.8×10^{33} g
length	r_0	1.0×10^6cm
magnetic field	B_0	10^8 G
time	P_0	4.6×10^{-4}s
velocity	v_0	1.4×10^{10}cm/s
density	ρ_0	1.3×10^{-5} g/cm^3
accretion rate	$\dot{M}_*$	2.8×10^{-9} $M_\odot$/yr
disc power	$\dot{E}_0$	1.66×10^{37} erg/s

Table 4.1: Mass, length, and magnetic field scales of interest and the corresponding scales of other derived quantities

$\alpha_\nu = 0.1$ and $\alpha_\eta = 0.1$. The field lines of the innermost loop are pulled in towards the star by the accreting disc matter. When this loop reaches the star's surface it opens up. The inner half of the loop extends vertically upwards from the star, supporting a magnetically dominated jet along the $Z-$axis. The outer half of the loop threading the disc projects outwards from the disc at about 45° to the disc normal, and it supports a magnetic disc wind. The middle and outer magnetic loops move inward only gradually, and they decrease in strength due to field line annihilation inside the disc.

Figure 4.4 shows the radial dependence of the inverse "plasma beta" which is the ratio of the magnetic pressure to the plasma pressure at the disc midplane,

$$\beta_0^{-1} = \frac{B_{Z0}^2}{8\pi p(R,0)} \,, \tag{4.8}$$

where $B_{Z0} \equiv B_Z(R, Z = 0)$. Note that $\beta_0^{-1} = (v_{A0}/c_{s0})^2/2$, where $v_{A0} = B_{Z0}/\sqrt{4\pi\rho}$ is the midplane Alfvén speed and c_{s0} is the midplane sound speed. For the assumed symmetry about the equatorial plane B_Z is the only non-vanishing field component at $Z = 0$. Initially β_0^{-1} is significantly less than unity over most of the disc ($R \gtrsim 5$). Consequently, the magneto-rotational instability would be expected to occur in an actual disc with the same parameters (Balbus & Hawley

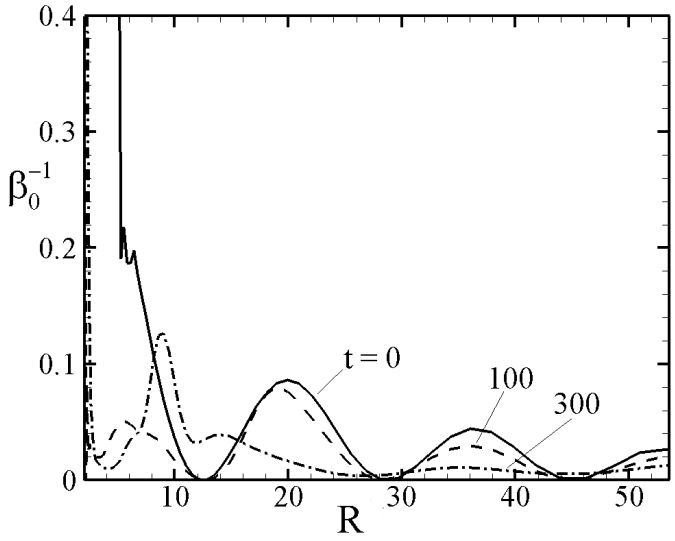

Figure 4.4: The ratio of magnetic pressure to the plasma pressure β_0^{-1} in the disc midplane at $t = 0$ (full), $t = 100$ (dashed) and $t = 300$ (dot-dashed) for $\alpha_v = 0.1$ and $\alpha_\eta = 0.1$.

1998). At later times, $[B_Z(R,0)]^2$ increases but the plasma pressure also increases so that the change in β_0^{-1} are not very large.

4.2.1 Opening of Field Loops and Field Annihilation

The initial three poloidal field loops ($t = 0$ panel of Figure 4.3), have footpoints at the approximate radii $R_k = 5,\ 20,\ 35,\ \&\ 50$ ($k = 1, .., 4$). The time-dependent opening of large-scale magnetic field loops with footpoints at different radii in a Keplerian disc has been well analyzed (Newman, Newman, & Lovelace 1992; Lynden-Bell & Boily 1994; Romanova et al. 1998; Ustyugova et al. 2000; Lovelace et al. 2002). We use the numerical condition of Lynden-Bell and Boily (1994) that a field loop opens after there is a differential rotation of the footpoints by > 3.63 radians. For each loop, the differential rotation in a time t_k is

$\Delta\phi = t_k[\Omega_K(R_k) - \Omega_K(R_{k+1})]$. With $\Delta\phi = 3.63$ we obtain the opening times for the three loops, $t_1 = 40.8$, $t_2 = 329$, and $t_3 = 760$ in our dimensionless units. The observed rapid opening of the first loop (Figure 4.3) agrees qualitatively with t_1. The fact the second loop does not open in a time $\sim t_2$ may be explained by the overlying magnetic field of the first loop. The long time t_3 required for the opening of the third loop means the diffusion of the magnetic field has sufficient time to cause significant field annihilation.

The time scale for the field to diffuse over a distance $\Delta R_k/2 = (R_{k+1} - R_k)/2$ can be estimated as $\tau_k \approx (\Delta R_k)^2/(4\eta_t)$, where η_t is evaluated at $\overline{R}_k = (R_k + R_{k+1})/2$. For $\alpha_\eta = 0.1$, we find $\tau_1 \approx 2500$, $\tau_2 \approx 1700$, and $\tau_3 \approx 1400$. Note that τ_3 for the outer loop is less than the duration of our runs so that the magnetic field decays significantly before the end of the runs.

4.2.2 Matter Advection in the Disc

Figure 4.5 shows the average accretion speed u_m of the disc matter as a function of R at different times, where

$$u_m \equiv -\frac{1}{\sigma(R)} \int_{-h}^{h} dZ \rho(R, Z) v_R(R, Z) \, . \tag{4.9}$$

Here,

$$\sigma(R) = \int_{-h}^{h} dZ \rho(R, Z) \, , \tag{4.10}$$

is the surface mass density of the disc. The conservation of mass gives

$$\frac{\partial(R\sigma)}{\partial t} - \frac{\partial(R\sigma u_m)}{\partial R} = -\frac{1}{\pi} \frac{\delta \dot{M}_w}{\delta R} \, , \tag{4.11}$$

where $\delta \dot{M}_w/\delta R = 2\pi R(\rho v_z)_{Z=h}$ is the mass outflow rate from the top surface of the disc to the wind. The mass accretion rate to the star from the upper half-space

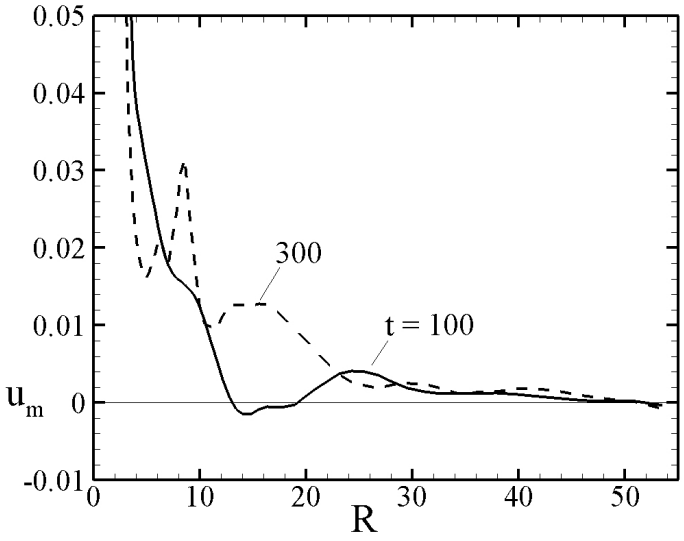

Figure 4.5: Radial accretion speed of the disc matter, equation (4.9), at t = 100 (full) and t = 300 (dashed) for $\alpha_\nu = 0.1$ and $\alpha_\eta = 0.1$.

is $\dot{M}_* = (\pi R \sigma u_m)_{R=r_0}$. We find that the ratio of the time-averaged mass loss rate of the wind is typically small compared to $\dot{M}_*$.

Figure 4.6 shows the midplane magnetic field $B_Z(R, 0)$ at different times. Because of the assumed symmetry of the magnetic field about the equatorial plane, this is the only non-zero field component at $Z = 0$.

Matter advection in the disc is measured by $u_m(R, t)$, which is determined by the disc's turbulent viscosity (which causes the radial outflow of angular momentum) *and* by the torque of the large-scale magnetic field (which causes a vertical outflow of angular momentum to magnetic jets or winds). This is described by a simple analytic model where

$$u_{\rm m} = u_{m\nu} + u_{mB} \ , \tag{4.12}$$

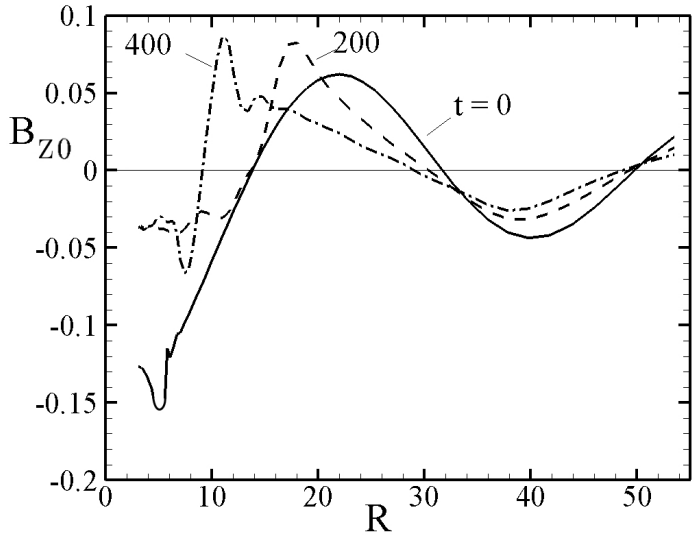

Figure 4.6: The magnetic field $B_Z(R, Z = 0)$ along the disc midplane at $t = 0$ (full), $t = 200$ (dashed) and $t = 400$ (dot-dashed) for $\alpha_\nu = 0.1$ and $\alpha_\eta = 0.1$.

where

$$u_{m\nu} = 3C_1\alpha_\nu\left(\frac{h}{R}\right)^2 v_K, \quad u_{mB} = \frac{-C_2 B_{\phi h} B_{Z0}}{\pi v_K \sigma}\,, \tag{4.13}$$

(Lovelace et al. 2009; 1994), where h is the half-thickness of the disc, $v_K = (GM/R)^{1/2}$ is the Keplerian velocity, σ is the surface mass density of the disc, $B_{\phi h} = B_\phi(R, h)$ is the toroidal magnetic field at the disc surface, $B_{Z0} = B_Z(R, Z = 0)$ is the midplane magnetic field, and C_1 and C_2 are dimensionless constants of the order of unity. The first term represents the accretion speed contribution due to the turbulent viscosity of the disc, while the second term the accretion speed contribution due to the outflow of angular momentum from the disc surfaces due to the twisted magnetic field in the corona.

Figure 4.7 shows the profiles of the toroidal magnetic field at the disc surface $B_\phi(R, h)$ at a sequence of times. This quantity is important for the outflow of angular momentum from the disc which in turn determines the magnetic

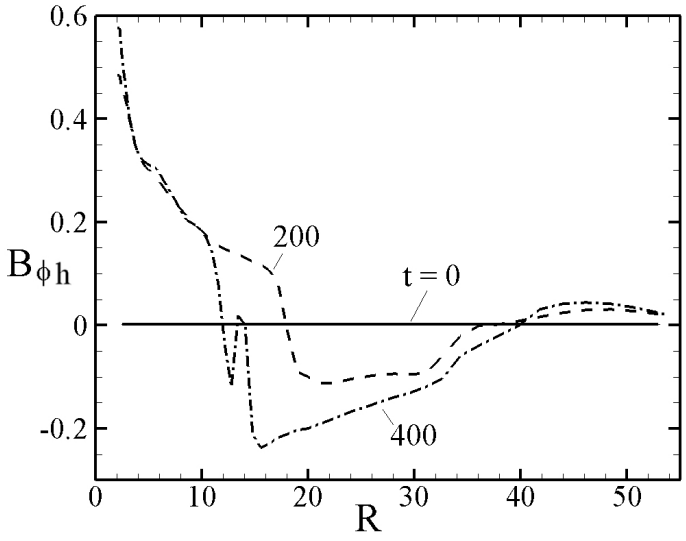

Figure 4.7: The toroidal magnetic field $B_\phi(R, Z = h)$ at the disc surface at $t = 0$ (full), $t = 200$ (dashed) and $t = 400$ (dot-dashed) for $\alpha_\nu = 0.1$ and $\alpha_\eta = 0.1$.

contribution to the accretion speed u_{mB} in equation (4.13).

Figure 4.8 shows the radial profiles of B_{Rh} at a sequence of times. This quantity is important for the radial diffusion of the magnetic field as previously discussed. Figure 4.9 shows the radial variation of h/R at a sequence of times.

Figure 4.10 shows that the twist of a sample magnetic field line above the disc is such that $B_{\phi h} B_{Z0} < 0$ which corresponds the to outflow of angular momentum from the disc.

We find that during early times ($t \lesssim 400$), the $B_Z(R, 0)$ field "propagates" inwards towards the star as shown in Figure 4.6. We study this motion by measuring the positions of the inner maximum of $B_Z(R, 0)$ as a function of time. The maximum moves inwards until interactions with the star cause a more complicated behavior. At the $B_Z(R, 0)$ maximum at a given time t, we calculate the

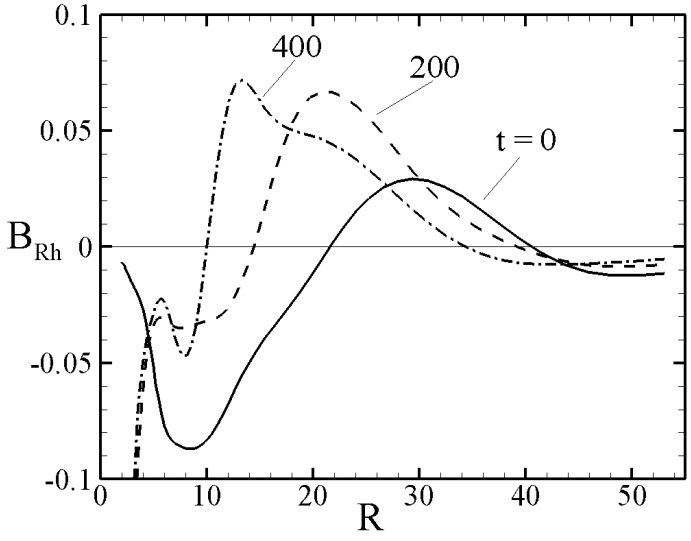

Figure 4.8: The radial component of the magnetic field $B_R(R, Z = h)$ at the disc surface at $t = 0$ (full), $t = 200$ (dashed) and $t = 400$ (dot-dashed) for $\alpha_\nu = 0.1$ and $\alpha_\eta = 0.1$. This quantity has an important role in determining the diffusive advection of the magnetic field $u_{B\eta}$ (equation 4.13).

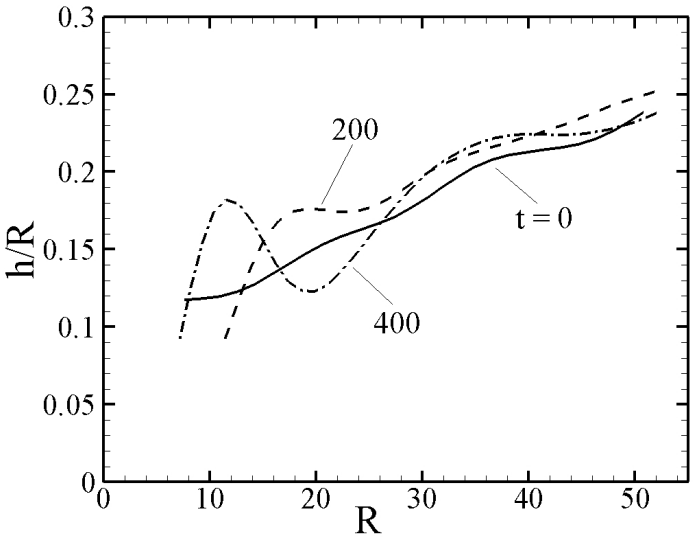

Figure 4.9: The ratio of the disc half thickness to the radius h/R as a function of R.

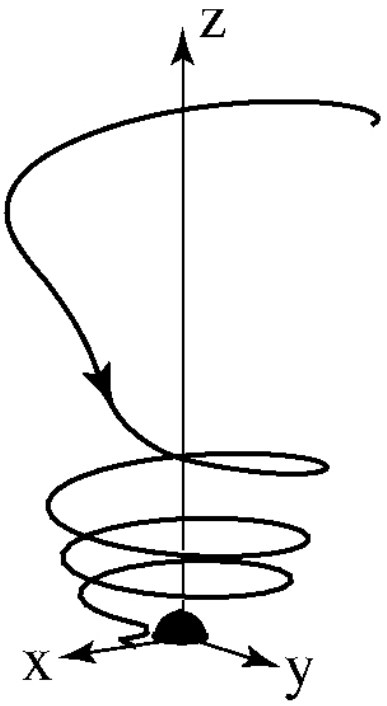

Figure 4.10: Three dimensional view of a magnetic field line originating from the disc at $R = 6$ at time $t = 300$. The twist of the field line is such that the field transports angular momentum out of the disc. That is, $B_Z B_\phi < 0$.

accretion speed $u_{\rm m}(R,t)$ in our simulation data using equation (4.9). We also calculate $B_{\phi h}(R,t)$, $B_{Z0}(R,t)$, h/R, and $\sigma(R,t)$ which permits us to compare the observed accretion speed with the prediction of the advection model (equation 4.13). We find that the reasonable values of $C_1 = 0.4$ and $C_2 = 0.2$ give satisfactory agreement between the model and our various simulation runs for $t \lesssim 400$.

Figure 4.12 shows the model and the measured simulation accretion speeds for sample cases.

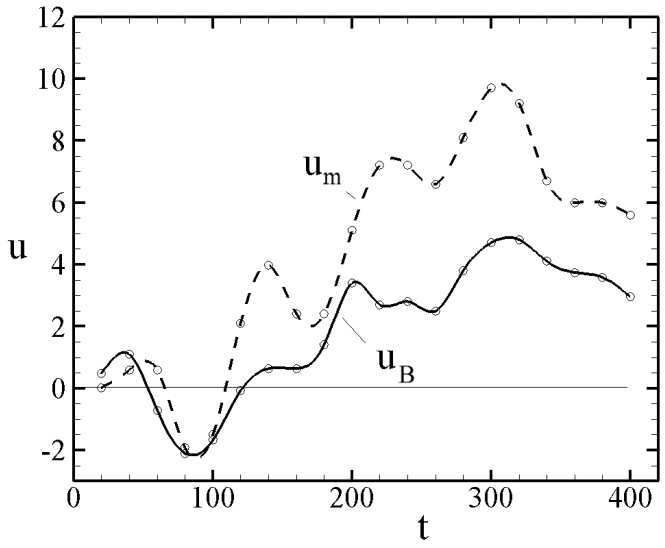

Figure 4.11: Accretion speed of the magnetic field u_B in the equatorial plane derived from the motion of the innermost zero crossing of $B_Z(R, Z = 0, t)$ and the matter accretion speed $u_{\rm m}$ at the same location for $\alpha_\nu = 0.1 = \alpha_\eta$. The initial radius of zero crossing is $R_{\rm O}(t = 0) = 13.7$.

4.2.3 Magnetic Field Advection in the Disc

The advection of the poloidal magnetic field is described by the equation

$$\frac{\partial(R\overline{B}_Z)}{\partial t} - \frac{\partial(R\overline{B}_Z u_{Bi})}{\partial R} = \frac{\partial}{\partial R}\left(-\frac{\eta_t R B_{Rh}}{h} + \eta_t R \frac{\partial \overline{B}_Z}{\partial R}\right), \tag{4.14}$$

(Lovelace et al. 1994), where $B_{Rh} = B_R(R, Z = h)$. For simplicity we have neglected terms of order $|\partial h/\partial R|$ relative to unity. Here,

$$u_{Bi} \equiv -\int_{-h}^{h} dZ B_Z(R, Z) v_R(R, Z) \Big/ \int_{-h}^{h} dZ B_Z(R, Z), \tag{4.15}$$

is the magnetic field advection speed of an ideal, perfectly conducting disc ($\eta_t = 0$). Note that the matter advection speed u_m is a density weighted average over the disc thickness of $-v_R$ whereas u_{Bi} is an average of $-v_R$ weighted by B_Z. For smooth profiles of ρ and B_Z the two speeds will be be comparable.

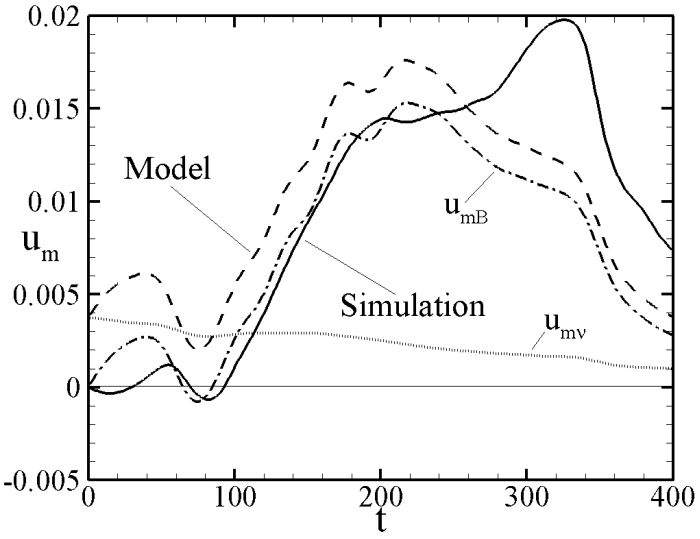

Figure 4.12: The solid curve shows the average accretion speed of the disc matter at the maximum of $B_Z(R, Z = 0)$ from the simulations for $\alpha_\nu = 0.1 = \alpha_\eta$. The initial radius of the maximum is $R = 22$. The dashed curve is from the advection model (equation 4.13)) with parameters $C_1 = 0.05$ and $C_2 = 0.2$. The model breaks down when the maximum approaches the star and interacts strongly with it. This happens at different times for different viscosity and diffusivity values.

The vertical magnetic flux threading the disc inside the first O-point where $\overline{B}_Z(R_\mathrm{O}, 0) = 0$ (or between successive O-points) decreases in general with time due to the diffusivity. From equation (4.14) we have

$$\frac{d}{dt}\int_0^{R_\mathrm{O}} R dR \overline{B}_Z = \left(-\frac{\eta_t R B_{Rh}}{h} + \eta_t R \frac{\partial \overline{B}_Z}{\partial R}\right)_{R=R_\mathrm{O}} . \tag{4.16}$$

For example, for $\overline{B}_Z < 0$ inside R_O, both terms on the right-hand side of equation (4.16) are seen to be positive so that the magnitude of the flux decreases.

For $\eta_t > 0$ the field advection speed is the sum of the ideal and diffusive contributions,

$$u_B = u_{Bi} + u_{B\eta} , \tag{4.17}$$

with

$$\frac{\partial(R\overline{B}_Z)}{\partial t} - \frac{\partial(R\overline{B}_Z u_B)}{\partial R} = 0 \,. \tag{4.18}$$

Here

$$u_{B\eta} = -\frac{\eta_t B_{Rh}}{h\overline{B}_Z} + \frac{\eta_t}{\overline{B}_Z}\frac{\partial \overline{B}_Z}{\partial R} \tag{4.19}$$

is the diffusive advection speed.

From our simulation data we can calculate the advection speed of the magnetic field u_{Bi} by tracking the location $R_{\rm O}(t)$ of the $B_Z(R, Z = 0)$ zero crossings which occur at "O-points" of the poloidal magnetic field $\mathbf{B}_p$. Close to the zero crossing, $B_Z(R, 0) = \text{const}(R - R_{\rm O})$ is an odd function of $R - R_{\rm O}$. Furthermore, $\overline{B}_Z$ is also an odd function of $R - R_O$. Thus $u_{B\eta}$ is an odd function about the O-point proportional to $(R - R_{\rm O})^{-1}$ because of the $\overline{B}_Z$ denominators in equation (4.19). The magnetic field moves symmetrically inward towards the O-point where it annihilates. The mathematical singularity is smoothed out by the finite grid. The magnetic field inside a current-carrying resistive wire behaves in the same way. Consequently, at $R = R_{\rm O}$ we have $u_{B\eta} = 0$. The diffusivity has no influence on the motion of the O-point. That is, $dR_{\rm O}/dt = -u_B = -u_{Bi}$.

We can compare field advection speed u_B (at an O-point) to the matter advection speed $u_{\rm m}$ at the same location. As mentioned these two speeds are expected to be comparable.

Figure 4.12 shows sample comparisons of u_B and $u_{\rm m}$. For a smaller diffusivity with fixed viscosity the difference between matter and field accretion speeds is smaller. For a larger viscosity relative to diffusivity, u_m is significanty larger than u_B.

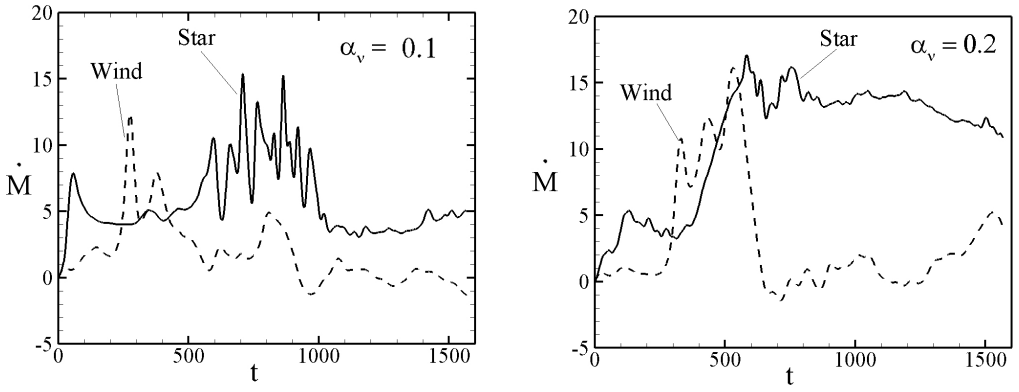

Figure 4.13: Dimensionless mass accretion rate to the star $\dot{M}_*$ and mass loss rate to the wind $\dot{M}_w$ for two viscosities with same diffusivity $\alpha_\eta = 0.1$.

4.2.4 Late Times

At late times ($t \gtrsim 1000$), the magnetic field decays appreciably owing to reconnection and field annihilation. Consequently the accretion speed is due mainly to the disc viscosity,

$$u_{\rm m} \approx u_{m\nu} \, . \tag{4.20}$$

The mass accretion rate to the star from the top half space is $\dot{M}_* = \pi(R\Sigma u_{\rm m})_*$, where Σ is the surface mass density of the disc and the asterisk subscript indicates evaluation outside the star.

Figure 4.13 shows the time dependence of the accretion rate to the star and the mass outflow rate in the wind for two viscosity values and $\alpha_\eta = 0.1$. For $0.05 \leq \alpha_\nu \leq 0.3$ we find that $\dot{M}_*$ at late times ($t > 1000$) is approximately proportional to α_ν. At late times $\dot{M}_*$ is independent of the diffusivity α_η.

4.2.5 Jet and Wind

In this work we observe both a collimated jet along the $Z-$axis and an uncollimated disc wind.

Jet

The fluxes of angular momentum and energy through the spherical surface [$r = 44,\ 0^\circ \leq \theta \leq 21^\circ$] are shown in Figure 4.14 and Figure 4.15 The angular momentum flux can be separated into a part from the matter and a part due to the magnetic field,

$$\dot{L} = \dot{L}_m + \dot{L}_f = \int d\mathbf{S} \cdot \left(\rho r \sin(\theta) v_\phi \mathbf{v}_p - \frac{r \sin(\theta) B_\phi \mathbf{B}_p}{4\pi} \right). \tag{4.21}$$

Similarly, the energy flux can be separated into contributions carried by the matter and that carried by the Poynting flux,

$$\dot{E} = \dot{E}_m + \dot{E}_f = \int d\mathbf{S} \cdot \left(\frac{1}{2} \rho \mathbf{v}^2 \mathbf{v}_p + \frac{c}{4\pi} \mathbf{E} \times \mathbf{B} \right). \tag{4.22}$$

The jet is strongly dominated by the electromagnetic field: The angular momentum flux is carried predominantly by the magnetic field and the energy flux is carried predominantly by the Poynting flux. Such jets were hypothesized by Lovelace (1976) and first observed in axisymmetric MHD simulations by Ustyugova et al. (2000).

Disc Wind

The rates of energy, angular momentum and mass flux through the surface [$r = 44,\ 21^\circ \leq \theta \leq 72^\circ$] is shown in Figure 4.16. We have chosen the upper bound for θ by requiring that the wind stay outside the disc.

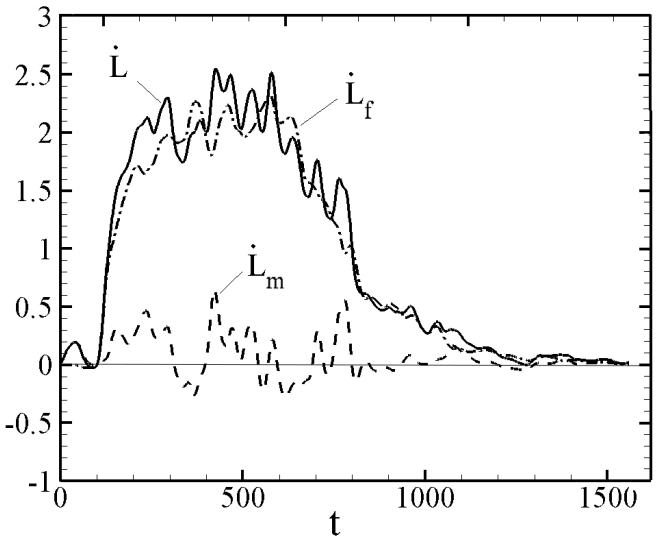

Figure 4.14: The jet angular momentum flux carried by the matter (dashed curve), the magnetic field (dot-dashed curve), and the total flux (solid curve) for $\alpha_\nu = 0.1$ and $\alpha_\eta = 0.1$.

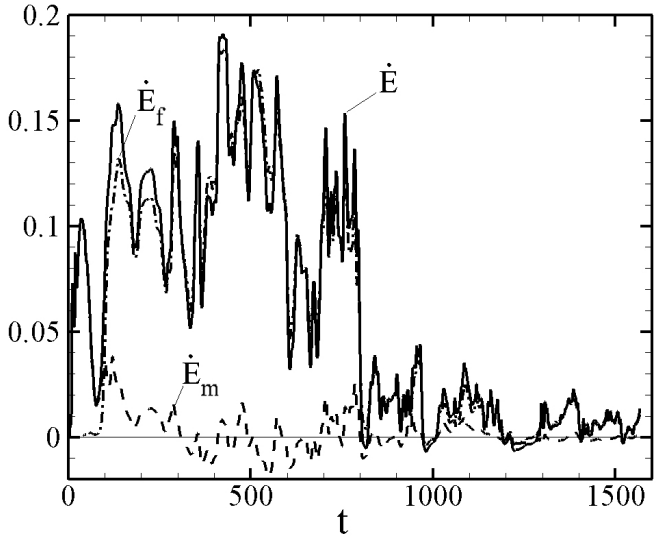

Figure 4.15: The jet energy flux carried by the matter (dashed curve), the Poynting flux (dot-dashed curve), and the total flux (solid curve) for $\alpha_\nu = 0.1$ and $\alpha_\eta = 0.1$. The jet is strongly dominated by the Poynting flux.

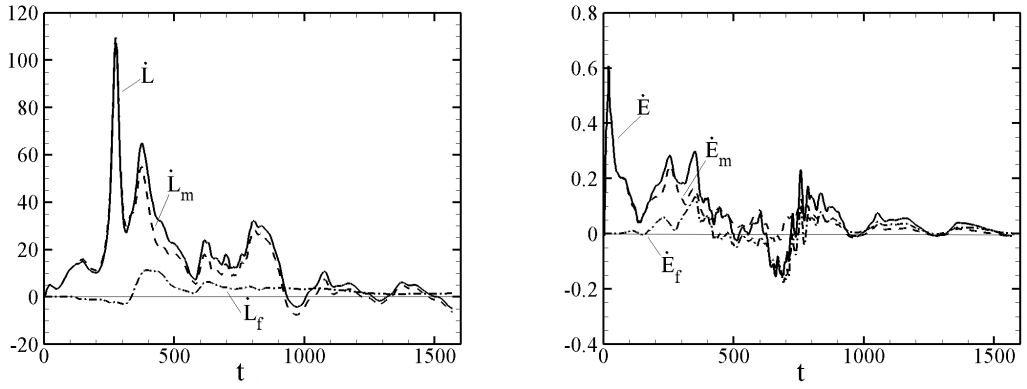

Figure 4.16: - *Left panel*: The wind angular momentum flux carried by the matter (dashed curve), the magnetic field (dot-dashed curve), and the total (solid curve) for $\alpha_\nu = 0.1$ and $\alpha_\eta = 0.1$. *Right panel*: The wind energy flux carried by the matter (dashed curve), the Poynting flux (dot-dashed curve), and the total flux(solid curve) for $\alpha_\nu = 0.1$ and $\alpha_\eta = 0.1$. The wind is strongly matter dominated.

Figure 4.16 shows the different components of the wind angular momentum flux and the components of the energy flux. The angular momentum and energy fluxes are dominated by the matter components. This is the opposite of the case for the jet.

Figure 4.17 and Figure 4.18 show the jet and wind total energy fluxes normalized to the "accretion power" $\dot{E}_{\rm acc} = GM_*\dot{M}_*/(2r_*)$. The large initial values of the ratios results from the fact that $\dot{M}_*$ is initially zero. Note that the two ratios are comparable.

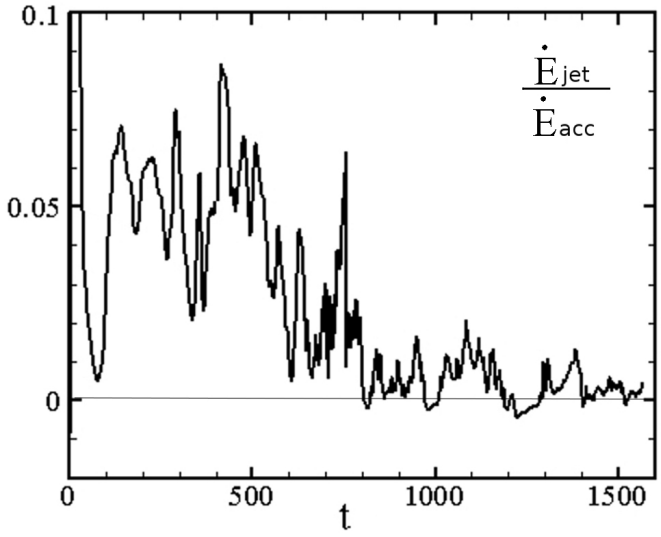

Figure 4.17: The total jet energy flux normalized by the "accretion power" $\dot{E}_{\rm acc} = GM_*\dot{M}_*/(2r_*)$ for $\alpha_\nu = 0.1$ and $\alpha_\eta = 0.1$.

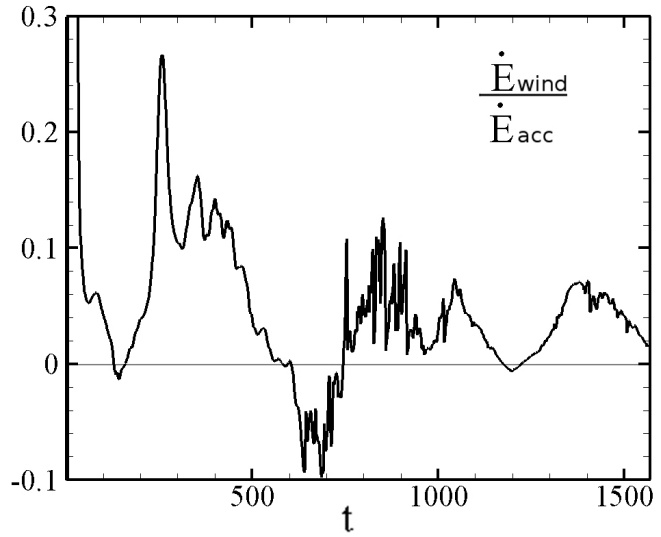

Figure 4.18: The total wind power also normalized by the accretion power $\dot{E}_{\rm acc}$ for $\alpha_\nu = 0.1$ and $\alpha_\eta = 0.1$. The large initial values of the ratios is due to the fact that the $\dot{M}_*$ is initially zero. The fact that $\dot{E}_{\rm wind}$ is temporarily negative is due to the fixed partition of the range of θ into wind and disc regions.

4.3 Conclusions

We have analyzed a set of axisymmetric MHD simulations of the evolution of a turbulent/diffusive accretion disc initially threaded by a weak magnetic field with midplane plasma beta β_0 is significantly larger than unity. The viscosity and magnetic diffusivity are modeled by two α parameters, one for the viscosity α_ν and the other for the diffusivity α_η. The coronal region above the disc is treated using ideal MHD. The initial magnetic field is taken to consist of three poloidal field loops threading the disc between its initial inner radius and to its ten times larger outer radius. This field configuration allows the derivation of the advection speed of the magnetic field.

Recent theoretical studies discussed the importance of the magnetic field extending from a turbulent disc into a low density non-turbulent/highly conducting corona (Bisnovatyi-Kogan & Lovelace 2007; Rothstein & Lovelace 2008; Lovelace et al. 2009; Bisnovatyi-Kogan & Lovelace 2012; Guilet & Ogilvie 2012, 2013). These treatments all considered stationary or quasi-stationary conditions *and* a disc threaded by a poloidal magnetic field of a single polarity. In contrast the simulations discussed here are strongly time-dependent and involve multiple poloidal field polarities in different regions of the disc. Consequently, a direct comparison of the theory and simulations is not possible. The simulations clearly show the inward advection of the magnetic field at about the same speed as the matter advection before the field decays by annihilation.

At early times ($t \lesssim 400$), we find that the innermost field loop twists and its field lines become open. For the different field loops we estimate two important time scales: One is the time scale for each loop to open due to differential

rotation of its foot points, and the other is the field annihilation time scale owing to the disc's magnetic diffusivity. The innermost field loop opens rapidly before there is significant annihilation. On the other hand the outer loop decays significantly before there is time for it to open. The twisting of the opened field lines of the inner loop leads to the formation of *both* an inner collimated magnetically dominated jet and at larger distances from the axis a matter dominated uncollimated wind. For later times (> 1000), the strength of the magnetic field decreases owing to field reconnection and annihilation in the disc. For the early times, we have derived from the simulations both the matter accretion speed in the disc $u_{\rm m}$ and the accretion speed of the magnetic field u_B. We show that the derived $u_{\rm m}$ agrees approximately with the predictions of a model where the accretion speed is the sum of a contribution due the disc's viscosity (which gives a radial outflow of angular momentum in the disc) and a term due to the twisted magnetic field at the disc's surface (which gives a vertical outflow of angular momentum) (Lovelace et al. 2009; 1994). At later times the magnetic contribution to $u_{\rm m}$ becomes small compared with the viscous contribution. Also for early times we find that $u_{\rm m}$ is larger than the magnetic field accretion speed u_B by a factor ~ 2 for the case where $\alpha_\nu = 0.1 = \alpha_\eta$.

APPENDIX

4.A Dependence on Grid Resolution

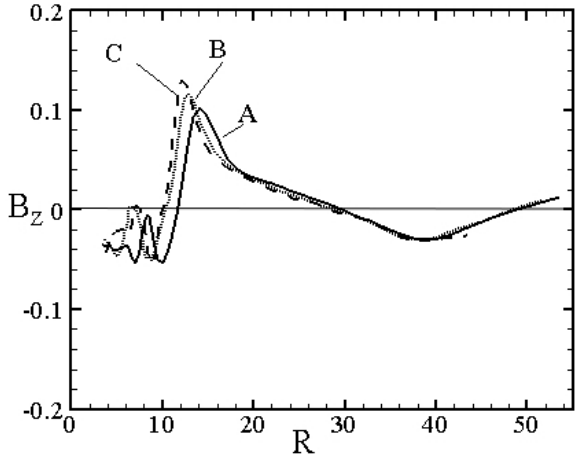

Figure 4.19: Radial dependences of $B_Z(R, Z = 0)$ for grid resolutions (N_θ, N_R) of $A = (31, 67)$, $B = (41, 87)$, and $C = (50, 100)$ at $t = 300$ for $\alpha_\nu = 0.1$ and $\alpha_\eta = 0.1$.

We have tested the dependence of our results on the grid by running higher resolution cases compared with resolution used for this study, $(N_\theta,\ N_R) = (31,\ 67)$. We have run cases with $(41,\ 87)$ and $(50,\ 100)$. Figure 4.19 shows the radial dependence of the mid plane magnetic field $B_Z(R, Z = 0)$ at $t = 300$ for the three grid resolutions. The radius of the first zero crossing of $B_Z(R, 0)$ decreases by about 14% going from the low to the intermediate resolution. It decreases by a further 2% going from the intermediate to the high resolution grid. Thus the convergence is rapid. This indicates the accuracy of the field advection speed u_B in Figure 4.11 and suggests that the actual speed is higher by about 16%.

CHAPTER 5

COUNTER-ROTATING DISCS

Commonly considered models of accretion discs have gas rotating in one direction with a turbulent viscosity acting to transport angular momentum outward and matter inward. However, observations indicate that there are more complicated, possibly transient, disc structures in some cases on a galactic scale, in galactic nuclei, and in discs around compact stellar-mass objects. Observations of normal galaxies have revealed co/counter-rotating gas/gas, gas/stars, and stars/stars discs in many galaxies of all morphological types — ellipticals, spirals, and irregulars (Rubin 1994a, 1994b; Galletta 1996; review by Corsini 2014). Theory and simulations of co/counter-rotating gas/gas discs predict enormously enhanced accretion rates resulting from the presence of the two components which can give rise to outbursts from these discs (Lovelace & Chou 1996; Nixon, King, & Price 2012).

Counter-rotation in disc galaxies appears in a variety of configurations including cases where (1) two cospatial populations of stars rotate in opposite directions, (2) the stars rotate in one direction and the gas rotates in the opposite direction, and (3) two spatially separated gas discs rotate in opposite directions (Corsini 2014). An example of case (1) is the galaxy NGC 4550 which has cospatial counter-rotating stellar discs (Rubin, Graham, & Kenney 1992). Examples of case (2) include the galaxy NGC 3626 (Ciri, Bettoni, & Galetta 1995) and NGC 4546 (Sage & Galletta 1994). An example of case (3) is the "Evil Eye" galaxy NGC 4826 in which the direction of rotation of the gas reverses going from the inner (180 km s^{-1}) to the outer disc (−200 km s^{-1}) with an inward radial accretion speed of more than 100 km s^{-1}in the transition zone, whereas the stars at all

radii rotate in the same direction as the gas in the inner disc, which has a radius of $\sim$ 1200 pc (Braun et al. 1994; Rubin 1994b).

On a stellar mass scale, Tang et al. (2012) have found evidence of accretion of an apparent inhomogeneous counter-rotating gas during the late stages of star formation. Accreted counter-rotating matter may encounter an existing co-rotating disc, for example, in low-mass X-ray binary sources where the accreting, magnetized rotating neutron stars are observed to jump between states where they spin up and those where they spin down. Nelson et al. (1997) and Chakrabarty et al. (1997) have proposed that the change from spin-up to spin-down results from a reversal of the angular momentum of the wind-supplied accreting matter.

A number of theoretical and computer simulation studies have explored the different physical processes arising in counter rotating discs. In the case of counter rotating cospatial stellar discs, the two-stream instability is predicted to couple the two components and give rise to low azimuthal mode number ($m = 1,\ 2$) spiral waves (Lovelace, Jore, & Haynes 1997). $N-$body simulations of counter rotating stellar discs show a prominent $m = 1$ spiral wave (Comins et al. 1997). The two-stream instability is also important for cospatial stellar/gas discs (Lovelace et al. 1997).

In the case of counter-rotating gas discs, the two components are necessarily spatially separated because otherwise the ensuing strong shocks would destroy the discs. The counter-rotating gas may come from later infall of "new" gas onto a preexisting co-rotating disc. A self-similar analytic solution was derived for accretion discs with isotropic $\alpha-$viscosity (Shakura & Sunyaev 1973) where the top half of the disc ($Z > 0$) rotates in one direction and the bottom half rotates in

the other direction (Lovelace & Chou 1996). The rotation can be Keplerian for accretion to a star or black hole or it can be a flat rotation for the case of a disc galaxy. The gas in the super-sonic shear layer between the two components has nearly free-fall inward radial velocity. The accretion rate is enhanced relative to a conventional disc by a factor of the order of $(R/h)^2\alpha^{-1/2} \gg 1$, where R is the radius and h is the disc's half-thickness. The Kelvin-Helmholtz instability is expected to be important in such shear layers. It has been studied earlier in planar supersonic shear layers (Ray 1981, 1982; Choudhury and Lovelace 1983). Gulati, Saini, & Sridhar (2012) studied the $m = 1,\ 2$ modes component Keplerian discs and found them to be unstable and a possible source of lopsided brightness distributions in galaxies. Using smooth particle hydrodynamic simulations, Nixon et al. (2012) modeled counter-rotating inner and outer AGN discs that were tilted with respect to one another and found that accretion rates could be $\gtrsim 100$ times greater than if they were planar. Also, using smooth particle hydrodynamic simulations, Alig et al. (2013) modeled counter-rotating gas discs with the aim of explaining the spiral-like filaments of gas feeding the galactic center's black hole SgrA*.

Spherical grid, axisymmetric hydrodynamic simulations of different configurations of counter-rotating discs were carried out by Kuznetsov et al. (1999). The interaction of the co- and counter-rotating components was mediated by the numerical viscosity. The present work discusses high-resolution axisymmetric hydrodynamic simulations of counter rotating discs including all components of the viscous stress tensor for an isotropic $\alpha-$viscosity.

On a stellar mass scale, Tang et al. (2012) have found evidence of accretion of an apparent inhomogeneous counter-rotating gas during the late stages

of star formation. Accreted counter-rotating matter may encounter an existing co-rotating disc as in low-mass X-ray binary sources where the accreting, magnetized rotating neutron stars are observed to jump between states where they spin up and those where they spin down. Nelson et al. (1997) and Chakrabarty et al. (1997) have proposed that the change from spin-up to spin-down results from a reversal of the angular momentum of the wind-supplied accreting matter.

5.1 Kelvin-Helmholtz Instability

The Kelvin-Helmholtz (KH) instability is a generic instability when there is a discontinuity in the velocity of a fluid. We investigate the KH instability in the context of a counter-rotating accretion disc . Section 5.1.1 develops the theory for the stability analysis and obtains explicit growth rates for the supersonic KH instability between radially separated co- and counter-rotating thin disc components. Section 5.1.2 discusses possible nonlinear consequences of the instability. Section 5.1.3 gives the main conclusions.

5.1.1 Theory

Disc Equilibrium

We consider the stability of a thin counter-rotating disc around a star or black hole. Figure 5.1 shows the rotation curve we consider. We use an inertial cylindrical (r, ϕ, z) coordinate system. The equilibrium has $(\partial/\partial t = 0)$ and $(\partial/\partial\phi = 0)$,

with the flow velocity $\mathbf{u} = u_\phi(r)\hat{\phi} = r\Omega\hat{\phi}$. That is, the accretion velocity u_r and the vertical velocity u_z are assumed negligible compared with u_ϕ. The equilibrium flow satisfies $-\rho r\Omega^2 = -dp/dr + \rho g_r$, where ρ is the density, p the pressure, $g_r = -\partial\Phi/\partial r$ and Φ the gravitational potential. We consider thin discs with half-thickness $h \approx (c_s/u_\phi)r \ll r$, where c_s is the sound speed. In this limit $\Omega = (g_r/r)^{1/2}[1 + O(h^2/r^2)]$. We consider Keplerian discs where $g_r = GM/r^2$ (with M the mass of the central object) as well as more general discs, for example, flat rotation curve discs relevant to galaxies where $g_r \propto r^{-1}$. We neglect the vertical structure of the equilibrium disc assuming $\partial/\partial z = 0$ for the equilibrium quantities (e.g., ρ, p, and u_ϕ). Our treatment parallels that of Lovelace, Turner, and Romanova (2009; denoted LTR09) but it generalizes that work to include the $z-$dependence of the perturbations.

Perturbation Equations

The perturbed quantities are: the density, $\tilde{\rho} = \rho + \delta\rho(r, \phi, z, t)$; the pressure is $\tilde{p} = p + \delta p(r, \phi, z, t)$; and the flow velocity is $\tilde{\mathbf{u}} = \mathbf{u} + \delta\mathbf{u}(r, \phi, z, t)$ with $\delta\mathbf{u} = (\delta u_r, \delta u_\phi, \delta u_z)$. We neglect the self-gravity of the disc. The equations for the perturbed flow are

$$\frac{D\tilde{\rho}}{Dt} + \tilde{\rho}\,\nabla\cdot\tilde{\mathbf{u}} = 0\,, \tag{5.1}$$

$$\frac{D\tilde{\mathbf{u}}}{Dt} = -\frac{1}{\tilde{\rho}}\nabla\tilde{p} - \nabla\Phi\,, \tag{5.2}$$

$$\frac{DS}{Dt} = 0\,, \tag{5.3}$$

where $D/Dt \equiv \partial/\partial t + \tilde{\mathbf{u}}\cdot\nabla$, and where $S \equiv \tilde{p}/(\tilde{\rho})^\gamma$ is the entropy of the disc matter.

We consider perturbations δp, $\delta\rho$.. of the form

$$f(r)\exp(im\phi + ik_z - i\omega t), \tag{5.4}$$

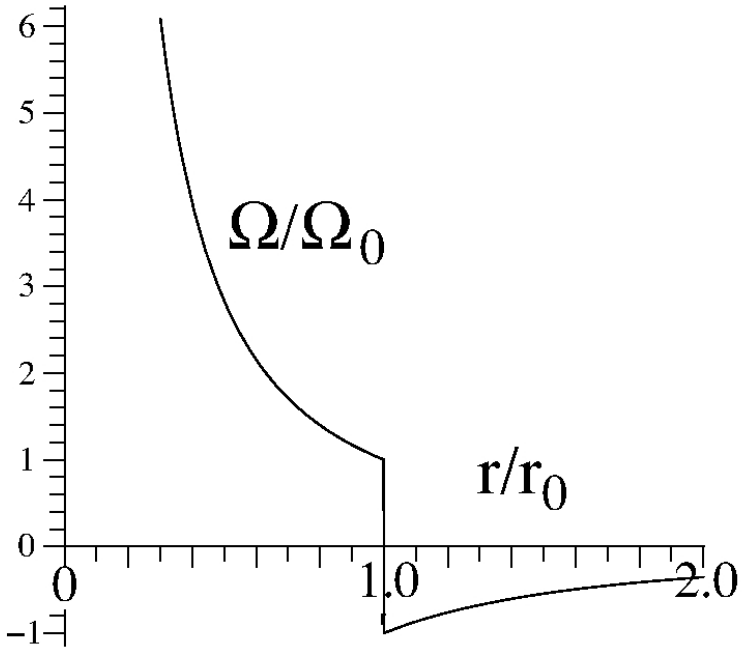

Figure 5.1: Angular velocity of the counter-rotating Keplerian disc where $g_r = GM/r^2$ with M the mass of the central object.

where $m = 0, 1, 2, ..$ is the azimuthal mode number, ω the angular frequency, and k_z the wavenumber in the $z-$direction. From equation (5.1), we find

$$i\Delta\omega\ \delta\rho = \nabla \cdot (\rho\ \delta\mathbf{u})\ , \tag{5.5}$$

where $\Delta\omega(r) \equiv \omega - m\Omega(r)$ and $\Omega = u_\phi/r$. From equation (5.2),

$$i\Delta\omega\delta u_r + 2\Omega\delta u_\phi = \frac{1}{\rho}\frac{\partial\delta p}{\partial r} - \frac{\delta\rho}{\rho^2}\frac{dp}{dr}\ , \tag{5.6}$$

$$i\Delta\omega\delta u_\phi - \frac{\kappa^2}{2\Omega}\delta u_r = ik_\phi\frac{\delta p}{\rho}\ , \tag{5.7}$$

$$i\Delta\omega\delta u_z = ik_z\frac{\delta p}{\rho}\ . \tag{5.8}$$

Here,

$$\kappa \equiv \left[\frac{1}{r^3}\frac{d(r^4\Omega^2)}{dr}\right]^{\frac{1}{2}}$$

is the radial epicyclic frequency and $k_\phi \equiv m/r$ is the azimuthal wavenumber. From equation (5.3) we have

$$\delta p = c_s^2 - \frac{i\rho c_s^2}{\Delta\omega L_S}\delta u_r \,, \tag{5.9}$$

where

$$\frac{1}{L_S} \equiv \frac{1}{\gamma}\frac{d\ln(S)}{dr} \,, \qquad c_s \equiv \left(\frac{\gamma p}{\rho}\right)^{1/2} \,, \tag{5.10}$$

with L_S the length scale of the disc's entropy variation, and c_s the sound speed.

Introducing $\Psi \equiv \delta p/\rho$, equations (5.6)-(5.8) can be rewritten as

$$\rho\delta u_r = i\mathcal{F}\left[\frac{\Delta\omega}{\Omega}\left(\frac{\partial\Psi}{\partial r} - \frac{\Psi}{L_*}\right) - 2k_\phi\Psi\right] \,, \tag{5.11}$$

$$\rho\delta u_\phi = \mathcal{F}\left\{\frac{\kappa^2}{2\Omega^2}\left(\frac{\partial\Psi}{\partial r} - \frac{\Psi}{L_S}\right) - k_\phi\left(\frac{\Delta\omega}{\Omega} + \frac{dp/dr}{\rho\Omega\Delta\omega L_S}\right)\Psi\right\} \,, \tag{5.12}$$

$$\rho\delta u_z = \rho\frac{k_z}{\Delta\omega}\Psi, \tag{5.13}$$

where

$$\mathcal{F} \equiv \frac{\rho\Omega}{\mathcal{D}} \,, \tag{5.14}$$

and

$$\mathcal{D} = \kappa^2 - (\Delta\omega)^2 - \frac{dp/dr}{\rho L_S} \,. \tag{5.15}$$

Equations (5.9) and (5.11) can be combined to give

$$\delta\rho = \frac{\rho\Psi}{c_s^2} - \frac{\mathcal{F}}{\Delta\omega L_S}\left[\frac{\Delta\omega}{\Omega}\left(\frac{\partial\Psi}{\partial r} - \frac{\Psi}{L_S}\right) - 2k_\phi\Psi\right]. \tag{5.16}$$

Equations (5.11)-(5.13) and (5.16) can now be substituted into equation (5.5) to give a single differential equation for $\Psi(r)$,

$$\begin{aligned}\frac{1}{r}\frac{\partial}{\partial r}\left(\frac{r\mathcal{F}}{\Omega}\frac{\partial\Psi}{\partial r}\right) = &\left[\frac{\rho}{c_s^2} + \frac{k_\phi^2\mathcal{F}}{\Omega} + \frac{1}{r}\frac{\partial}{\partial r}\left(\frac{r\mathcal{F}}{\Omega L_S}\right) + \frac{\mathcal{F}}{\Omega L_S^2}\right]\Psi \\ &+ \left[2k_\phi\mathcal{F}\frac{d\ln(g\mathcal{F})}{dr}\right]\frac{\Psi}{\Delta\omega} + \left[\frac{k_\phi^2(dp/dr)\mathcal{F}}{\rho\Omega L_S} - \rho k_z^2\right]\frac{\Psi}{(\Delta\omega)^2} \,,\end{aligned} \tag{5.17}$$

where $g \equiv \exp(2\int dr/L_S)$. This equation generalizes equation (13) of LTR09 by including the $z-$dependence of the perturbations which contributes the last term in this equation.

Specific Model

In order to simplify the analysis we consider barotropic disc matter where $L_S^{-1} \to 0$ so that $g = 1$. Further, we consider the counter-rotation curve shown in Figure 5.1, namely,

$$\Omega = \begin{cases} (g_r/r)^{1/2} & r < r_0 \,, \\ -(g_r/r)^{1/2} & r > r_0 \,. \end{cases} \tag{5.18}$$

We can then solve equation (5.17) for Ψ_- for $r < r_0$ and Ψ_+ for $r > r_0$ and then match the solutions to the jump-condition across $r = r_0$ which follows from the equation.

We consider solutions of the form

$$\begin{aligned} \Psi_- &\propto \exp\left[+ k_{r-}(r - r_0)\right], \qquad r < r_0 \\ \Psi_+ &\propto \exp\left[- k_{r+}(r - r_0)\right], \qquad r > r_0 \end{aligned} \tag{5.19}$$

We assume $|k_{r\pm}|r_0 \gg 1$ so that radial variations of the equilibrium quantities can be neglected. In order that the perturbations decay going away from r_0, we must have $\Re(k_{r\pm}) > 0$, which can be checked a posteriori.

For $r \gtrless r_0$, equation (5.17) gives the dispersion relations

$$c_s^2(-k_{r\pm}^2 + k_\phi^2) = [\kappa^2 - (\Delta\omega_\pm)^2]\left[\frac{k_z^2 c_s^2}{(\Delta\omega_\pm)^2} - 1\right], \tag{5.20}$$

where $\Delta\omega_\pm \equiv \omega - m\Omega_\pm$. For $k_z = 0$, the dispersion relations take the more familiar form $(\Delta\omega_\pm)^2 = \kappa^2 + c_s^2(-k_{r\pm}^2 + k_\phi^2)$.

It is useful to introduce the following dimensionless variables,

$$\overline{k}_z = k_z h,\ \ \overline{k}_\phi = k_\phi h,\ \ \overline{\Omega} = \frac{\Omega}{\Omega_0},\ \ \overline{\kappa} = \frac{\kappa}{\Omega_0},\ \ \overline{\Delta\omega} = \frac{\Delta\omega}{\Omega_0}\ , \tag{5.21}$$

where $h = c_s/\Omega_0$ and $\Omega_0 = \sqrt{g_r(r_0)/r_0}$. Dropping the overbars gives $k_{r\pm}(\omega)$,

$$k_{r\pm}^2(\omega) = k_\phi^2 - [\kappa^2 - (\Delta\omega_\pm)^2]\left[\frac{k_z^2}{(\Delta\omega_\pm)^2} - 1\right]\ . \tag{5.22}$$

Multiplying equation (5.17) by r, integrating over r from $r_0-\epsilon$ to $r_0+\epsilon$, letting $\epsilon \to 0$, and taking into account that $\Psi(r)$ is continuous across r_0 gives

$$\frac{k_{r+}}{\mathcal{D}_+} + \frac{k_{r-}}{\mathcal{D}_-} = \mathcal{R}(\omega)\ , \tag{5.23}$$

where

$$\mathcal{R}(\omega) = k_\phi\left(\frac{1}{\mathcal{D}_+} + \frac{1}{\mathcal{D}_-}\right)\left(\frac{1}{\Delta\omega_+} + \frac{1}{\Delta\omega_-}\right)\ . \tag{5.24}$$

The left-hand side of equation (5.23) is from the left-hand side of equation (5.17). The right-hand side, $\mathcal{R}$, is from the right-hand term of equation (5.17) involving $d\mathcal{F}/dr$ which is $d\mathcal{F}/dr = (\mathcal{F}_+ - \mathcal{F}_-)\delta(r - r_0)$.

For the assumed thin discs, $\overline{\Omega} = 1 + O(h^2/r_0^2)$ for Keplerian discs and other rotation curves. On the other hand,

$$\mathcal{D}_\pm = \begin{cases} 1 - (\Delta\omega_\pm)^2 & \text{Keplerian}\ , \\ \kappa^2 - (\Delta\omega_\pm)^2 & \text{other rotation curves}\ , \end{cases} \tag{5.25}$$

and $\Delta\omega_\pm = \omega \pm m$ with ω measured in units of Ω_0.

Equation (5.23) can be squared twice to obtain

$$G(\omega) = \left(\frac{k_{r+}^2}{\mathcal{D}_+^2} - \frac{k_{r-}^2}{\mathcal{D}_-^2} - \mathcal{R}^2\right)^2 - \frac{4k_{r-}^2\mathcal{R}^2}{\mathcal{D}_-^2} = 0\ . \tag{5.26}$$

The possibility of spurious roots of this equation not satisfying equation (5.23) has to be checked a posteriori. Equation (5.26) can be expanded out as a 16th order polynomial in ω.

Important properties of $G(\omega)$ are readily verified: Firstly, for $m = 0$ the perturbation is stable, $\mathcal{R} = 0$ and therefore $k_{r+} = k_{r-} = 0$ so that either $\omega = \pm\kappa$ (radial epicyclic motion) or $\omega = \pm k_z$ (vertically propagating sound wave). For this reason we consider $m \geq 1$ in the following. Secondly, $G(\omega) = G(-\omega)$. Thirdly, $[G(\omega)]^* = G(\omega^*)$. It follows that the solutions for ω of $G(\omega) = 0 = [G(\omega)]^*$ are either purely real or purely imaginary.

The roots of $G(\omega)$ can be located by making a contour plot of

$$F(\omega) = \{\Re[G(\omega)]\}^2 + \{\Im[G(\omega)]\}^2 , \tag{5.27}$$

in the $\omega = \omega_R + i\omega_I$ plane with Maple or Mathematica. Figure 5.2 shows the the unstable roots for low m values for a Keplerian disc with $h/r_0 = 0.1$. There is stability (ω = real) for $k_z < k_{zc}(m)$. For this range of k_z, the ω roots are real. We have verified that for $k_z > k_{zc}$ the roots satisfy equation (5.23) as well as the conditions $\Re(k_{r\pm}) > 0$ needed for the modes to be localized around r_0. Figure 5.3 shows the real and imaginary parts of $k_{r\pm}$ as a function of k_z for $m = 1$ also for a Keplerian disc with $h/r_0 = 0.1$.

A significant simplification of the dispersion relation (5.26) is possible in the limit where $k_z \gg k_\phi = m(h/r_0)$. In this limit,

$$k_{r\pm} = -\mathcal{D}_\pm \left(\frac{k_z^2}{\Delta\omega_\pm^2} - 1 \right) , \tag{5.28}$$

and

$$\frac{k_{r+}^2}{\mathcal{D}_+^2} = \frac{k_{r-}^2}{\mathcal{D}_-^2} . \tag{5.29}$$

By combining equations (5.28) and (5.29) we obtain a function with roots that can be determined analytically. By rewriting this function as an ordinary polynomial, we obtain a 9-th order polynomial. Factoring out the $\omega = 0$ root gives

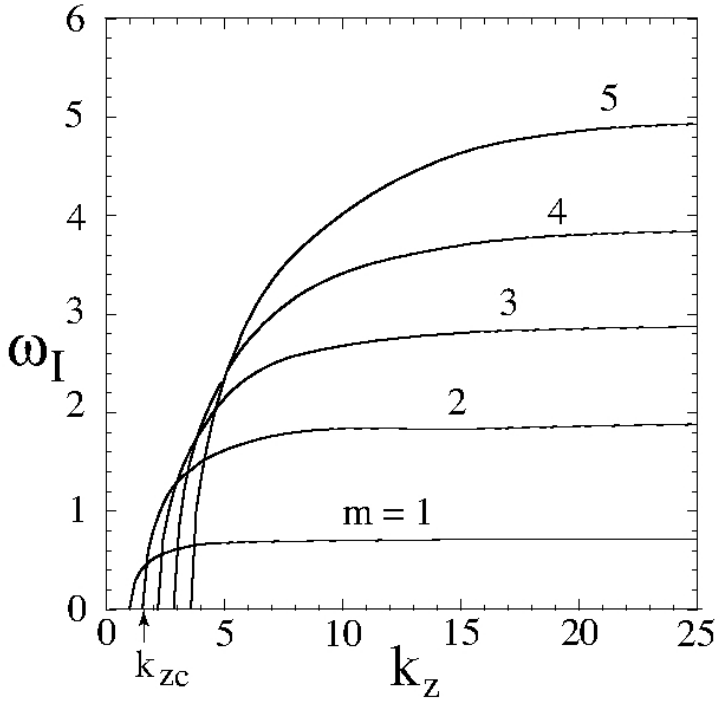

Figure 5.2: Wavenumber dependence of the growth rate of the instability, $\Im(\omega) = \omega_I$, for different values of m for a Keplerian disc with $h/r_0 = 0.1$. Note that ω_I is in units of Ω_0 and k_z is in units of h^{-1}.

the 8-th order polynomial

$$\begin{aligned}\omega^8 - (2\kappa^2 + 2k_z^2 + 4m^2)\omega^6 + (\kappa^4 + 5k_z^2\kappa^2 \\ + 2m^2\kappa^2 + 2k_z^2m^2 + 6m^4)\omega^4 + (-4k_z^2\kappa^4 - 2m^2\kappa^4 + 6k_z^2m^2\kappa^2 \\ + 2m^4\kappa^2 + 2k_z^2m^4 - 4m^6)\omega^2 + (k_z^2\kappa^6 - 4k_z^2m^2\kappa^4 + m^4\kappa^4 \\ + 5k_z^2m^4\kappa^2 - 2m^6\kappa^2 - 2k_z^2m^6 + m^8) = 0\ . \quad (5.30)\end{aligned}$$

Rewriting the equation in this form removes the duplicate solutions from the original polynomial. There are four real roots, $\omega_R = \pm(m \pm \kappa)$ which are the normal modes of a unidirectional disc, and the four roots

$$\begin{aligned}\omega &= \pm\left[k_z^2 + m^2 + \sqrt{k_z^2(-\kappa^2 + k_z^2 + 4m^2)}\right]^{1/2}\ , \\ \omega &= \pm\left[k_z^2 + m^2 - \sqrt{k_z^2(-\kappa^2 + k_z^2 + 4m^2)}\right]^{1/2}\ .\end{aligned} \quad (5.31)$$

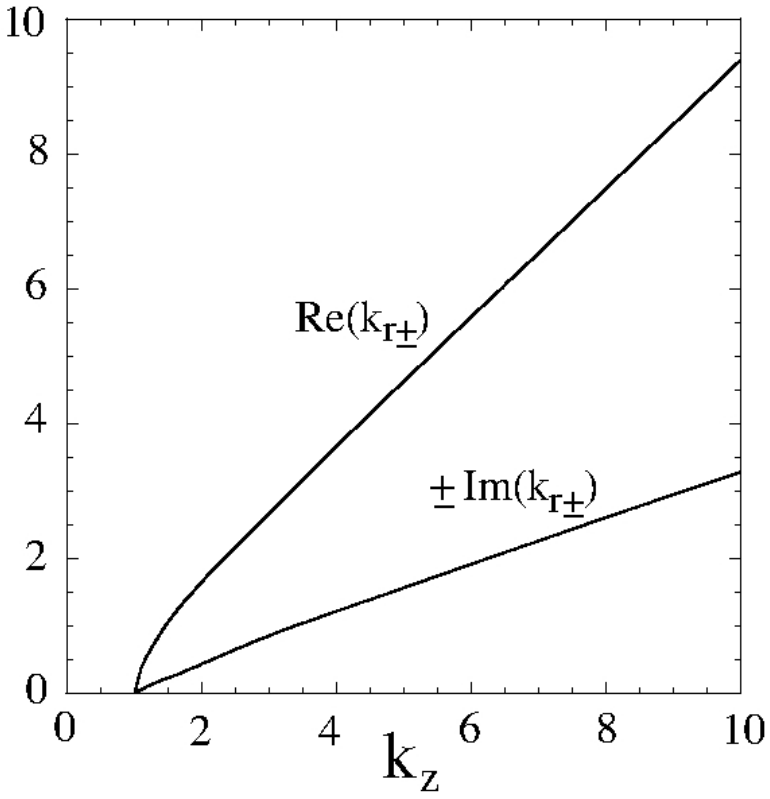

Figure 5.3: Radial wavenumber, $\Re(k_{r\pm})$ and $\Im(k_{r\pm})$, as a function of k_z for $m = 1$ for a Keplerian disc with$h/r_0 = 0.1$. The wavenumbers are in units of h^{-1}.

The first set of roots give stable oscillations. The second set gives purely imaginary ω values. The unstable root is

$$\omega_I = \left[\sqrt{k_z^2(k_z^2 + 4m^2 - \kappa^2)} - m^2 - k_z^2 \right]^{1/2} . \tag{5.32}$$

For k_z large compared with unity, $\omega_I \to m$.

Solving for $\omega_I = 0$ gives the threshold value

$$k_{zc} = \left[\frac{m^4}{2m^2 - \kappa^2} \right]^{1/2} . \tag{5.33}$$

This expression agrees accurately with the solutions obtained from the full dispersion relation (equation 5.23). Note that for a Keplerian disc, $\kappa = 1$, so that

all of the modes $m = 1, 2, ..$ are unstable. For flat rotation curves relevant to disc galaxies, u_ϕ =const, so that $\kappa = \sqrt{2}$ and consequently the mode $m = 1$ is stable. This mode is also stable for a rigid rotation curve disc where $\kappa = 2$.

The growth rates found here are in rough agreement with the predictions for a planar vortex sheet $\omega^2 = (k_\parallel c_s)^2[1 + \mathcal{M}_p^2/4 - (1 + \mathcal{M}_p^2)^{1/2}]$, where $\mathcal{M}_p \equiv (k_\phi/k_\parallel)\mathcal{M}_T \leq \mathcal{M}_T$ with $k_\parallel = \sqrt{k_\phi^2 + k_z^2}$ the wavenumber parallel to the interface, and $\mathcal{M}_T = 2r_0\Omega_0/c_s$ the Mach number of the total velocity jump (see, e.g., Choudhury & Lovelace 1984). In this case, instability $\omega^2 < 0$ occurs for $\mathcal{M}_p < 2^{3/2}$ which corresponds to $k_z h > m(1/2 - h^2/r_0^2)^{1/2} \approx m/\sqrt{2}$. This agrees with equation (33) for $\kappa = 0$.

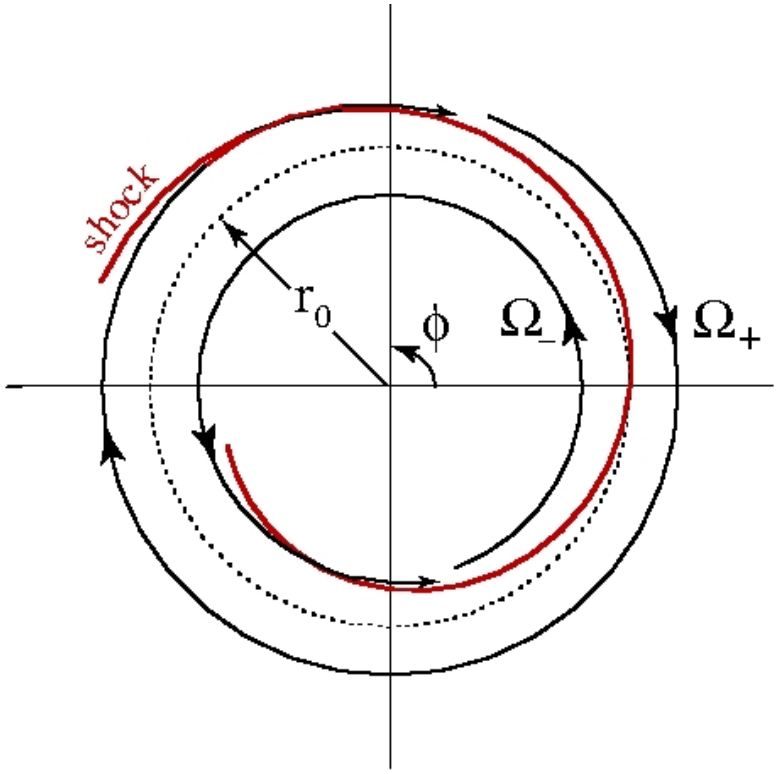

Figure 5.4: Polar plot of a one armed ($m = 1$) perturbation which has steepened to form an oblique shock. The gas crossing the shock is deflected towards the interface of the two components.

5.1.2 Nonlinear Evolution

Although the growth rate increases with increasing wavenumber k_z, the large k_z modes are not expected to be important because their growth will saturate at a small amplitude $\delta r \sim k_z^{-1}$ and involve mixing only small amounts of co- and counter-rotating matter. For this reason we consider the long wavelength modes, $k_z \sim h^{-1}$ and $k_\phi \geq r_0^{-1}$. The perturbations have the form

$$\Psi_\pm \propto \exp\left[\mp \Re(k_{r\pm})(r - r_0)\right] \exp\left[i(m\phi \mp \Im(k_{r\pm})(r - r_0)\right] . \tag{5.34}$$

The maximum of the perturbation is a tightly-wrapped leading spiral $r = r_0 \pm m\phi/\Im(k_{r\pm})$ with m arms. Figure 5.4 shows the nature of the spiral for $m = 1$.

The spiral wave can lead to the formation of an oblique shock under some conditions. Upstream of the wave, the magnitude of the normal normal component of the gas velocity relative to the wave is $u_n = \theta r_0 \Omega_0$, where $\theta = m|\Im(k_{r\pm})r_0|^{-1} \ll 1$. If the upstream normal Mach number $\mathcal{M}_n = u_n/c_s > 1$ there is an oblique shock. On the downstream side the normal Mach number is less than unity. For $r > r_0$ the gas is deflected inward and acquires a radial velocity $u_r = -\beta r_0 \Omega_0$, where $\beta = [2/(1 + \gamma)](1 - \mathcal{M}_n^{-2})\theta$. For $r < r_0$, the oblique shock gives outward radial velocity $u_r = \beta r_0 \Omega_0$.

The co- and counter-rotating disc components have a natural *repulsion* for each other for the following reason. The mixing of the two components will involve strong shocks. A possible geometry for $m = 1$ is sketched in Figure 5.5 where there are two strong standing shocks, each with Mach number $\mathcal{M} = u_\phi/c_s \gg 1$. In the region between the shocks, the angular momenta of the two components is annihilated and the gas is strongly heated. The ratio of the gas temperatures downstream to upstream of the normal shock is $T_2/T_1 \approx 1 + 2(\gamma -$

$1)\gamma\mathcal{M}^2/(\gamma+1)^2$. This ratio is ~ 20 for $\mathcal{M} = 10$ and $\gamma = 7/5$. The heated gas will expand vertically increasing its scale height by a factor $\sqrt{T_2/T_1} \gg 1$. With no centrifugal force, the gas will free-fall over the surfaces of the inner disc towards the disc's center.

The mass loss rate from this process is $\dot{M}_{\rm ann} = 4mhr_0\Delta r\rho\Omega_0$, where Δr is the radial amplitude of the interface perturbation. This loss rate is larger than the Shakura-Sunyaev (1973) accretion rate by a factor of order $(m/\pi)(\Delta r/h)(\mathcal{M}/\alpha)$ where α is the dimensionless viscosity coefficient for a disc rotating in one direction. It is commonly estimated to be in the range $10^{-3} - 0.1$. The Kelvin-Helmholtz instability evidently gives a spatially localized effective viscosity coefficient $\alpha_{\rm eff} \sim (m/\pi)\mathcal{M}$ assuming $\Delta r \sim h$. Thus the region between the co- and counter-rotating components will be rapidly emptied of gas and a gap will form. Subsequently, the outer disc will spread inward and the inner disc outward due to the turbulent viscosity. Consequently the gap will close after a definite period and the mentioned heating and annihilation of angular momentum will repeat.

5.1.3 Conclusions

Observations of galaxies and models of accreting systems point to the occurrence of counter-rotating discs where the inner part of the disc ($r < r_0$) is co-rotating and the outer part is counter-rotating. This work analyzes the linear stability of radially separated co- and counter-rotating thin discs. The strong instability is the supersonic Kelvin-Helmholtz instability. The growth rates are of the order of or larger than the angular rotation rate at the interface $\Omega(r_0)$. The instability is absent if there is no vertical dependence of the perturbation, that

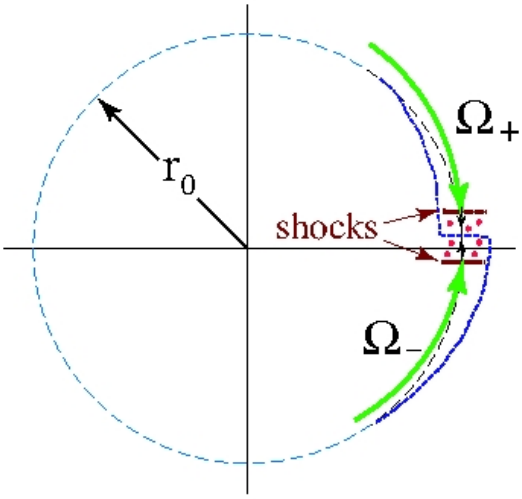

Figure 5.5: Polar plot suggesting the formation of strong normal shocks leading the annihilation of the angular momenta of the co- and counter rotating components and the heating of this gas.

is, if $k_z = 0$. That is, the instability is essentially a three-dimensional instability. Thus this instability is not captured by the analysis of Li and Narayan (2004) where $k_z = 0$ and where the gas is treated as incompressible. Counter-rotating Keplerian discs are unstable for azimuthal mode numbers $m = 1, 2, ..,$ whereas for for a flat rotation curve relevant to disc galaxies the unstable mode numbers are $m = 2, 3, ...$ We note that when there is a density changes across the interface there is necessarily a corresponding change in the entropy. This changes the jump condition across the interface and leads in general to propagating unstable modes where $\omega = \omega_R + i\omega_I$ with $\omega_R \neq 0$ and $\omega_I > 0$.

The nonlinear phase of the instability will involve the mixing of co- and counter-rotating gas which will involve strong shocks, strong heating of the

gas, and annihilation of the angular momenta of the two gas components. The heated gas will expand vertically and since it has zero angular momentum it will free-fall to the disc's center over the surface of the inner disc. Thus the region between the co- and counter-rotating components will be rapidly emptied of gas and a gap will form. In effect the two components have a repulsive interaction. This is suggestive of the Leidenfrost effect (Leidenfrost 1966) where a liquid droplet is levitated above a hot surface by the vapor pressure between the droplet and the surface. Subsequent to the gap formation, the outer disc will spread inward and the inner disc outward due to the turbulent viscosity. Consequently the gap will close after a definite period and the heating and annihilation of angular momentum will repeat.

Three-dimensional hydrodynamic simulations are of course required to fully understand the nonlinear evolution of the counter-rotating discs. Although axisymmetric disc simulations do not allow for the Kelvin-Helmholtz instability, the inclusion of viscosity can model the effect of the turbulent viscosity due to the instability. In an early study by Kuznetsov et al. (1999) the effective viscosity was the numerical viscosity due to the finite grid. In a recent study by Dyda et al. (2014), a high resolution grid was used with all components of the viscous stress tensor are included to model an isotropic Shakura-Sunyaev $\alpha-$viscosity. Both studies clearly show the development of a gap between the co- and counter-rotating components and enhanced accretion. The study by Dyda et al. (2014) shows the quasi periodic closing and opening of the gap.

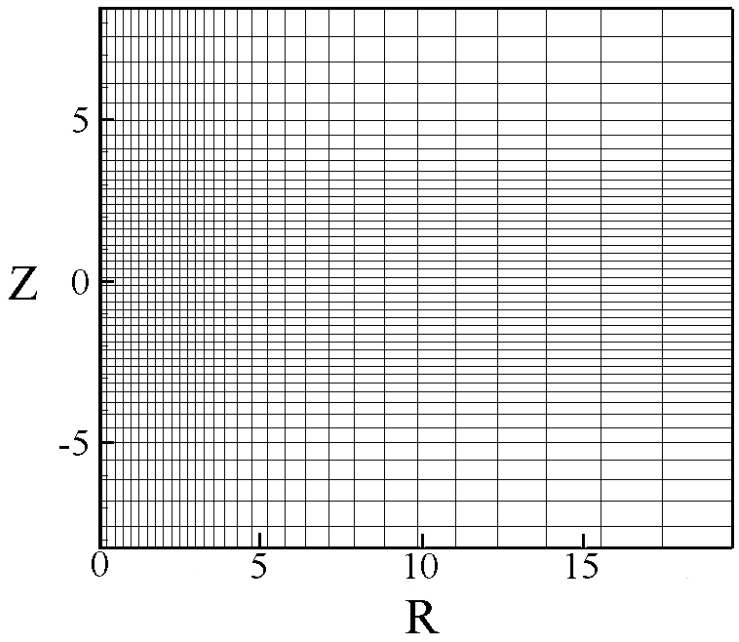

Figure 5.6: Sparse version of our grid showing 20% of the cells used. The simulations used $N_R \times N_Z = 150 \times 250$ grid cells.

5.2 Numerical Simulations

We perform some numerical hydrodynamis simulations to study some simple geometries involving an accretion disc and a source of counter-rotating matter. In the vertically offset torus geometry, we take a sub-Keplerian accretion disc and reverse the toroidal velocity of the matter for a torus in the disc. Likewise in the vertically separated geometry we reverse the toroidal velocity above a certain scale height in the disc. In the radially separated geometry the inner and outer parts of the disc have opposite Keplerian orbital velocity. In Section 5.2 we discusses the numerical methods, the simulation parameters and results. Section 5.2.2 gives the conclusions.

Initial Conditions

Matter Distribution Initially the matter of the disc and corona are assumed to be in mechanical equilibrium (Romanova et al. 2002). The initial density distribution is taken to be barotropic with

$$\rho(p) = \begin{cases} p/T_{\rm disc} & p > p_b \ \text{ and } \ R \geq R_d \ , \\ p/T_{\rm cor} & p < p_b \ \text{ or } \ R \leq R_d \ , \end{cases} \tag{5.35}$$

where p_b is the level surface of pressure that separates the cold matter of the disc from the hot matter of the corona and R_d is the initial inner disc radius. At this surface the density has an initial step discontinuity from value $p/T_{\rm disc}$ to $p/T_{\rm cor}$.

Because the density distribution is barotropic, the initial angular velocity magnitude is a constant on coaxial cylindrical surfaces about the $z-$axis. Consequently, the pressure can be determined from the Bernoulli equation

$$F(p) + \Phi + \Phi_c = \text{const} \ , \tag{5.36}$$

where $\Phi = -GM/\sqrt{R^2 + Z^2}$ is the gravitational potential, $\Phi_c = \int_R^\infty \xi d\xi \, \omega^2(\xi)$ is the centrifugal potential, and

$$F(p) = \begin{cases} T_{\rm disc} \ln(p/p_b) & p > p_b \ \text{ and } \ R \geq R_d \ , \\ T_{\rm cor} \ln(p/p_b) & p < p_b \ \text{ or } \ R \leq R_d \ . \end{cases} \tag{5.37}$$

The initial half-thickness of the disc h is taken to be $h/R = 0.200$ and the inner disc radius $R_d = 2$.

Angular Velocity The magnitude of the initial angular velocity is constant along cylinders of constant R. Inside of R_d, the matter rotates rigidly with angu-

lar velocity of the star

$$\Omega = (1 - 0.003)\Omega_K(R_d) \qquad R \leq R_d \ . \tag{5.38}$$

Inside the disc the angular velocity of the disc is slightly sub-Keplerian.

For the simulations of vertically separated co- and counter-rotating components, we consider a positive angular velocity of the lower part of the disc. The upper counter-rotating part of the disc has a negative angular velocity. That is,

$$\Omega = \begin{cases} -(1 - 0.003)\Omega_K(R) & Z > 0 \text{ and } \rho \leq \rho_c \ , \\ (1 - 0.003)\Omega_K(R) & \text{elsewhere} \ . \end{cases} \tag{5.39}$$

We parametrize these runs in terms of the initial ratio of disc mass counter-rotating with the star to the disc mass rotating with the star which we define as Δ. The counter-rotating floor density ρ_c is determined by the choice of Δ.

For the simulations where the co- and counter-rotating components are radially separated at the radius R_c, we consider

$$\Omega = \begin{cases} (1 - 0.003)\Omega_K(R) & R_d < R < R_c \ , \\ -(1 - 0.003)\Omega_K(R) & R > R_c \ . \end{cases} \tag{5.40}$$

Computational Domain and Boundaries

Our simulation region has three boundaries: the axis, the surface of the star and the external boundaries. For each dynamical variable we impose a boundary condition consistent with our physical assumptions.

We assume axisymmetry about the axis. On the star and the external boundaries we want to allow fluxes and impose free boundary conditions $\partial \mathcal{F}/\partial n = 0$ where $\mathcal{F}$ is a dynamical variable and n is the vector normal to the boundary.

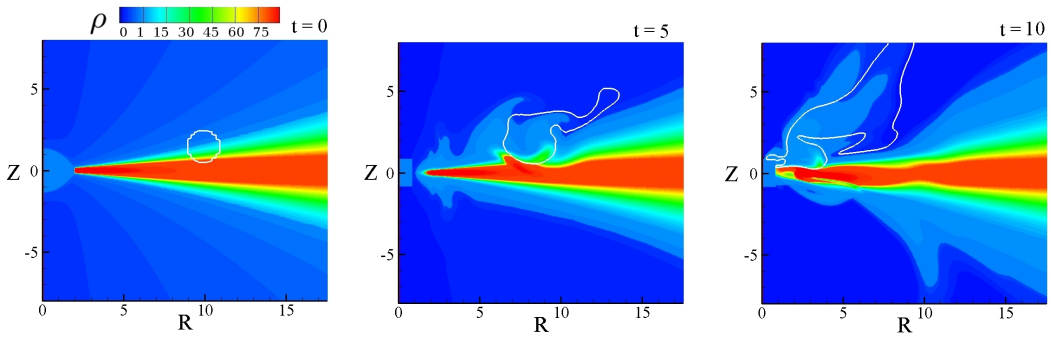

Figure 5.7: Density ρ (color) and angular velocity $\Omega = 0$ countours (white lines) for $t = 0,\ 5,\ 10$ for the torus problem. The initial counter rotating torus (left-hand panel) is observed to free-fall into the star (right-hand panel).

The hydrodynamic equations are written in dimensionless form so that the simulation results can be applied to different systems. The mass of the central star is taken as the reference unit of mass, $M_0 = M_?$. The reference length, r_0 , is taken to be the radius of the star. The initial in- ner radius of the disc is $R_d = 2r_0$. The reference value for the velocity is the Keplerian velocity at the radius r_0 , $v_0 = (GM_0/r_0)^{1/2}$. The reference time-scale is the period of rotation at r_0 , $P_0 = 2\pi r_0/v_0$.

At the external boundary along the edge of the disc $-5 < Z < 5$, we allow new matter to flow into the simulation region. We impose the condition that the matter must be accreting $v_R < 0$. In the coronal region, we prescribe outflow conditions and allow matter and entropy to exit the simulation region.

In addition to the boundary conditions imposed for the well-posedness of our problem we impose additional conditions on variables at the boundaries to eliminate numerical artifacts the simulations.

Our simulation uses a grid $N_R \times N_Z = 150 \times 250$ cells. The star has a radius

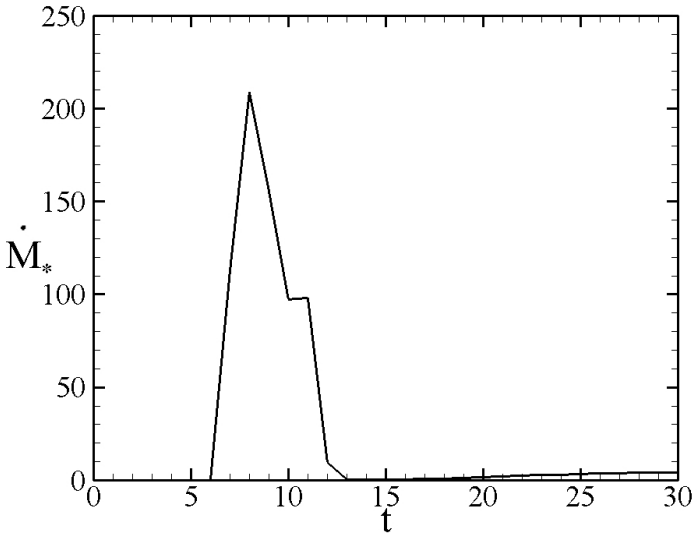

Figure 5.8: Mass accretion rate to the star $\dot{M}_*$ as a function of time for a counter-rotating torus of matter initially located at $R_0 = 10$. After the burst of accretion, accretion to the star continues at a small rate due to the disc's viscosity.

of 1 in units of the simulation and is cylindrical in shape. It extends 10 grid cells above and below the equatorial plane. In the R-direction, the first 60 grid cells have length $dR = 0.05$. Later cell lengths are given recursively by $dR_{i+1} = 1.025 dR_i$. Similarly, in the Z-direction the first 30 grid cells above and below the equatorial plane have length $dZ = 0.05$. Later cell lengths are given recursively by $dZ_{j+1} = 1.025 dZ_j$. We show a sparse version of our grid, showing every 5th grid in Fig. 5.6.

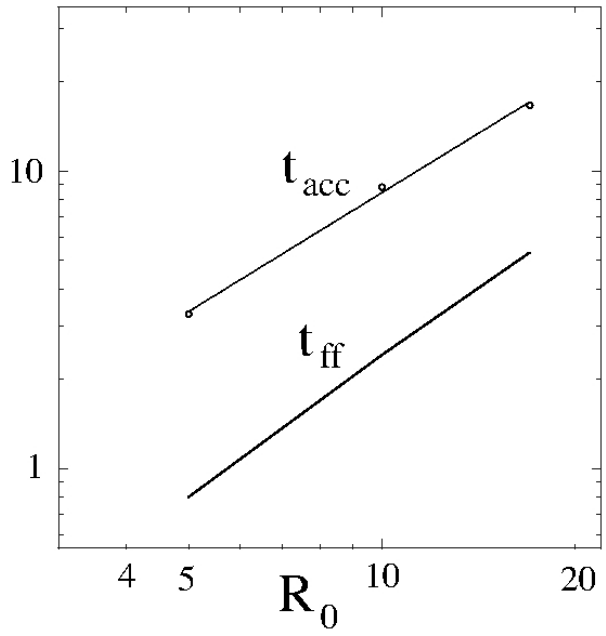

Figure 5.9: Accretion time t_{acc} (arbitrary scale) for torus of counter-rotating matter as a function of its initial radius $R_0 = 5, 10, 17$ and free fall times from R_0, $t_{ff} = [2R_0^3/(9GM)]^{1/2}$.

5.2.1 Results

Vertically Offset Torus

Here, we consider an equilibrium consisting of a co-rotating disc with a counter-rotating torus of a small amount of mass with major axis R_0 and minor axis $r \ll R_0$ located at (R_0, Z_0). The mass of the torus is 1% of the disc's total mass. This is for the purpose of modeling the accretion of a counter-rotating cloud onto the surface of a preexisting co-rotating disc. Figure 5.7 shows the infall of the torus at several times. The torus falls inward over the top surface of the disc towards the star. Even though the torus has a very small mass fraction it induces axisymmetric warping of the disc. When it reaches the star it gives a

large spike in the stellar accretion rate $\dot{M}_*$ as shown in Figure 5.8.

The infall time of the torus from R_0 to the star, $t_{\rm acc}(R_0)$, can be compared to the time of free-fall $t_{\rm ff} \approx [2R_0^3/(9GM_*)]^{1/2}$ for $R_0 \gg R_*$ for a blob of non-rotating matter to free-fall to the star. Figure 5.9 shows the two time scales as a function of R_0. The accretion time-scale $t_{\rm acc}$ is about a factor of 3 longer than the free-fall time and it is $\propto R_0^{1.32}$. This makes sense because the free-fall time assumes that the torus is initially at rest, whereas in the simulations the torus is initially counter-rotating. The torus first loses it's angular momentum to the main disc on a viscous time scale which can be estimated as $t_\nu \sim t_{\rm ff}(Z/h)^2\alpha_\nu^{-1}$. This can account roughly for the factor of 3. Note that at the interface between the oppositely rotating components there can be a strong supersonic Kelvin-Helmholtz instability (Quach, Dyda, & Lovelace 2014) which locally increases the turbulent viscosity coefficient by a large factor.

Vertically Separated Components

Here, we consider cases where the co-rotating and counter-rotating components are vertically separated. This situation could arise from the infall of counter-rotating gas onto the surface of a preexisting co-rotating disc. That is, the disc matter at some distance above the midplane is counter-rotating with Keplerian velocity while the matter below this height is co-rotating. The fraction of the surface mass density which is counter-rotating is denoted by Δ. A conventional disc rotating in one direction has $\Delta = 0$ and a Shakura-Sunyaev accretion rate $\dot{M}_{SS}$ which is a function of the viscosity coefficient α_ν. For $\Delta > 0$ the mass accretion rate is normalized by the value for $\Delta = 0$. That is, $\dot{m} \equiv \dot{M}_*/\dot{M}_{SS}$ for the same α_ν values. A summary of results for these runs is shown in Table 5.1.

Δ	α_ν	$(\dot{M}_*)_p$	$(\dot{m})_p$	M_T	t_w	$\Delta Z(R)$					
						$t =$	5			15	
						$R =$	5	10	15	5	10	15
0.01	0.03	236	23,600	5,000	50.0		0.45	0.56	0.56	0.77	1.15	1.38
	0.1	144	758	2,030	38.6		0.85	1.06	1.36	1.56	2.18	2.11
	0.2	68.4	79.5	1,040	45.2		1.02	1.29	1.85	2.15	2.67	2.43
	0.3	26.1	13.4	460	39.3		1.12	1.46	1.69	2.30	3.06	2.46
0.02*	0.1	288	1,516	4,400	40.0		0.77	0.98	1.14	1.55	2.19	2.11
0.1	0.1	1,406	7,400	31,300	49.0		0.58	0.70	0.85	0.78	1.46	1.86
0.5	0.03	-	-	602,700	-		0.19	0.31	0.41	0.28	0.59	0.83
	0.1	-	-	260,000	-		0.37	0.60	0.75	0.50	1.17	1.65
	0.2	-	-	32,590	-		0.60	0.91	1.14	0.86	1.92	2.56
	0.3	-	-	15,560	-		0.84	1.19	1.47	1.24	2.66	3.42

Table 5.1: Summary of results for vertically separated components for different counter-rotating mass fractions Δ and viscosity coefficients α_ν. The asterisk indicates symmetric wedges above and below the midplane. We measure the peak mass accretion rate $(\dot{M}_*)_p$, peak mass accretion rate normalized to a Keplerian disc $(\dot{m})_p$, the total mass accreted while there is a counter-rotating component M_T and the time required for all counter-rotating matter to accrete t_w. For times $t = 5$ and $t = 15$ we measure the thickness of the shear layer $\Delta Z(R)$, at radii $R = 5, 10, 15$.

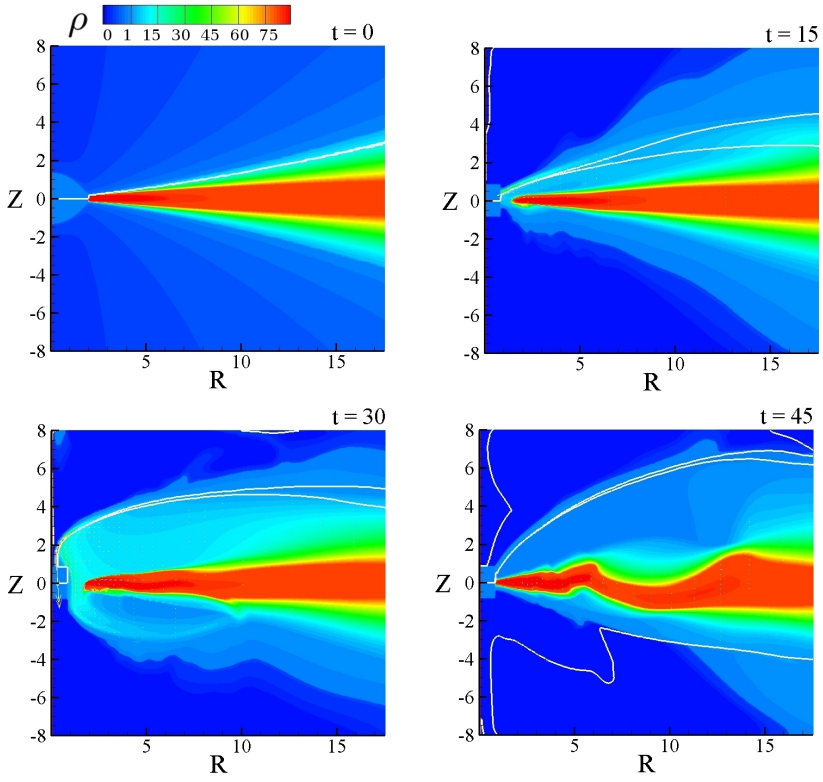

Figure 5.10: Density ρ (color) and angular velocity $\Omega = \pm 0.01$ countours (white lines) for $t = 0, 15, 30, 45$ for the case $\Delta = 0.01$ and $\alpha_\nu = 0.1$. The initial counter rotating layer in the upper half plane (top left-hand panel), the shear layer accretes to the star (top right-hand panel), moving upwards (bottom left-hand paneel) before all counter-rotating matter has lost its angular momentum to the main disc and oscillations are induced in the disc (bottom right-hand panel). Notice the large amplitude axisymmetric warping induced in the disc.

For $\Delta > 0$, a shear layer forms between the co- and counter-rotating components. Due to the viscosity, the angular momentum of the counter-rotating matter is lost to the co-rotating matter. In effect, the angular momenta of the two components is annihilated. The matter with zero angular momentum then accretes to the star with approximately free-fall speed. Figure 5.10 shows the behavior for $\Delta = 0.01$. After some time all counter-rotating matter has exchanged angular momentum with the main disc, and has accreted onto the star (left-hand

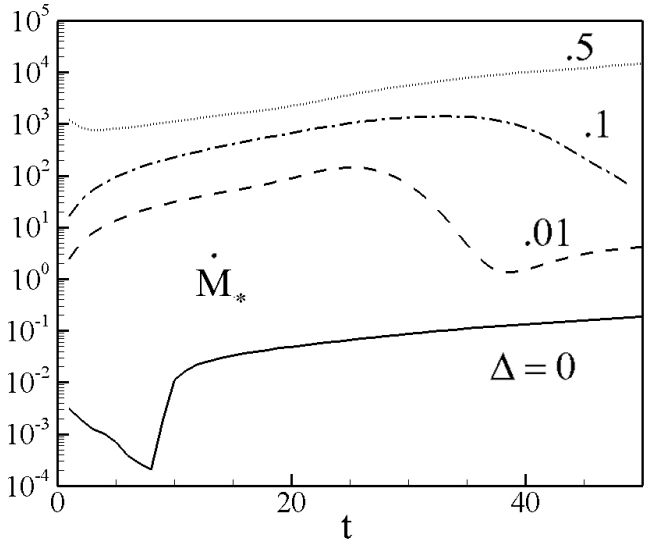

Figure 5.11: Mass accretion rate $\dot{M}$ as a function of time t for mass fractions $\Delta = 0,\ 0.01,\ 0.1,\ 0.5$ and viscosity coefficient $\alpha_\nu = 0.1$.

panel). This excites disc oscillations and the system continues to evolve (right-hand panel). Notice that this small mass fraction of counter-rotating matter excites large amplitude axisymmetric warping of the main disc. Large amplitude warping was found in the earlier axisymmetric simulations by Kuznetsov et al. (1999).

We measure the peak mass accretion rate to the star $(\dot{M}_*)_p$ and the peak mass accretion rate normalized to the rate for a standard accretion disc $(\dot{m})_p$. For $\Delta \leq 0.1$ we indicate the time t_w for which all the counter-rotating matter has accreted onto the star. Figure 5.11 shows the logarithm of the mass accretion rate to the star as a function of time for different Δ values. Figure 5.12 shows on a linear scale the mass accretion rate as a function of time for $\Delta = 0.01$.

For $\Delta \leq 0.1$, there is an initial period of rapid accretion during which angular momentum is exchanged between the counter-rotating layer and the main part

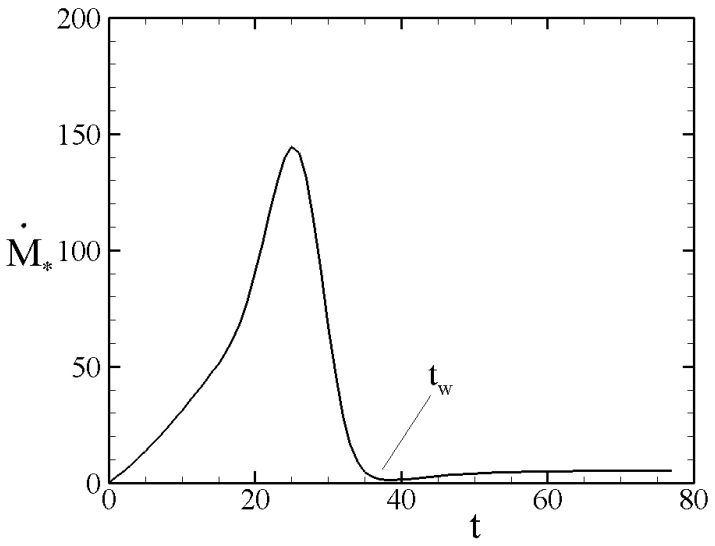

Figure 5.12: Mass accretion rate to the star $\dot{M}_*$ as a function of time for $\Delta = 0.01$ and $\alpha_v = 0.1$. Here, t_w indicates the time at which all counter-rotating matter has accreted onto the star.

of the disc. The mass accretion rate peaks at a rate $(\dot{M}_*)_p$ of $10^2 - 10^4$ times larger than the accretion rate of a conventional disc rotating in one direction. After the counter rotating matter is accreted, the accretion rate drops down to the value of conventional disc.

The duration of the period of enhanced accretion t_w does not depend significantly on the amount of counter-rotating matter. Also, it does not depend on the viscosity of the disc. This supports the conclusion that a layered counter-rotating system of initial radius R will be transient, existing only on the free-fall time scale $t_{\rm ff} \sim R^{3/2}/\sqrt{GM}$. This is consistent with our simulation results for a counter rotating torus.

As a consistency check that our results are not due to some asymmetry in our code, the $\Delta = 0.01$ run was repeated with counter rotating layers both above

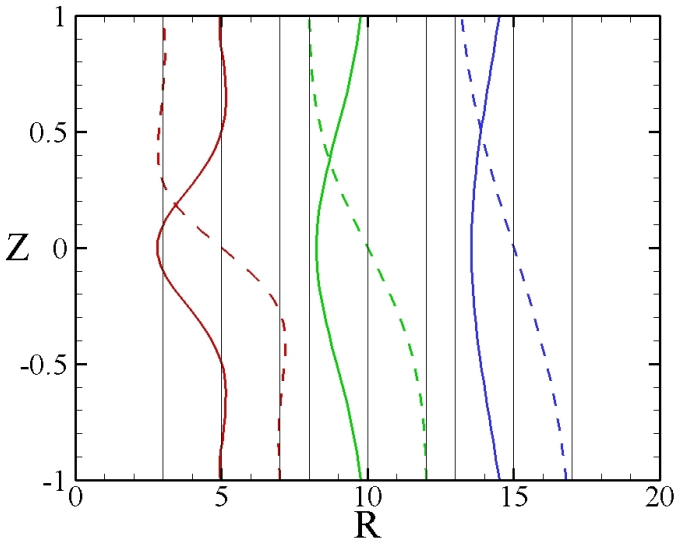

Figure 5.13: Radial and angular velocity profiles as a function of Z $v_r(R,Z)$ (solid curves) and $\Omega(R,Z)$ (dashed curves) at radii $R = 5$ (red), 10 (green) and 15 (blue) in units of the local Keplerian velocity and angular velocity (indicated by the vertical lines) for the case $\Delta = 0.5$, $\alpha_\nu = 0.1$ at $t = 15$. The velocity profiles are approximately Gaussian and peaked at $Z = 0$ where $\Omega = 0$.

and below the equatorial plane. This result is included above, indicated by an asterisk, and we see that inclusion of the second layer simply doubles the amount of matter accreting onto the star but does not change the accretion time. The reported shear layer thicknesses are the average of the upper and lower shear layers. We note that the layers thickness grows slightly more slowly, but by $t = 15$ has reached the same thickness as with the single layer case. This is likely due to the pressure from the opposite shear layer. This pressure is responsible in the single layer case for the rising of the shear layer. In this case, it acts to compress the opposite shear layer and slow it's growth.

The thickness of the shear layer is determined by the angular momentum transfer rate between the counter-rotating components and by the angular mo-

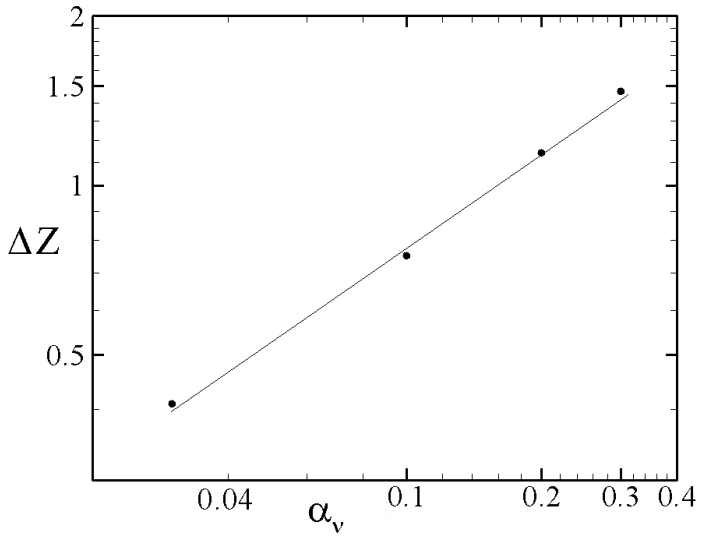

Figure 5.14: Full width at half-maximum of the radial velocity destribution $\Delta Z(R)$ as a function of viscosity α_ν for $R = 15$ and $t = 15$ for the case $\Delta = 0.5$. The fit for radii $R = 5, 10, 15$ and $t = 5, 15$ gives a power law dependence $\Delta Z \propto \alpha_\nu^{0.59\pm0.03}$, in general agreement with the self-similar solution $\Delta Z \propto \sqrt{\alpha_\nu}$ of Lovelace and Chou 1996).

mentum required for that matter to begin to free fall. For larger counter-rotating mass fractions, the growth rate of the layer thickness is smaller as more angular momentum is required to slow the layer down. Increasing the viscosity increases the rate of angular momentum transfer and hence the thickness of the layer. Note that the case $\Delta = 0.5$ can be compared with the analytic self-similar solution of Lovelace and Chou (1996) which predicts a shear layer thickness $\Delta Z \propto \sqrt{\alpha_\nu}$. Figure 5.13 shows the radial and angular velocity profiles as a function of Z at different radii at $t = 15$ for $\Delta = 0.5$. The shear layer thickness $\Delta Z(R)$ is taken to be the full width at half maximum of the radial velocity profiles. We find $\Delta Z \propto \alpha_\nu^{0.59\pm0.03}$ as shown in Figure 5.14. There is reasonable agreement between the theory and simulations even though the theoretical model is independent of time. A similar analysis for the $\Delta = 0.01$ case gives $\Delta Z \propto \alpha_\nu^{0.42\pm0.08}$.

This suggests that the steady state behaviour of the shear layer is largely insensitive to the mass fraction of the counter-rotating layer.

For $\Delta = 0.5$, Lovelace and Chou (1996) also predicted the ratio of mass accretion rates of the counter-rotating disc to the standard Shakura-Sunyaev rate and found $\dot{m} = \dot{M}_*/\dot{M}_{SS} \sim (R/h)^2\alpha_\nu^{-1/2}$. Our mass accretion rates for counter rotating discs are time dependent, so that we tried accretion rates at various times and found the results to be largely insensitive to the time chosen. Figure 5.15 shows the data and the power law fit which gives $\dot{m} \propto \alpha_\nu^{-1.33}$. This dependence is insensitive to whether we fit to the peak mass accretion rate or the time averaged accretion rate. The dependence on α_ν is much stronger than predicted by Lovelace and Chou (1996).

The viscous stress term $\tau_{ZR} \propto -\partial v_R/\partial Z$ in equation (3.8) is found to have an essential role in the counter rotating disc flows. Without this term the shear layer thickness in some cases is artificially thin and set by the grid resolution.

Radially Separated Components

Here, we consider an inner corotating Keplerian disc and an outer counter-rotating Keplerian disc relevant to the "Evil Eye" galaxy NGC 4826 (Braun et al. 1994; Rubin 1994b) although the galaxy's rotation curve is not Keplerian. The top left-hand panel of Figure 5.16 shows the initial disc which has a jump discontinuity in the rotation direction at $R_c = 10$. Although the disc is in mechanical equilibrium, a gap rapidly forms between the co- and counter-rotating components (top right-hand panel). Owing to the viscosity there is mixing of the two oppositely rotating components. The angular momenta of the compo-

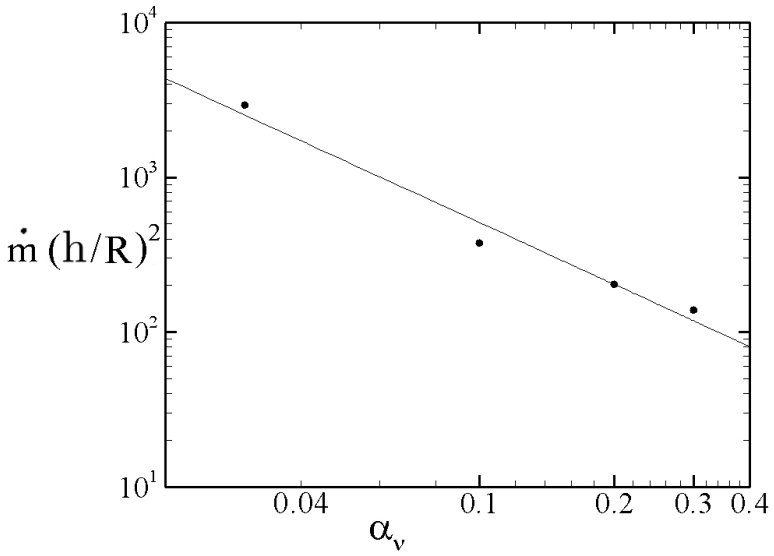

Figure 5.15: Mass accretion rate to the star as a function of the viscosity coefficient α_ν for $\Delta = 0.5$. The fit yields a power law dependence of $\dot{m} \propto (R/h)^2 \alpha_\nu^{-1.33\pm0.03}$, in disagreement with the self-similar solution $\dot{m} \propto (R/h)^2 \alpha_\nu^{-1/2}$ of Lovelace and Chou (1996).

nents of the mixed gas is annihilated so that the centrifugal force vanishes. This gas then falls inward towards the disc's center. As a result the outer radius of the inner co-rotating disc begins to oscillate as matter piles up on the inner edge of the gap (bottom left-hand panel). These oscillations damp and the gap begins to fill as matter from the counter-rotating disc moves inward due to the viscosity (bottom right-hand panel).

Figure 5.17 shows the oscillations of the outer radius of the inner disc $R_{\rm in}(t)$ for different values of R_c. The angular frequency of the oscillations ω_R can be compared with the radial epicyclic frequency (which for a Keplerian disc is the same as Ω_K) evaluated at average value of $R_{\rm in}(t)$, $\overline{\kappa}$. For $R_c = 5, 10, 15$, we find $\omega_R/\overline{\kappa} = 1.37, 1.56.$ and 1.91, respectively.

In addition to the oscillations of $R_{\rm in}$, the inner and outer edges of the gap

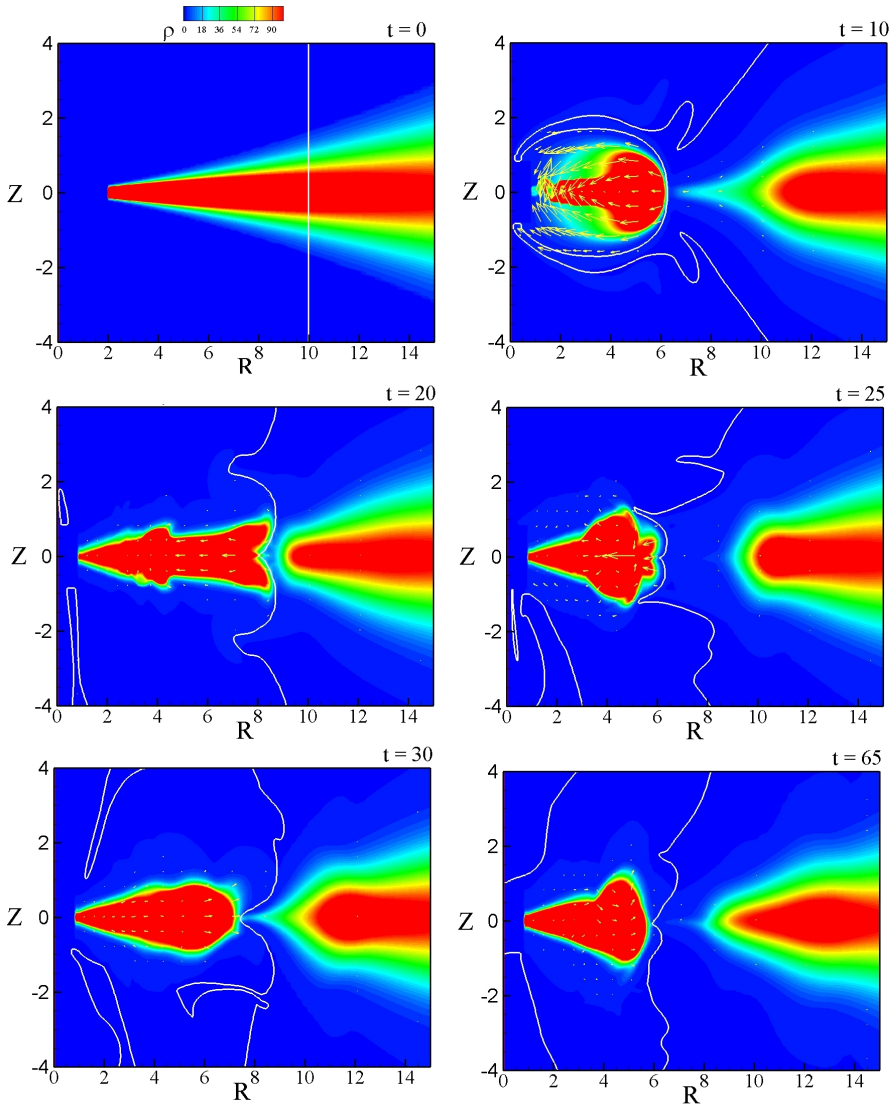

Figure 5.16: Plot of density ρ (color) and angular velocity $\Omega = 0$ countour (white line) for $t = 0, 10, 20, 25, 30, 65$. The initial radius of the boundary between the co- and counter-rotating components $R_c = 10$. A gap rapidly opens in the disc layer due to the mixing of the two components. This in turn excites a radial, axisymmetric breathing mode. Subsequently, the inner disc oscillates quasi-periodically.

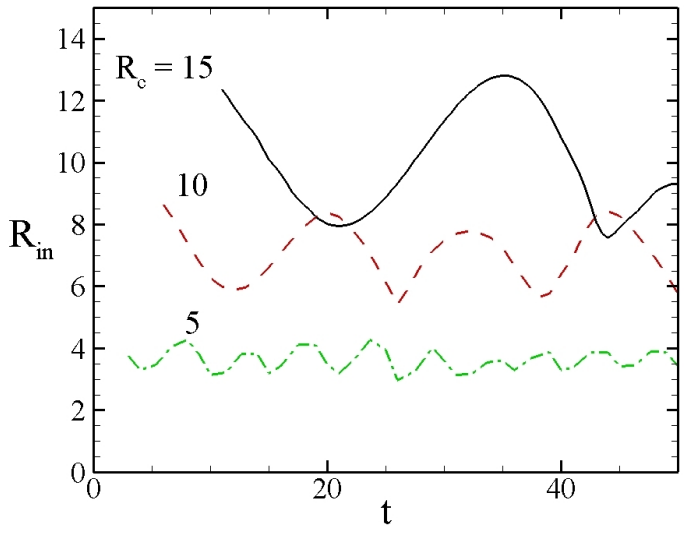

Figure 5.17: Outer radius of the inner disc as a function of time for initial counter-rotating boundary at $R_c = 5, 10, 15$. The frequency of the oscillations is approximately the radial epicyclic frequency at the average value of $R_{\rm in}$.

slowly move inward due to viscosity. Figure 5.18 shows this inward motion for different values of the viscosity coefficient α_ν. The inward motion is enhanced at larger viscosities, but the frequency of the radial oscillations does not change significantly.

We find that the average mass accretion rates to the star are ~ 25 times larger than that of a conventional disc rotating in one direction with the same viscosity. This can be understood qualitatively as follows. The contact of the oppositely rotating components leads to the annihilation of the angular momenta of the mixed gas. This non-rotating gas then tends to free-fall towards the star by moving over the surface of the inner disc. As it moves inward it excites the radial oscillation of the inner disc shown in Figures 5.17 and 5.18. The increased accretion rate is largely independent of the initial position of the counter-rotating

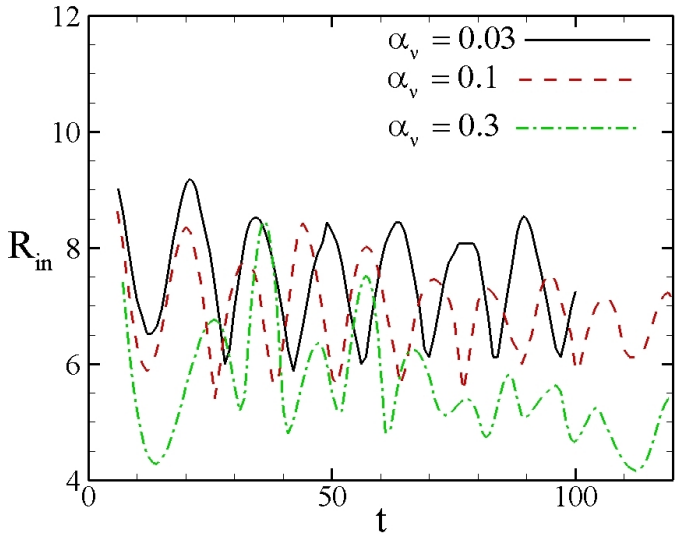

Figure 5.18: Outer radius of the inner disc as a function of time for initial counter-rotating boundary at $R_c = 10$ and viscosity coefficients $\alpha_\nu = 0.03, 0.1, 0.3$. The frequency is only weakly dependent on the disc viscosity. Increasing disc viscosity causes the minima of the oscillations to decrease more rapidly. The amplitude of the oscillations also decreases.

boundary. Moving the boundary from $R_c = 10$ to $R_c = 15$ increases the mass accretion rate by a factor of 1.3.

5.2.2 Conclusion

Observations of galaxies and models of accreting systems point to the occurrence of counter-rotating discs. Such discs may arise from the accretion of a counter-rotating gas onto the surface of an existing co-rotating disc or from the addition of counter-rotating gas at the outer radius of the existing disc. Axisymmetric 2.5D hydrodynamic simulations have been used to study two main cases – one where the oppositely rotating components are vertically separated

and the other where they are radially separated. The simulations incorporate an isotropic $\alpha-$viscosity including all of the terms in the viscous stress tensor including the important term τ_{RZ}. Near the interface, the two components mix and their angular momenta annihilate. This mixed gas has no centrifugal support and consequently tends to free-fall toward the star.

For vertically separated components we investigated a range of mass fractions Δ in the counter-rotating component. The simulations indicate that the counter-rotating matter extending out to a radius R accretes to the star on a time-scale about three times the free-fall time from this radius independent of Δ. The factor of three is likely due to the time required for the mixing of the two components. The accretion rate to the star can be enhanced by factors 10^2 to 10^4 over the rate for a disc rotating in one direction with the same viscosity. Such a burst of accretion could lead to a comparably enhanced burst of a magnetically driven jet (e.g., Lii et al. 2012). Future investigation of counter-rotating systems including a large scale magnetic field may confirm this.

The presence of a counter rotating layer is observed to excite a large amplitude axisymmetric warp in the disc similar to the warping observed in the earlier study by Kuznetsov et al. (1999). For the case where the two components have the same mass the simulation results are compared with the analytic self-similar solution of Lovelace and Chou (1996). The dependence of the shear layer thickness on the viscosity agrees approximately with this theory but not with predicted mass accretion rate dependence on viscosity.

For the case of radially separated components we observed a more modest increase by a factor ~ 25 in the accretion rate over that of a conventional disc. The mixed gas at the interface tends to fall inward and this is observed to excite

radial oscillations of the inner disc with a frequency of the order of the radial epicyclic frequency.

Important future work will be full 3D hydrodynamic simulations including the heating and cooling of the gas of counter-rotating discs. This will account for the supersonic Kelvin-Helmholtz instability, which is a 3D instability, as well as the strong shocks which it induces (see Quach et al. 2014). The time-scale of mixing of the two components and their loss of angular momentum is expected to be shortened compared with the present results.

CHAPTER 6

ASYMMETRIC JETS AND WINDS

Astrophysical jets are observed from many disc accreting objects ranging from Young Stellar Objects (YSOs) to systems with white dwarfs, neutron stars and black holes (BHs) (e.g., Livio 1997). The jets transport angular momentum away from the disc and thereby facilitate accretion to the central object. A large-scale magnetic field threading the disc is thought to have a key role in launching and collimating the jets (e.g., Lovelace et al. 2014).

There is clear evidence mainly from *Hubble Space Telescope* (HST) observations that YSOs often show an asymmetry between the jet and the counter jet. In HH30 the jet has more structure than the counter jet in the form of knots, suggesting different mass densities or different acceleration mechanisms (Mundt et al. 1990; Ray et al. 1996). The mass flux of the jet is approximately constant along its entire length whereas the counterjet's mass flux varies by a factor of 2 along its length (Bacciotti et al. 1999). RW Aur A exhibits a jet with velocity approximately twice that of its counter jet and a mass flux 2 – 3 times as large (Woitas et al. 2002, Hartigan & Hillenbrand 2009, Melnikov et al. 2009). Likewise LkHα 233 exhibits a jet with a knotted structure, whereas its counter jet has no knots but has similar velocity (Perrin & Graham 2007). FS Tau B has been observed to have a jet with a higher velocity but a lower density than its counter jet (Liu et al. 2012). Rotation measurements of T Tauri jets find evidence of jets counter-rotating with respect to the accretion disc or of the opposite rotation of jets in the northern and southern hemispheres (Sauty et al. 2012). Studies have shown that the jet/counter jet structure are different, with radial velocity differences of $\sim 10 - 25$ km/s (Coffey et al. 2004; Ray et al. 2007 for a review). One of

the few exceptions is HH 212 which exhibits nearly symmetric jet/counterjet (Zinnecker 1998). Ellerbroek et al. (2013) found HH 1042 to have jets with similar mean velocities but the knotted structure and velocity spread suggests an asymmetric launching mechanism. Whelan et al. (2014) have studied the jet/counter jets mass outflow rates and stellar accretion rates in ESO-Hα Par-Lup 3-4 to constrain lauching mechanisms. Though most observations show some sort of asymmetry in the outflows, this may be a result of asymmetries in the ambient medium and not the launching mechanism (Carratti o Garatti 2013, White 2014).

Relatively little theoretical and computational work has been directed at understanding the asymmetry of the YSO jets. A theoretical study by Wang et al. (1992) considered disc magnetic fields composed of dipole and quadrupole components and found that the magnetically driven jets could in some cases be highly asymmetric. Chagelishvili et al. (1996) investigated how a quadrupolar disc dynamo interacting with a stellar dipole could give rise to one sided jets. Lovelace et al. (2010) carried out axisymmetric MHD simulations of disc accretion to stars with magnetic field consisting of different combinations of aligned dipole and quadrupole field components and without the assumption of symmetry about the equatorial plane. The simulations showed that for conditions where there is a significant quadrupole component in addition to the dipole component, a dominantly one-sided conical wind tends to form on the side of the equatorial plane with the larger value of the intrinsic axial magnetic field. For cases where the quadrupole component is absent or very small, dominantly one-sided outflows also form, but the direction of the flow flip-flops between upward and downward on a time-scale of $\sim$ 30 d for a protostar. von Rekowski (2003) and von Rekowski & Brandenburg (2006) investigated outflows gener-

ated by time dependent stellar and disc dynamos. Matsakos et al. (2012) investigated how field alignment between the disc and star and pressure distribution in the ambient cloud caused velocity asymmetries in protostellar jets. Fendt and Sheikhnezami (2013) investigated how thermal and density asymmetries in the disc can lead to asymmetries in the outflow. Velazquez (2014) performed 3D hydrodynamical simulations to study the case of asymmetric jet launching from protoplanetary discs that are preferentially fed matter from one side of the disc by a binary companion. Stute et al. (2014) showed that relaxing axisymmetry has little effect on MHD driven winds.

Classical T Tauri stars (CTTS) commonly show evidence of a stellar dipole and higher order multipoles with field strengths $\sim 1-2$ kG at the stellar surface (Jardine, Collier Cameron & Donati 2002; Donati et al. 2007, 2008). Furthermore, it is known from MHD simulations that any large-scale magnetic field threading the star's accretion disc tends to be advected inward due partly to viscous transport in the disc and partly due to angular momentum loss to outflows (e.g., Dyda et al. 2012). A large-scale magnetic field is thought to be responsible for driving and collimating the jets from young stellar objects. The origin of the required magnetic fields is not established, though a strong possibility is that dynamo processes in the rotating, convective stars. For example, the Zeeman signature in GQ Lup (Donati et al. 2012) and DN Tau (Donati et al. 2013) suggests that the magnetic fields of T Tauri stars are generated by non-stationary dynamos. Observations of disc-accreting stars show strong correlation between the magnitude of the star's dipole magnetic field and the rotation period of the star (Vidotto et al, 2014). It is commonly thought that the observed magnetic fields of young stars arise from dynamo processes inside the rotating convective stars. However, it is possible that dynamo processes operate in both the

accretion disc and in the star as considered by von Rekowski and Brandenburg (2006). One then has the possibility that the magnetic field generated in the disc is accreted onto the star and thereby modifies the stellar field changing the star's dipole, quadrupole, and octupole moments for example (Dyda et al. 2015). Time dependent dynamo processes could also be responsible for driving periodic or quasi-periodic outflows (Stepanovs, Fendt & Sheikhnezami 2014). It is therefore important to understand the interaction of the dipole field of a rotating star with the disc field. In particular, we are interested in how the symmetry of the stellar plus disc field configuration affects the symmetry or asymmetry of the outflow or jets.

We consider four classes of magnetic field configurations - a pure disc field (DISC), a pure stellar dipole field (DIP), a disc field with anti-aligned stellar dipole field (ADIP) and a disc field with parallel aligned stellar dipole field (PDIP).

In DISC runs we consider an initial reference *disc-field* the same as that studied by Zanni et al. (2007) in axisymmetric FLASH code simulations which assumed symmetry about the disc plane. These simulations exhibited a stable, symmetric inner disc wind. Later work by Fendt and Sheikhnezami (2013) considered the same disc field but without assuming symmetry about the equatorial plane. They found that this field gave rise to symmetric outflows, but that asymmetric outflows occurred if the disc density and temperature were asymmetric about the equatorial plane.

In addition to the mentioned disc-field, we consider accretion onto magnetized rotating stars with an aligned dipole magnetic field with magnetic moment μ. Previous work by Lovelace et al. (2010) found that a pure dipole in the

"propeller regime" exhibits asymmetric outflows. In the propeller regime, the radius of the star's magnetosphere $R_{\rm m}$ (where the pressure of the disc matter is of the order of the magnetic energy density of the star's dipole field) is larger than the corotation radius $R_{\rm cr} = (GM/\Omega_*^2)^{1/3}$ (where the rotation rate of the star equals the Keplerian rotation rate of the disc) (Illarionov & Sunyaev 1975). In the propeller regime a large fraction of the accreting disc matter may be expelled from the system (Lovelace, Romanova & Bisnovatyi-Kogan 1999; Romanova et al. 2004, 2005; Ustyugova et al. 2006; Lii et al. 2014). A qualitative picture of the accretion is that matter accumulates at the magnetospheric boundary and compresses the magnetosphere inward until $R_m < R_{cr}$ and funnel flow accretion occurs. The funnel flow spontaneously breaks the system symmetry about the equatorial plane and strong outflows are generated in the opposite hemisphere (Lii et al. 2014). As the matter reservoir at the magnetospheric boundary is depleted, the magnetosphere expands outwards and the system can "forget" which side had a funnel flow. This process repeats on time scales of roughly 40 days for CTTS, with the side determining the funnel flow being randomly determined, leading to episodic, asymmetric outflows (Lii et al. 2014). The DIP simulations are used to compare our simulations with stellar dipoles to these previous works.

Moreover, we consider the two cases where the stellar dipole field at the magneotspheric radius is parallel (PDIP) or anti-parallel (ADIP) to the disc-field. This offers two types of behaviors which can break the symmetry about the equatorial plane. In the anti-parallel case (ADIP), the stellar dipole field may reconnect with the disc field as it is advected inward. Analogous reconnection occurs between the solar wind magnetic field and the magnetic field of the earth when the two fields are anti-parallel (e.g., Hargreaves 1992). This reconnection

occurs at the magnetopause (inside the Earth's bow shock) where the subsonic solar wind runs into the Earth's magnetosphere. In the parallel case (PDIP), the disc field causes additional pressure at the magnetospheric boundary, reducing the magnetospheric radius and altering the field line geometry outside the magnetosphere.

In Sec. 6.1 we discuss the numerical methods used and the simulation parameters. Section 6.2 discusses the four main cases simulated. Section 6.2.1 describes results for the pure disc-field (DISC) for different disc densities or plasma β values. Section 6.2.2 describes results for a pure stellar dipole field (DIP), a disc-field and a parallel stellar dipole (PDIP) and a disc-field and an anti-parallel stellar dipole (ADIP). Section 6.3 gives the main conclusions from this work and its implications for observations.

6.1 Numerical Methods

6.1.1 Dimensional Variables

The MHD equations are written in dimensionless form so that the simulation results can be applied to different types of stars. We assume that the central object is a CTTS with mass $M_* = 0.8M_\odot$, a radius $R_* = 2R_\odot$ and a magnetic field magnitude $B_* = 3\times10^3$ G which is typical for the magnitude of the stellar dipole. We define dimensionful quantities with a 0 subscript, to denote typical values of physical parameters at a reference radius R_0. The mass scale is set by the stellar mass so $M_0 = M_*$. The reference length, $R_0 = 0.1$AU, is taken to be the scale of a typical inner disc radius. Assuming a stellar dipole field, the magnetic field strength $B_0 = B_*/\mu(R_*/R_0)^3$. The mass, length and magnetic field scales allow us

Parameters	Symbol	Value
mass	M_0	1.59×10^{33} g
length	R_0	1.50×10^{12}cm
magnetic field	B_0	8.04×10^{-2} G
time	P_0	3.53×10^{-2} y
velocity	v_0	8.42×10^{7}cm/s
density	ρ_0	7.24×10^{-15} g/cm^3
accretion rate	$\dot{M}_0$	2.72×10^{-7} $M_\odot$/yr
temperature	T_0	4.26×10^{7} K
dipole strength	μ	2.69×10^{35} G cm^3

Table 6.1: Mass, length, and magnetic field scales of interest and the corresponding scales of other derived quantities for a CTTS. One can obtain the physical values from the simulation values by multiplying by the corresponding dimensional quantity above.

to define all other dimensionful quantities.

The reference value for the velocity is the Keplerian velocity at the radius R_0, $v_0 = (GM_0/R_0)^{1/2}$. The reference time-scale is the period of rotation at R_0, $P_0 = 2\pi R_0/v_0$. From the MHD equations, we get the relation $\rho_0 v_0^2 = B_0^2/4\pi$, where ρ_0 is a reference density. This allows us to define the reference density ρ_0 of the disc. The reference mass accretion rate is $\dot{M}_0 = 4\pi\rho_0 v_0 R_0^2$. The reference temperature $T_0 = v_0^2/2 \times m_H/k_B$ where m_H is the atomic mass of hydrogen and k_B is the Boltzmann constant is obtained by taking the ratio of the reference pressure and reference density. One can obtain dimensionful quantities from simulation results by multiplying by the appropriate dimensionful quantity in Table 6.1

Results obtained in dimensionless form can be applied to objects with widely different sizes and masses. However, the present work focuses on CTTS with the typical values shown in Table 6.1. A more detailed description of our code and numerical methods can be found in Koldoba et al. (2015).

6.1.2 Initial Conditions

Magnetic Field

The initial magnetic fields are taken to be linear combinations of the disc-field (Zanni et al. 2007) defined by the flux function

$$\Psi_d = \frac{4}{3} B_0 R_0^2 \left(\frac{R}{R_0}\right)^{3/4} \frac{m^{5/4}}{\left(m^2 + Z^2/R^2\right)^{5/8}} \,, \tag{6.1}$$

and a fixed dipole field centered in the star which has the flux function

$$\Psi_D = \frac{\mu R^2}{\left(R^2 + Z^2\right)^{3/2}} \,, \tag{6.2}$$

where μ = const is the star's dipole moment. Our base case is taken to be $\mu = 30$, but we also consider cases with $\mu = 10, 20$. The dimensionless parameter m in Eqn. 8 determines the bending of the disc-field lines in the poloidal plane with the limit $m \to \infty$ corresponding to purely vertical field lines. We assume $m = 1$. The poloidal magnetic field components are given by

$$B_Z = \frac{1}{R}\frac{\partial \Psi}{\partial R}, \qquad\qquad B_R = -\frac{1}{R}\frac{\partial \Psi}{\partial Z} \,. \tag{6.3}$$

The relative strengths of the disc and dipole field components are characterized by the radius R_B where the stellar dipole and disc-field have equal values in the midplane of the disc at $t = 0$. We take $R_B = 2.8, 4.1, \& \ 5$. The magnetospheric radius R_m is determined by plotting the angular velocity of the matter in the equatorial plane as a function of R. The change from the constant stellar rotation to Keplerian occurs at R_m. As mentioned at the start of the chapter, the propeller regime occurs for $R_m > R_{\rm cr}$.

Our simulations cover a wide range of dipole and disc-field combinations. In particular, we consider a pure disc-field (DISC), a pure stellar dipole (DIP),

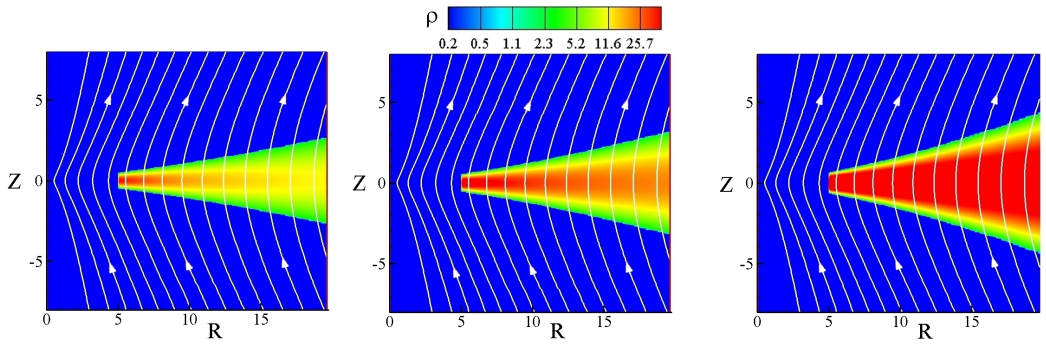

Figure 6.1: The initial density ρ and poloidal field lines for radially distributed disc-field in the cases of Bernoulli parameters *Left:* $\mathcal{B}_0 = 3 \times 10^{-4}$ *Center:* $\mathcal{B}_0 = 5 \times 10^{-4}$, and *Right:* $\mathcal{B}_0 = 1 \times 10^{-3}$. Increasing the Bernoulli parameter increases the midplane disc density and the disc scale height.

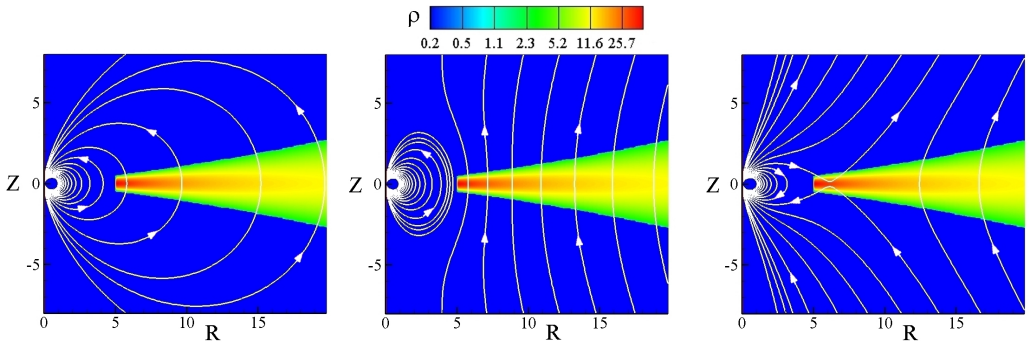

Figure 6.2: Plot of density ρ and poloidal field lines for a stellar dipole (left), a stellar dipole and parallel disc-field (center), and a stellar dipole and an anti-parallel disc-field.

a dipole and parallel disc-field (PDIP), and a dipole with an anti-parallel disc-field (ADIP). Figure 6.1 shows the initial disc density and poloidal field lines for the disc-field DISC. Figure 6.2 shows the same quantities for cases including an aligned stellar dipole magnetic field (DIP, PDIP & ADIP).

Matter Distribution

Initially, matter of the disc and corona are assumed to be in mechanical equilibrium (Romanova et al. 2002). The initial density distribution is taken to be barotropic with

$$\rho(p) = \begin{cases} p/T_{\rm disc}, & p > p_b \ \text{ and } \ R \geq R_d \ , \\ p/T_{\rm cor}, & p < p_b \ \text{ or } \ R \leq R_d \ , \end{cases} \tag{6.4}$$

where p_b is the level surface of pressure that separates the cold matter of the disc from the hot matter of the corona and R_d is the initial inner disc radius. The initial inner radius of the disc is $R_d = 5R_0$. At this surface the density has an initial step discontinuity from value $p/T_{\rm disc}$ to $p/T_{\rm cor}$. The initial dimensionless temperature in the disc is $T_{\rm disc} = (p/\rho)_{\rm disc} = 5 \times 10^{-4}$, and the initial temperature in the corona is $T_{\rm cor} = (p/\rho)_{\rm cor} = 0.5$.

Because the density distribution is barotropic, the initial angular velocity is a constant on coaxial cylindrical surfaces about the $z-$axis. Consequently, the pressure can be determined from the Bernoulli equation

$$F(p) + \Phi + \Phi_c = \mathcal{B}_0 \ , \tag{6.5}$$

where $\mathcal{B}_0$ is Bernoulli's constant,$\Phi = -GM/\sqrt{R^2 + Z^2}$ is the gravitational potential with $GM = 1$ in the code, $\Phi_c = \int_R^\infty r dr\, \Omega^2(r)$ is the centrifugal potential, and

$$F(p) = \begin{cases} T_{\rm disc} \ln(p/p_b) & p > p_b \ \text{ and } \ R \geq R_d \ , \\ T_{\rm cor} \ln(p/p_b) & p < p_b \ \text{ or } \ R \leq R_d \ . \end{cases} \tag{6.6}$$

Varying $\mathcal{B}_0$ allows one to vary the initial midplane disc density. We consider three values of the Bernoulli parameter $\mathcal{B}_0 = 3\times10^{-4}, 5\times10^{-4}$ and 10^{-3}, which we refer to as the diffuse, intermediate and dense disc cases respectively. The initial

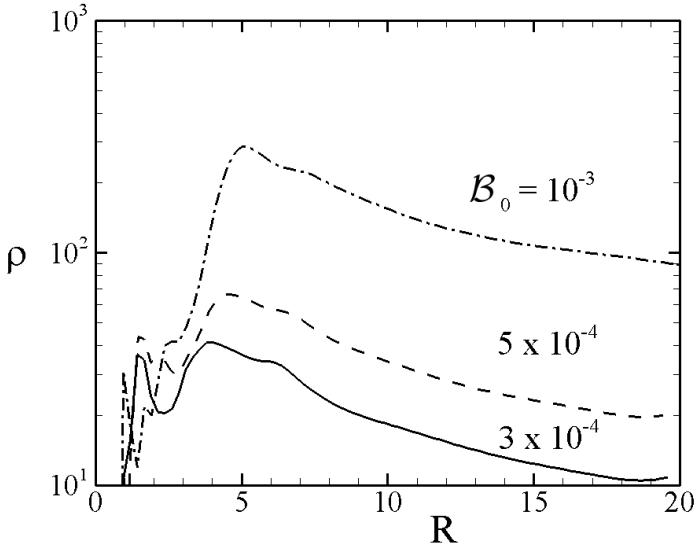

Figure 6.3: Initial midplane density profile $\rho(R, 0)$ as a function of radius for different values of the Bernoulli parameter $\mathcal{B}_0 = 3 \times 10^{-4}, 5 \times 10^{-4}$ and 10^{-3}.

half-thickness of the disc h is taken to be $h/R = 0.100$ at the inner disc radius $R_d = 5$.

Figure 6.3 shows the radial dependence of the midplane disc density for the different Bernoulli parameters. Figure 6.4 shows the initial radial dependence of the midplane $\beta = 8\pi p/B^2$ (the ratio of the gas pressure to the magnetic pressure) for the different Bernoulli parameters.

Angular Velocity

The initial angular velocity of the disc is slightly sub-Keplerian,

$$\Omega = (1 - 0.003)\Omega_K(R) \qquad R > R_d \,, \tag{6.7}$$

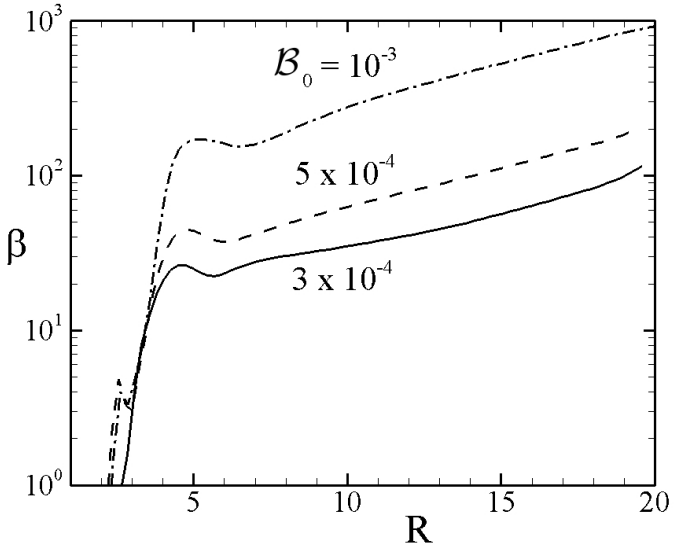

Figure 6.4: Initial radial dependences of the midplane $\beta = 8\pi p/B^2$ for the different Bernoulli parameters.

Inside of R_d, the matter rotates rigidly with angular velocity

$$\Omega = (1 - 0.003)\Omega_K(R_d) \qquad R \leq R_d. \tag{6.8}$$

The corotation radius $R_{\rm cr}$ is the radius where the angular velocity of the disc equals that of the star; that is, $R_{\rm cr} = (GM/\Omega_*^2)^{1/3}$. In this study we have chosen $R_{\rm cr} = 1.5$. For the considered stellar dipole fields and accretion rates, the systems are in the strong propeller regime where R_m is significantly larger than $R_{\rm cr}$.

6.1.3 Boundary Conditions

Our simulation region has three boundaries: the axis, the surface of the star and the external boundaries. For each dynamical variable we impose a boundary condition consistent with our physical assumptions.

We assume axisymmetry about the axis. On the star and the external bound-

aries we want to allow fluxes and impose free boundary conditions $\partial \mathcal{F}/\partial n = 0$ where $\mathcal{F}$ is a dynamical variable and n is the vector normal to the boundary.

At the external boundary along the edge of the disc we allow new matter to flow into the simulation region. We impose the condition that the matter must be accreting $v_r < 0$. In the coronal region, we prescribe outflow conditions and allow matter, entropy and magnetic flux to exit the simulation region.

The star is taken to be cylindrical in shape with radius $R_* = 1$ and height $Z_* = 2$. Free boundary conditions are imposed on the variables ρ, p and $\mathbf{B}$. The velocity vectors are required to align with the magnetic field lines on the star via $\mathbf{v} = (\mathbf{B} \cdot \mathbf{v})\mathbf{B}/|\mathbf{B}|^2$. In addition, we require that matter on the stellar boundary flow into the star. We treat the corner of the star by averaging over the nearest neighbour cells in the R and Z directions.

In addition to the boundary conditions imposed for the well-posedness of our problem we impose additional conditions on variables at the boundaries to eliminate numerical artifacts of the simulations.

Our simulation uses a grid of 154×225 cells. The star has a radius of 1 in units of the simulation and is cylindrical in shape. It extends 10 grid cells above and below the equatorial plane. In the R-direction, the first 30 grid cells have length $dR = 0.05$. Later cell lengths are given recursively by $dR_{i+1} = 1.025 dR_i$. Similarly, in the Z-direction the first 30 grid cells above and below the equatorial plane have length $dZ = 0.05$. Later cell lengths are given recursively by $dZ_{j+1} = 1.025 dZ_j$. Figure 6.5 shows a sparse version of our grid with only every 7th gridline in the $R-$direction and every 9th gridline in the $Z-$direction are shown.

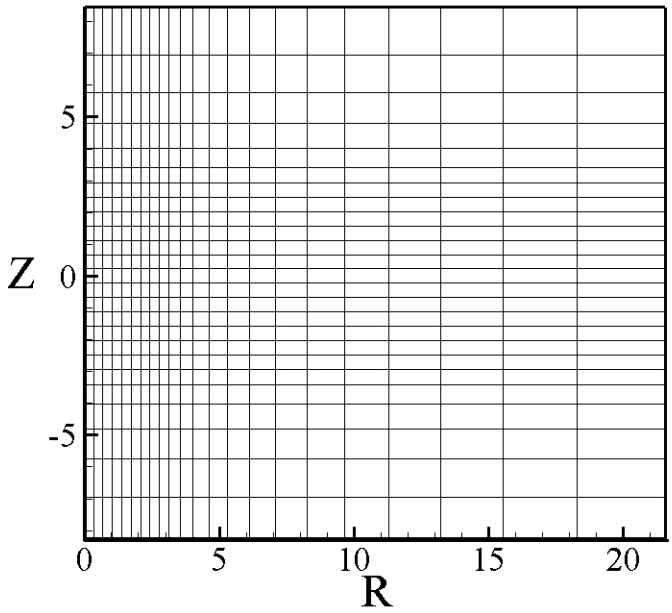

Figure 6.5: Sparse version of grid used in the simulations, showing every 7th gridline in the $R-$direction and every 9th gridline in the $Z-$direction.

6.2 Results

We are interested in the mass, angular momentum, and energy outflow from the disc. We have also calculated these fluxes at larger values of $|Z|$ and found this did not significantly change the values. We argue it is best to avoid the last few simulation region cells to avoid boundary effects while being as far away from the star as possible to allow the matter to be accelerated by the magnetic field. We note that mass fluxes are more symmetric when measured near the surface of the disc but this is observationally less interesting than the flux at large Z. In addition, for the mass flux we require that $v_z > 0.1$ which corresponds to an observationally interesting value of $\gtrsim$ 200km/s. A summary of our runs, their key parameters and results are found in Table 6.2.

Type	μ	B_0	$\mathcal{B}(10^{-4})$	Outflow Summary
	0	1	3	Long lasting, symmetric
DISC	0	1	5	Quasi-periodic
	0	1	10	Persistently asymmetric
	10	0	3	Strong disc/mag. wind
DIP	20	0	3	Strong disc/mag. wind
	30	0	3	Strong disc/mag. wind
	10	1	3	No magnetospheric wind
PDIP	20	1	3	Weak disc/strong mag. wind
	30	1	3	Weak disc/strong mag. wind
	10	-1	3	Suppressed
ADIP	20	-1	3	Suppressed
	30	-1	3	Suppressed

Table 6.2: Summary of key parameters in our runs and a qualitative summary of the outflows observed.

6.2.1 Pure Disc-Field DISC

In this series of runs we varied the Bernoulli parameter $\mathcal{B}_0$ which determines the initial matter configuration (Eqn. 6.5). We take $\mathcal{B}_0 = 3 \times 10^{-4}, 5 \times 10^{-4}$ and 10^{-3}. Increasing the Bernoulli parameter increases the midplane density, and therefore the total mass of the disc. The initial midplane density profiles are shown in Fig. 6.3. For simplicity, we refer to them as the diffuse or low-β ($\mathcal{B}_0 = 3\times10^{-4}$), intermediate ($\mathcal{B}_0 = 5 \times 10^{-4}$), and dense or high-$\beta$ ($\mathcal{B}_0 = 10^{-3}$) discs, respectively.

For the same disc-fields, the three disc configurations exhibit qualitatively different behaviors of their outflows. The diffuse low-β disc exhibits symmetric ($\pm Z$), long lasting outflows as observed by Fendt and Sheikhnezami (2013). The intermediate disc exhibits oscillatory behaviour, with the jet flip-flopping several times before settling at late time to steady symmetric outflows. The dense high-β disc exhibits outflows which are persistently asymmetric. This is the result of the excess accumulation of matter in one or the other of the two hemi-

spheres near the magnetosphere which then feeds more matter into one or the other outflows. Murphy, Ferreira and Zanni (2010) have shown that the important criteria for launching outflows is that $\beta \sim 1$ at the disc surface. Our results show that the character of these outflows is affected by the midplane β.

Diffuse Low-β Disc

Figure 6.6 shows the mass flux $\dot{M}$ through the upper hemisphere (solid red line) and lower hemisphere (dashed blue line) of the low β disc as a function of time. This configuration exhibits outflows with mass fluxes of order 0.1% of the stellar accretion rate. For ease in comparing the outflows, we plot the average mass flux asymmetry $\Delta\dot{M} = (\dot{M}_t - \dot{M}_b)/(\dot{M}_t + \dot{M}_b)$ as a function of time. We notice that $t < 400$ is characterized by sporadic asymmetries of order 10% of the outflow rate. For $t > 400$ the asymmetry is still roughly 10% but is persistently in the lower half plane. The upper contour plot shows the average velocity, weighted by mass, of outflows along the upper (red) and lower (blue) boundaries.

This serves as a calibration run in the respect that it reproduces the results of Fendt and Sheikhnezami (2013) which found persistent, symmetric outflows for $t < 500$ in our simulation units. Their outflow was measured near the surface of the disc, at a distance of $z = 3H$. We note that our outflows are more symmetric when measured at smaller heights, notably the small asymmetry near $t \sim 100$ vanishes. However, as we are ultimately interested in outflows which exceed the local escape velocity, we choose to measure outflows closer to the outer boundary to allow the outflows to be magnetically accelerated. We also note that both outflows are launched with comparable velocities.

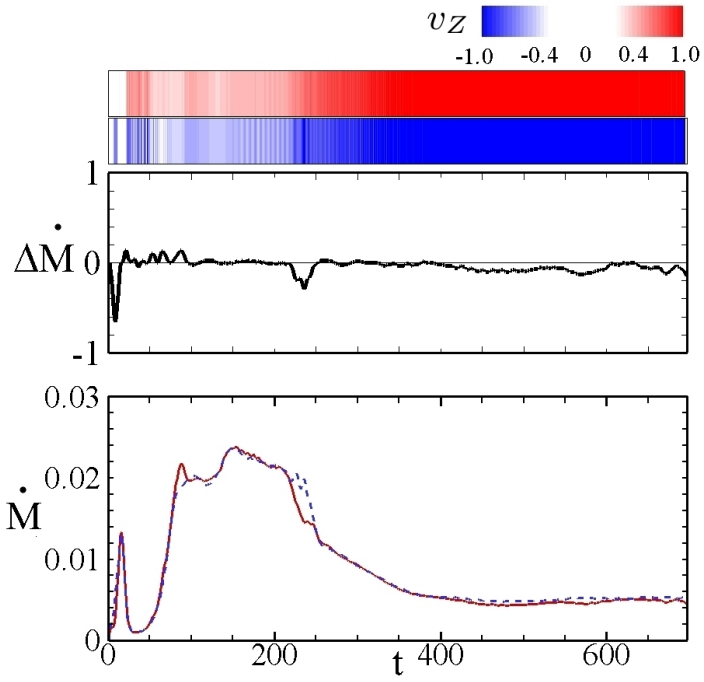

Figure 6.6: *Diffuse low–β disc:* The lower plot shows the mass flux $\dot{M}$ through the upper (solid red line) and lower (dashed blue line) boundaries. The middle plot shows the mass flux difference, normalized to average total mass flux $\Delta\dot{M} = (\dot{M}_t - \dot{M}_b)/(\dot{M}_t + \dot{M}_b)$ as a function of time. The upper plot shows the average velocity of outflows, weighted by mass along the upper (red) and lower (blue) boundaries. Both the mass flux and velocity of outflows is symmetric in this case.

Intermediate Disc

Figure 6.7 shows the mass flux $\dot{M}$ through the upper hemisphere (solid red line) and lower hemisphere (dashed blue line) as a function of time. After an initial period of symmetric outflows, we observe for times $100 < t < 400$ quasi-periodic, oscillating, outflows. For times $t > 400$ the outflows are again symmetric with asymmetries on the order of a few percent.

The oscillations in the outflows are caused by a periodic motion of the field lines. In one hemisphere the field lines become more vertical, reducing the out-

flow, whereas in the other they become more inclined relative to the $Z-$axis. This increases the outflow, as matter is more readilly launched along inclined field lines (e.g., Lii et al. 2012). As shown in Fig. 6.8 the structure then reverses, the more vertical field lines becoming more horizontal and vice versa. This leads to quasi-periodic oscillations in the mass outflows with a period $T \sim 80$ and an amplitude of roughly 50%. At the peak of the oscillation, there is therefore a factor of ~ 3 between the upper and lower mass flux. For a T Tauri star with our choice of reference units this corresponds to variations on a time scale of roughly 2.8 years. The oscillations are caused by Alfvén waves which propagate with a speed $v_A \sim \beta^{-1/2} c_s \sim \beta^{-1/2} h/R v_K$. The time-scale τ for passage of the wave across the disc a distance $\sim 2h$ is $\tau \sim 2\sqrt{\beta} R/v_K \sim \sqrt{\beta} R^{3/2}$. We find a midplane $\beta \approx 40$ and take $R \approx 3$, the radius from which strong outflows are launched and find $\tau \sim 60$, which agrees approximately with the observed period $T \sim 80$.

We note that though the peak mass flux through each hemisphere is comparable during this oscillatory phase, the velocity of the outflows is not. In particular, the bottom jets velocity $v_Z \approx -0.1$ during mass flux minima but rises to $v_Z \approx -0.8$ and -1.5 during its two peaks. The top jet on the otherhand has $v_Z \approx 0.2$ during outflow minima and peaks at $v_Z = 0.3$ and 0.4. A mass flux maxima of the bottom jet therefore could explain RW Aur A observations for instance, where the jet has a mass flux of 2-3 times the counter jet and a velocity roughly twice as great.

At late times, $t > 600$, a persistent asymmetry of the outflows is observed. This occurs because the original matter in the main part of the disc has been depleted and new matter is being added along the right boundary. This induces an asymmetry in the outer part of the disc which in turn induce disc oscilla-

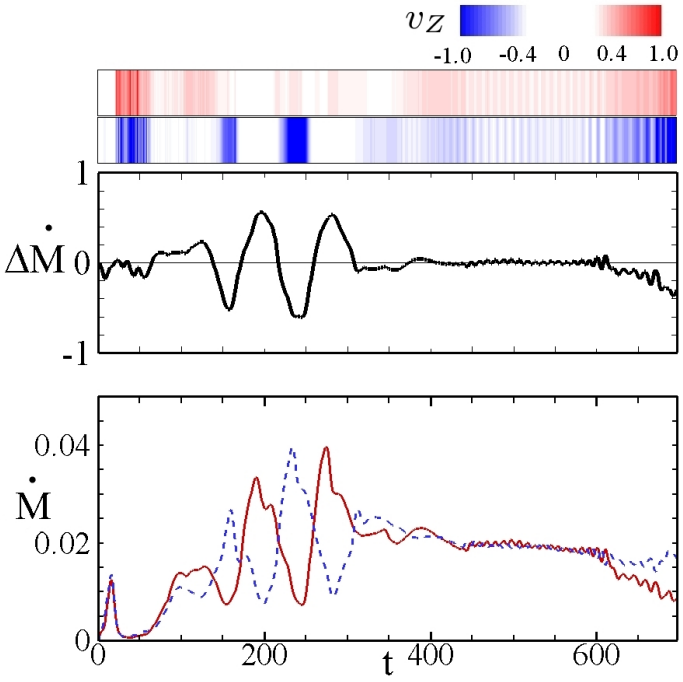

Figure 6.7: *Intermediate density disc:* The bottom panel shows the mass flux $\dot{M}$ through the upper (solid red line) and lower (dashed blue line) boundaries. The middle panel shows the mass flux difference, normalized to average total mass flux $\Delta\dot{M} = (\dot{M}_t - \dot{M}_b)/(\dot{M}_t + \dot{M}_b)$ as a function of time. The upper plot shows the average velocity of outflows, weighted by mass along the upper (red) and lower (blue) boundaries. Though the mass flux is symmetric during the oscillatory period $100 < t < 400$ the velocity of outflows is greater across the lower boundary.

tions that lead to a tilted disc. This asymmetry appears to be due to our outer boundary condition.

Dense High-β Disc

A more massive disc results in a higher density of matter close to the star. At late times the disc half thickness h/R is roughly 5 times greater than for the diffuse disc in the very inner disc $R \lesssim 5$. The matter available for outflows is hence greater but is also more strongly influenced by inner disc oscillations.

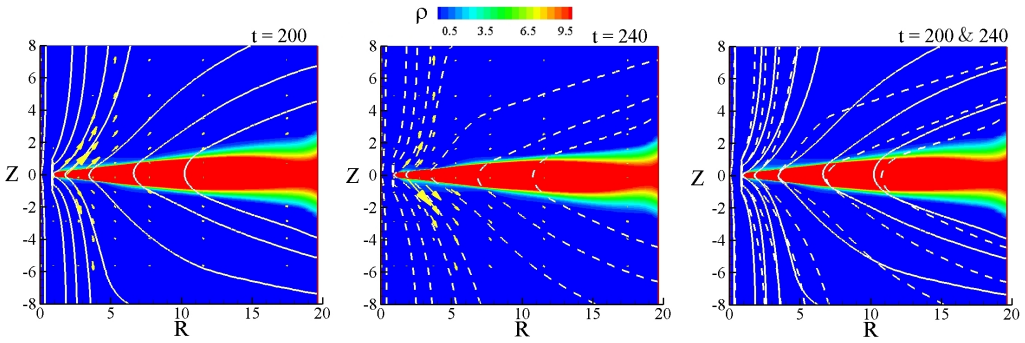

Figure 6.8: *Intermediate density disc:* Density ρ (color), poloidal field lines Ψ (white) and coronal mass flux $\rho \mathbf{v}_p$ (yellow). The left-hand panel is at $t = 200$, and the center panel is at $t = 240$. The right-hand panel shows a superposition of the field lines at these two times which corresponds to a maxima in the mass outflow in the upper and lower hemispheres, respectively. Note that the field line structure exchanges between the two hemispheres at the two times, with the more inclined field lines being associated with stronger outflows.

Radially propagating disc waves cause matter to preferentialy accumulate in the upper or lower hemisphere leading to stronger outflows. However, unlike in the dipole case where the magnetosphere re-expands after a strong outflow, reestablishing a symmetric disc, these asymmetries persist until strong vertical disc oscillations develop or the asymmetric matter reservoir is depleted.

As in the case of the intermediate disc, there are strong oscillations of the inner disc field. These lead to spontaneous one sided outflows as the field lines become more inclined to the $Z-$axis (Fig. 6.9). The outflows turn off as the field becomes more vertical. However, unlike in the intermediate disc case these oscillations are not coupled between the two hemispheres. The field lines in the top and bottom hemispheres oscillate and rearrange themselves largely independently of one another. For denser discs, poloidal field lines going through the disc are approximately frozen-into the disc which moves relatively slowly. Con-

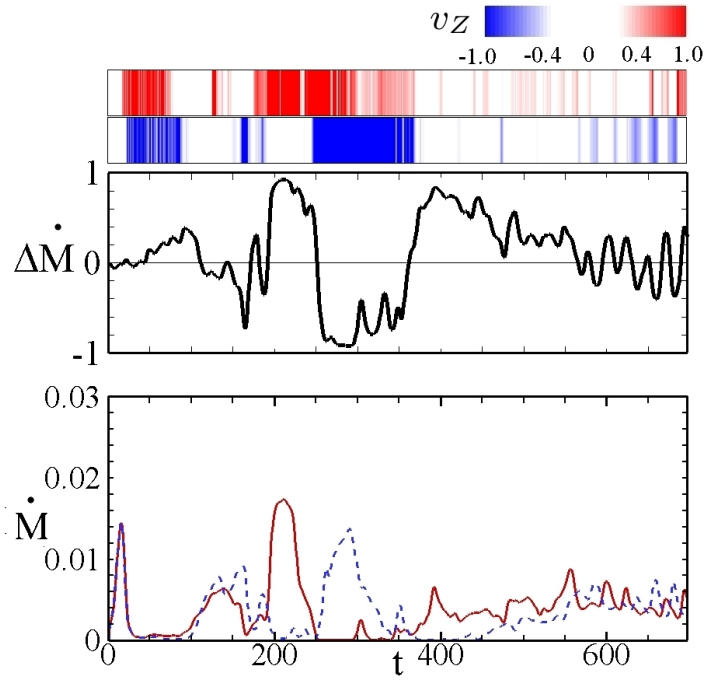

Figure 6.9: *Dense high-β disc:* The bottom panel shows the mass flux $\dot{M}$ through the upper (solid red line) and lower (dashed blue line) boundaries. The middle panel shows the mass flux difference, normalized to average total mass flux $\Delta\dot{M} = (\dot{M}_t - \dot{M}_b)/(\dot{M}_t + \dot{M}_b)$ as a function of time. The upper plot shows the average velocity of outflows, weighted by mass along the upper (red) and lower (blue) boundaries.

sequently, the field motion above and below the disc are uncoupled, allowing the field lines to have greater curvature around the midplane of the disc. This is consistent with an observation made by Tzeferacos et al (2009), where simulations with discs with larger plasma β supported field lines with greater curvature. These early time asymmetries last on time scales of order $T \sim 100 \sim 3.5y$. In constrast, at late times asymmetries last on order of $T \sim 10 \sim 0.35y$. This suggests that as the disc has a chance to reach a more stable configuration, timescales of asymmetries will decrease.

6.2.2 Stellar Dipole

A rotating star with a dipole field in the propeller regime exhibits quasi-episodic, one sided outflows (Lovelace et al. 2010). Matter builds up at the magnetospheric boundary, compressing the dipole until there is a symmetry breaking and the built up matter accretes to the star in a one-sided funnel flow. The funnel flow leads to a one-sided outflow in the opposite hemisphere, after which the matter pressure is decreased, the magnetosphere re-expands and the process can begin anew.

To minimize the asymmetries induced by disc oscillations, this set of simulations uses the parameters for a diffuse disc. However, the simulations with an intermediate disc showed no qualitative differences in the results. We consider the simple case of a stellar dipole aligned with the rotation axis of the star. In addition, there may be a disc-field. There are two possible configurations - one where the two fields are parallel and the other where they are anti-parallel.

In the anti-parallel configuration there is an X-type magnetic neutral line in the disc (see Figure 6.2). As the large scale disc-field advects inwards, it annihilates with the dipole, allowing matter to accrete onto the star in a continuous fashion, different from the episodic matter inflows of a pure dipole. Despite the additional energy available to launch outflows due to the increased stellar accretion rate, the field line geometry does not result in enhanced outflows.

In a parallel configuration, the large scale field compresses the dipole, reducing the magnetospheric radius. The key parameters for determining the strengths of magnetospheric outflows is the relative position of the magnetospheric radius R_m and the co-rotation radius $R_{\rm cr}$. When $R_{\rm cr} < R_m$ we are in the

propeller regime and have strong magnetospheric outflows. Keeping other parameters fixed, one can therefore imagine increasing the strength of the large disc-field and turning off the propeller. A second type of outflow is an inner disc wind, magneto-centrifugally launched from open field lines threading the disc. Though the disc wind is launched over the entire disc, mass flux is dominated by outflows from the inner part of the disc. Therefore, increasing R_m until it is at the radius of the inner disc wind significantly reduces this outflow, as the open field lines are pushed outwards.

For our base case we consider a stellar dipole with dimensionless magnetic moment $\mu = 30$. With an anti-parallel disc-field of the type considered in the previous section, this configuration initially has an X type neutral line at $R = 6$ (see Figure 6.2). The neutral line should be at a radius large enough so that the dipole is not fully compressed by the disc and its effect essentially negated. However, since most outflows from the disc-field are generated at small radii, the neutral line should not be too far out either.

In the parallel field configuration we consider dipoles with $\mu = 10,\ 20,\ 30$. These correspond to initial magnetospheric radii of $R_m = 2.8,\ 4.1,\ 5$ respectively. The co-rotation radius is $R_{\rm cr} = 1.5$ so that initially the system is in the strong propeller regime.

Pure Stellar Dipole Field DIP

This case is useful for comparison with Lovelace et al. (2010) and for future runs that include a large scale disc-field. Figure 6.10 shows that the outflows are quasi-episodic and dominantly asymmetric. Two types of outflows are ob-

served. In the first, mass accretes onto the star via a funnel flow onto either the top or the bottom of the star. At the same time, in the opposite hemisphere, the dipole loop expands and reconnects forming magnetic islands. These magnetic islands carry off matter. These were the types of outflows seen by Hayashi et al. (1996) for instance, but without the funnel flow, since their simulations were not bipolar. As in Hayashi we see a current sheet in the middle of the expanding loop. However, we do not see any significant heating of the gas as the loop expands. These outflows tend to have a greater velocity. In the second type of outflow, the disc pushes on the dipole, but has insufficient pressure to accrete onto the star. The magnetosphere re-expands, generating an episodic outflow (see Figure 6.11). Our results are in close agreement with Lovelace et al (2010) that found episodic outflows for stellar dipoles and Lii et al. (2014) who found episodic outflows for stellar dipoles in the strong propeller regime. Both types of outflows occur on time scales $T \sim 10 \sim 0.35y$ with a time scale $T \sim 50 \sim 17y$ between events.

Two qualitatively different types of outflows are observed: magnetospheric winds and disc winds. Figure 6.11 shows a time when both types of outflows occur simulaneously. The magnetospheric winds are launched perpendicular to the field lines of the stellar dipole. In contrast, the disc wind is launched along open field lines piercing the disc and extending off to infinity. Both outflows are inherently asymmetric, collimated by a toroidal magnetic field begining in the disc and extending into the corona. The disc wind is driven by field lines that are open in one hemisphere but closed and connected to the star in the other hemisphere. This corresponds to an outflow event that was not correlated to any stellar accretion.

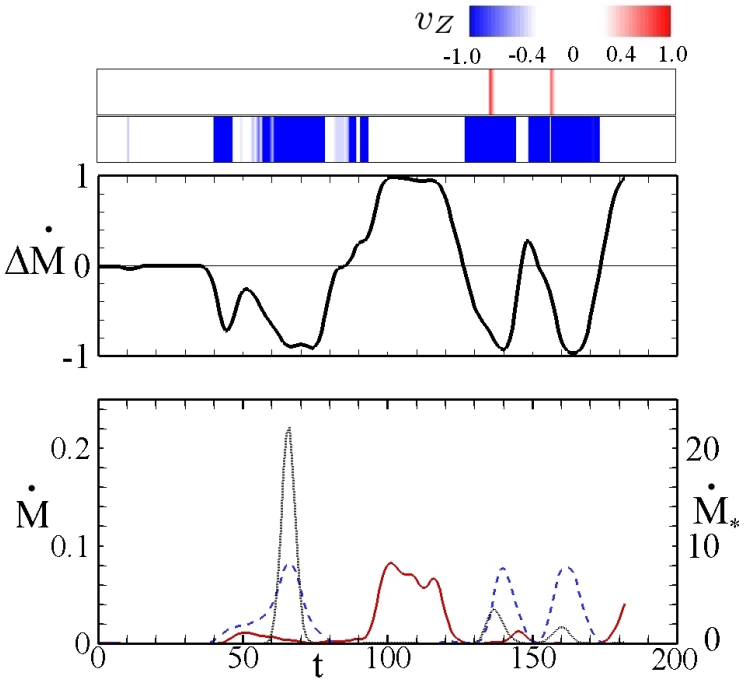

Figure 6.10: *Pure Stellar Dipole:* Lower panel shows stellar mass accretion rate $\dot{M}_*$ (dotted black line line) and mass outflow $\dot{M}$ (red solid line for upper hemisphere; blue dashed line for lower hemisphere) as a function of time. The middle panel shows the mass flux difference, normalized to average total mass flux $\Delta\dot{M} = (\dot{M}_t - \dot{M}_b)/(\dot{M}_t + \dot{M}_b)$ as a function of time. The upper plot shows the average velocity of outflows, weighted by mass along the upper (red) and lower (blue) boundaries. The right-hand vertical axis for the outflows has been scaled so $\dot{M}/\dot{M}_* = 10^{-2}$. Note the two types of outflows. When the stellar accretion rate correlates to the matter outflow this corresponds to funnel flow accretion in one hemisphere and outflow in the other. The three such events correspond to funnel flow accretion in the upper hemisphere and ejections in the lower hemisphere. These outflows occur at fast velocity. Outflow when there is no stellar accretion corresponds to matter pushing against the magnetosphere in one hemisphere and being ejected outwards without matter accretion to the star.

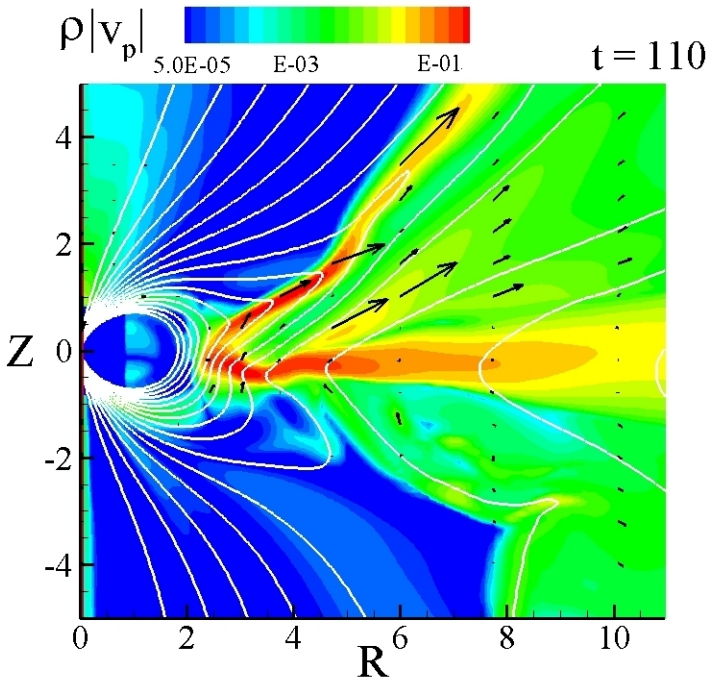

Figure 6.11: *Pure Stellar Dipole:* Poloidal mass flux $\rho|\mathbf{v}|$ (color), magnetic field lines (white lines) and coronal poloidal mass flux vectors $\rho\mathbf{v}_p$ at $t = 110$ for the case of a pure stellar dipole field. Note the presence of two outflows, a magnetospheric wind and a disc wind.

Figure 6.12 shows sample streamlines and field lines of the magnetospheric and disc winds along the length of the outflow. We note that the magnetospheric wind has a density 10 times greater than the disc wind, but comparable velocity at fixed distance from the launching point. This may be useful in explaining observations where jet/counter jet densities differ by a factor of a few. Also we note that the toroidal magnetic field drops to zero in the center of the magnetospheric wind, indicating the presence of a neutral layer.

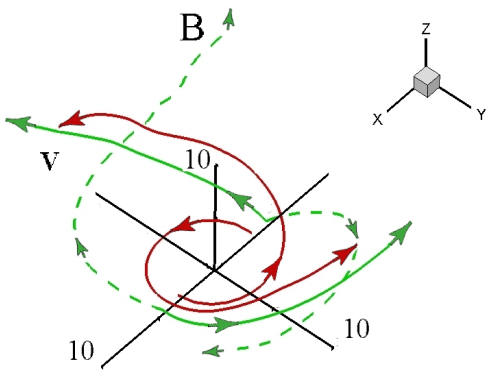

Figure 6.12: *Pure Stellar Dipole:* The solid red lines are streamline of the magnetospheric wind while the solid green lines are the streamlines for the disc wind. The dashed green lines are magnetic field lines anchored at the same point in the disc. All data is at $t = 110$ for a pure stellar dipole field with $\mu = 30$.

Stellar Dipole and Parallel Disc-Field PDIP

These simulations feature two types of episodic outflows. In the first, matter builds up at the magnetospheric boundary and begins to diffuse across the stellar dipole field. The initial top-bottom symmetry breaks spontaneously with the disc accreting onto the star in a funnel flow in one hemisphere. In the opposite hemisphere, matter is then pushed out by the re-expanding magnetosphere owing to the decrease in pressure from the disc due to the stellar accretion. In this type of ejection the stellar accretion rate and the outflow rates correlate strongly. Figure 6.13 shows a snapshot of an episodic magnetospheric and disc wind outflow. Figure 6.14 shows the sporadic nature of these outflows which occur in this case at $t = 50,\ 85,\ 159,\ \&\ 191$.

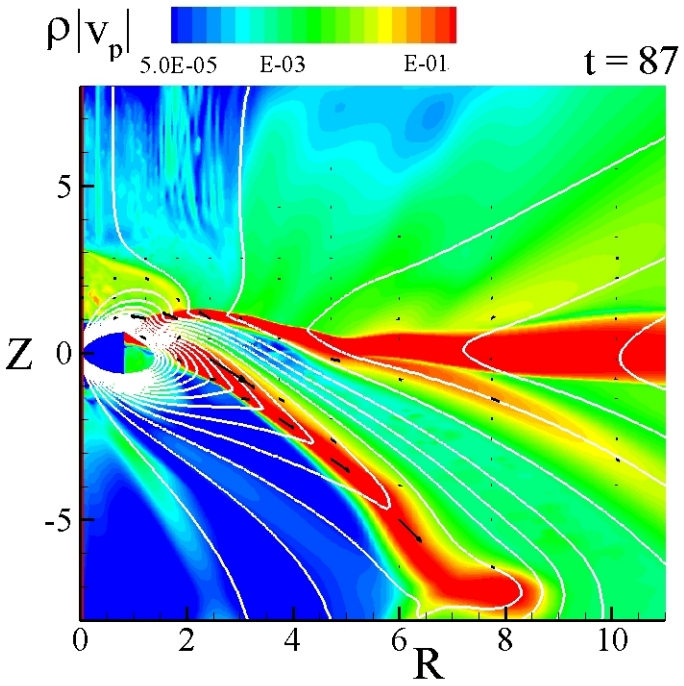

Figure 6.13: *Stellar Dipole plus Parallel Disc Field:* Poloidal mass flux $\rho|\mathbf{v}|$ (color), magnetic field lines (white lines) and coronal poloidal mass flux vectors $\rho\mathbf{v}_p$ at $t = 87$ for the case of a stellar dipole and a parallel disc field. Note the presence of a magnetospheric and disc wind, though the latter is considerably weaker.

The observed outflows are dominated by a magnetospheric wind, launched by a re-expanding magnetosphere, that had been compressed due to ram pressure from the disc. In contrast to the pure dipole the disc wind component is suppressed. This is a result of the field line geometry near the star. Owing to its centrifugal launching, the disc wind is dominated by outflows coming from the innermost region of the disc. In the case of a pure stellar dipole field, the inner disc supports field lines tilted away from the $Z-$axis which favors the formation of a disc wind. However, in the case of a stellar dipole and a parallel disc-field, the field lines in the inner disc are nearly vertical. The inclined field lines required for a disc wind are pushed out to larger radii and the strength of the

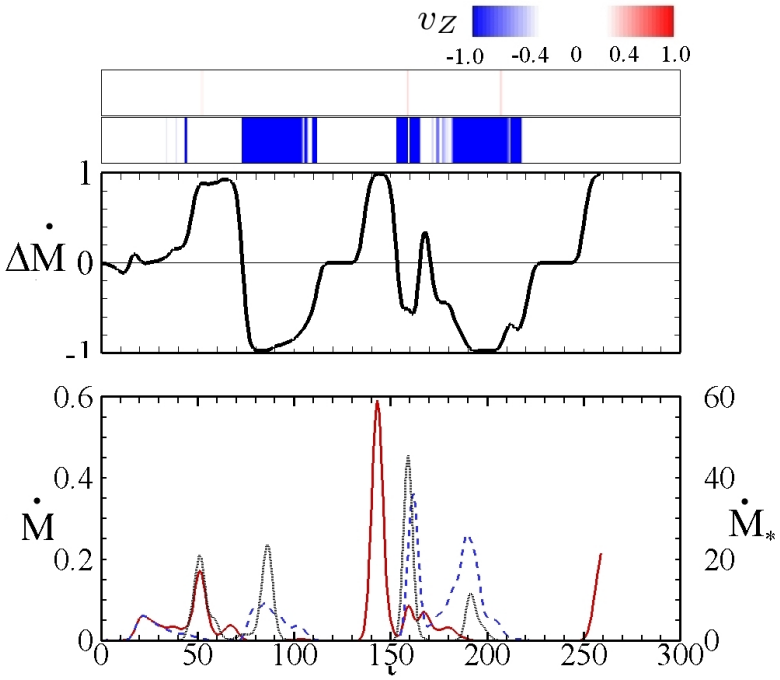

Figure 6.14: *Stellar Dipole plus Parallel Disc-Field:* Lower panel shows stellar mass accretion rate $\dot{M}_*$ (dotted black line line) and mass outflow $\dot{M}$ (red solid line for upper hemisphere; blue dashed line for lower hemisphere) as a function of time. The middle panel shows the mass flux difference, normalized to average total mass flux $\Delta\dot{M} = (\dot{M}_t - \dot{M}_b)/(\dot{M}_t + \dot{M}_b)$ as a function of time. The upper plot shows the average velocity of outflows, weighted by mass along the upper (red) and lower (blue) boundaries. The right-hand vertical axis for the outflows has been scaled so $\dot{M}/\dot{M}_* = 10^{-2}$. Note that there are two types of outflows. When the stellar accretion rate correlates with the matter outflow this corresponds to funnel flow accretion in one hemisphere and outflow in the other. These outflows have a greater average velocity. Outflow when there is only small accretion corresponds to matter pushing against the magnetosphere in one hemisphere and being ejected outwards without matter accreting.

wind is correspondingly decreased. Interestingly, turning down the strength of the disc-field relative to the dipole field can turn the inner disc wind back on by allowing for a field line geometry more favorable to outflows, as in the case of the pure dipole.

The parallel disc-field acts to increase the magnetospheric wind outflows by increasing the stellar mass flux. The loss of angular momentum to outflows acts to increase the accretion rate of the disc (Dyda et al. 2012). As a result, accretion is increased by roughly a factor of 4, even though the midplane magnetic β at the magnetospheric boundary is roughly contant for the two cases. This increased stellar $\dot{M}_*$ results, on average in an increased magnetospheric wind mass flux. However, the effect is not great enough to vary the time scales of the episodic outflows which in both cases remain at roughly order $T \sim 50 \sim 17y$. This result suggests that the addition of a large scale disc-field will increase the overall mass flux of outflows, and increase the spread in the outflow's velocity distribution, owing to the fact that the magnetosphere is further compressed.

We can turn off the magnetospheric wind and turn back on the inner disc wind by decreasing the strength of the dipole field. We consider dimensionless dipoles $\mu = 10,\ 20,\ 30$. At $t = 0$ these correspond to $R_m = 2.8,\ 4.1,\ 5$, respectively. All cases produce strong episodic outflows. During such outflows we measure the magnetospheric radius and find $R_m = 1.4,\ 2.1,\ 2.2$. In the case $\mu = 10$ we are no longer in the propeller regime, that is to say $R_m \lesssim R_{\rm cr}$. We can compare this to the case of the pure dipole where $R_m = 2.6,\ 3.0,\ 3.3$ during outflows. In the case $\mu = 10$, the pure dipole outflows are stronger than those with a parallel disc-field by a factor of $\sim 2-3$. In contrast, the $\mu = 20, 30$ parallel disc-field cases are stronger than the pure dipole cases by a factor of $\sim 2-5$. This points up the

μ	Type	R_m	$\dot{M}$	$\dot{M}/\dot{M}_*(\%)$	v	$v/v_K(R_m)$
10	DIP	2.6	0.055	1.7	0.48	0.77
	PDIP	1.4	0.009	0.4	0.20	0.40
20	DIP	3.0	0.078	0.7	0.49	0.85
	PDIP	1.8	0.141	4.2	0.23	0.31
30	DIP	3.3	0.083	0.1	0.33	0.60
	PDIP	2.1	0.364	0.8	0.38	0.55

Table 6.3: Magnetospheric radius R_m, mass flux $\dot{M}$, characteristic velocity v and scaled velocity $v/v_K(R_m)$ for different stellar dipoles μ in the case of a pure stellar dipole DIP and stellar dipole and parallel disc-field PDIP.

importance of the field line geometry in determining the strength of outflows. Adding magnetic flux in a disc field can hinder outflows if it compresses the magnetospheric radius to values less than $R_{\rm cr}$. On the other hand, if $R_m > R_{\rm cr}$ then adding a large scale field can enhance outflows by increasing the accretion rate and providing more energy to drive outflows.

Table 6.3 gives the magnetospheric radius R_m, mass outflow rate $\dot{M}$, characteristic outflow velocity v and scaled outflow velocity $v/v_K(R_m)$ for different stellar dipole moments μ in the case of a pure dipole and disc-field during typical outflow events correlated with stellar accretion. We measure the characteristic outflow velocity by time averaging the velocity of the outflow at Z = 5 during the outflow event. All outflows are magnetospheric winds, except for the anti-parallel $\mu = 10$ case where magnetospheric ejections were absent because $R_m < R_{\rm cr}$. We notice that the magnetospheric radius is an increasing function of the dipole strength. For constant dipole strength, the addition of a disc-field further reduces R_m. Further we note that outflow mass flux is typically a few percent of the accretion mass flux. The outflow velocity is roughly 75% of the Keplerian velocity at the launching radius. We note that in the PDIP case $\mu = 10$,

$R_m < R_{\rm cr}$. We are no longer in the propeller regime and this results in a lower outflow velocity. Increasing μ results in increasing the magnetospheric radius which in turn increases the strength of the propeller and the outflow velocity. For pure stellar dipoles, the magnetospheric radius does not vary appreciably. The dipole is compressed until there is an equilibrium between the matter and magnetic pressure. This leads to little variation in the size of typical outflows. We note that in the case of $\mu = 10$, despite the fact that propeller has been turned off, the presence of a dipole field does inhibit accretion on the star. This induces disc oscillations which leads to asymmetries in the outflows. This effect persists until late times, at which point the magnetosphere has been completely compressed by the advected large scale field and outflows become symmetric.

The largest outbursts were not correlated to mass accreting on the star. Rather there was a re-expantion of the magnetosphere, launching a "knot" of matter. The characteristic density of the "knot" was $\rho \sim 20$, roughly 10 times greater than magnetospheric ejection for the pure dipole. This accounts for the mass flux being a factor of 10 greater. We note the velocity of these much stronger outflows are roughly a factor of 2 slower than the corresponding magnetespheric ejections in the pure dipole case.

Dipole and Anti-Parallel Disc-Field ADIP

In the case of anti-parallel dipole and disc fields, reconnection occurs as the disc-field is advected inwards and runs into the stellar dipole field. We find funnel flow accretion to the poles of the star as found earlier by Miller and Stone (1997). This type of accretion is favored for this field geometry because at the X-point there is no magnetic pressure and matter can move freely onto the field lines

connecting the disc and the poles of the star.

As magnetic flux from the disc-field advects inwards, the X-point in the disc moves outwards. This has the effect of moving the open field lines threading the disc outwards. This causes the characteristic outflow speed, set by the local Keplerian velocity, to decrease. Outflows are hence diminished in this type of field configuration, and should die down at late times as sufficient magnetic flux is advected inwards and the inner disc field lines move outward.

Figure 6.15 shows the mass flux $\dot{M}$ through the upper and lower hemispheres. As the large scale field is advected inwards and annihilates with the dipole, the X-point moves into the lower hemisphere. This causes a top/bottom disc asymmetry, as matter preferentially falls into the lower hemisphere. This leads to a stronger outflow rate in the lower hemisphere at late times. Figure 6.16 shows a snapshot of the disc and poloidal magnetic field

The field line geometry is not favorable for launching inner disc winds. Despite initially being in contact with the disc (see Figure 6.2), field lines anchored to the star quickly move into the corona so that there is no efficient mechanism for mass loading onto them from the disc. The innermost open field lines anchored in the disc are at $R > 7$, so that the disc wind is weak. Based on the velocity cutoff of $v_{max} \approx 0.2$ in Figure 6.17 we would have estimated this launching radius as $R \approx 25$.

The stellar mass accretion rate $\dot{M}_* \sim 0.5$ which is a factor of ~ 10 times smaller than the accretion rate of the pure disc-field. In contrast with the pure dipole, annihilations of the disc-field with the stellar dipole reduces the dipole strength and allows for matter to more easily accrete onto the star. This leads to a nearly

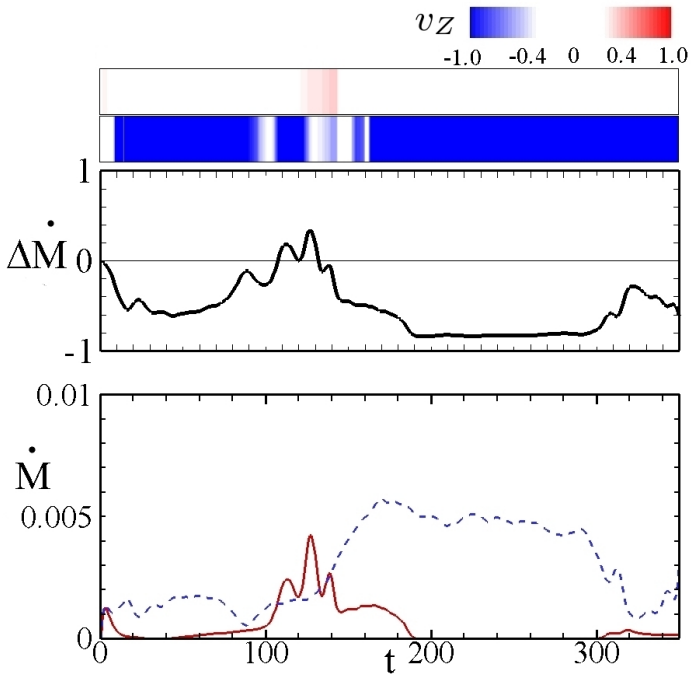

Figure 6.15: *Stellar Dipole plus Anti-Parallel Disc-Field:* The lower panel shows the mass flux $\dot{M}$ through the upper (solid black line) and lower (dashed red line) boundaries as a function of time. The upper panel shows the mass flux difference, normalized to average total mass flux $\Delta\dot{M} = (\dot{M}_t - \dot{M}_b)/(\dot{M}_t + \dot{M}_b)$ as a function of time. We note that outflows are $\sim$ 100 times weaker than in the DIP and PDIP cases.

constant accretion rate, unlike the case of the pure dipole where accretion occurs in episodic funnel flow events. The total mass accretion during the interval $0 < t < 200$ is comparable in the cases of the pure dipole and the dipole with parallel disc-field. This suggests that the total energy loss in each case is the same. The parallel configuration, owing to the lack of outflows, converts a much smaller fraction of this energy into outflows.

Figure 6.17 shows the fraction of mass in outflows with a given poloidal velocity for the various combinations of stellar dipole and disc field. Over such long time scales the mass outflow is to a high degree of accuracy symmetric be-

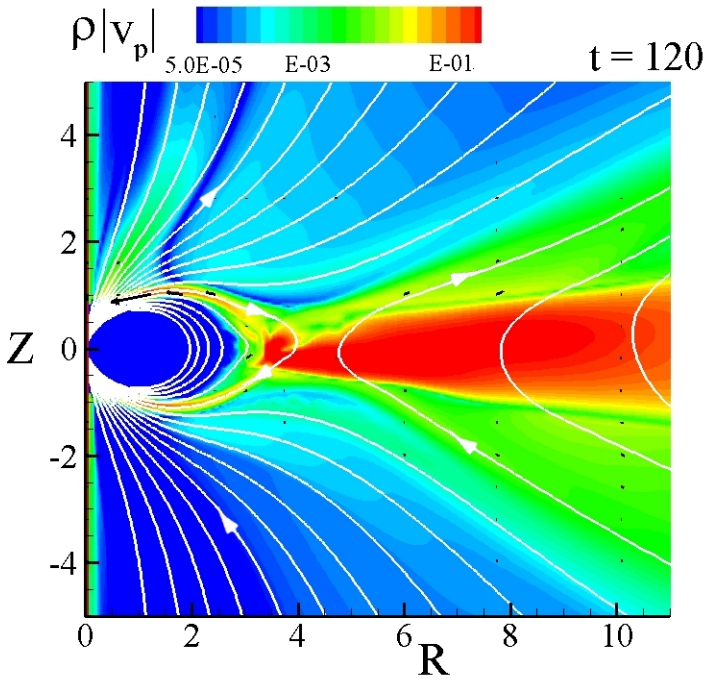

Figure 6.16: *Stellar Dipole plus Anti-Parallel Disc Field ADIP:* Poloidal mass flux $\rho|\mathbf{v}|$ (color), magnetic field lines (white lines) and coronal poloidal mass flux vectors $\rho\mathbf{v}_p$ at $t = 120$ for the case of a stellar dipole and an anti-parallel disc field. We note the weakeness of the disc wind despite the funnel flow accretion onto the star.

tween the two hemispheres so we only plot our results for $v_p > 0$. We further note several interesting features. The distributions have a sharp velocity cutoff at $v_{max} = 0.5,\ 0.65,\ 1.0$ in the cases of the DIP, PDIP and DISC respectively. These velocities correspond to those of a Keplerian disc at radii $R_K = 1.6,\ 1.33,\ 1.0$. The velocity cutoff directly corresponds to the Keplerian velocity at the innermost launching radius. In the case of the disc-field, this is the surface of the star and therefore $v_{max} = 1$. In cases with a dipole field this is the magnetospheric radius $R_m > 1$ which leads to $v_{\max} < 1$. In the case of the parallel disc-field, the disc-field compresses the dipole field and decreases the magnetospheric radius. Hence the maximum observed velocity is higher than in the case of a pure

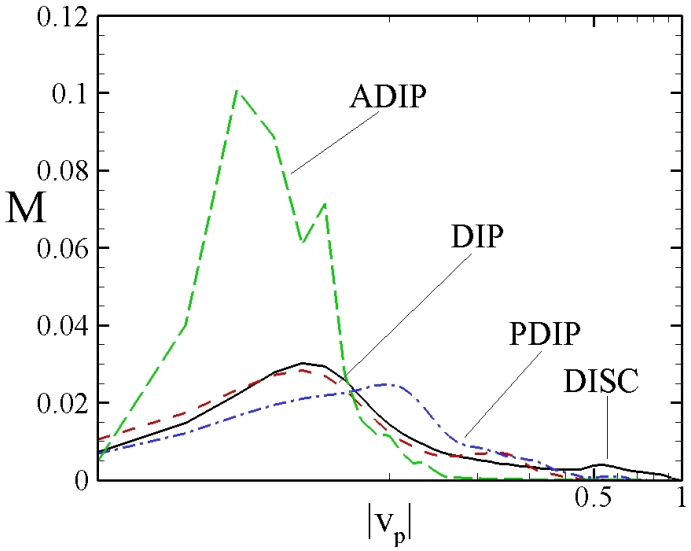

Figure 6.17: Fraction of total mass outflowed as a function of poloidal velocity for DISC (solid black line), DIP (red dashed line) , PDIP (blue dash-dot-dot line) and ADIP (green long dash line) simulations. The velocity cutoff is set by the Keplerian velocity scale at the innermost launching radius. In the case of the disc-field, this is at the surface of the star and therefore $v_{max} = 1$. In cases with a dipole field this is the magnetospheric radius $R_m > 1$ and therefore $v_{\rm max} < 1$. For the PDIP case, the disc field compresses the magnetosphere and the peak appears at larger v_p than for the DIP case. We show the plot for $v_p > 0$ since the full distribution is symmetric.

dipole. Also the peak in the distribution is shifted to higher velocities. This provides information about the field structure near the star: A large scale field will have outflows over the entire velocity range whereas the presence of a dipole may have a cutoff at $v_{\rm max} \propto R_m^{-3/2}$ since outflows will not be launched at radii $R < R_m$.

6.3 Conclusion

Here we summarize some of our main conclusions.

1. The distributed disc-fields (DISC) in the absence of a stellar field produce symmetric outflows for low density, low midplane-β discs. This limit agrees with study by Fendt and Sheikhnezami (2013). For larger disc densities, there is a decoupling of Alfvén waves between the upper and lower hemispheres and this leads to oscillations in the outflows between the two hemispheres. For even higher disc densities there the jet outflows are strongly asymmetric with the outflow changing episodically from one hemisphere to the other.

2. For a stellar dipole field in the absence of a disc-field (DIP), two types of outflows are observed - magnetospheric winds from the magnetospheric radius R_m and disc winds from somewhat larger radii. Both components have similar velocities but the magnetospheric winds have significantly higher densities and thus carry most of the mass outflow $\dot{M}$. The asymmetry of the outflows between the top and bottom hemispheres increases as the magnetospheric radius R_m increases beyond the corotation radius $R_{\rm cr}$ as found earlier by Lovelace et al. (2010).

3. Introducing a disc-field parallel to the stellar dipole field (PDIP) acts to reduce the magnetospheric radius R_m and changes the inner disc field structure. The field lines in the inner disc field lines are more aligned with the $Z-$axis and as a result the disc wind component is suppressed. At the same time the characteristic outflow velocity of the magnetospheric winds is increased owing to the reduced magnetospheric radius. Outflows are correspondingly more powerful. The outflows are episodic and strongly asymmetric about the equatorial plane.

The asymmetry of the outflows is not affected by the initial midplane plasma β of the disc.

4. For a disc-field which is anti-parallel to the stellar dipole field (ADIP), we observe reconnection between the field components analogous in some respects to the reconnection between the subsonic solar wind magnetic field and the earth's dipole field at the magnetopause which is inside the Earth's bow shock (e.g., Hargreaves 1992). This reconnection acts to prevent a build up of poloidal magnetic flux outside the magnetosphere. As a result magnetospheric outflows are suppressed. At the same time accretion to the star is enhanced.

Our results suggest that multi-component outflows, disc winds and magnetospheric winds, occur for a stellar dipole field in the absence of a large-scale disc-field. Inward advection of a large scale disc-field acts to turn off the disc wind component so that there is only a magnetospheric wind. We observe a cut-off in the maximum velocity of outflows related to the inner launching radius. This suggests that by measuring the velocity of outflows, one can estimate the launching radius. Measurement of the dipole component of the magnetic field would then allow one to estimate the matter pressure at the magnetospheric boundary.

Ellerbroek et al. (2013) found they could reproduce the knotted structure of outflows from HH1042 with a simple periodic outflow model. One possible solution that was consistent with observations was one where the jet and counter jet were out of phase by a half period. Observations were consistent with a period $T \sim 10-100$y Our DISC simulation with intermediate β enters into a regime with period $T = 2.82y\,(R_0/0.1\mathrm{AU})^{3/2}$. This agrees with the observed periods with a reasonable tuning of the inner disc length scale R_0.

Woitas (2002), Hartigan & Hillenbrand (2009) and Melnikov et al. (2009) have found that RW Aur A has a jet with velocity roughly 2 times greater and density roughly 2-3 times as large as its counter jet. This is the type of behaviour seen in our intermediuate β DISC run where in the oscillatory phase, the bottom jet mass flux peaks at a rate roughly 3 times greater than the top jet and has a velocity 2-3 times greater.

CHAPTER 7

DISC DYNAMOS

Magnetic fields play a key role in transporting angular momentum away from protostellar systems, thereby allowing matter to accrete on time scales consistent with models of protostellar evolution. Turbulent viscosity in the accretion disc, most likely generated by the magnetorotational instability (MRI), plays a key role in setting the accretion rate in the disc (Balbus & Hawley 1991). Astrophysical jets and winds are the dominant mechanisms for transporting angular momentum away from protostellar systems. Magnetic fields play a central role in the launching and collimation of these outflows. The origin of these large-scale, ordered, magnetic fields required for sustaining jets and winds is at present not well understood.

One possibility is that the magnetic field is advected inwards from the interstellar medium or ambipolar diffusion (see Shu, Adams & Lizano 1987 for review). Another possibility is that the field is generated locally via a dynamo mechanism. It is interesting therefore, to simulate the effects of a magnetic disc dynamo on protostellar evolution.

Different theoretical dynamo models have been proposed. The mean field dynamo (Moffatt, 1978) relies on a magnetic field that is disordered on small scales interacting through the mean motion of the disc on large scales. Tout & Pringle's (1992) mechanism relied on the Parker instability, MRI and magnetic reconnections.

Observations suggest that a dynamo mechanism is responsible, at least in part, for the magnetic fields near protoplanetary stars. Empirical evidence sug-

gests there is a correlation between the magnitude of large scale magnetic fields and seed fields, suggesting a related dynamo mechanism is responsible for generating them (Vidotto et al, 2014). Rotational modulation of Zeeman signature in GQ Lup (Donati et al. 2012) and DN Tau (Donati et al. 2013) suggests that the magnetic fields of T Tauri stars are generated by non-stationary dynamos.

Much work has been done to understand the dynamo process in the context of generating turbulent magnetic fields to understand the MRI. Stratified shearing box simulations with zero net vertical magnetic flux exhibit a flipping of the mean toroidal magnetic field flux on time scales of roughly 10 orbits (Brandenburg et al. 1995; Shi et al. 2010; Davis et al. 2010, Simon et al. 2012). This effect is found to be more sporadic as the amount of net vertical magnetic flux is increased (Bai & Stone 2013). Full 3D simulations (Stone et al. 1996) of turbulent field evolution largely agreed with these shearing box models. Del Zanna et al. (2014) implemented a disc dynamo in the GRMHD code ECHO and found exponential growth of toroidal magnetic fields from a seed poloidal field. Sadowski et al. (2014) used a sub-grid model in the GRMHD code KORAL to simulate a dynamo in a thick disc in 2D and found accretion rates were comparable to 3D simulations. The disc dynamo played a key role, by allowing for the regeneration of poloidal magnetic field which drove the disc to a state characteristic for a 3D MRI disc. Schober et al (2012) have shown that dynamo mechanisms can amplify magnetic fields during the formation of primordial halos by converting kinetic energy from turbulence into magnetic energy. von Rekowski (2003) found that an α^2 dynamo can launch outflows even without an external field. Bardou et al. (2001) simulated the back-reaction of outflows on the disc dynamo and found a vertical velocity can enhance the action of the dynamo. In a series of papers Torkelsson & Brandenburg (1994a;1994b;1994c) studied the parity of

generated fields and growth rates of dipolar and quadrupolar magnetic fields from linear and non-linear α-dynamo effects. They found their growth to be chaotic for large enough dynamo number. Stepanovs, Fednt & Sheikhnezami (2014) generated episodic outflows with a time dependent mean field disc dynamo.

In this paper we perform axisymmetric MHD simulations of an α-dynamo operating inside a protostellar accretion disc. We provide an initial weak poloidal seed magnetic field and track its growth and the corresponding MHD outflows. Our goal is to undertand how the disc dynamo affects the corresponding outflows and the late time magnetic field structure. The structure of this paper is as follows. In Section 2 we review the disc dynamo contribution to the equations of motion and describe our MHD code. In section 3 we present results, describing how outflows and magnetic field structure around the star are affected by the initial seed field, the dynamo parameter α_d, the disc viscosity α_ν and the magnetic diffusivity α_η. We conclude in Section 4 and discuss implications for future work and observational prospects for classical T Tauri stars (CTTS).

7.1 Dynamo Model

7.1.1 Basic Equations

The plasma flows are assumed to be described by the equations of non-relativistic magnetohydrodynamics (MHD) described in Section 3.1. However, we assume that a dynamo effect is generated by the turbulent fluctuations of

the velocity δv. We introduce a dynamo term of the form

$$A = -\frac{\tau}{3}\langle \delta\mathbf{v} \cdot \nabla \times \delta\mathbf{v} \rangle = Z\Omega_K \alpha_d, \tag{7.1}$$

that is the product of the decorrelation time of the velocity fluctuations τ and the mean helicity of the turbulence. We parametrize this by an α prescription, with the strength of the effect parametrized by the α-dynamo parameter α_d. See Kulsrud (1999) for review of the mean field theory dynamo. α_d is a dimensionless number that we vary in our simulations and the prefactor of the height in the disc Z times the local Keplerian angular velocity Ω_K was chosen by dimensional analysis. The induction equation (3.1) then becomes In a non-rotating reference frame the equations are

$$\frac{\partial \mathbf{B}}{\partial t} - \nabla \times (\mathbf{v} \times \mathbf{B}) + \nabla \times (\eta_t \nabla \times \mathbf{B}) + \nabla \times (A\mathbf{B}) = 0\,, \tag{7.2}$$

We define the dynamo number

$$N_d = \frac{A\Omega_K h^3}{\eta_t^2} \approx \frac{\alpha_d}{\alpha_\eta^2}. \tag{7.3}$$

Dynamo effects are thought to be important for $N_d > N_c$ for some critical dynamo number (Stepinski & Levy 1988).

7.1.2 Disc Averaged Equations

To gain some insight into the dynamo process, consider a thin, axisymmetric, Keplerian disc with diffusivity η and radial infall velocity v_R operating an α-dynamo. We will ignore any vertical motion v_Z and neglect the Z dependence of Ω and v_R. Breaking the induction equation (7.2) into (R, ϕ, Z) components, we

find

$$-\frac{1}{R}\frac{\partial}{\partial Z}\left(\frac{\partial \Psi}{\partial t}\right) = \frac{\partial}{\partial Z}\Bigg[-AB_\phi + \frac{v_R}{R}\frac{\partial \Psi}{\partial R} - \frac{\eta}{R}\left(R\frac{\partial}{\partial R}\left(\frac{1}{R}\frac{\partial \Psi}{\partial R}\right) + \frac{\partial^2 \Psi}{\partial Z^2}\right)\Bigg], \tag{7.4a}$$

$$\frac{\partial B_\phi}{\partial t} = -\frac{\partial \Omega}{\partial R}\frac{\partial \Psi}{\partial Z} + \frac{\partial}{\partial Z}\left(-\frac{A}{R}\frac{\partial \Psi}{\partial Z} + \eta\frac{\partial B_\phi}{\partial Z}\right) - \frac{\partial}{\partial R}\left(\frac{A}{R}\frac{\partial \Psi}{\partial R} + v_R B_\phi - \frac{\eta}{R}\frac{\partial (RB_\phi)}{\partial R}\right), \tag{7.4b}$$

$$\frac{\partial}{\partial R}\left(\frac{\partial \Psi}{\partial t}\right) = \frac{\partial}{\partial R}\Bigg[AB_\phi R - v_R\frac{\partial \Psi}{\partial R} + \eta\left(R\frac{\partial}{\partial R}\left(\frac{1}{R}\frac{\partial \Psi}{\partial R}\right) + \frac{\partial^2 \Psi}{\partial Z^2}\right)\Bigg], \tag{7.4c}$$

where Ψ is the magnetic flux function. Two types of solutions are possible, depending on the symmetries of Ψ and B_ϕ - a "dipole" like solution where $\Psi(Z) = \Psi(-Z)$ and $B_\phi(Z) = -B_\phi(-Z)$ and a "quadrupole" solution where $\Psi(Z) = -\Psi(-Z)$ and $B_\phi(Z) = B_\phi(-Z)$ (see Kulsrud 2005). To solve the problem exactly we make a gauge choice, for example $\Psi(0) = 0$ and boundary conditions at $Z = \pm h$ such as $\partial\Psi/\partial Z = 0$. Intuitively then, one may think of the flux function as a cosine in the dipole like case and as a sine in the quadrupole case

$$\Psi(Z) = \begin{cases} \Psi_0 \cos\left(\frac{\pi Z}{h}\right) & \text{"dipole"}, \\ \Psi_0 \sin\left(\frac{\pi Z}{2h}\right) & \text{"quadrupole"}. \end{cases} \tag{7.5}$$

We work in the thin disc, $h \ll R$, approximation. The variation in the flux function over the half disc thickness is therefore in each case $\Delta\Psi \approx \Psi_0$ but the variation in its derivative for each case is $\Delta\Psi/\Delta Z_{\text{dip}} \approx 2\Delta\Psi/\Delta Z_{\text{quad}}$. Therefore integrating over the upper half part of the disc, and replacing all quantities with their vertically averaged quantities $\int_0^h B_\phi dz = h\bar{B}_\phi$, $\int_0^h -\frac{1}{R}\frac{\partial \Psi}{\partial Z} = h\bar{B}_R$ and ignoring terms involving B_Z, the R and ϕ components give us the coupled system

$$\frac{\partial \bar{B}_\phi}{\partial t} = (\frac{3}{2}C_1 + C_2\alpha_d)\Omega\bar{B}_R - \frac{\eta}{h^2}\bar{B}_\phi, \tag{7.6a}$$

$$\frac{\partial \bar{B}_R}{\partial t} = C_2 \alpha_d \Omega \bar{B}_\phi - \frac{\eta}{h^2} \bar{B}_R. \tag{7.6b}$$

where $C_1 = 1(-1)$ and $C_2 = 2(-1)$ in the dipole (quadrupole) case. Using $\eta = \alpha_\eta \Omega h^2$, we combine (7.6) and find

$$\begin{aligned} &\frac{\partial^2 \bar{B}_R}{\partial t^2} + 2\alpha_\eta \Omega \frac{\partial \bar{B}_R}{\partial t} \\ &\qquad + \left[\alpha_\eta^2 - C_2 \alpha_d \left(3/2 C_1 + C_2 \alpha_d\right) + \right] \Omega^2 \bar{B}_R = 0. \end{aligned} \tag{7.7}$$

Taking $\bar{B}_R \propto \exp(\sigma \Omega t)$ we find growth rates

$$\sigma = -\alpha_\eta \pm \sqrt{C_2 \alpha_d (3/2 C_1 + C_2 \alpha_d)}. \tag{7.8}$$

Taking $\alpha_d \ll 1$ we approximate

$$\sigma + \alpha_\eta \approx \begin{cases} \pm \sqrt{3\alpha_d} & \text{“dipole”}, \\ \pm \sqrt{3\alpha_d/2} & \text{“quadrupole”}. \end{cases} \tag{7.9}$$

Substituting back into (7.6) we find

$$\bar{B}_R \approx \begin{cases} \pm \sqrt{\frac{2\alpha_d}{3}} \bar{B}_\phi & \text{“dipole”}, \\ \mp \sqrt{\frac{2\alpha_d}{3}} \bar{B}_\phi & \text{“quadrupole”}. \end{cases} \tag{7.10}$$

The toroidal field component is primarily generated by the differential rotation of the disc. It is also the dominant contribution to the magnetic field. Therefore, at late times when the matter and magnetic pressure in the disc are in equilibrium, we expect the toroidal component to saturate. This would imply that the radial field should also saturate, to a value proportional to $\sqrt{\alpha_d}$. For this reason, we scale all our magnetic field plots to $\sqrt{\alpha_d}$. Also, for $\alpha_d, \alpha_\eta \ll 1$ the growth rate $\sigma \propto \sqrt{\alpha_d}$ and we scale all times by a factor of $\alpha_d^{-1/2}$. We note that requiring a positive growth rate $\sigma > 0$ implies $N_d \gtrsim 1/3$. Though we have neglected order one numbers, this provides an inuitive picture for why there is a critical dynamo number - if the diffusion time scale is too fast compared to

the dynamo time scale then the field will diffuse away and never grow. Stepinski & Levi (1988) found purely growing dynamo modes for dynamo number $R_m = (R/h)^{3/2}\,\alpha_d/\alpha_\eta^2 \sim 100$ which agrees with this result up to some $O(1)$ numbers.

To gain additional insight into the thin disc equations, consider a Taylor series expansion of the dipole solution in powers of the disc scale height. Taking

$$\Psi = \Psi_0(R,t) + Z^2\Psi_2(R,t), \tag{7.11a}$$

$$B_\phi = ZB_1(R,t), \tag{7.11b}$$

and expanding (7.4) in like powers of Z yields

$$\frac{\partial\Psi_0}{\partial t} - \frac{(\nu-\eta)}{R}\frac{\partial\Psi_0}{\partial R} = \eta\left[\frac{\partial^2\Psi_0}{\partial R^2} + 2\Psi_2\right], \tag{7.12a}$$

$$\frac{\partial\Psi_2}{\partial t} - \frac{(\nu-\eta)}{R}\frac{\partial\Psi_2}{\partial R} = \alpha_d\Omega R B_1 + \eta\frac{\partial^2\Psi_2}{\partial R^2}, \tag{7.12b}$$

$$\begin{aligned}\frac{\partial B_1}{\partial t} - \frac{\partial}{\partial R}\left[\frac{(\nu+\eta)}{R}B_1\right] = \\ \frac{\Omega}{R}(3-4\alpha_d)\Psi_2 + \frac{\alpha_d\Omega}{R}\left(\frac{5}{2R}\frac{\partial\Psi_0}{\partial R} - \frac{\partial^2\Psi_0}{\partial R^2}\right) + \eta\frac{\partial^2 B_1}{\partial R^2},\end{aligned} \tag{7.12c}$$

where we have set $v_R = -\nu/R$ and assume η is constant in the disc. (7.12a) shows that the lowest order component of the poloidal flux function advects inwards, and diffuses away because it interacts with itself and the higher order terms of the flux function. (7.12b) shows the evolution of the next higher order component of the flux function. The evolution of both Ψ_0 and Ψ_2 depends on a term proportional to $\nu - \eta$ so we expect the relative strength of the viscosity and diffusivity to have an effect. The poloidal field B_1 acts as a source for the second order poloidal flux Ψ_2. Its evolution, described by (7.12c), depends on the sum $\nu + \eta$ so any difference in behaviour will come from the fact that it is coupled to the flux function.

7.1.3 Initial Conditions

Magnetic Field & Dynamo

Our simulations use an extended disc field (Zanni, 2007) as a seed field for the dynamo, defined by the poloidal flux function

$$\Psi_{\rm disc} = \frac{4}{3} B_0 R_0^2 \left(\frac{R}{R_0}\right)^{3/4} \frac{m^{5/4}}{(m^2 + Z^2/R^2)^{5/8}}, \tag{7.13}$$

where the poloidal magnetic field components can be computed via

$$B_Z = \frac{1}{R}\frac{\partial \Psi}{\partial R}, \qquad\qquad B_R = -\frac{1}{R}\frac{\partial \Psi}{\partial Z}. \tag{7.14}$$

The parameter m determines how much the field lines bend in the R-Z plane with the limit $m \to \infty$ corresponding to purely vertical field lines. In this study we set $m = 1$.

The field generated by the dynamo can be expanded using a multipole expansion

$$\Psi = \mu_{\rm dip}\Psi_{\rm dip} + \mu_{\rm quad}\Psi_{\rm quad} + \mu_{\rm oct}\Psi_{\rm oct} + ... \tag{7.15}$$

where

$$\Psi_{\rm dip} = \frac{R^2}{(R^2 + Z^2)^{\frac{3}{2}}}, \tag{7.16}$$

is the dipole contribution to the potential,

$$\Psi_{\rm quad} = \frac{3}{4}\frac{R^2 Z}{(R^2 + Z^2)^{5/2}}, \tag{7.17}$$

is the quadrupole contribution and

$$\Psi_{\rm oct} = \frac{R^2(4Z^2 - R^2)}{2(R^2 + Z^2)^{7/2}}, \tag{7.18}$$

is the octupole contribution. These are expected to be the dominant modes excited by the disc dynamo. The disc dynamo is given by

$$A(R,Z) = \begin{cases} 0 & R < R_{\rm dyn}\ , \\ \alpha_d Z \sqrt{\frac{GM}{R^3}} e^{-(\rho_{\rm dyn}/\rho)^2} \tanh(\frac{R-R_{\rm dyn}}{\Delta R}) & R > R_{\rm dyn}\ . \end{cases} \tag{7.19}$$

In our simulations we have set $R_{\rm dyn} = 5, \rho_{\rm dyn} = 0.1$ and $\Delta R = 1$. This is the form of the $\alpha-$dynamo described in (7.1) but with an exponential factor to continuously cut it off from operating in the corona and a hyperbolic tangent to continuously cut it off at an inner radius $R_{\rm dyn}$. We found it necessary to impose an inner disc cutoff to avoid numerical instabilities at the surface of the star.

Matter Distribution

Initially the matter of the disc and corona are assumed to be in mechanical equilibrium (Romanova et al. 2002). The initial density distribution is taken to be barotropic with

$$\rho(p) = \begin{cases} p/T_{\rm disc} & p > p_b \ \text{ and } \ R \geq R_d\ , \\ p/T_{\rm cor} & p < p_b \ \text{ or } \ R \leq R_d\ . \end{cases} \tag{7.20}$$

where p_b is the level surface of pressure that separates the cold matter of the disc from the hot matter of the corona and R_d is the initial inner disc radius. At this surface the density has an initial step discontinuity from value $p/T_{\rm disc}$ to $p/T_{\rm cor}$.

Because the density distribution is barotropic, the initial angular velocity is a constant on coaxial cylindrical surfaces about the $Z-$axis. Consequently, the pressure can be determined from the Bernoulli equation

$$F(p) + \Phi + \Phi_c = \mathcal{B}_0\ , \tag{7.21}$$

here $\mathcal{B}_0$ is Bernoulli's constant,$\Phi = -GM/\sqrt{R^2+Z^2}$ is the gravitational potential,

with $GM = 1$ in the code, $\Phi_c = \int_R^\infty r dr\, \omega^2(r)$ is the centrifugal potential, and

$$F(p) = \begin{cases} T_{\rm disc} \ln(p/p_b) & p > p_b \ \text{ and } \ R \geq R_d \ , \\ T_{\rm cor} \ln(p/p_b) & p < p_b \ \text{ or } \ R \leq R_d \ . \end{cases} \tag{7.22}$$

We take the Bernoulli parameter $\mathcal{B}_0 = 3 \times 10^{-4}$ in our simulations. The initial half thickness of the disc $h/R = 0.1$ at the initial inner disc edge $R_d = 5$.

Angular Velocity

The initial angular velocity of the disc is slightly sub-Keplerian,

$$\Omega = (1 - 0.003)\Omega_K(R) \qquad R > R_d \ , \tag{7.23}$$

Inside of R_d, the matter rotates rigidly with angular velocity

$$\Omega = (1 - 0.003)\Omega_K(R_d) \qquad R \leq R_d. \tag{7.24}$$

The corotation radius R_c is the radius where the angular velocity of the disc equals that of the star; that is, $R_c = (GM/\Omega_*^2)^{1/3}$. In this study we have chosen $R_c = 2$.

7.1.4 Boundary Conditions

Our simulation region has three boundaries: the axis, the surface of the star and the external boundaries. For each dynamical variable we impose a boundary condition consistent with our physical assumptions.

We assume axisymmetry about the axis. On the star and the external boundaries we want to allow fluxes and impose free boundary conditions $\partial \mathcal{F}/\partial n = 0$ where $\mathcal{F}$ is a dynamical variable and n is the vector normal to the boundary.

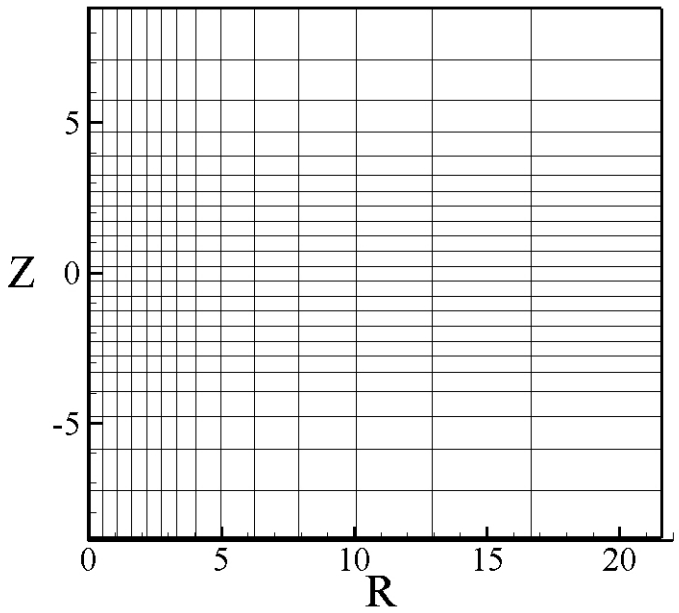

Figure 7.1: Sparse version of grid used in the simulations, showing every 11th gridline in the R direction and every 10th gridline in the Z direction.

At the external boundary along the edge of the disc we allow new matter to flow into the simulation region. We impose the condition that the matter must be accreting $v_r < 0$. In the coronal region, we prescribe outflow conditions and allow matter, entropy and magnetic flux to exit the simulation region.

The star is taken to be cylindrical in shape with radius $R_* = 1$ and height $Z_* = 2$. Free boundary conditions are imposed on the variables ρ, p and $\mathbf{B}$. In addition, we require that matter on the stellar boundary flow into the star. We treat the corner of the star by averaging over the nearest neighbour cells in the R and Z directions.

Our simulation uses a grid $N_R \times N_Z = 154 \times 230$ cells. The star has a radius of 1 in units of the simulation and is cylindrical in shape. It extends 10 grid

Parameters	Symbol	Value
mass	M_0	1.59×10^{33} g
length	R_0	1.50×10^{12}cm
magnetic field	B_0	8.04×10^{-2} G
time	P_0	3.53×10^{-2} y
velocity	v_0	8.42×10^{7}cm/s
density	ρ_0	7.24×10^{-15} g/cm^3
accretion rate	$\dot{M}_0$	2.72×10^{-7} $M_\odot$/yr
temperature	T_0	4.26×10^{7} K
dipole strength	$\mu_{\rm dip}$	2.69×10^{35} G cm^3
quadrupole strength	$\mu_{\rm quad}$	4.04×10^{47} G cm^4
octupole strength	$\mu_{\rm oct}$	6.05×10^{59} Gcm^5

Table 7.1: Mass, length, and magnetic field scales of interest and the corresponding scales of other derived quantities for a CTTS. One can obtain the physical values from the simulation values by multiplying by the corresponding dimensional quantity above.

cells above and below the equatorial plane. In the R-direction, the first 60 grid cells have length $dR = 0.05$. Later cell lengths are given recursively by $dR_{i+1} = 1.025 dR_i$. Similarly, in the Z-direction the first 30 grid cells above and below the equatorial plane have length $dZ = 0.05$. Later cell lengths are given recursively by $dZ_{j+1} = 1.025 dZ_j$. We show a sparse version of our grid, showing every 11th gridline in the R direction and every 10th gridline in the Z direction in Figure 7.1.

7.1.5 Dimensional Variables

The MHD equations are written in dimensionless form so that the simulation results can be applied to different types of stars. We assume that the central object is a CTTS with mass $M_* = 0.8 M_\odot$, a radius $R_* = 2 R_\odot$ and a magnetic field with magnitude $B_* = 3 \times 10^3$ G on the stellar surface, which is typical for the

magnitude of the stellar dipole. We define dimensionful quantities with a 0 subscript, to denote typical values of physical parameters at a reference radius R_0. The mass scale is set by the stellar mass so $M_0 = M_*$. The reference length, $R_0 = 0.1$AU, is taken to be the scale of a typical inner disc radius. Assuming a stellar dipole field, the magnetic field strength $B_0 = B_*(R_*/R_0)^3$. The mass, length and magnetic field scales allow us to define all other dimensionful quantities.

The reference value for the velocity is the Keplerian velocity at the radius R_0, $v_0 = (GM_0/R_0)^{1/2}$. The reference time-scale is the period of rotation at R_0, $P_0 = 2\pi R_0/v_0$. From the relation $\rho_0 v_0^2 = B_0^2/4\pi$, we define the reference density ρ_0 of the disc. This also defines a reference pressure The reference mass accretion rate is $\dot{M}_0 = 4\pi\rho_0 v_0 R_0^2$. The reference temperature $T_0 = v_0^2/2 \times m_H/k_B$ where m_H is the atomic mass of hydrogen and k_B, the Boltzmann constant, is obtained by taking the ratio of the reference pressure $p_0 = B_0^2/8\pi$ and the reference density. The dimensions of the coefficients in the multipole exapnsion of the flux function are obtained by scaling the refence field by the appropriate power of R_0 - $\mu_{\rm dip} = B_0 R_0^3$, $\mu_{\rm quad} = \mu_{\rm dip} R_0$ and $\mu_{\rm oct} = \mu_{\rm dip} R_0^2$.

Results obtained in dimensionless form can be applied to objects with widely different sizes and masses. However, the present work focuses on CTTS with the typical values shown in Table 7.1. One can obtain dimensionful quantities from simulation results by multiplying by the appropriate dimensionful quantity above. A more detailed description of our code and numerical methods can be found in Koldoba et al. (2015).

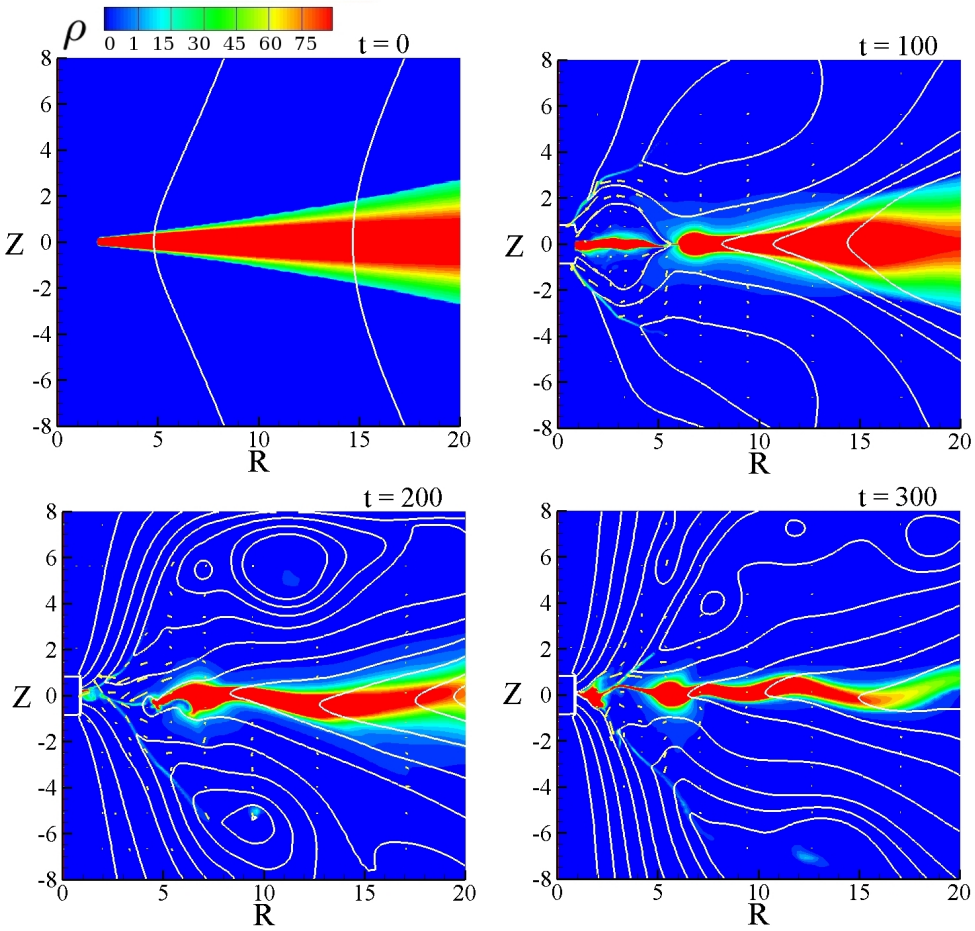

Figure 7.2: Density ρ (color), poloidal field lines Ψ (white) and poloidal velocity $v_{\rm p}$ for the case $N_d = 10$. t = 0 shows the initial large scale field. By t = 100 the dynamo has changed the field structure in the inner part of the disc. By t = 200 the field has developed a parallel dipole structure near the star, which interacts with the large scale field to produce an X-point at $R \approx 6$. By t = 300 the dipole structure has pushed out the inner part of the disc.

7.2 Results

The α-dynamo converts a poloidal magnetic field into a toroidal magnetic field and vice versa. We provide an initial poloidal seed field. The differential disc rotation causes a twisting of this poloidal field, producing a toroidal field. The α dynamo in turn converts this toroidal field into poloidal field. This is a positive feedback loop and the poloidal field continues to grow until other physical effects halt the growth. This could have interesting observational implications, as seed fields too weak to launch MHD outflows can grow to values which can support observable outflows.

We find two qualitatively different regimes in our dynamo simulations - a *weak dynamo* regime where dynamo effects are only important in the inner disc and a *strong dynamo* regime where dynamo effects affect the entire disc and the magnetic field quickly comes to dominate the disc dynamics. We discuss our results for each of these cases below.

7.2.1 Weak Dynamo

Below we show poloidal plots of disc density ρ, magnetic flux contours Ψ and poloidal velocity vectors $v_{\rm p}$ of a typical run in the weak dynamo regime (Fig. 7.2). We see that magnetic flux of the disc increases as a function of time, and the flux builds up on the star as it advects inwards with the accreting matter. The dynamo only changes the field geometry in the inner part of the disc $R \lesssim 10$ where loops form, even though the dynamo is operating for all radii $R > R_{\rm dyn} = 5$. In the outer parts of the disc field lines become more inclined relative to their

initial configuration, just like in the case where the dynamo is not operating.

Any magnetic field can be expanded in a general multipole expansion. As our code is in cylindrical coordinates, projecting out the multipole components is slightly more involved than taking the inner product of the flux function with the Legendre polynomials. We show how to extract the dipole $\mu_{\rm dip}$, quadrupole $\mu_{\rm quad}$ and octupole $\mu_{\rm oct}$ moments from our simulations in Appendices 7.A.1 - 7.A.3. We use this method to study the time dependence of the multipole moments. This gives us a sense of the geometry of the generated magnetic field around the star. This is important because measurements using the Zeeman-Doppler technique have shown that magnetic fields around young stars are often complex, exhibiting dipole and higher order fields (e.g Donati & Collier Cameron 1997; Donati et al. 1999; Jardine et al. 2002).

Runs were performed with seed field amplitudes ranging between $B_0 = 10^{-2} - 10^{0}$. These correspond to midplane plasma $\beta = 10^{1} - 10^{5}$. For $\beta \gg 10^{1}$, corresponding to seed fields $B_0 \ll 1$, the results were largely independent of the initial magnetic field. For larger field values, the dynamo had comparatively little effect, and the simulation behaved as for the case $\alpha_d = 0$ where the disc dynamo is explicitly turned off. Growth of the dipole and higher order moments around the star is due to advection and rearrangement of the field, and not the generation of new magnetic flux. Cowling's antidynamo theorem (1934) states that a self-sustained, axisymmetric field cannot be maintained - in essence non axisymmetric velocity components must counteract the diffusion of the field. Our simulations run on the order of 600 orbits at $R = 1$, corresponding to roughly 6 orbits at $R = 20$. The typical diffusion time $\tau \sim R^2/\eta_t \gg 1$, meaning we can evade the antidynamo theorem because we have not waited sufficiently

long for the field to diffuse away. In fact, after $t = 600$ the total magnetic flux threading the star and disc decreased roughly 5% from its initial value. The flux on the star increased roughly 100% and the flux threading the disc decreased approximately 20%.

For fixed diffusivity $\alpha_\eta = 0.1$ and seed field amplitude $B_0 = 0.1$ we plot the dipole (Fig. 7.3), quadrupole (Fig. 7.4) and octupole moments (Fig. 7.5) as a function of time for dynamo numbers $N_d = 1, 5, 10$ ($\alpha_d = 0.01, 0.05$ and 0.1). We have scaled the time by $\alpha_d^{1/2}$ and the dipole moment by $\alpha_d^{-1/2}$, as suggested by the linear analysis of Section 7.1.2. Empirically, we see this scaling yields similar behaviour for runs with different dynamo strength parameter when $\alpha_d \ll 1$. We find qualitatively different behaviour of the dipole, quadrupole and octupole moments. The dipole moment grows to a value of approximately $\mu_{\rm dip} \approx -N_d^{1/2}$. It saturates to this value on time scales $\tau \sim \alpha_d^{-1/2}\Omega_K(R_{\rm dyn})^{-1}$. The quadrupole moment oscillates about $\mu_{\rm quad} = 0$, which is what we would expect given the symmetry of the initial seed field. The magnitude of these oscillations increases with increasing dynamo number. At late times the amplitude of the oscillations dies down. The octupole moment begins to oscillate at the same time that the dipole mode begins to grow. In the cases where $\alpha_d = 0.05$ or 0.1 when the dipole reaches its asymptotic value, the octupole moment quickly assumes the opposite sign so that the late time octupole moment saturates at the same time as the dipole but with opposite polarity. We can understand the relative polarity of the dipole and octupole components from the thin disc equations and the form of the seed field. The diffusion and viscous term in (7.12b) depends on the gradient of the flux function (second term on LHS). For a seed field $\Psi \sim R^p$ it will diffuse/advect at a rate $\propto pR^{p-1}$ For a disc field $\Psi_{\rm disc} \sim R^{3/4}$ so the leading order component will diffuse inward. Higher order components will carry ad-

ditional powers of R^{-1} so their sign will change as the power law dependence changes from $p > 0$ to $p < 0$. This does not happen however in the weakest dynamo case $\alpha_d = 0.01$. This suggests that the lower order multipole moments are excited first, and higher order multipoles will be excited and grow as the lower order poles reach a saturation value. The octupole moment saturates to a value of $\mu_{\rm oct} \approx -N_d^{1/2}$ as suggested by the linear theory. For weaker dynamos, the higher order modes are not excited. These results are consistent with the symmetries of the seed field - the disc dynamo is a symmetric function of position Z, therefore we expect to excite symmetric (dipole and octupole) and not asymmetric (quadrupole) modes. Reversing the polarity of the seed field reverses the signs of the generated multipoles, but does not otherwise change the results, as expected.

We term this the weak dynamo regime, because the physics is largely determined by what is happening in the inner disc. In particular, we performed simulations where we varied the cutoff radius $5 \leq R_{\rm dyn} \leq 8$ but kept the dynamo coefficient A in (7.19) constant by varying α_d. The late time moments changed by roughly 10% and growth rates and times were similarly affected. Poloidal field plots retained the same qualitative character, where a large loop formed near the cutoff radius but field lines in the outer disc tilted more towards the equatorial plane of the disc.

The disc averaged equations predict that the exponential growth rate $\sigma \propto \sqrt{\alpha_d}\Omega_K$, scaling like $\sqrt{\alpha_d}$ and the local Keplerian angular velocity. We plot vertically integrated $\bar{B}_Z$ at radii $R = 10, 15$ and 20 as a function of angular phase $\Omega_K t$ for the case $\alpha_d = 0.1$ (Fig. 7.6). We scale the magnetic field by $\alpha_d^{-1/2}$ and the phase by $\alpha_d^{1/2}$ for ease in comparison of the other simulations. We see that there is in-

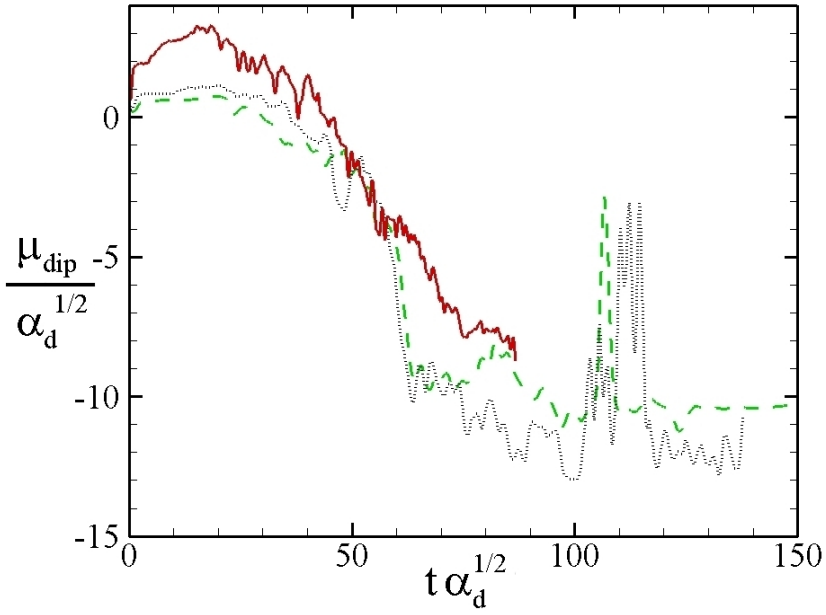

Figure 7.3: Dipole moment $\mu_{\rm dip}$ as a function of time for dynamo numbers $N_d = 1$ (red, solid), 5 (black, dot) and 10 (green, dash). These runs had a constant disc diffusivity $\alpha_\eta = 0.1$ and the dynamo number was varied using the $\alpha_{\rm dyn}$ parameter. By scaling the time axis to $\alpha_d^{1/2}$ and the dipole moment $\mu_{\rm dip}$ to $\alpha_d^{-1/2}$ we see the universal scaling of the late time dipole moment and of the growth rate.

deed a period of exponential growth lasting a time scale of $O(1)$ where the field likewise changes by $O(1)$. The scaling (7.9) suggests that $\sigma \approx \sqrt{3}$ in these units but we find, averaging the rates for these three radii and $\alpha_d = 0.01, 0.05$ and 0.1 runs $\sigma = 2.0 \pm 1.0$. This suggests that our linear analysis where we dropped order one numbers is valid during this short time. At late times a gap begins to form for $R < R_{\rm dyn}$, as the inner disc becomes magnetically dominated owing to the advected magnetic flux.

The magnetic field strength in the disc is also found to increase in time. We estimate the field in the disc by integrating over all cells with density $\rho > \rho_{floor} =$

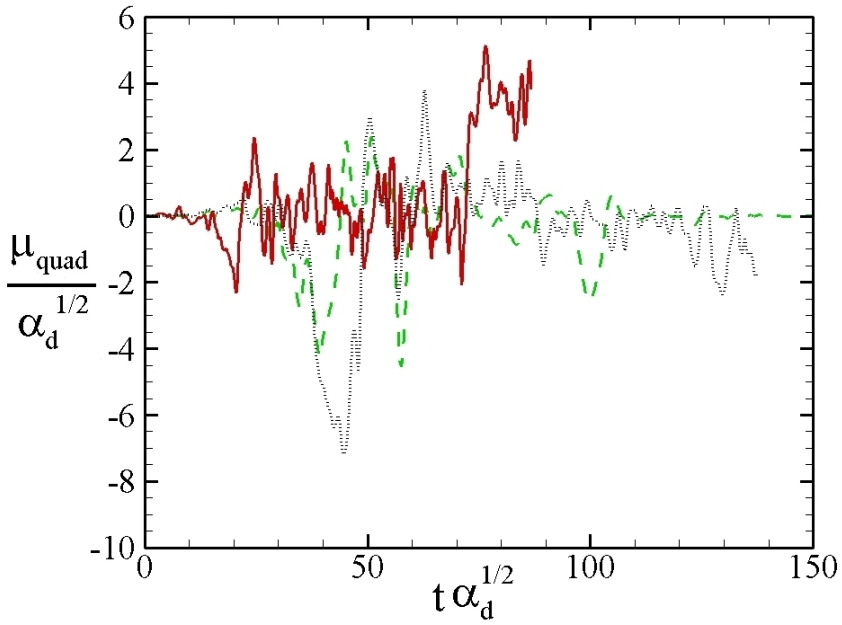

Figure 7.4: Quadrupole moment $\mu_{\rm quad}$ as a function of time for dynamo numbers $N_d = 1$ (red, solid), 5 (black, dot), 10 (green, dash). These runs had a constant disc diffusivity $\alpha_\eta = 0.1$ and the dynamo number was varied using the $\alpha_{\rm dyn}$ parameter. We have scaled the time axis to $\alpha_d^{1/2}$ and the quadrupole moment $\mu_{\rm quad}$ to $\alpha_d^{-1/2}$.

1.0 and define the averaged field in the disc via

$$\bar{B}_i = \left(\frac{\int_{\rho>\rho_{\rm floor}} (B_i)^2 \, dV}{\int_{\rho>\rho_{\rm floor}} dV} \right)^{1/2} . \tag{7.25}$$

We define the averaged field in this way because B_R and B_ϕ are antisymmetric about the disc plane and would average out to zero otherwise when integrating over the entire disc. We show a plot of $\bar{B}_R/\bar{B}_\phi$ and $\bar{B}_R$ as functions of time in Fig. 7.7 and Fig. 7.8 . We see that the radial magnetic field is an increasing function of time and grows nearly linearly. We see that the ratio of radial to toroidal magnetic field is, to an order one number, constant over the simulation time. This suggests that the simple picture whereby differential rotation

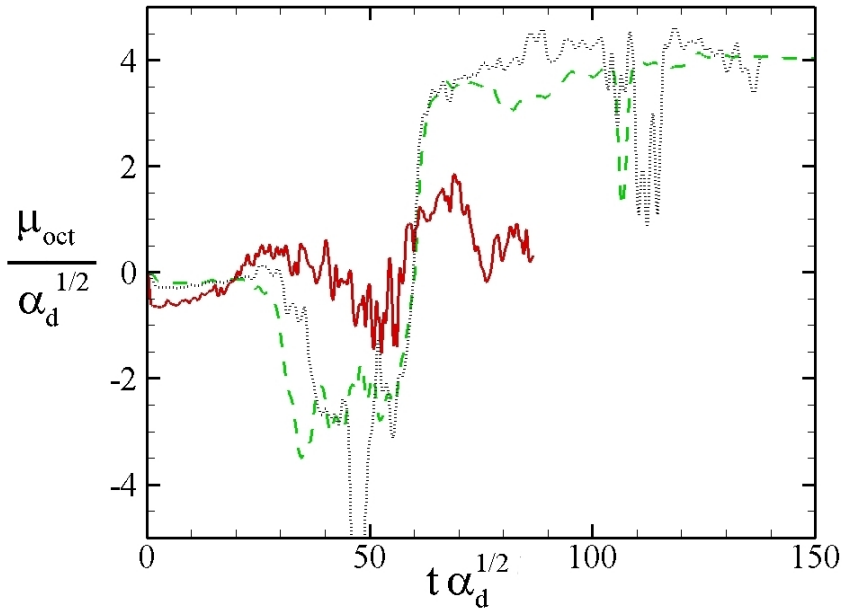

Figure 7.5: Octupole moment $\mu_{\rm oct}$ as a function of time for dynamo numbers $N_d = 1$ (red, solid), 5 (black, dot) and 10 (green, dash). These runs had a constant disc diffusivity $\alpha_\eta = 0.1$ and the dynamo number was varied using the $\alpha_{\rm dyn}$ parameter. Note how the octupole component has the opposite sign of the dipole component at late times.

creates toroidal field, and the α-dynamo transforms this field into poloidal field is qualitatively correct. Unlike on the surface of the star, where the field saturates at late times in the simulation, the integrated field in the disc continues to grow because in the outer parts of the disc where $R \sim 20$, $\tau \sim \Omega_K^{-1}$. Since the growth rate is set by the local Keplerian time, on time scales of the simulation the outer part of the disc does not have time to saturate with magnetic field, whereas near the star, where time scales are expected to be shorter and field is advected inwards at a faster rate the field has time to saturate. We can estimate the growth rate of $\bar{B}$ by assuming a local exponential growth rate $\sigma t \Omega_K$. Then $\bar{B} = \int B_0^2 e^{2\sigma t \sqrt{GM} R^{-3/2}} R dR \sim t^{4/3}$. We find $\bar{B} \sim t^{1.1}$ so a slightly weaker dependence

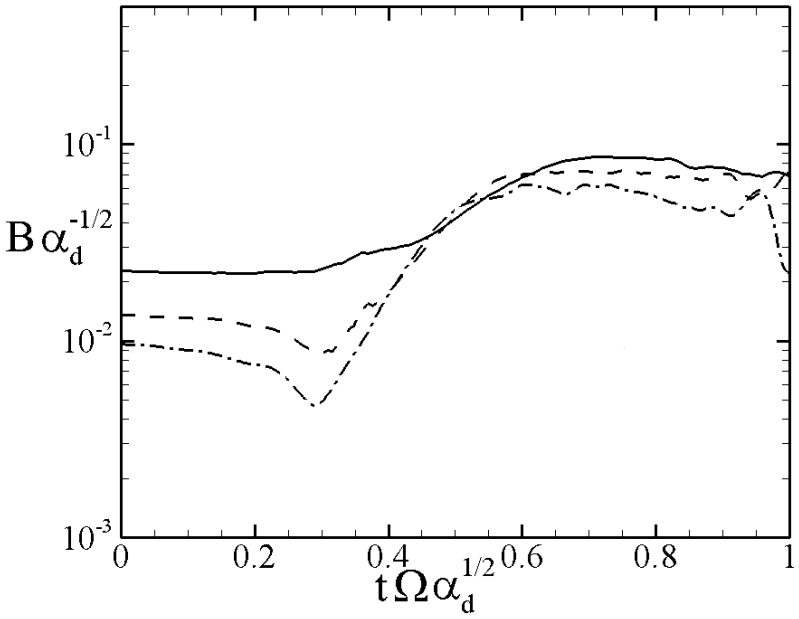

Figure 7.6: Vertically integrated magnetic field $\bar{B}_Z$ at radii R = 10(solid), 15(dash) and 20(dash – dot) as a function of angular phase Ωt scaled by $\alpha_d^{1/2}$ for the case $\alpha_d = 0.1$. The exponential growth predicted by the linearized regime occurs for phase angles $t\Omega\sqrt{\alpha_d} \ll 1$

than predicated by this model. However, it provides a semi-quantitative understanding of how polynomial growth is achieved globally whereas growth is exponential locally.

An interesting question is how the field generated by the dynamo affects matter outflows. We measure the total mass flux $\dot{M}$ at the outer boundaries $Z = \pm 5$ for various dynamo numbers (Fig. 7.9). Choosing to measure mass flux along boundaries in the range $3 < Z < 8$ had little effect on the results. We also require that any matter flux have a velocity $|v_p| > 0.1$, which corresponds to an observationally interesting $v \sim 200$km/s. We note that non trivial outflows are generated for dynamo number $N_d = 10$. The outflows begin at approximately

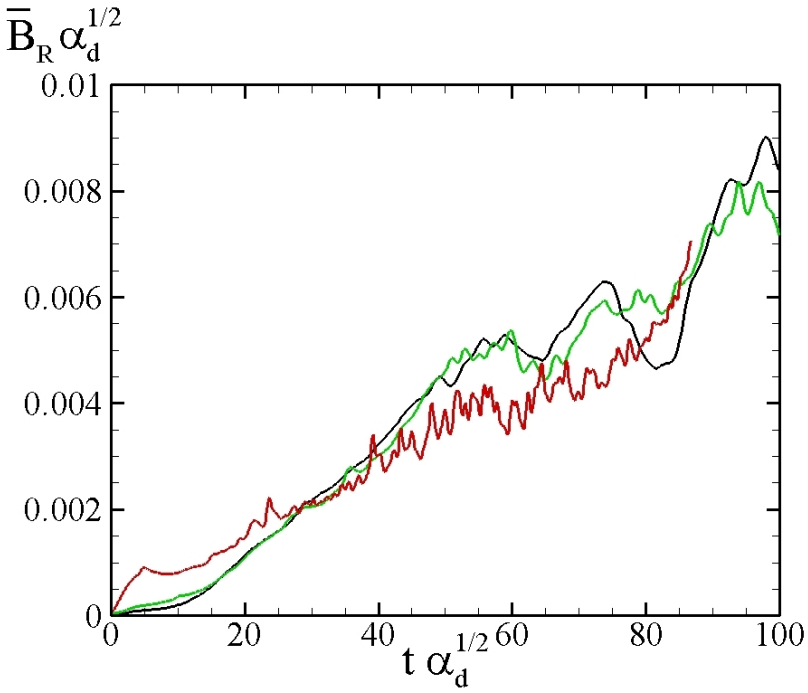

Figure 7.7: Average radial magnetic field strength $\bar{B}_R$ computed from 7.25 for the cases $\alpha_d = 0.01$ (red), 0.05 (green) and 0.1 (black). Unlike the field around the star, the disc averaged magnetic field does not have time to saturate on time scales of the simulation.

$t = 150$ inner disc orbits, corresponding to a time $t \sim 5$yrs for T Tauri stars. This is when the dipole moment reaches its saturation value and the plasma $\beta < 1$ in the inner parts of the disc near $R = R_{\rm dyn}$. Disc dynamos are therefore suitable candidates to explain time varying outflows observed in T Tauri systems with observed time scales between outflows of $10 - 100$yrs. Such a model has previously been explored by Stepanovs, Fendt and Sheikhnezami (2014) where the dynamo was explicitly turned on and off to produce time varying outflows. Though oscillatory, the mass flux $\dot{M} \approx 0.025$ or approximately $6.8 \times 10^{-9} M_\odot$/yr for a T Tauri star, which is consistent with observational values. The start of outflow generation corresponds to a decrease in the ratio of matter to magnetic pressure β. We plot this parameter, averaged over the thickness of the disc, as a function of radius for $t = 0,\ 100,\ 200$ and 300 in Fig. 7.10. Winds are primarily

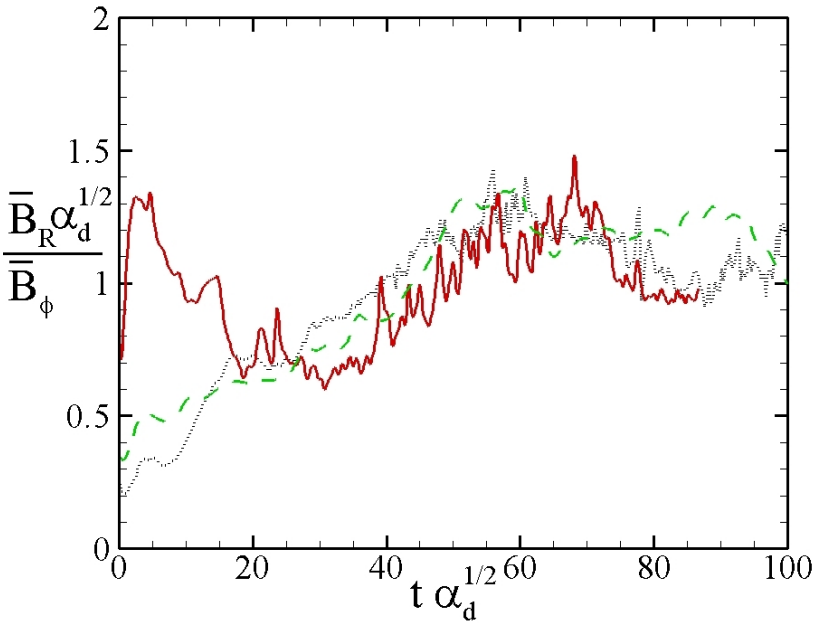

Figure 7.8: Average radial magnetic field strength $\bar{B}_R/\bar{B}_\phi$ computed from 7.25 for the cases α_d = 0.01 (red), 0.05 (green) and 0.1 (black). This ratio varies by an order one number, suggesting that the picture where toroidal field is built up via differential rotation and a fraction of this is converted to poloidal field via dynamo action is qualitatively correct.

launched from the inner part of the disc. We see that the region $R_* < R < 5$ becomes magnetically dominated ($\beta < 1$) for $t > 200$, consistent with the formation of a gap for $R < R_{\rm dyn}$. The time of outflow generation also corresponds to the time at which the stellar multipoles asymptote to their late time values. At this time our linear analysis (7.4) breaks down because we can no longer ignore the v_Z velocity component. Flux can now flow in the Z direction, thereby halting the growth of flux on the surface of the star. We note that though the stellar dipole and octupole moments saturate, other features of the disc remain non-stationary - the stellar mass flux and mass flux in the wind continue to vary with time. This is consistent with the picture that winds are primarily affected

by the disc, in particular near the inner disc where the mass flux is greatest. Outflows can be enhanced via dynamo growth on time scales of the simulation. Cowling's theorem can be circumvented because the timescales for magnetic field growth are shorter than the diffusion timescale.

The time when significant outflows are generated corresponds to the time when the dipole moment reaches its saturation value of $\mu_{\rm dip} \approx 3$. We compare this to a run where the initial magnetic field is a dipole with magnetic moment $\mu_{\rm dip} = 3$, corresponding to this late time magnetic moment of the dynamo generated field. This field configuration generates outflows roughly an order of magnitude smaller than the late time dynamo configuration, but at earlier times - since the stellar dipole moment is already present, it can begin generating outflows right away without first having to be generated in the disc. Torkelsson and Brandenburg (1994a) showed that if a stellar dipole is used as the seed field, the field generated in the disc has opposite polarity. Dyda et al. (2015) showed that anti-aligned stellar dipole and disc fields had suppressed outflows compared to a purely disc field because the field line structure in the inner part of the disc was not conducive to mass loading. Our results here are consistent with this, where the case with a seed disc field has the strongest outflows. If the dynamo is turned off, this stellar dipole configuration settles to a configuration with $\mu_{\rm dip} \approx 2.5$ and the higher order moments are zero. If the dynamo is turned on, the dipole moment grows and saturates to $\mu_{\rm dip} \approx 4$, and the octupole moment saturates to $\mu_{\rm oct} \approx -0.5$. Since $\Psi_{\rm dip} \propto R^{-1}$ the leading order component of the flux function gradient in (7.12b) has the opposite sign of the case for $\Psi_{\rm disc} \sim R^{3/4}$ and the stellar dipole becomes more positive. We observe the same behaviour as for the disc field where the dipole and octupole have the same sign until saturation, at which time it quickly reverses direction. Though the disc dynamo generates

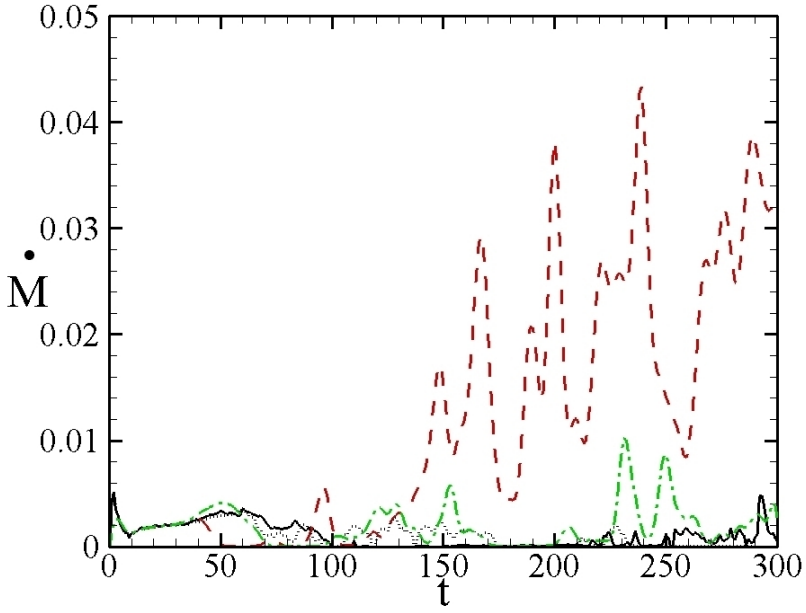

Figure 7.9: Total mass flux $\dot{M}$ as a function of time for dynamo numbers N_d = 0 (black, dotted), 1 (black, solid), 5 (green, dash − dot), 10 (red, dash) (α_d = 0, 0.01, 0.05, 0.1). Observationally significant outflows occur after t = 150.

a dipole component of the magnetic field, it is unclear whether a disc dynamo can generate a closed magnetosphere which has been shown to generate strong outflows in the propelor regime.

We vary the dynamo number by keeping $\alpha_d = 0.1$ fixed and varying the magnetic diffusivity from $0.03 \leq \alpha_\eta \leq 0.3$. The viscosity is also kept constant at $\alpha_\nu = 0.3$. Below we plot the dipole moment as a function of time for these various runs. As before, the dipole moment saturates to a certain value. Interestingly, the sign of the dipole moment depends on the magnetic diffusivity. For $\alpha_\eta \leq 0.05$ then $\mu_{\rm dip} > 0$ and for $\alpha_\eta \geq 0.07$ then $\mu_{\rm dip} < 0$ (Fig. 7.11). Empircally the field line structure is different in these two regimes. In the case of larger diffusivity, the field lines in the outer part of the disc are mostly vertical, threading

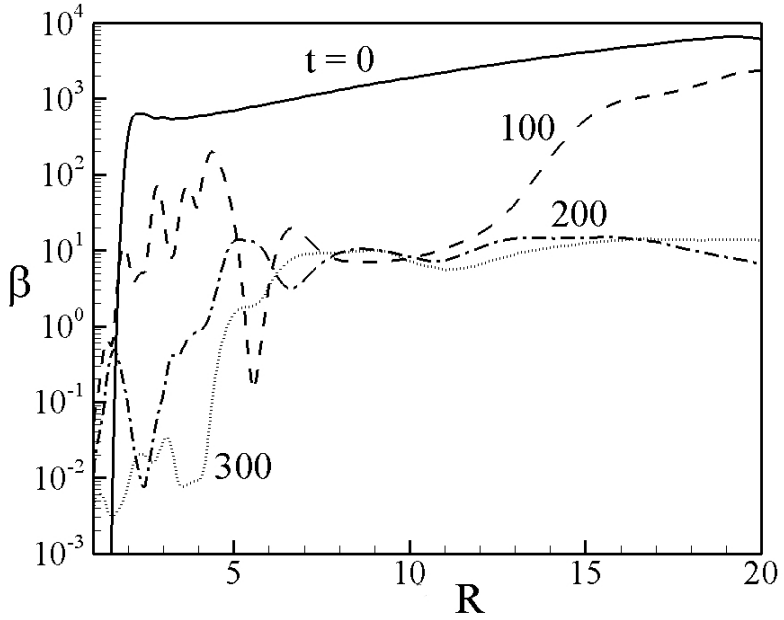

Figure 7.10: Plasma $\beta = 8\pi P/|\mathbf{B}|^2$ as a function of radius for t = 0 (solid), 100 (dash), 200 (dash-dot) and 300 (dotted) in the case $\alpha_d = 0.1$. Note that when the inner disc $R < 5$ becomes magnetically dominated, an inner disc wind begins to outflow.

through the disc. In contrast, for the smaller diffusivity cases the field lines are nearly *parallel* with the disc. This is what we would expect as field lines will naturally tilt towards the disc if they are frozen in to the matter and the matter accretes inwards. Decreasing the dynamo parameter $\alpha_d = 0.01$ had no effect on the sign of the generated dipole moment - in fact, the late time value $\mu_d \propto \alpha_d^{-1/2}$ holds for $\alpha_d < 0.1$ suggesting that the effect is not due to a changing dynamo number. Rather, the sign of the late time dipole moment depends on the sign of the poloidal field at early times near the star. This is controlled by the relative strengths of viscous and diffusive effects. The sign change in the generated dipole is likely due to an increase in viscous effects in the disc. The Prandtl number in the case where a large positive dipole grew was $\mathcal{P} = 10$ whereas for other

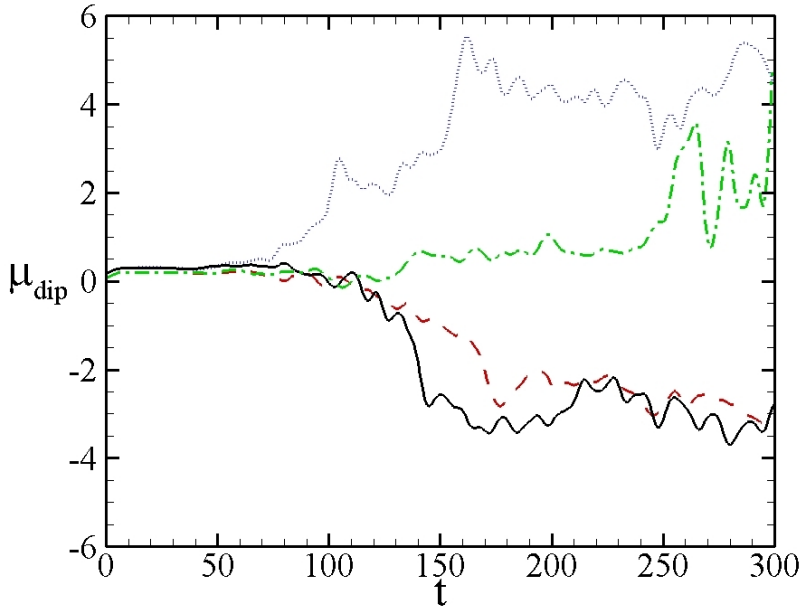

Figure 7.11: Dipole moment $\mu_{\rm dip}$ as a function of time for fixed $\alpha_d = 0.1$ and viscosity $\alpha_\nu = 0.3$ with varying magnetic diffusivity $\alpha_\eta = 0.1$ (black, solid), 0.07(red,dash), 0.05 (green, dash-dot) and 0.03 (blue, dotted).

runs this ratio was $\mathcal{P} \lesssim 1$. In cases where the late time dipole moment asymptotes to a negative value, the poloidal field in the upper hemisphere is negative at early times. This is reversed for cases where the dipole moment asymptotes to a positive value. As described in Section 7.1.2, changing the relative strength of the viscosity and diffusivity changes the sign of a term govewrning the flux function evolution. Since the flux function is coupled to the toroidal field, we expect this to change the sign of the toroidal field.

7.2.2 Strong Dynamo

For $\alpha_d > 0.1$ the evolution of the disc is qualitatively different. We show poloidal plots of the disc density ρ, magnetic flux contours Ψ and poloidal velocity vectors v_p of a typical run in the strong dynamo regime in Fig. 7.12. Magnetic loops form for all radii $R > R_{\rm dyn}$ unlike in the weak dynamo regime where loops only form close to $R_{\rm dyn}$. Though loops form along the entire length of the disc, the magnetic pressure is strongest in the inner portions of the disc. This innermost loop opens up due to the differential rotation of the disc and pushes out the flux from the outer disc. Because the dynamo is much stronger, the disc becomes magnetically dominated and unstable. The dynamo time scale is too short and disrupts the evolution of the disc on time scales of the simulation. It begins to warp and eventually breaks up as a gap opens near $R \sim R_{\rm dyn}$ where the magnetic pressure is dominant. Because the disc becomes unstable and breaks up we can only study these cases for $t \sim 100$ inner disc orbits. The linear theory, (7.8) suggests that the growth rate $\sigma \propto \alpha_d$ when $\alpha_d \sim 1$. However this is not seen in our simulations. In this regime we do not see a period of exponential growth suggesting that if it occurs, it is for such a short period of time as to be unnoticeable. The gap can open on much faster time scales owing to an accretion rate of order a few larger than in the weak dynamo regime. The loop like structure of the generated field causes the field components to alternate signs in the disc plane, and field anihillations lead to chaotic behaviour.

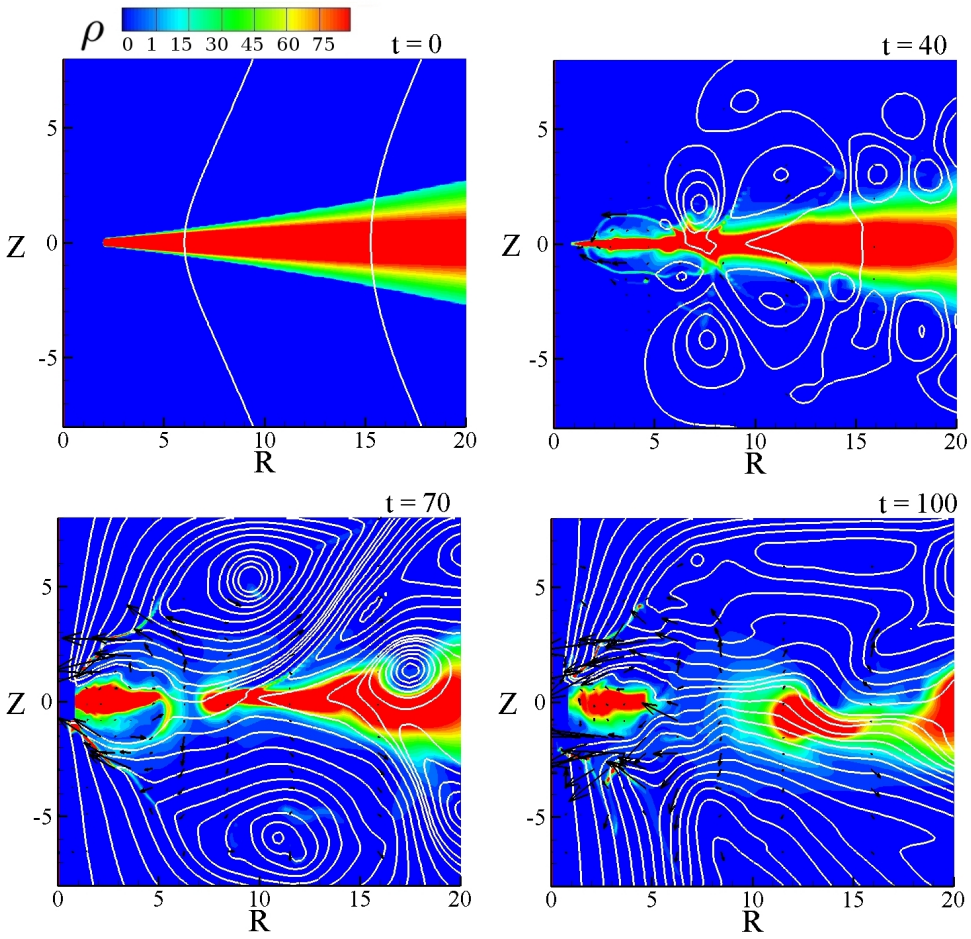

Figure 7.12: Density ρ (color), poloidal field lines Ψ (white) and poloidal velocity $v_{\rm p}$ for the case $N_d = 28$ ($\alpha_d = 0.28$). t = 0 shows the initial large scale seed field. By t = 40 magnetic loops have formed along the entire length of the disc. At t = 70 we can see the quadrupolar nature of the field as loops are advected inwards. At late times these loops expand into open field lines. The magnetic pressure has grown enough to seriously disrupt the disc and open a gap at $R_{\rm dyn} = 5$.

7.3 Conclusion

We investigated the effects of an α-dynamo operating within an accretion disc. Simulation results were affected by three dimensionless parameters controlling the dynamo strength α_d, the disc viscosity α_ν and the magnetic diffusivity α_η. Our main findings are summarized below.

1. An initial poloidal seed magnetic field threading the disc grows via the disc dynamo - the differential rotation of the disc creates a toroidal magnetic field, which is converted to poloidal magnetic field via dynamo action. This process repeats until at late times the poloidal field strength saturates to a value $\propto \sqrt{\alpha_d}$. The local growth rate of the field during early times is exponential and set by the local Keplerian velocity and the strength of the dynamo with $\sigma \propto \Omega_K \alpha_d^{1/2}$

2. The dynamo excites dipole and octupole modes, allowing for the growth of these modes on the star. Quadrupole modes are suppressed at late times, owing to the symmetry of the initial seed field. Dipole and octupole modes saturate to values of opposite polarity with magnitudes $\propto \sqrt{\alpha_d}$. This has interesting observational consequences since a disc dynamo could be responsible for the observed dipole and higher order multipoles observed on T Tauri stars.

3. A seed field that is too small to generate observationally interesting outflows can grow on time scales $\tau \sim \Omega_K^{-1} \alpha_d^{-1/2}$ to values which are high enough to launch observationally significant outflows. This suggests that disc dynamos may be important in generating the large scale, ordered magnetic fields needed for MHD launched outflows.

4. A stellar dipole seed field generates a field with outflows ~ 10 weaker than

a disc seed field because of interactions between the late time disc field and the stellar dipole. This may be useful in distinguishing between systems that advected their magnetic field from the ISM and those that generated them local via a dynamo mechanism.

5. Increasing the Prandtl number causes the polarity of the late time dipole moment to change. The field evolution is therefore a function of three time scales: the dynamo, viscous and diffusive times.

6. For larger values of the dynamo parameter $\alpha_d \gtrsim 0.1$ the disc becomes magnetically dominated on time scales $\tau \sim \Omega_K^{-1}$ - a gap forms in the inner disc where the dynamo is strongest, eventually leading to the break up of the entire disc as the growth of the field goes unchecked.

Physically these findings can be reconciled by understanding that three time scales are at play - the dynamo time scale, the viscous time scale and the diffusive time scale. If the dynamo time scale dominates, the viscous disc becomes magnetically dominated and breaks up. If the diffusive time scale dominates then the field does not grow sufficiently to launch outflows. When time scales are comparable we are in the "weak dynamo" regime where outflows can be enhanced but the overall disc dynamo is not disrupted. The relative strength of the viscous and diffusive effects determines the sign of the late time dipole field.

Because results are sensitive to the magnetic diffusivity in the disc, it is important to perfrom full 3D simulations where the diffusivity is treated more realistically than an α parameter prescription. When there is no dynamo present, the poloidal field is small, the diffusivity is low and poloidal field gradients are

not smoothed out. Turning on the dynamo increases the poloidal field, which should increase the diffusivity and therefore smooth out magnetic field gradients. This should allow for a stronger dynamo as more flux is diffused outwards, owing to the enhanced diffusivity.

APPENDIX

7.A Numerically Extracting Multipole Moments

Any magnetic field can be described by its multipole expansion. Below, we derive formulae for the axysymmetric dipole, quadrupole and octupole components of a magnetic multipole expansion in terms of surface integrals in cylindrical coordinates. These are used to numerically extract the multipole coefficients of the magnetic field configurations in our simulations.

7.A.1 Dipole Moment

Consider a dipole moment, symmetric about the Z-axis with flux function given by

$$\Psi = \mu_{\rm dip} \frac{R^2}{\left(R^2 + Z^2\right)^{3/2}}, \tag{7.26}$$

and poloidal magnetic fields

$$B_R = 3\mu_{\rm dip} \frac{RZ}{\left(R^2 + Z^2\right)^{5/2}}, \tag{7.27}$$

$$B_Z = \mu_{\rm dip} \frac{(2Z^2 - R^2)}{\left(R^2 + Z^2\right)^{5/2}}. \tag{7.28}$$

Given a general magnetic field, we want to extract its dipole moment from its multipole expansion at any given time. In general the dipole moment is given by

$$\mathbf{m} = \frac{1}{2} \int d\mathbf{V} \left[\mathbf{r} \times \mathbf{J}\right] = \frac{c}{8\pi} \int d\mathbf{V} \left[\mathbf{r} \times (\nabla \times \mathbf{B})\right], \tag{7.29}$$

where we work in CGS units and have used Ampere's law. We will integrate over a cylinder $0 < R < a$, $-h < Z < h$, $0 < \phi < 2\pi$ enclosing the star. We

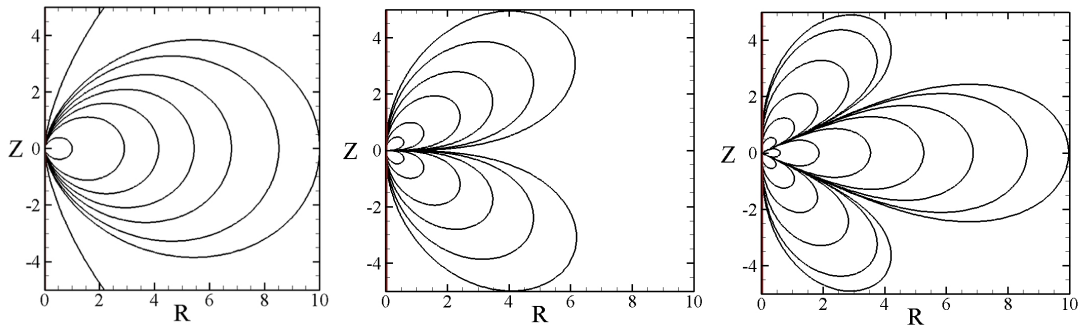

Figure 7.13: Flux lines of axially symmetric dipole (left), quadrupole (center) and octupole (right).

also assume the boundary condition $\Psi(0, Z) = 0$ Using vector identities we may write

$$\mathbf{m} = \frac{c}{8\pi} \int d\mathbf{V} \left[\nabla (\mathbf{r} \cdot \mathbf{B}) - (\mathbf{r} \cdot \nabla) \mathbf{B} - (\mathbf{B} \cdot \nabla) \mathbf{r} \right]. \tag{7.30}$$

We are interested in the $\hat{Z}$ component of the magnetic moment, μ_{dip}. We calculate the contribution to μ_{dip} from each of the above three terms below.

$$\begin{aligned} T_1 \equiv \int d\mathbf{V}\, \nabla_Z (\mathbf{r} \cdot \mathbf{B}) &= \int d\mathbf{S}_Z (\mathbf{r} \cdot \mathbf{B}) \\ &= 2\pi \int_0^a R dR\, (\mathbf{r} \cdot \mathbf{B}) \Big|_{-h}^{h}, \end{aligned} \tag{7.31}$$

where we have used the divergence theorem to convert the volume integral to a surface integral over the sides of the cylinder and only the top and bottom contribute to the Z-component. Using the definition of magnetic field in terms of the flux function we may write

$$T_1 = 2\pi \int_0^a dR\, R^2 B_R \Big|_{-h}^{h} + 2\pi h \Big[\Psi(a, h) + \Psi(a, -h) \Big]. \tag{7.32}$$

The Z-component contribution from the second term is

$$\begin{aligned} T_2 &= -\int d\mathbf{V} \left[(\mathbf{r} \cdot \nabla) \mathbf{B} \right]_Z \\ &= -2\pi \int R dR\, dZ \left(R \frac{\partial}{\partial R} + Z \frac{\partial}{\partial Z} \right) B_Z. \end{aligned} \tag{7.33}$$

Integrating the first term by parts and using the definition of the magnetic flux function we may write

$$T_2 = -2\pi \int_{-h}^{h} dZ\Big[a^2 B_Z(a,Z) - 2\Psi(a,Z) - RZB_R(a,Z)\Big]. \tag{7.34}$$

The third term can be dealt with by rewriting it in terms of the flux function and explicitly carrying out the integration in R to yield

$$T_3 = -2\pi \int_{-h}^{h} dZ\, \Psi(a,Z). \tag{7.35}$$

Combining these terms we arrive at the result

$$\begin{aligned}\mu_{\rm dip} =& \frac{c}{4}\Bigg\{ \int_0^a dR\, R^2 B_R(R,Z)\Big|_{-h}^{h} + h\Big[\Psi(a,h) + \Psi(a,-h)\Big] \\ &- \int_{-h}^{h} dZ\Big[a^2 B_Z(a,Z) - \Psi(a,Z) - aZB_R(a,Z)\Big]\Bigg\},\end{aligned} \tag{7.36}$$

which is easy to implement in our cylindrical code.

7.A.2 Quadrupole Moment

Consider a quadrupole moment, symmetric about the Z-axis with flux function given by

$$\Psi = \frac{3\mu_{\rm quad}}{4} \frac{R^2 Z}{(R^2+Z^2)^{5/2}}, \tag{7.37}$$

and poloidal magnetic fields

$$B_R = -\frac{3\mu_{\rm quad}}{4} \frac{R(R^2-4Z^2)}{(R^2+Z^2)^{7/2}}, \tag{7.38}$$

$$B_Z = \frac{3\mu_{\rm quad}}{4} \frac{(Z^2-3R^2)}{(R^2+Z^2)^{7/2}}. \tag{7.39}$$

Its quadrupole moments are $D_{11} = D_{22} = -D_{33}/2$ where

$$\begin{aligned}\mu_{\rm quad} \equiv D_{33} &= \int d\mathbf{V}\ \ [\mathbf{r}\cdot(\nabla\times\mathbf{J})]\, Z^2 \\ &= 2\int d\mathbf{V}\ Z\ (\mathbf{r}\times\mathbf{J})_Z\end{aligned} \tag{7.40}$$

where as with the dipole, we are interested in the Z-component of μ_{quad}. Using Maxwell's equations we can write

$$\mu_{\text{quad}} = \frac{c}{2\pi} \int d\mathbf{V} Z \Big[\mathbf{r} \times (\nabla \times \mathbf{B}) \Big]_Z. \tag{7.41}$$

As with the dipole case, this expression can be expanded using a vector identity as

$$\mu_{\text{quad}} = \frac{c}{2\pi} \int d\mathbf{V}\, Z \Big[\nabla (\mathbf{r} \cdot \mathbf{B}) - (\mathbf{r} \cdot \nabla) \mathbf{B} - (\mathbf{B} \cdot \nabla) \mathbf{r} \Big]_Z. \tag{7.42}$$

As in the dipole case we calculate each of these terms separately. We are interested in the $\hat{Z}$ component of the quadrupole moment.

$$\begin{aligned} T_1 &\equiv \int d\mathbf{V}\, Z\, \nabla_Z (\mathbf{r} \cdot \mathbf{B}) \\ &= - \int d\mathbf{V} (\mathbf{r} \cdot \mathbf{B}) \hat{z} + Z (\mathbf{r} \cdot \mathbf{B}) \Big|_{-h}^{h}, \end{aligned} \tag{7.43}$$

where we have integrated by parts. Writing out the magnetic field in term of the flux function, we expand the first term and carry out some of the intergrals. The second term we evaluate on the top and bottom of the cylinder which yields

$$\begin{aligned} T_1 = 2\pi \int_0^a dR\, R\, \Psi(R, z) \Big|_h^h - 2\pi \int_{-h}^h dZ\, Z\, \Psi(a, Z) \\ + 2\pi \int_0^a dR\, R\, Z\, (R B_R + Z B_Z) \Big|_{-h}^h. \end{aligned} \tag{7.44}$$

Expanding the second term and carrying out the angular integral we find

$$\begin{aligned} T_2 &\equiv - \int d\mathbf{V} Z (\mathbf{r} \cdot \nabla) \mathbf{B} \\ &= -2\pi \int dR\, dZ \left(Z R^2 \frac{\partial B_z}{\partial R} + Z^2 R \frac{\partial B_z}{\partial Z} \right). \end{aligned} \tag{7.45}$$

Performing integration by parts for the R integral on the first term and then writing it out in terms of the flux function allows the integral in R to be evaluated, yielding

$$\begin{aligned} T_2 = 2\pi \int_{-h}^h dZ\, 2Z\, \Psi(a, Z) - a^2 Z B_z(a, Z) \\ + 2\pi \int_{-h}^h dZ a Z^2 B_R(a, Z). \end{aligned} \tag{7.46}$$

For the final term, we take the divergence, expand it in terms of the flux function, carry out the integral in R and find

$$T_3 = -\int d\mathbf{V} Z(\mathbf{B}\cdot\nabla)Z = -2\pi\int_{-h}^{h} dZ\, Z\, \Psi(a,Z). \tag{7.47}$$

Combining these terms we arrive at the result

$$\begin{aligned}\mu_{\rm quad} = c\int_0^a dR\Big[R\Psi(R,Z) + RZ(RB_R + ZB_Z)\Big]\Big|_{-h}^{h} \\ + c\int_{-h}^{h} dZ\Big[aZ^2 B_R(a,Z) - a^2 Z B_z(a,Z)\Big].\end{aligned} \tag{7.48}$$

7.A.3 Octupole Moment

Consider an octupole moment, symmetric about the Z-axis with flux function given by

$$\Psi = \frac{\mu_{\rm oct}}{2}\frac{R^2(4Z^2 - R^2)}{(R^2+Z^2)^{7/2}}, \tag{7.49}$$

and poloidal magnetic fields

$$B_R = \frac{5\mu_{\rm oct}}{2}\frac{RZ(4Z^2 - 3R^2)}{(R^2+Z^2)^{9/2}}, \tag{7.50}$$

$$B_Z = \frac{\mu_{\rm oct}}{2}\frac{(8Z^4 - 24Z^2R^2 + 3R^4)}{(R^2+Z^2)^{9/2}}. \tag{7.51}$$

The octupole moment is given by

$$\mu_{\rm oct} \equiv 2\sqrt{\frac{\pi}{7}} M_{30}, \tag{7.52}$$

where

$$M_{30} = \frac{1}{4}\int d\mathbf{V}\,[\mathbf{r}\times\mathbf{J}]\cdot\nabla\left(r^3 Y_{30}\right), \tag{7.53}$$

and

$$r^3 Y_{30} = \sqrt{\frac{7}{4\pi}} r^3 P_3(\cos\theta) = \frac{1}{4}\sqrt{\frac{7}{\pi}} Z\left(2Z^2 - 3R^2\right), \tag{7.54}$$

is a spherical harmonic that we have written in terms of the Legendre polynomial P_3. Expanding the cross product and using Amperes law to write out the current in terms of the magnetic field and evaluating the azimuthal integral we find

$$\begin{aligned}\mu_{\text{oct}} = \frac{3c}{16}\Bigg[4\int dRdZR^2Z^2\left(\frac{\partial B_R}{\partial Z} - \frac{\partial B_Z}{\partial R}\right) \\ - \int dRdZR^4\left(\frac{\partial B_R}{\partial Z} - \frac{\partial B_Z}{\partial R}\right)\Bigg].\end{aligned} \tag{7.55}$$

Evaluate each of these terms separately. The first term is

$$\begin{aligned}T_1 &\equiv \int dRdZR^2Z^2\left(\frac{\partial B_R}{\partial Z} - \frac{\partial B_Z}{\partial R}\right) \\ &= \int dRR^2h^2B_R\Big|_{-h}^{h} - 2\int dR\, dZR\Psi + 2\int dRRZ\Psi\Big|_{-h}^{h} \\ &- \int dZZ^2a^2B_Z(a,Z) + 2\int dZZ^2\Psi(a,Z),\end{aligned} \tag{7.56}$$

where we have used integration by parts and the definition of magnetic field in terms of the magnetic flux function. Similarly, the second term is

$$\begin{aligned}T_2 &\equiv \int dRdZR^4\left(\frac{\partial B_R}{\partial Z} + \frac{\partial B_Z}{\partial R}\right) \\ &= \int dRR^4B_R\Big|_{-h}^{h} - \int dZa^4B_Z(a,Z) \\ &- 8\int dRdZR\Psi + 4\int dZa^2\Psi(a,Z).\end{aligned} \tag{7.57}$$

Combining these terms we find

$$\begin{aligned}\mu_{\text{oct}} =& \frac{3c}{16}\Bigg[4\int dR\, R^2h^2B_R\Big|_{-h}^{h} + 8\int dR\, RZ\Psi\Big|_{-h}^{h} \\ &- 4\int dZ\, Z^2a^2B_Z(a,Z) + 8\int dZ\, Z^2\Psi(a,Z) \\ &- \int dR\, R^4B_R\Big|_{-h}^{h} + \int dZa^4B_Z(a,Z) \\ &- 4\int dZ\, a^2\Psi(a,Z)\Bigg].\end{aligned} \tag{7.58}$$

We note the cancellation of the volume integrals in T_1 and T_2, allowing the final expression to again only depend on surface integrals.

CHAPTER 8

CONCLUSIONS

Many astrophysical systems of interest consist of a central object, an accretion disc and a large scale magnetic field. The key dynamics of these systems involve angular momentum exchange and can be successfully modeled by MHD. We performed 2.5D axisymmetric MHD simulations to study a variety of phenomena associated with these types of systems.

We considered magnetic "loops" which arise naturally as solutions of the time independent MHD equations. We showed that these loops lead to the formation of Poynting dominated jets and matter driven winds, that carry angular momentum away from the system. We showed that the magnetic field acts to advect matter towards the star as predicted by thin disc models.

We showed that in systems where some matter was counter-rotating relative to the main parts of the disc, angular momentum was efficiently exchanged at the rotating/counter-rotating boundary and led to large ($10^2 - 10^4$) enhancements in the accretion rate.

We showed that accretion discs threaded by a disc field and/or a stellar dipole which were symmetric about the disc plane would still, at late time, produce asymmetric outflows. This is interesting as most observations have shown jet/counter-jets to be asymmetric in some way.

Finally we showed that an α-dynamo operating in the disc could grow a seed field initially too weak to launch observable outflows sufficiently to launch observable outflows.

BIBLIOGRAPHY

[1] Arfken, G.B., Weber, H.J., Harris, F.E., 2012, Mathematical Methods for Physicists.

[2] Alig, C., Schartmann, M., Burkert, A., & Dolag, K. 2013, ApJ, 771, 119

[3] Bacciotti, F., Eisloffel, J., & Ray, T.P. 1999, A&A, 350, 917

[4] Balbus, S.A., & Hawley, J.F. 1998, Rev. Mod. Phys., 70, 1

[5] Balsara, D.S., Spicer, D.S. 1999, J. Comp. Phys., 149, 270.

[6] Bardeen, J.M., Press, W.H., Teukolsky, S.A., 1972, ApJ, 178, 347.

[7] Bisnovatyi-Kogan, G.S., & Ruzmaikin, A.A. 1976, Ap&SS, 42, 401

[8] Bisnovatyi-Kogan, G.S. & Lovelace, R.V.E. 2007, ApJ, 667, L167

[9] Bisnovatyi-Kogan, G.S. & Lovelace, R.V.E.,2012, ApJ, 750, 109

[10] Blandford, R.D., Payne, D.G., 1982, MNRAS 199, 883.

[11] Braun, R., Walterbos, R.A.M., Kennicutt, R.C., & Tacconi, L.J. 1994, ApJ, 420, 558

[12] Caratti o Garatti, A., Garcia Lopez, R., Weigelt, G., Tambovtseva, L.V., Grinin, V.P., Wheelwright, H., Ilee, J.D., 2013, A&A, 554, A66

[13] Chagelishvili, G. D., Bodo, G., & Trussoni, E. 1996, A&A, 306,329

[14] Chakrabarty, D., Bildsten, L., Finger, M. H., Grunsfeld, J. M., Koh, D. T., Nelson, R. W., Prince, T. A., Vaughan, B. A., & Wilson, R. B. 1997, ApJ, 481, L101

[15] Choudhury, S.,R., & Lovelace, R.V.E, 1984, ApJ, 283, 331

[16] Ciri, R., Bettoni, & Galletta, G. 1995, Nature, 375, 661

[17] Coffey, D., Bacciotti, F., Woitas, J., Ray, T.P., & Eislöffel, J. 2004, ApJ, 604, 758

[18] Comins, N.F., Lovelace, R.V.E., Zeltwanger, T., & Shorey, P. 1997, ApJ, 484, L33

[19] Corsini, E.M. 2014, in *Counter-Rotation in Disk Galaxies*, ASP Conference Series, Vol. 486, Eds. E. Iodice & E. M. Corsini (ASP: San Francisco), p. 51

[20] Donati, J.-F.;, Jardine, M. M., Gregory, S. G., Petit, P., Bouvier, J., Dougados, C., Menard, F., Collier Cameron, A., Harries, T. J., Jeffers, S. V.;, & Paletou, F. 2007, MNRAS, 380, 1297

[21] Donati, J.-F., Jardine, M. M., Gregory, S. G., Petit, P., Paletou, F.; Bouvier, J., Dougados, C., Ménard, F., Collier Cameron, A., Harries, T. J., Hussain, G. A. J., Unruh, Y., Morin, J., Marsden, S. C., Manset, N., Aurière, M., Catala, C., & Alecian, E. 2008, MNRAS, 386, 1234

[22] Donati, J.F., Gregory, S.G., Alencar, S.H.P., Hussain, G., Bouvier,Dougados, C., J., Jardine, M.M., Ménard, F., Romanova, M.M.2012, MNRAS, 425, 2948

[23] Donati, J.F., Gregory, S.G., Alencar, S.H.P., Hussain, G., Bouvier, J., Jardine, M.M., Ménard, F., Dougados, C., & Romanova, M.M. 2013, MNRAS, 436, 881

[24] Dyda, S., Lovelace, R.V.E., Ustyugova, G.V., Lii, P.S., , Romanova, M.M., & Koldoba, A.V., 2013, ApJ, 432, 127

[25] Dyda, S., Lovelace, R.V.E., Ustyugova, G.V., Romanova, M.M., & Koldoba, A.V. 2015a, MNRAS. 446, 613.

[26] Dyda, S., Lovelace, R.V.E., Ustyugova, G.V., Lii, P.S., Romanova, M.M., & Koldoba, A.V. 2015b, MNRAS. 450, 481.

[27] Dyda, S., Lovelace, R.V.E., Ustyugova, G.V., & Koldoba, A.V., Wasserman, I.M., 2015c in prep

[28] Ellerbroek, L. E., Podio, L., Kaper, L., Sana, H., Huppenkothen, D., de Koter, A., & Monaco, L. 2013, A&A, 551, A5

[29] Fendt, C., & Sheikhnezami, S., 2013, ApJ, 774, 12

[30] Galetta, G. 1996, in *Barred Galaxies*, IAU Colloq. 157, Eds. R. Buta, D. Crocker, & B. Elmegreen, ASP Conference Series, 91, 11

[31] Godunov, S.K., 1959, Math. Sbornik, 47, 271.

[32] Grad, H., Rubin, H., 1958, Proceedings of the 2nd UN Conf. on the Peaceful Uses of Atomic Energy, Vol. 31, 190.

[33] Guan, X., & Gammie, C.F. 2009, ApJ, 697, 1901

[34] Guilet, J. & Ogilvie, G.I. 2012, MNRAS, 424, 2097

[35] Guilet, J. & Ogilvie, G.I. 2013, MNRAS, 430, 822 (arXiv:1212.0855)

[36] Gulati, M., Tarun, D.S., & Sridhar, S. 2012, MNRAS, 424, 348

[37] Hargreaves, J.K. 1992, *The Solar-Terrestrial Enviroment*, (Cambridge Univ. Press: Cambridge), chap. 5

[38] Hartigan, P., Hillenbrand, L., 2009, ApJ, 705, 1388

[39] Hayashi, M.R., Shibata, K., & Matsumoto, R. 1996, ApJ, 468:L37 L40

[40] Illarionov, A.F., & Sunyaev, R.A., 1975, A&A, 39,185

[41] Jardine M., Collier Cameron A., & Donati J.-F. 2002, MNRAS, 333, 339

[42] Koldoba, A., Ustyugova, G., Romanova, M.M., Lii, P., Comins, C., Dyda, S., Lovelace, R.V.E., 2015, New Astronomy, submitted.

[43] Kuznetsov, O. A., Lovelace, R. V. E., Romanova, M. M., & Chechetkin, V. M. 1999, ApJ, 514, 691

[44] Landau, L.D., Lifshitz, E.M., 1959, A Course of Theoretical Phisics.

[45] Leidenfrost, J.G. 1966, Int. J. Heat Mass Transfer, 9, 1153

[46] Lesur, G., Longaretti, P.Y., 2009, A&A, 504, 309.

[47] Li, L., & Narayan, R., 2004, ApJ, 601, 414

[48] Lii, P.S., Romanova, M.M., Ustyugova, G.V., Koldoba, A.V., & Lovelace, R.V.E. 2014, MNRAS, 441, 86

[49] Lii, P., Romanova, M.M., & Lovelace, R.V.E. 2012, MNRAS, 420, 2020

[50] Liu, C., Shang, H., Pyo, T., Takami, M., Walter, F., Yan, C., Wang, S., Ohashi, N., Hayashi, M., 2012, ApJ, 749, 62.

[51] Livio M., 1997, in Wickramasinghe D. T., Bicknell G. V., & Ferrario L., eds, IAU Coll. 163. ASP Conf. Ser. Vol. 121; Accretion Phenomena and Related Outflows. Astron. Soc. Pac., San Francisco, p. 845

[52] Lovelace, R.V.E. 1976, Nature, 262, 649

[53] Lovelace, R.V.E., Berk, H.L., Contopoulos, J., 1991, ApJ, 379, 696.

[54] Lovelace, R.V.E., & Chou, T., 1996, ApJ, 468, L25

[55] Lovelace, R.V.E., Jore, K.P., & Haynes, M.P. 1997, ApJ, 475, 83

[56] Lovelace, R.V.E., Li, H., Koldoba, A.V., Ustyugova, G.S., & Romanova, M.M. 2002, ApJ, 572, 445

[57] Lovelace, R. V. E., Mehanian, C., Mobarry, C.M., & Sulkanen, M.E. 1986, ApJS, 62, 1

[58] Lovelace, R. V. E., Newman, W. I., & Romanova, M. M. 1997, ApJ, 484, 628

[59] Lovelace, R.V.E., Romanova, M.M., & Bisnovatyi-Kogan, G.S. 1995, MNRAS, 275, 244

[60] Lovelace, R. V. E., Romanova, M. M., & Bisnovatyi-Kogan, G. S. 1999, ApJ, 514, 368

[61] Lovelace, R.V.E., Romanova, M.M., & Newman, W.I. 1994, ApJ 437, 136

[62] Lovelace, R. V. E., Romanova, M. M., Ustyugova, G. V., & Koldoba, A. V. 2010, MNRAS, 408, 2083

[63] Lovelace, R.V.E., Romanova, M.M., Lii, P., & Dyda, S. 2014, Comp. Astrophys. and Cosmol., 1, id3, 10pp

[64] Lovelace, R.V.E., Rothstein, D.M., & Bisnovatyi-Kogan, G.S. 2009, ApJ, 701, 885

[65] Lovelace, R.V.E., Turner, L., & Romanova, M.M. 2009, ApJ, 701, 225

[66] Lubow, S. H., Papaloizou, J. C. B., & Pringle, J. E. 1994, MNRAS, 267, 235

[67] Lynden-Bell, D., & Boily, C. 1994, MNRAS, 267, 146

[68] Matsakos, T., Vlahakis, N., Tsinganos, K., Karampelas, K., Sauty, C., Cayatte, V., Matt, S. P., Massaglia, S., Trussoni, E., & Mignone, A. 2012, A&A, 545, A53

[69] Melnikov, S., Eisloffel, J., Bacciotti, F., Woitas, J., Ray, T.P., 2009, A&A, 506, 763.

[70] Miller, K.A., Stone, J.M., 1997, ApJ, 489: 890-902.

[71] Mundt, R., Buehrke, T., Solf, J., Ray, T. P., & Raga, A. C. 1990, A&A, 232, 37

[72] Murphy, G.C., Ferreira, J., Zanni, C., 2010, A&A 512, A82.

[73] Nelson, R. W., Bildsten, L., Chakrabarty, D., Finger, M. H., Koh, D. T., Prince, T.A., Rubin, B. C., Scott, D. M., Vaughan, B. A., & Wilson, R, B. 1997, ApJ, 488, L117

[74] Newman, W.I., Newman, A.L., & Lovelace, R.V.E. 1992, ApJ, 392, 622

[75] Nixon, C.J., King, A.R., & Price, D.J. 2012, MNRAS, 422, 2547

[76] Paczyński, B., & Wiita, P. 1980, A&A, 88, 23

[77] Pariev, V.I., Colgate, S.A., Finn J.M. 2007, ApJ 658: 129-160.

[78] Perrin, M., Graham, J. R., 2007, ApJ, 670, 499

[79] Quach, D., Dyda, S., & Lovelace, R.V.E. 2015, MNRAS, 446, 622

[80] Ray, T.P. 1981, MNRAS, 196, 195

[81] Ray, T.P. 1982, MNRAS, 198, 617

[82] Ray, T. P., Mundt, R., Dyson, J. E., Falle, S. A. E. G., & Raga, A. C. 1996, ApJ, 468, L103

[83] Ray, T., Dougados, C., Bacciotti, F., Eisl ffel, J., & Chrysostomou, A. 2007, Protostars and Planets V, 231

[84] A.D. Rogava, G.R. Khujadze, General-Relativistic Model of Magnetically Driven Jet,General Relativity and Gravitation, Vol. 29, No. 3, 1997, arXiv:gr-qc/9604041v1

[85] Romanova, M.M, Ustyugova, G.V., Koldoba, A.V., Chechetkin, V.M., & Lovelace, R.V.E., 1998, ApJ 500, 703

[86] Romanova, M.M, Ustyugova, G.V., Koldoba, A.V., Chechetkin, V.M., &Lovelace, R.V.E. 2002, ApJ, 578, 420

[87] Romanova, M. M., Ustyugova, G. V., Koldoba, A. V., & Lovelace, R. V. E. 2004, ApJ, 616, L151

[88] Romanova, M. M., Ustyugova, G. V., Koldoba, A. V., & Lovelace, R. V. E. 2005, ApJ, 635, L165

[89] Romanova, M.M, Ustyugova, G.V., Koldoba, A.V., Chechetkin, V.M., Lovelace, R.V.E. 2002, ApJ, 578, 420

[90] Rothstein, D.M., & Lovelace, R.V.E. 2008, ApJ, 677, 1221

[91] Rubin, V.C. 1994a, AJ, 107, 173

[92] Rubin, V.C. 1994b, AJ, 108, 456

[93] Rubin, V.C., Graham, J.A., Kenney, J.D.P. 1992, ApJ, 394, L9

[94] Ryu, D., Jones, T.W., Frank, A., 1995, ApJ, 442, 228.

[95] Sage, L.J., & Galletta, G., 1994, ApJ, 108, 1633S.

[96] Sauty, C., Cayatte, V., Lima, J. J. G., Matsakos, T., & Tsinganos, K. 2012, ApJ, 759, L1

[97] Shafranov, V.D., 1966, Reviews of PLasma Physics, 2, 103.

[98] Shakura, N.I., & Sunyaev, R.A. 1973, A&A, 24, 337

[99] Stepanovs, D., Fendt, C., Sheikhnezami, S., 2014, ApJ, 796,29.

[100] Stute, M., Gracia, J., Vlahakis, N., Tsinganos, K., Mignone, A., & Massaglia, S. 2014, MNRAS, 439: 3641

[101] Tang, Y.W., Guilloteau, S., Pietu, V., Dutrey, A., Ohashi, N., & Ho, P.T.P., 2012, A & A, 547, A84

[102] K.S. Thorne, R.H. Price, D.A. Macdonald, Black Holes: The Membrane Paradigm, 1986.

[103] Tzeferacos, P., Ferrari, A., Mignone, A., Zanni, C., Bodo, G., Massaglia, S., 2009, MNRAS, 400, 820.

[104] Tzeferacos, P., Ferrari, A., Mignone, A., Zanni, C., Bodo, G., Massaglia, S., 2013, MNRAS, 428, 3151.

[105] D.A. Uzdensky, 2004, ApJ 603:652-662.

[106] Ustyugova, G.V., Koldoba, A.V., Romanova, M.M, Lovelace, R.V.E. 2006, ApJ, 646, 304

[107] Ustyugova, G.V., Lovelace, R.V.E., Romanova, M.M., Li, H., & Colgate, S.A. 2000, ApJ, 541, L21

[108] van Ballegooijen, A. A. 1989, in Accretion Disks and Magnetic Fields in Astrophysics, ed. G. Belvedere (Dordrecht: Kluwer), 99

[109] Velazquez, P.F., Riera, A., Raga, A.C., Toledo-Roy, J.C., 2014, ApJ, 794, 128.

[110] Vidotto, A.A., Gregory, S.G., Jardine, M., Donati, J.F., Petit, P., Morin, J., Folsom, C.P., Bouvier, J., Cameron, A.C., Hussain, G., Marsden, S., Waite, I.A., Fares, R., Jeffers, S., do Nascimento, J.D., 2014, MNRAS, 441:2361-2374.

[111] von Rekowski, B., Brandenburg, A., Dobler, W. & Shukurov, A. 2003, A&A, 398, 825

[112] von Rekowski, B., Brandenburg, A., 2006, Astron. Nachr, 327, 53.

[113] Wang, J.C.L., Sulkanen, M.E., & Lovelace, R.V.E. 1990, ApJ, 355, 38

[114] Wang, J. C., Sulkanen, M.E, Lovelace, R.V.E., 1992, ApJ, 390, 46

[115] S. Weinberg, Gravitation and Cosmology:Principles and Applications of the General Theory of Relativity, 1972.

[116] Whelan, E.T., Bonito, R., Antoniucci, S., Alcala, J.M., Giannini, T., Nisini, B., Bacciotti, F., Podio, L., Stelzer, B., Comeron, F., 2014, A&A, 565, A80

[117] White, M.C., Bicknell, G.V., McGregor, P.J., Salmeron, R., 2014, MNRAS, 442, 28.

[118] Woitas, J., Ray, T.P., Bacciotti, F., Davis, C.J., & Eislöffel, J. 2002, ApJ, 580, 33

[119] Zanni, C., Ferrari, A., Rosner, R., Bodo, G., Massaglia, S., 2007, A&A 469, 811828

[120] Zinnecker, H., McCaughrean, M. J., & Rayner, J. T. 1998, Nature, 394, 862